



HAL
open science

Nervous system exploration using tractography to enhance pelvic surgery in children with tumors and malformations

Cecile Muller

► **To cite this version:**

Cecile Muller. Nervous system exploration using tractography to enhance pelvic surgery in children with tumors and malformations. Neuroscience. Université Paris Cité, 2020. English. NNT : 2020UNIP5066 . tel-04085364

HAL Id: tel-04085364

<https://theses.hal.science/tel-04085364>

Submitted on 28 Apr 2023

HAL is a multi-disciplinary open access archive for the deposit and dissemination of scientific research documents, whether they are published or not. The documents may come from teaching and research institutions in France or abroad, or from public or private research centers.

L'archive ouverte pluridisciplinaire **HAL**, est destinée au dépôt et à la diffusion de documents scientifiques de niveau recherche, publiés ou non, émanant des établissements d'enseignement et de recherche français ou étrangers, des laboratoires publics ou privés.

Université de Paris

École doctorale Interdisciplinaire Européenne

FRSFR Frontières de l'Innovation en Recherche et Education

ED 474

Laboratoire UMRS1163 IHU Imagine-Institut des Maladies Génétiques

Exploration de l'anatomie du système nerveux pelvien par tractographie pour l'amélioration de la prise en charge chirurgicale d'enfants atteints de tumeurs et malformations pelviennes.

Nervous System Exploration Using Tractography To Enhance Pelvic Surgery In Children With Tumors and Malformations

Par Cécile Muller

Thèse de doctorat de NEUROSCIENCES ET TROUBLES

NEURONAUX

Dirigée par Isabelle Bloch et par Sabine Sarnacki

Présentée et soutenue publiquement le 4 septembre 2020

Devant un jury composé de :

Guillaume Morel, Professeur des Universités, Sorbonne Université (Rapporteur)

Eric Vibert, PUPH, Université Paris Sud (Rapporteur)

Nicholas Ayache, Professeur des Universités, INRIA (Examineur)

Hervé Brisse, Docteur en Médecine, Institut Curie (Examineur)



Except where otherwise noted, this is work licensed under <https://creativecommons.org/licenses/by-nc-nd/3.0/fr/>

Contents

1	Introduction	9
2	State of the art	15
2.1	Pediatric surgery	16
2.1.1	Pediatric surgical pathologies	16
2.1.2	Surgical complications of pelvic surgery	29
2.1.3	Development of nerve sparing surgery: from post-mortem dissections to in vivo radiology	29
2.1.4	Pelvic nervous network (PNN) anatomy	31
2.2	Pediatric MRI	35
2.2.1	Pelvic MRI	35
2.2.2	Diffusion weighted imaging (DWI)	39
2.2.3	Diffusion tensor imaging (DTI)	39
2.2.4	Tractography segmentation	43
2.2.5	Tractography of peripheral nerves: state of the art	44
2.3	Conclusion	48
3	Clinical data characteristics and MRI acquisition	49
3.1	Patients and pathologies	49
3.1.1	Tumors	52
3.1.2	Malformations	55
3.2	Definition of the MRI image acquisition parameters	60
3.3	Database organization	62
3.4	Conclusion and Discussion	63
4	Segmentation, 3D visualization and portability work-flow	65
4.1	Segmentation and 3D visualization	65
4.1.1	Software benchmark	65
4.1.2	Semi-automatization of the segmentation process	67
4.2	Portability work-flow	68
4.3	Conclusion	71
5	Pre and post-processing methodology for DTI tractography of pelvic nerves	73
5.1	DTI ROI based tractography: preliminary study	74
5.1.1	Introduction	74
5.1.2	Method	74
5.1.3	Results	75
5.1.4	Conclusion on the preliminary study and proposed solutions	76
5.2	Pre and post-processing work-flow for pelvic diffusion images	77
5.2.1	Pre-processing	77
5.2.2	Post-processing	79
5.3	Choice of the parameters of the diffusion sequence	80
5.3.1	Method	80

5.3.2	Results	82
5.4	Design of specific description of the pelvic nervous network (PNN) anatomy	88
5.4.1	Introduction	88
5.4.2	Description methodology	88
5.4.3	Somatic System	89
5.4.4	Autonomous system: S = Sympathetic and ParaS = Parasympathetic.	94
5.5	Anatomy-aware tractography method: the Pelvic Query Language (PQL)	97
5.5.1	Introduction	97
5.5.2	PQL principle	98
5.5.3	PQL validity tested on a ROI based tractogram	103
5.5.4	PQL validity tested on a whole pelvis tractogram tractogram	106
5.5.5	Qualitative and quantitative comparison between PQL and ROI based tractograms	119
5.6	Conclusion and Discussion	122
6	Exploring the pelvic nervous network using tractography in pediatric patients with ano-rectal malformations	123
6.1	Introduction	123
6.2	Methods	124
6.2.1	Population description and imaging protocol of the study	124
6.2.2	Objective of the study	128
6.2.3	Evaluation measures and normalization for group comparison	128
6.2.4	Statistical tools	133
6.3	Results	134
6.3.1	Global description	134
6.3.2	Symmetry study	140
6.3.3	ARM vs control	144
6.3.4	ARM with SA or SD vs ARM without SA or SD	146
6.3.5	Low ARM vs High ARM	151
6.4	Conclusion and Discussion	155
6.5	Clinical validation of tractography: a case report	158
6.5.1	Introduction	158
6.5.2	Clinical history	158
6.5.3	Imaging protocols	158
6.5.4	Results	158
6.5.5	Discussion	160
6.5.6	Conclusion	160
7	Validation of tractography by Light Sheet Fluorescent Microscopy in a human fetal model	163
7.1	Introduction	163
7.2	Methodology	165
7.2.1	MRI	165
7.2.2	Pathological examination	165
7.2.3	Light Sheet Fluorescent Microscopy (LSFM)	167
7.2.4	Image post-processing	169
7.3	Results	170
7.3.1	Fetus 1	170
7.3.2	Fetus 2	171
7.3.3	Fetus3	171
7.3.4	Fetuses 4 and 5	172
7.3.5	Fetus 6	173
7.3.6	Fetus7	174
7.3.7	Comparison between tractography and LSFM results	175
7.4	Conclusion and Discussion	176

8	Conclusion and Perspectives	179
8.1	Conclusion	179
8.2	Perspectives	181
9	Appendix	183
9.1	Figures	183
9.2	Publications	191



Acknowledgments

Je voudrais tout d'abord remercier mes directrices thèse, Mesdames Isabelle Bloch et Sabine Sarnacki, pour leur soutien et leur encadrement tout au long de ce travail de thèse, et ce malgré les diverses péripéties !

Je voudrais également remercier toutes les personnes sans qui ce travail n'aurait pas été possible:

- les membres du service de chirurgie pédiatrique de l'hôpital Necker: Jean-Baptiste Marret, Eva Miller, Quoc Peyrot, Pierre Meignan, Thomas Blanc Cécilia Crétolle.

- les membres du service de radiologie pédiatrique de l'hôpital Necker: Nathalie Boddaert, Laureline Berteloot, David Grévent.

- Bétina Bessières du service de foetopathologie de l'hôpital Necker.

- les membres du LTCI de Telecom Paris: Pietro Gori, Alessio Virzi, et une mention spéciale pour Alessandro Delmonte, pour son aide, son écoute et sa patience!

- les membres de l'Institut de la vision, pour leur accueil et leur bienveillance à mon égard: Morgane Belle et Alain Chedotal.

Merci à Nicholas Ayache et Luc Soler pour leurs conseils avisés et leurs encouragements tout au long de mon travail.

Je remercie également Olivier Nosjean du laboratoire Servier, pour son soutien moral et financier pendant cette thèse.

Je voudrais également remercier de tout coeur mon compagnon Benjamin, pour son amour, son écoute, son accompagnement, et son aide pour la partie statistique de mon travail.

Enfin, je voudrais remercier tous mes proches, mes parents, ma famille et mes amis, qui m'ont écoutée avec patience, soutenue dans les moments difficiles, encouragée à tenir bon, à garder confiance en moi et en ma capacité à mener ce travail à son terme. Merci Michel, Lise, Caroline, Rachel, Anne-Laure, Céline, Guillaume, Cécile, Lucie, Jacques, Georges, Florian, Stephanie, et tous les autres...

A toi Joachim.

Abstract

Pelvic surgery raises the challenge of preservation of nerves that handle urinary, genital and digestive functions, especially in children where these structures may be modified by large tumors or rare malformations. Both functional outcome and quality of life heavily depend on the accurate appraisal of the pelvic nervous network anatomy during the surgical management, either pre-, per and post-operatively.

Recent works on 3D nerve visualization, that rely on cadavers' dissections or intra-operative use of probes detecting myelin-binding fluorophores, do not provide pre- or post-operative analysis of the pelvic nervous anatomy. Magnetic resonance neurography requires a slice by slice manual segmentation of the nerves.

Diffusion MRI, associated with tractography algorithms, is currently the only technique allowing for in-vivo exploration of the nervous network with no need for manual nerve segmentation. In contrast to brain imaging that motivated a lot of work, only few studies focus on peripheral nerves visualization.

In collaboration with pediatric radiologists and image processing researchers from Telecom ParisTech school, we propose in this thesis a method for pelvic tractography analysis based on patient-specific organ segmentation. First tested on healthy subjects, this method is then applied to a series of 40 pediatric patients presenting pelvic malformations and tumors. Both qualitative and quantitative analysis of pelvic tractograms are presented and discussed. In collaboration with researchers from the Institut de la Vision, we also present the results of an attempt to validate tractography results by Lightsheet microscopy 3D immunochemistry in a human fetal model. Finally, we present how the tractography results are integrated in the 3D patient specific models which are used in clinical practice.

Résumé

La chirurgie pelvienne pose le défi de la préservation des nerfs qui gèrent les fonctions urinaires, génitales et digestives, en particulier chez les enfants où ces structures peuvent être modifiées par de volumineuses tumeurs ou de malformations rares. Tant le résultat fonctionnel que la qualité de vie dépendent fortement de l'évaluation précise de l'anatomie du réseau nerveux pelvien pendant la prise en charge chirurgicale, que ce soit en pré, per ou post-opératoire.

Les travaux récents sur la visualisation nerveuse en 3D, qui reposent sur les dissections de cadavres ou l'utilisation peropératoire de sondes fluorescentes se liant à la myéline, ne fournissent pas d'analyse pré ou postopératoire de l'anatomie nerveuse pelvienne. La neurographie par résonance magnétique nécessite elle une segmentation manuelle coupe par coupe des nerfs.

L'IRM de diffusion, associée aux algorithmes de tractographie, est actuellement la seule technique permettant l'exploration in vivo du réseau nerveux sans nécessité de segmentation nerveuse manuelle. Contrairement à l'imagerie cérébrale qui a motivé beaucoup de travail, seules quelques études se concentrent sur la visualisation des nerfs périphériques.

En collaboration avec des radiologues pédiatres et des chercheurs en traitement d'images de l'école Télécom ParisTech, nous proposons dans cette thèse une méthode d'analyse de la tractographie pelvienne basée sur la segmentation d'organes pelviens spécifiques au patient. D'abord testée sur des sujets sains, cette méthode est ensuite appliquée à une série de 40 patients pédiatriques présentant des malformations pelviennes et des tumeurs. L'analyse qualitative et quantitative des tractogrammes pelviens est présentée et discutée. En collaboration avec des chercheurs de l'Institut de la Vision, nous présentons également les résultats d'une tentative de validation des résultats de tractographie par microscopie Lightsheet en immunohistochimie 3D dans un modèle foetal humain. Enfin, nous présentons comment les résultats de la tractographie sont intégrés dans les modèles 3D spécifiques aux patients qui sont utilisés en pratique clinique.

Chapter 1

Introduction

Pelvic pediatric surgery raises the challenge of preservation of nerves that handle urinary, genital and digestive functions, especially in situations where these structures may be modified by tumors or malformations. Each pathology is a rare disease if considered alone, but their variety and their frequency in children turn them into a real topic and a very interesting area of research for pediatric surgeons. Our goal is to ensure these children an optimal surgical result, which entails negative margins and long term survival in the case of a tumor, the reconstruction of an anatomy close to normality in a case of a malformation, while preserving the existing healthy tissues, especially nervous networks. This balance is mandatory to guarantee the best long term results, in terms of continence and life quality.

Achieving this goal highly benefits from surgical centers with a high income of patients presenting rare diseases. These centers develop an expertise which allows a surgical management precisely adapted to each child. Indeed, the pediatric surgery department of Necker hospital handles one of the largest cohorts of children in France with various abdomino-pelvic tumors, such as neuroblastoma [13, 36, 99, 100], rhabdomyosarcoma [46, 63], sacro-coccygeal tumors [66], ovarian tumors [177], and neonatal cancer [155]. Surgeons of the department indeed care about long term issues such as fertility [101, 176], and surgical sequelae in children with cancer [163]. Moreover, the rare disease center MAREP associated with this department (centre de référence **M**alformations **A**no-**R**ectales **E**t **P**elviennes) is one of the leading centers on the subject [12, 61, 179] with a broad range of expertise on many aspects, such as quality of life [54, 129], management planning for rare disease centers [60], genetics insights [62], anatomical correlations with other malformations [145] or research on possible etiological risk factors [216]. As a consequence, we want to enrich this existing expertise by focusing on pelvic nerve preservation.

Nerve preservation, or so called "nerve sparing surgery" techniques, aim at avoiding functional morbidity such as urinary or digestive incontinence and fertility or sexual dysfunction. Surgeons dealing with pelvic pathologies in adults mostly developed these techniques based on cadavers and fetal dissections, in order to enhance the management of prostate cancer [29, 151, 159], rectal cancer [42, 85, 108], and for the treatment of endometriosis or cervical cancer in women [106, 119, 221]. In pediatric surgery, no specific technique has been developed regarding the rarity of pelvic malformations and tumors and the high anatomical variations in each type. Few nerve sparing techniques in the field of perineal surgery for malformations such as hypospadias repair [17, 19, 20] or feminizing genitoplasty have been reported [21, 88, 180]. None have been developed for the inner pelvis.

The pelvis presents a complex 3D structure standing at the crossroads of the digestive, urinary and genital channels richly vascularized and innervated by complex networks. Somatic functions of pelvic organs are ensured by the sacral plexus, originating from the spine and issuing from L5 vertebral canal and S1 to S4 sacral holes. Autonomous functions are ensured by the pre-sacral sympathetic/parasympathetic networks originating from the neural crest cells migration. Being directly involved in both conscious and unconscious motricity and sensitivity of organs and skin, the main nerve bundles to be preserved during surgery are the sacral and pudendal plexuses, the pudendal nerve, and the inferior hypogastric plexus. By nature, malformation and tumors modify this normal anatomy and display a high variability linked to age and genetic background, explaining that an optimal surgical gesture requires both expertise and solid anatomical knowledge. Moreover, the complexity of the pelvic nervous network (PNN) makes its thorough understanding quite confidential, and limited to the area of expertise of a few surgeons and anatomists. Still, their knowledge stays theoretical based on anatomical textbooks, lacking means of pre-, per- or post-operative radiological work-up. We are indeed unable to localize precisely the nervous network for each patient specifically and to adapt our surgical management in consequence.

We must underline the absence of existing radiologic atlas for PNN, as compared to brain anatomical atlases. This is the consequence of the nerves being quite thin structures, which are not easily seen using conventional tools such as computer tomography scanner (CT-scan) or classic magnetic resonance imaging (MRI). A non-invasive technique representing precisely the pelvic nervous anatomy would however be of huge interest for the surgeon in pre-operative planning, image guidance for nerve sparing surgery, and follow-up.

Recent works on 3D nerve visualization [?, 28] or intra-operative use of probes detecting myelin-binding fluorophores [57], do not provide methods for pre- or post-operative analysis of patient specific pelvic nervous anatomy. Among imaging tools, MRI is the reference for imaging the pelvis and specific MRI-derived techniques may provide a good contrast to visualize the nerves. For example, pelvic MRI neurography as presented in [124] is a promising technique but stays time consuming, and requires a high radiologic expertise to perform the slice by slice manual segmentation of the nerves.

Diffusion MRI, associated with tractography algorithms, is currently the only non-invasive technique allowing for in-vivo exploration of the nervous network [24] with no need for manual nerve segmentation. It uses the tendency of water molecules to move in a preferable direction (anisotropy) along linear structures such as nerve fibers under a magnetic field. Tractography is the method of visualizing this anisotropy in 3D, the result resembling nervous tracts. In contrast to brain imaging that motivated a lot of work during the past decades, only few studies focused on peripheral nerves, and especially PNN [82, 93, 199]. These preliminary studies concern only a few cases, use a classic region-of-interest (ROI) based method for tractography, show promising results on the proximal sacral nerves but not on distal nerves such as the pudendal nerve, and fail to represent the inferior hypogastric plexus. To our knowledge, no study has been performed using a whole pelvis tractogram associated with segmentation methods, similar to state of art methods in brain tractography in adults and a fortiori in children, a population that arises even more challenges in terms of MRI acquisition parameters, artifacts management, resolution, control groups etc.

Aside from its advantages, tractography stays a mathematical representation of the anisotropy of the tissue within a determined space of the diffusion image. The correspondence with the anatomical truth shall still be proved and verified with comparison studies using immunochemistry. A few works in brain anatomy compared standard histology or immunochemistry slices with fractional anisotropy (FA) maps [139], or tractograms with post-mortem surgical dissections [79]. Some authors focused on 3D immunochemistry of the pelvic nerves in fetuses [143], using a tedious process of manual slice by slice segmentation and registration. But there is no study to date in a human model matching 3D tractography and 3D immunochemistry, not in brain, and even less in PNN.

3D visualization of nerves makes even more sense when integrated in a patient specific 3D model. The relationships between nerves and organs such as bones, muscles, bladder, rectum or vessels is at the center of the surgical concern. Moreover, these 3D patients specific models are the first steps towards image guided surgery, which is the current revolution in our field, mixing the latest imaging and non-invasive surgical techniques. 3D patient specific models have proved to reduce the time required for the surgery by giving the surgeon a major awareness of the patient anatomy and of the relationships between the surgical target and the surrounding structures. As demonstrated by the surgeon's experience, the more the anatomy of the surgical region of interest is complex (like the pelvis), the more a complete 3D reconstruction is useful. This gives the surgical staff a powerful planning tool to improve the management of critical interventions, as presented in a few examples from the general surgical field in [81, 127].

Some surgical specialties are pioneers in image guided surgery, like neurosurgery, closely followed by ear-nose and throat (ENT) surgery, orthopaedic surgery or cardio/endo-vascular procedures, and use in daily clinical routine 3D visualization and stereo-tactic navigation processes. These innovations are not available for surgeons dealing with general surgery. The reason is that automatic synchronisation of the 3D patient specific modeling of soft, heterogeneous and deformable structures, that move during the surgery according to breathing and spontaneous bowel movement still remains a technological challenge. This approach stays in the research field and is essentially developed in expert centers for adult surgical care like IRCAD Institute in Strasbourg, or EndoCAS navigator platform in Pisa [11, 130, 131, 135, 184]. To our knowledge, there is no surgical pediatric program aiming at integrating advanced imaging techniques in the clinical management of pediatric patients. There is therefore a gap to be filled, taking into account the very specific anatomy and the rarity of pediatric pathologies.

Pediatric general surgeons do not have even access in daily clinical practice to the mandatory first step of image guided surgery, the patient specific 3D modeling. This can be obtained by post processing various types of medical images, like CT-scan, US scan, endo-vascular X-Rays, or MRI. Most common and used approaches for 3D modeling are surface and volume rendering [158], but these methods based on the intensity of the voxel with no characterization of its anatomical nature are useless for the abdomen, due to the heterogeneity of the signal of the anatomical structures. Segmentation tools are mandatory to obtain a comprehensive, relevant and useful 3D abdominal model. However, most of the available segmentation and 3D modeling software with semi-automatic tools (according to the degree of user interaction required) are organ-specific, and initially designed for well contrasted structures such as brain, face, bones and vessels, in CT scan. In abdomino-pelvic MRI, the only possibility is strictly manual segmentation, which is tedious, time consuming and presents a poor intra or inter-operator reproducibility. Moreover, very few software are user-friendly for non-expert in medical imaging, such as surgeons or medical doctors. The radiologist would be the best candidate to handle these tools, but still the time of manual segmentation (a dozen hours for a whole pelvis entirely segmented manually for instance), is not compatible with his/her clinical activity, which is again mainly centered on the diagnosis phase and perfectly handled with only 2D images. On the other hand, research engineers or application engineers, which may be able to perform this 3D modeling from the technical point of view, do not possess the anatomical knowledge required for it.

Optimal tools should be quick, easy to use for non digital expert with a minimum of anatomical knowledge, efficient and robust. Their design shall arise from interdisciplinary teams of surgeons, radiologists and research engineers, who pool their expertise to built new semi-automatic tools specific to abdominal and pelvic surgery for children, as in our IMAG2 laboratory. This thesis arose from this context of research. We aim here at developing a methodology for pelvic tractography, that is usable for image guided surgery of pediatric patients with pelvic tumors and malformations. The manuscript is organized as follows:

In Chapter 2 we present the state of art about the pediatric pathologies we are dealing with, as well as their general surgical treatment, the available anatomical knowledge about PNN, and the principle of tractography and its applications in the peripheral nervous system including the PNN.

In Chapter 3 are described the database constitution with patient's clinical characteristics, and the work performed on image acquisition parameters specific to both MRI anatomical and diffusion sequences, in order to optimize the process of 3D modeling and tractography respectively.

In Chapter 4 is summarized the collaborative work with Alessio Virzi during his PhD and the Master students Jean-Baptiste Marret, Eva Mille and Quôc Peyrot on the evaluation of the segmentation results, 3D visualization and the portability work-flow required to use the 3D patient specific models in a context of daily clinical practice.

In Chapter 5 is developed a methodology for pelvic tractography segmentation, in collaboration with Alessandro Delmonte, research engineer in IMAG2 laboratory.

In Chapter 6, we apply the aforementioned method on a series of 40 pediatric patients, and describe the results from a qualitative and quantitative point of view.

In Chapter 7, a validation model of tractography is developed, by comparing tractography with 3D immuno-histochemistry data by Lightsheet microscopy, in a human fetal model.

In Chapter 8, we discuss the potential perspectives of our work.

List of abbreviations:

PNN = pelvic nervous network

ARM = ano-rectal malformation

MRI = magnetic resonance imaging

DWI = diffusion weighted imaging

DTI = diffusion tensor imaging

ROI = region of interest

SNR = signal to noise ratio

FA = fractional anisotropy

MD = mean diffusivity

WMQL = white matter query language

PQL = pelvic query language

VUR = vesico-ureteral reflux

SA = sacral agenesis

SD = spinal dysraphism

RMS = rhabdomyosarcoma

MMT = malignant mesenchymal tumor

GCT = germ cell tumor

SCT : sacro-coccygeal teratoma

NF1 = neurofibromatosis type 1

NF2 = neurofibromatosis type 2

PNST = peripheral nerve sheath tumor

ES = Ewing sarcoma



Chapter 2

State of the art

This section aims at describing the state of the art in the two fields related to the topic of the thesis: pediatric pelvic surgery, and pediatric pelvic MRI.

Section 2.1 focuses on the specificity of pediatric patients with pelvic pathology and on their surgery. Their management requires a wide range of surgeries with specific potential complications, nerve injury being a major cause. Surgeons have therefore developed several techniques of "nerve sparing surgery". These techniques benefit from the increasing knowledge of the precise PNN anatomy.

Section 2.2 summarizes the imaging protocols used in this work, namely magnetic resonance imaging (MRI) acquisitions. MRI presents many advantages, especially for pelvic imaging and in the field of pediatrics. MRI also provides useful specific sequences such as diffusion MRI which are then associated with tractography algorithms. Peripheral nerves tractography is a growing field of interest, and this section will focus on the existing work on this topic, especially in the pelvic area. A subsection will also be dedicated to tractography segmentation methods, that are of interest in the main scope of the thesis.

2.1 Pediatric surgery

2.1.1 Pediatric surgical pathologies

Abdominal and pelvic pediatric surgery mainly concerns malformations and tumors present in fetuses, newborns, infants, and teenagers [166].

2.1.1.1 Malformations

Ano-rectal malformations (ARM). The incidence of ARM is 1:5000 births, the various forms being described in Figures 2.1 and 2.2 by Alamo et al [3]. These developmental anomalies of the caudal pole not only concern the rectum opening level but also the muscular complex of levator ani muscle and anal sphincter. These two malformative characteristics determine both the surgical approach and the long term continence prognosis [61, 122]. The surgical technique is chosen depending on the level of the fistula, with an eventual supplementary abdominal approach in high ARMs. The surgical repair must replace the anal opening within the muscular complex at the right distance between the coccyx and the uro-genital openings. The post-operative management must take into account the surgical findings, the quality of the muscular complex, and the presence or not of a sacral anomaly or a spinal dysraphism. In order to address these major concerns, the preoperative anatomical description first relied during the past decades on classical 2D contrasted X-ray views as seen in Figure 2.3, featuring the organ cavities with the level of the malformation. However, adequate information can be tricky to obtain without an appropriate technique of contrast filling of the colon, as recently emphasized by Kraus et al [114]. Adequate occlusion of the stoma may be difficult to obtain, and impacted meconium within the fistula may prevent the contrast liquid to show the level of communication between the digestive and the urinary tract. Nowadays, more insights can be given by pelvic MRI, as developed in Section 2.2. Its main advantage is to provide within a single radiologic exam a complete information about the type of ARM and a description of the surrounding bony, muscular and spinal structures.

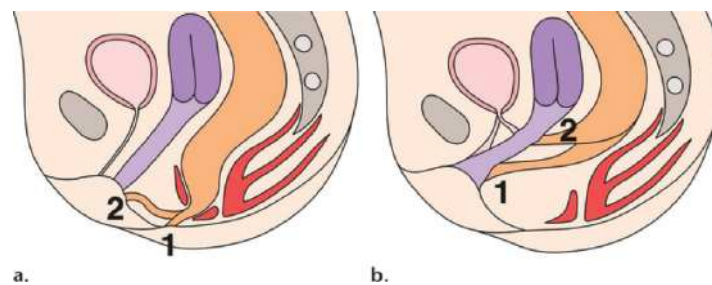


FIGURE 2.1: Potential locations of fistulas in females with ARMs according to the Krickenbeck classification. **(a)** Low-type ARMs have an external opening in the perineum (1) or vestibular area (2). **(b)** Cloacal anomaly is a complex anatomic disorder that manifests as a unique external perineal opening with a short (1) or long (2) common canal for the genital, urinary, and digestive systems. Isolated rectovaginal fistulas are extremely rare and are considered a variant of cloacal anomaly [3].

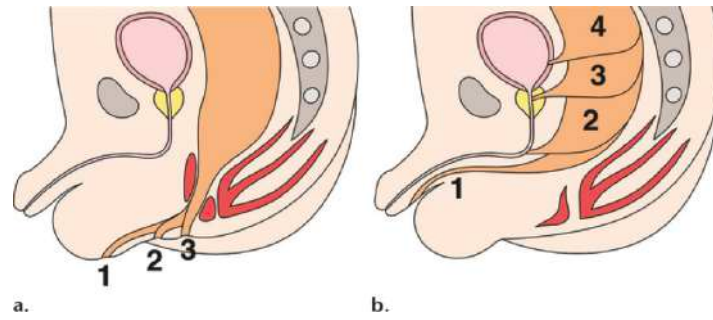


FIGURE 2.2: Potential locations of fistulas in males with ARMs according to the Krickbeck classification. (a) Low-type ARMs have an external anocutaneous opening in the scrotum (1) or perineum (2, 3). (b) Intermediate- and high-type ARMs extend anteriorly to the base of the penis (1), the bulbar (2) or prostatic (3) urethra, or the urinary bladder (4) [3].

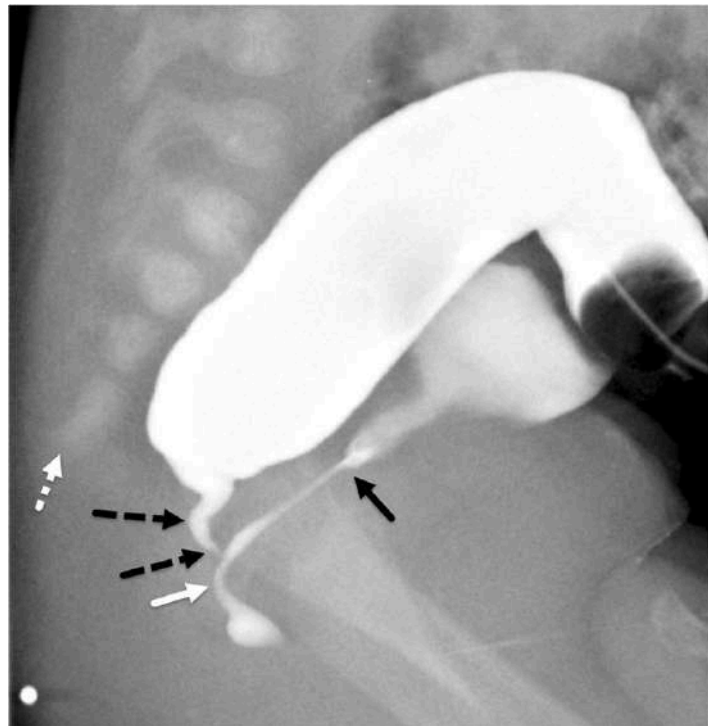


FIGURE 2.3: Distal colostogram in a 1-month-old boy showing the recto-prostatic urethral fistula (dashed black arrows), which is proximal to the bend of the urethra (solid white arrow) and below the presumed bladder neck (solid black arrow), although the bladder is not that well distended and the bladder neck might be slightly more caudal than shown. Note that the entire distal colon segment, distal spine (dashed white arrow) and radio-opaque marker for anal dimple are all in view in this true lateral image (femurs overlapping) [114].

Some **urological malformations** are common to both female and male children, while others, involving also the genital system, are obviously gender specific. Common malformations to both sex are mostly represented by:

- vesico-ureteral reflux (VUR), which has a reported incidence of 1% in general population of children, augmented to 30% in children with an episode of urinary tract infection or a sibling with VUR, and around 25% with an abnormal prenatal US-scan [2, 166]. The main surgical goal is to suppress the reflux by adequately re-positioning the ureteral openings within the posterior bladder muscular wall, in order to prevent urinary infections and renal damage;
- neurogenic bladder, which is mostly related to acquired or congenital lesions that affect bladder innervation. Acquired lesions may be the result of brain, spinal cord, or pelvic nerves injury, or the effect of tumor, infection or vascular lesions affecting these same structures. Congenital lesions include spina bifida, neural tube defects (from occult spinal dysraphism to myelomeningocele), degenerative muscular disorders, cerebral palsy, sacral agenesis, and ARM [10, ?, 166]. The main surgical goal is to provide a bladder of adequate volume, that may be emptied either naturally or by the mean of intermittent catheterizations, achieve social continence and prevent renal dysfunction. The choice of the surgical technique and the post-operative management therefore rely on an accurate pre-operative evaluation of bladder function, spine status and pelvic nerve impairment.

In girls, most common malformations are:

- urogenital sinus, that may be isolated or associated with a disorder of sexual differentiation [4]. In this latter case, most of the patients present a congenital adrenal hyperplasia (reported prevalence of 1/10,000, see Figure 2.4). Aside of the endocrinologic management, the main surgical goal is to provide an acceptable external genitalia aspect and two different openings for urinary and genital systems, using the adequate surgical technique depending on the severity of the case;
- female hypospadias, only represented in the literature by a few case reports [4, 111];
- gynecological malformations, that present a wide scope of variations of the utero-vaginal anatomy. Their analysis, classification and understanding require solid basic knowledge in the developmental embryology of Wolff and Müller ducts [4], as shown in Figure 2.5. The most well-known pathology (about 1/4000 female births) is represented by the Rokintansky-Küster-Hauser syndrome, that consists in lateral and partial Müllerian aplasia. Both surgical technique and patient information about fertility issues rely on an adequate pre-operative assessment of the precise type of the malformation.

In boys, most common malformations are:

- posterior urethral valve: it is the most common anomaly of fetal lower urinary tract obstruction that is characterized by an abnormal congenital obstructing membrane that is located within the posterior urethra associated with significant obstruction of the male bladder restricting normal bladder emptying (reported incidence of 1/25 000 male births [?]). Accurate pre- and post-natal evaluation of the bladder and uretere dilatation and also renal impairment are mandatory for an optimal surgical management;
- hypospadias: it is a displacement of the urethral meatus on the ventrum of the penis, see Figure 2.6. This abnormality is associated with a varying bent, twisted penis and opened dorsal prepuce, and presents a reported incidence from 5 to 20/10 000 births depending on the countries [?]. Surgical expertise is especially mandatory in this type of genital malformation to ensure a good prognosis. Indeed, both cosmetic result, and erectile function depending on penile innervation preservation are the main goals of surgical repair.

Disorders of sexual differentiation are a specific field of expertise at the frontier of both genders [118]. The main challenges focus on ethics for gender assignment, endocrinology and surgery of the external genital organs, which is outside the scope of the inner pelvis anatomy.

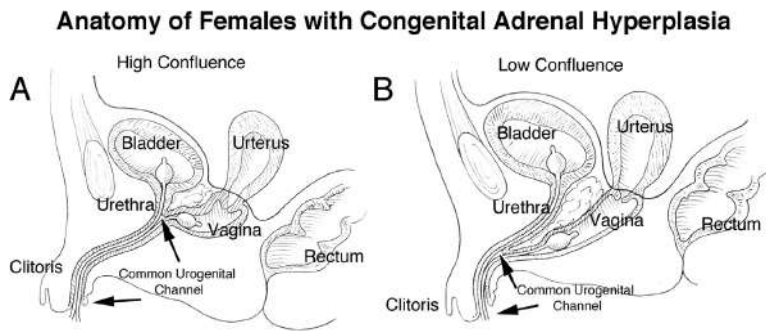


FIGURE 2.4: Schematic representation of anatomy of females with virilization secondary to congenital adrenal hyperplasia. (A) High confluence. Note that the urethra and vagina meet close to the bladder neck. (B) Low confluence. Note that the urethra and vagina meet closer to the opening of the common urogenital sinus on the underside of the hypertrophied clitoris [22].

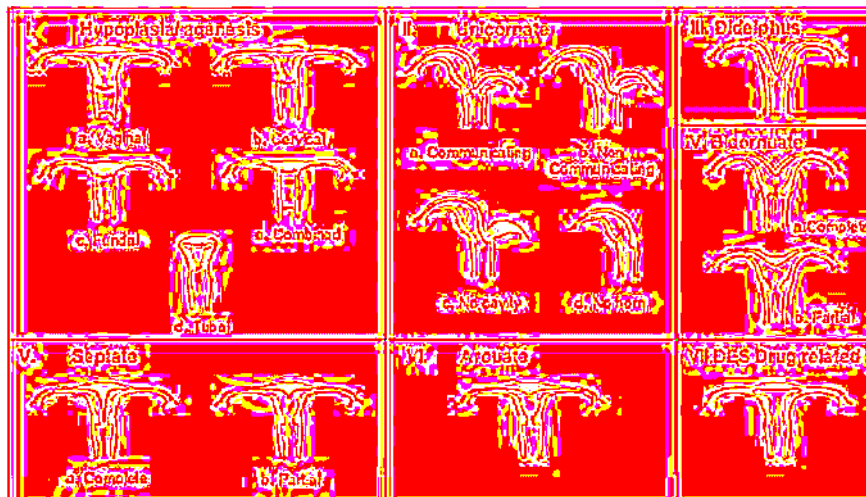


FIGURE 2.5: The classification system of Müllerian duct anomalies used by the American Fertility Society [44].

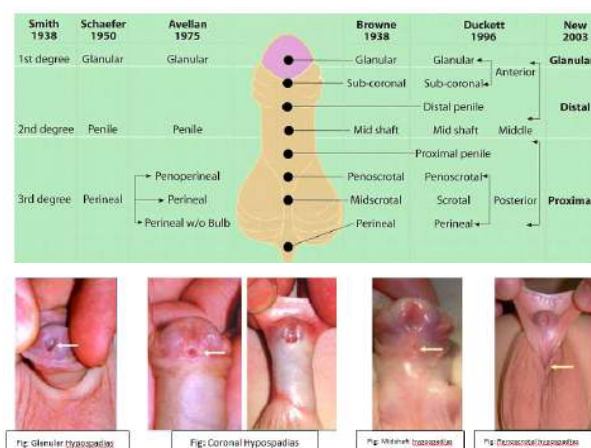


FIGURE 2.6: The classification of hypospadias [?].

Abdomino-pelvic wall defects cover a broad range of malformations [?], the extrophy-epispiadias complex being the most complicated to surgically deal with. It is a spectrum of rare genito-urinary malformations (reported incidence of 1/10 000 births [?]) ranging in severity from epispiadias and classical bladder exstrophy to exstrophy of the cloaca as the most severe form. Depending on severity, it may involve the urinary system, the musculo-skeletal system, the pelvis, the pelvic floor, the abdominal wall, the genitalia and sometimes the spine and the anus. The global appreciation in 3D of the malformation is currently at the center of the latest research on this topic: accurately evaluate pre-and post-operatively the bony, muscular and nervous structures should ensure the best choice in terms of surgical technique and overall management [187, 192].

As this work deals with malformations of the caudal part of the body, and focuses more specifically on the pelvic innervation, the anomalies of the distal part of both bone and spine should also be here acknowledged: sacral agenesis and spinal cord dysraphism. Indeed, an abnormal distal spine or sacrum may be concomitant to the abnormal development of the pelvic nerves.

Sacral agenesis carries an estimated prevalence of 1 per 100,000 births. Mottet et al [144] recently performed an extensive review on this pathology, and proposed a systematic prenatal approach based on nine etiologic items: clinical context, type of sacral agenesis, associated spinal cord malformations, mobility of lower limbs, investigation of the pre-sacral region, analysis of gastrointestinal tract, analysis of the genito-urinary tract, associated vertebral defects, and cytogenetic analysis. They concluded that sacral agenesis is rarely isolated, with commonly associated ano-rectal and genito-urinary malformations, their type defining the continence prognosis. In the specific case of ano-rectal malformations, expert surgeons promoted the use of the sacral ratio on X-Rays, as seen in Figure 2.7, in order to enhance both the diagnosis and the prediction of the prognosis of the patients [121, 161]. It may also be a warning sign of spinal cord dysraphism, that should be investigated either pre- and post-natally with a spine MRI.



FIGURE 2.7: Sacral ratio (SR) calculation on face and profile X-Ray views of the sacrum: On the face view (left image), normal $SR = BC/AB = 0.74$; on the profile view (right image), normal $SR = BC/AB = 0.77$ [161].

Spinal cord dysraphism classification is a subject of debate among radiologists and neurosurgeons, aside of the classical open/closed dysraphism distinction [194, 223]. From an embryological point of view, the dysraphism associated with an ano-rectal malformation happens to be secondary to an accident that occurred during the secondary neurulation, except for the short spinal cord which occurs during gastrulation [195]. Most frequent closed dysraphism are a spinal lipoma associated or not with a tethered cord, a low conus medullaris or a short spinal cord [144, 145, 154], as seen in Figure 2.8. When a patient with an ano-rectal malformation also presents a spinal dysraphism, the whole surgical management must be adapted to the type of the dysraphism, according to the need for neurosurgery and the known prognosis in terms of continence [69, 121]. In the same way, any anatomical investigation of the pelvic peripheral nerves and any interpretation of the radiologic results must take into account the spine status: the presence and the type of the dysraphism if present.

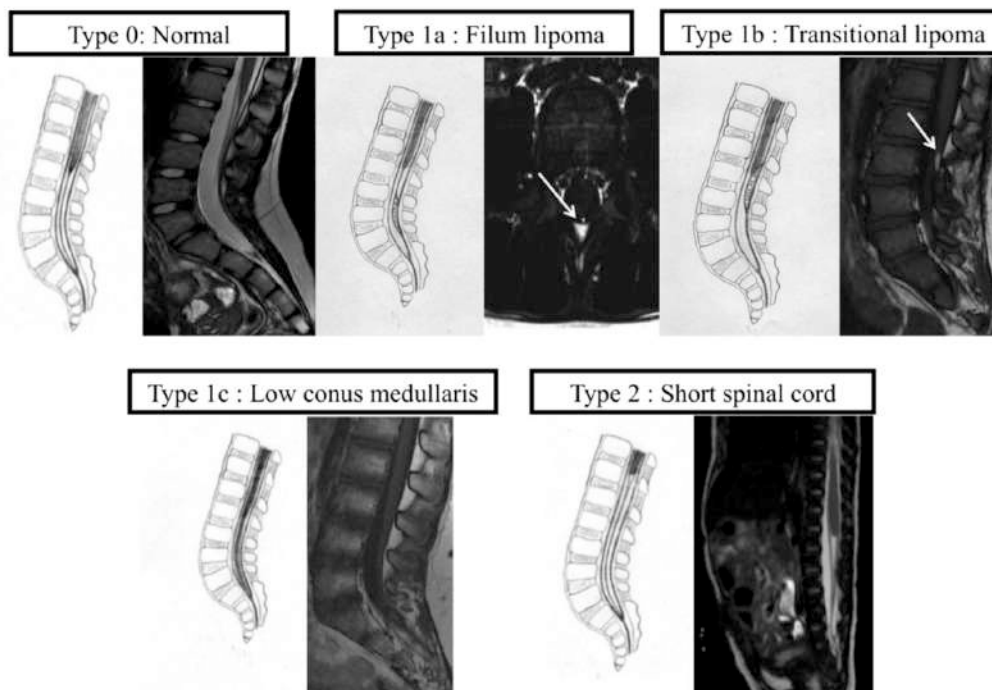


FIGURE 2.8: Dysraphism classification, showing schematic drawings and corresponding sagittal view on MRI. Type 0: Normal spine. Type 1a: Filum lipoma: the lipoma is situated exclusively on the filum. Type 1b: Transitional lipoma: the lipoma is situated on both the filum and the distal part of the spine. Type 1c: Low conus medullaris: there is a lack of filum, the spine extends till the sacrum. Type 2: Short spinal cord: the spine is cut around the 8th dorsal vertebra, with a lack of filum, as it can be seen in cases of real regression syndrome or sirenomelia [145].

A pelvic pathology that typically stands at the frontier of tumor and malformation is **the Currarino syndrome** [65]. It is an autosomal dominant (MNX1(HLXB9) homeobox gene found in 1998 [174]) congenital malformation characterized by three main clinical features: an anterior sacral bone defect (sickle-shaped sacrum or sacral agenesis below S2), an ARM, and a pre-sacral mass (anterior meningocele, teratoma or rectal duplication). Additional associated malformations have been described, like renal or ureteral duplications, hydronephrosis, horseshoe kidney, bicornuate uterus, and also neural tube defects. Among these, the most common malformations are tethered cord and lipoma of the filum, but lipoma of the conus, dermal sinuses, and diastematomyelia have also been described [223], as seen in Figure 2.9. While there is a consensus for surgery when only an ano-rectal malformation is present, it is not the case for the management of a concomitant pre-sacral mass. A one-stage approach treating intestinal, tumoral and neurological anomalies may be proposed, if all clinical, radiological and genetic features have been correctly assessed in a expert center [64]. From an oncological point of view, 15 cases of malignant pre-sacral lesions have been recently described in a review of the literature by Rod et al [173]. The authors advocate to systematically search for the Currarino syndrome in all patients with a pre-sacral mass and to propose a removal even in asymptomatic patients.

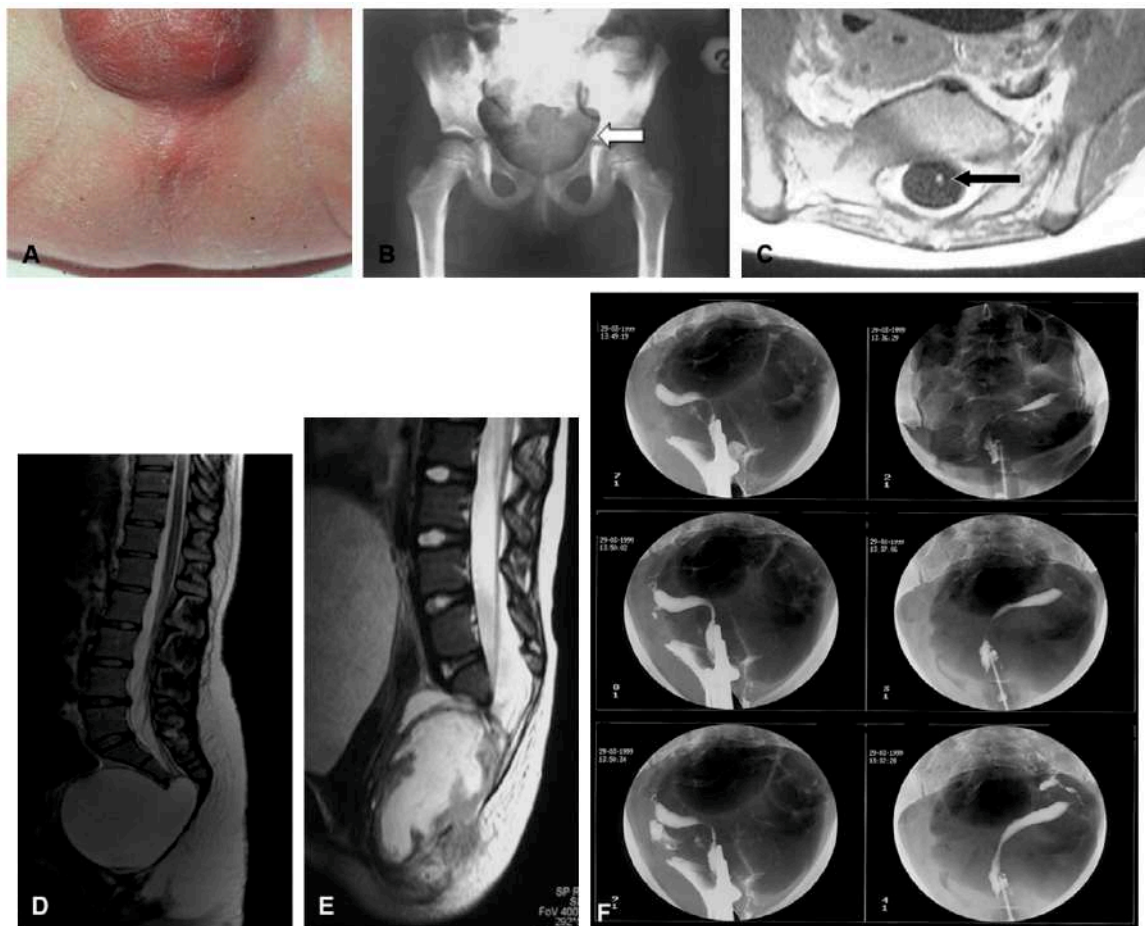


FIGURE 2.9: Currarino syndrome. (A) Photograph of anal imperforation; (B) hemi-sacral agenesis on X-Ray; (C) lipoma of the filum on axial MRI view; (D) anterior meningocele on sagittal MRI view; (E) anterior teratoma on sagittal MRI view; (F) double horn uterus with a vaginal wall on X-Ray with vaginal contrast filling [223].

2.1.1.2 Tumors

Pelvic tumors may be classified according to their pathological type and/or anatomical origin within the pelvis, with various levels of malignancy. The most frequent pelvic tumors are germ cell tumors either located in the ovary, testis or sacro-coccygeal area, urogenital rhabdomyosarcoma (RMS) and neurogenic tumors such as ganglioneuroma, ganglioneuroblastoma, and neurofibroma. More rare tumors are Ewing sarcoma of the pelvic bone, non RMS malignant mesenchymal tumors (MMT), and lymphatic tumors/malformations. Each pathology requires a specific surgical technique performed by an experienced surgeon with a good knowledge of these lesions, depending on the tumor type, its prognosis, its location/extension, and the age of the child.

1. Germ cell tumors (GCT):

- Ovarian tumors: pediatric ovarian neoplasms have an estimated incidence of 2.6 cases per 100,000 girls per year, represent 10-20% of all ovarian neoplasms and 1-2 % of all childhood malignancies [95]. The most common types are GCTs that comprise mature and immature teratoma as seen in Figure 2.10, highly malignant tumors such as Yolk sac tumor, choriocarcinoma and mixed GCT, and other rare tumor types such as dysgerminoma, seminoma and gonadoblastoma [160]. The other types of ovarian tumors aside of GCT are sex cord stromal tumors (juvenile granulosa, Sertoli/Leydig and rare theca cell tumors) and epithelial tumors (serous and/or mucinous cystadenoma). The surgical management is well defined in children, based on serum tumor markers, tumor resectability and presence or not of metastases. However, some challenging situations remain in their diagnosis and treatment: the ovarian origin of huge tumors may be difficult to assess, abdominal pain may be related to an adnexal torsion, and prognosis may be compromised by missing the malignant character of the tumor (75% of ovarian lesions are benign). A complete resection is mandatory for malignant lesions, while the preservation of healthy ovarian tissue is crucial for benign lesions. Mini-invasive techniques such as laparoscopy may be of great help for diagnosis and staging, but laparotomy is safer for tumor resection in order to avoid spillage and recurrence [177].



FIGURE 2.10: Example of an ovarian teratoma in a 12-years-old girl on a T2-weighted coronal MRI view. Source: IMAG2 laboratory.

- Testicular tumors: pediatric testicular tumors represent 1-2% of all pediatric solid tumors, with an annual incidence of 0.5 to 2 per 100,000 boys and approximately 75% are malignant. GCT represent 65-85% of them, with two thirds of the patients presenting with a benign teratoma, and the last third a malignant Yolk sac tumor as seen in Figure 2.11. Other tumors aside GCT are non germ cell tumors (NGCT) such as gonadal stromal tumors (Granulosa, Leydig, Sertoli, Mixed), gonadoblastoma and paratesticular RMS. Both diagnosis and surgical management are well defined, with serum tumor markers and abdominal imaging looking for lymph node involvement, testicular sparing surgery (enucleation) for benign lesions (Teratoma, Sertoli, Leydig, Granulosa) and inguinal radical orchidectomy in malignant lesions (Yolk sac tumor, para-testicular RMS), with associated chemotherapy and retroperitoneal lymph node biopsy according to staging [53, 166].



FIGURE 2.11: Testicular Yolk sac tumor on ultrasound scan. Case courtesy of Dr Hani Salam, Radiopaedia.org, rID: 7677.

- Sacro-coccygeal teratoma: sacro-coccygeal teratoma (SCT) is the most common site of extracranial GCT, ranging from benign mature teratoma to malignant GCT. It is also the most common neonatal tumor, with a male:female ratio of 1:4, but with a low incidence of 8 cases/100.000 newborns. Challenges are numerous in the surgical management of these primary huge extra pelvic tumors often diagnosed prenatally with a risk of heart failure, blood loss during surgery, aesthetic shape of the bottom, and functional outcome of a displaced colon/anus/vagina in case of an important intra-pelvic component as seen in Figures 2.12 and 2.13. Tumor resection within the first hours of life is the standard management for benign lesions: it must include the coccyx while paying attention to preserve the rectal posterior wall and the end of the sacral plexus. A close follow-up is mandatory during the first years of life, combining the alfa-foeto-protein serum marker and pelvic ultrasound or MRI, in order to diagnose an eventual malignant local relapse. Older infants are more likely to present with a primary malignant tumor, with a poorer prognosis, requiring adjuvant chemotherapy [8, 66].

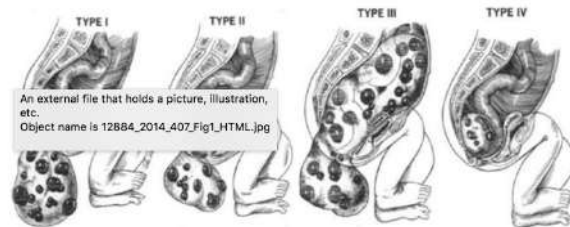


FIGURE 2.12: Altman classification of SCTs [6].



FIGURE 2.13: Type II SCT on T2-weighted MRI sagittal view. Case courtesy of Dr Ashutosh Gandhi, Radiopaedia.org, rID: 20644.

-
2. Urogenital (UG) RMS: UG RMS represents 12-20 percents of all pediatric RMS and can arise from the vagina, vulva, uterus, paratesticular region, prostate, or bladder [8] as in Figure 2.14. Several pathological types may be encountered: botrioid and spindle cell RMS (most favorable prognosis), embryonal (intermediate prognosis and most common), alveolar (poorer prognosis), undifferentiated sarcoma (also poor prognosis). RMS of the genital tract is a more favorable site compared to bladder prostate or urachal site [46]. The latest guidelines of management are more and more conservative, in order to limit pelvic functional morbidity. They include chemotherapy, external radiotherapy or brachytherapy when possible, and non-mutilating surgery, with encouraging results [45, 138]. Embryonal RMS may also occur in a context of predisposition syndrome like neurofibromatosis type 1 (NF1) for example, with similar outcome compared to sporadic embryonal RMS [63].

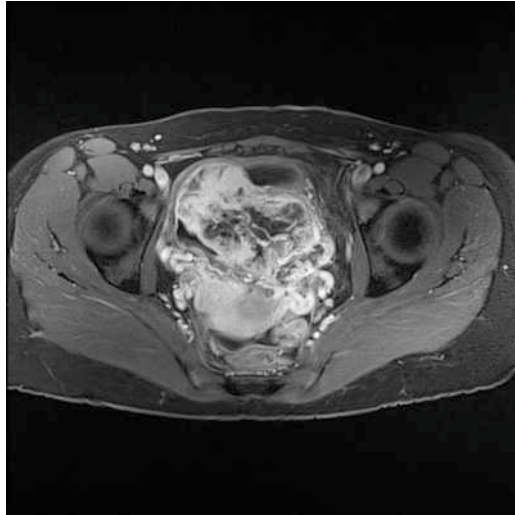


FIGURE 2.14: Bladder RMS T2-weighted MRI axial view. Case courtesy of Dr Jeremy Jones, Radiopaedia.org, rID: 27231.

3. Neuroblastic tumors: neurogenic tumors are the most common extracranial solid tumors in children. The treatment is stratified according to age, tumor location, stage, histoprognosis, and tumor biology [132]. Recent collaborative works emphasized the need for combining imaging and genetics to define the best management according to the prognosis of the subgroups [36, 100]. Pelvic tumors as in Figure 2.15 represent 5% of all sites, carrying the best prognosis due to their more frequent favorable biological status and localized nature, and being accessible for minimally invasive surgery [99].



FIGURE 2.15: Parasacral neuroblastoma with intraspinal extension on a T2-weighted sagittal MRI view. Case courtesy of Dr Ali Thomas, Radiopaedia.org, rID: 47616.

4. Other rare tumors:

- Peripheral nerve sheath tumor (PNST): PNST is a neoplasm arising from a peripheral nerve or showing nerve sheath differentiation. PNSTs may be subdivided into benign and malignant (MPNST) variants. Several distinct benign sub-types have been recognized, including schwannoma (neurilemoma, neurinoma), neurofibroma, and perineurioma. The etiology of PNSTs is usually unknown. However, several hereditary disorders are known to predispose to benign and malignant PNSTs, notably neurofibromatosis type 1 (NF1) and neurofibromatosis type 2 (NF2), both being inherited in an autosomal dominant fashion. NF1 is caused by mutations in the NF1 gene on chromosome 17 and is characterized by several phenotypic features including multiple neurofibromas and MPNSTs. The incidence of MPNST is in general rare, but half of all cases arise in NF1 patients. NF2, caused by mutations in the NF2 gene on chromosome 22, predisposes to schwannomas, predominantly affecting the spine and the intracranial nerves [137].

Neurofibromas are the most prevalent PNST and during childhood, they may develop in numerous locations anywhere throughout the body as plexiform neurofibromas that involve multiple nerve bundles, and especially around the brachial and lumbosacral plexi [90, 186], as seen in Figure 2.16. These benign tumors can cause a serious morbidity, such as pain, neurological deficit, organ malfunction and later in life they present a risk of malignant transformation to a malignant peripheral nerve sheath tumor (MPNST). These tumors are highly aggressive sarcomas associated with a poor prognosis, and present an estimated lifetime risk of 8-13 % in patients with NF1 [77]. An open or percutaneous biopsy may be indicated, but it can miss the site of malignancy in heterogeneous lesions. While clinical trials on personalized molecular treatments are still pending, surgery with total resection of the tumor and negative margins is still the best treatment option today for MPNSTs [72], taking into account that they do not respond well to chemotherapy or radiotherapy [80]. NF1 patients must be yearly clinically examined during childhood [73] and some centers advocate a whole-body magnetic resonance imaging (MRI) in adolescents and young adults [90].

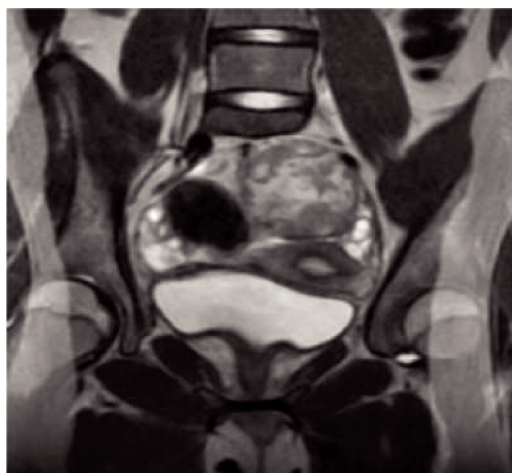


FIGURE 2.16: Pre-sacral benign neurofibroma in a 12 years old girl with NF1 on T2-weighted MRI coronal view. Source: IMAG2 laboratory.

-
- Ewing sarcoma: Ewing sarcoma (ES) stands for the second most common malignant bone tumor in children. Pelvic tumors account for around 20% of them, with a well known inferior prognosis due to its deep location, complex anatomy and relationships with surrounding organs such as bladder, rectum, genital organs and nerves, as seen in Figure 2.17. The outcome did however improve during the last years thanks to progresses in the combination of both surgical techniques and local radiotherapy, especially in children [1, 78]

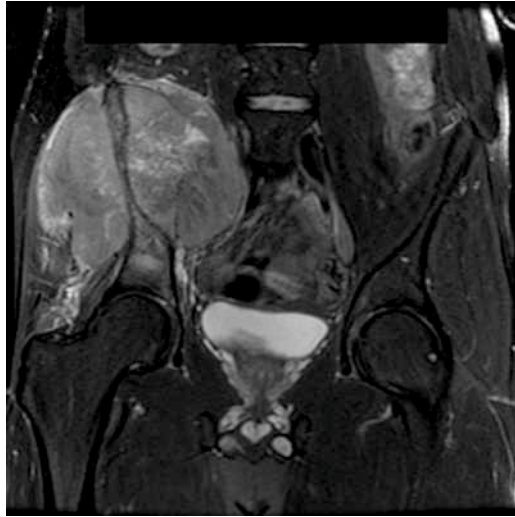


FIGURE 2.17: Ewing Sarcoma of the right hemi-pelvis on a frontal T2-weighted MRI view. Case courtesy of Prof Frank Gaillard, Radiopaedia.org, rID: 7845.

- Non RMS Mesenchymal malignant tumors (MMT): among pediatric soft tissue tumors, non RMS MMT account for 40 percents of them, with a common pathology to adult patients, but a specific evolution, and an intermediate malignancy: the most common encountered types are synovialosarcoma, peripheral nerve sheath tumors, fibrosarcoma and leiomyosarcoma. Surgery is their best treatment option (except for synovialosarcoma which is chemo and radio-sensitive), to achieve local control [133].

To conclude on pediatric pelvic pathologies, we have demonstrated that their are both numerous and miscellaneous. However, their share the following common characteristic: their prognosis is highly dependent on the quality of the surgical management, which itself is based on an accurate pre-operative assessment. The latter must be adapted to the pathology itself and to the child's anatomical specificity, in order to minimize surgical complications of pelvic surgery.

2.1.2 Surgical complications of pelvic surgery

Indeed, each pathology requires a specific surgical technique, adapted to the type of the malformation or to the tumor prognosis, the age of the child, and the experience of the surgeon.

Surgical complications of pediatric pelvic surgery are mostly represented by the functional impairment of the three systems tightly gathered within the pelvic anatomical space: unitary, genital and digestive systems.

Fecal or urinary incontinence can severely impair the quality of life of children with a pelvic disease [54, 94, 171, 172, 220], and also raises sexual or fertility issues [168, 204, 211]. The morbidity observed after surgical reparation of a pelvic malformation or the resection of a pelvic tumor is the result of lesions linked to the pre-existing disease, or imputable to the surgical gesture. Injuries linked to surgery may be mandatory to ensure the cure of the disease or accidental. Functional impairment can be the consequence of the lesion of one of the pelvic organs (rectum, bladder, genitourinary system), or due to the lesion of the surrounding networks of muscles, vessels and especially pelvic nerves. Even if most of the procedures are well standardized, the results remain highly surgeon dependent. Given this uncertainty, a more precise description of the pelvic nervous anatomy before and after surgery would be of great interest to enhance our practice.

2.1.3 Development of nerve sparing surgery: from post-mortem dissections to in-vivo radiology

So far, even without a pre- or post-operative radiologic evaluation of the pelvic nerves, surgeons aimed at developing surgical techniques to preserve the local nervous networks based on theoretical anatomical knowledge. This is called "nerve-sparing surgery". Surgeons dealing with pelvic pathologies mostly developed this technique based on cadavers and fetal series, in order to enhance the management of prostate cancer [29, 151, 159], rectal cancer [42, 85, 108], and for the treatment of endometriosis or cervical cancer in women [106, 119, 221].

Cadaver studies help the performer of the study to enhance his/her anatomical knowledge and can lead to some useful conclusions about the improvement of a surgical technique. However, it is hardly transmittable to the surgical community with a written article including only a few 2D pictures or photos. 3D nervous anatomy based on dissection and immunochemistry may only be performed on small subjects such as fetuses. In Balaya et al study [14] for example, the dissection of 3 female fetuses led the authors to conclude that the superior hypogastric plexus could be injured during para-aortic lymphadenectomy, that following the ureter and resecting the medial fibrous part of the utero-sacral ligament may spare the hypogastric nerves, and that no dissection should be performed under the crossing point of the ureter and the uterine artery to spare the inferior hypogastric plexus during an hysterectomy. However the manual slice by slice segmentation of immuno-chemistry samples is very tedious and lacks precision in their 3D visual results. Moreover, even if the fetal nervous pelvic anatomy seems to be settled after 8 weeks of gestation according to Arango et al [7], surgeons still need to extrapolate the results obtained in an healthy fetal specimen to a child or and adult patient with a pathological anatomy.

In pediatric surgery, no specific technique has been developed regarding the rarity of pelvic malformations and tumors and the high anatomical variations in each type. Few nerve sparing techniques in the field of perineal surgery for malformations such as hypospadias repair [17, 19, 20] or feminizing genitoplasty have been reported [21, 88, 180]. These techniques benefit from the knowledge of the precise pelvic nervous network anatomy of a few pathological cases, focusing on both autonomous systems represented by the hypogastric plexus and sensori-motor system represented by the sacral plexus and more specifically the pudendal nerve. For all other pediatric pelvic pathologies, surgery is however conducted without the pre-operative vision of the patient specific nervous network or the per-operative identification of those nerves.

To address this surgical concern, surgeons have to enhance their pre, per and post-operative anatomical knowledge of the patient, using an in-vivo non-invasive radiological tool. Pre-operative planning is the first step towards image guided pelvic surgery, as described by Bertrand et al [28]. In this work on 8 cadavers, the authors showed that classical T1-weighted FAT SAT MRI sequences allowed to reconstruct the 3D structure of the whole pelvic innervation including the sacral roots, the pudendal nerve and the autonomous pelvic innervation from the superior hypogastric plexus to the division branches of the inferior hypogastric plexus. The manual slice by slice reconstruction process stays however very time consuming (48 h per pelvis) and demands a very high experience in pelvic anatomy and MRI. Moreover, if MRIs of cadavers are not influenced by motion artifacts, they are characterized by cell death and temperature changes, showing different contrasts compared with MRIs performed in vivo, and requiring adaptive settings that are not directly applicable to patients.

In the continuity of this work, Wisjmuller et al [217] recently showed that in-vivo classical MRI T1-weighted sequences also allow for manual delineation of the sacral plexus, sympathetic and parasympathetic plexuses, pudendal, and levator ani nerves. Again, the segmentation technique is very time consuming, with also the necessary association of radiologist and anatomist to correctly assess the path of the nerve, and to make the distinction with vessels for example. In their study, the healthy volunteer subjects bore apparently a high body mass index: the pelvic fat induces a much better contrast especially for the delineation of small nerves, which is not the case in children. Also, the 3D representation of the inferior hypogastric plexus was quite incomplete compared to its classical anatomical description. This may be explained by the limitation of manual delineation when it comes to localize a thin and complex network, compared to a single nerve bundle such as the pudendal or levator ani nerve.

A parallel work performed by Li et al [124] showed that MRN (magnetic resonance neurography) also allows for manual delineation of pelvic nerves on 3D-STIR-SPACE sequences. But the same drawback arises: it is a time consuming technique and requires high skills in 3D reconstruction and precise anatomical knowledge of the pelvic nerves. Indeed, in an extensive review of the potential application of MRN, that uses highly weighted fat-suppressed T2 or STIR sequences, Muniz Neto et al [147] emphasized a wide range of clinical applications in lumbo-sacral pathologies, such as tumors and injuries. However, they did not address the issue of neither the autonomous system nor the 3D visualization, that is very useful for surgeons compared to classical 2D images.

After the pre-operative evaluation, per-operative guidance should act as a complementary help to identify and preserve the pelvic nervous network during the surgery. This may be performed with nerve imaging by fluorescence for example, as in the work by Cotero and al. and Barth and al. in animal models [18, 57]. However, their binding fluorofore exclusively stains myelinated fibers and still has to be proved safe and efficient in humans. Franchini et al. [85] highlighted the use-fullness of augmented reality through real time cartography of vessels and ureters during total meso-rectum excision for rectal cancer, but the authors are still working on nerve visualization through fluorescence and nerve tractography. Another way to monitor in real time an eventual nerve damage is intra-operative nerve stimulation as in [86]. The authors combined a robotic approach and an electric stimulation using the bipolar forceps of the da Vinci robot of the sacral root to help the surgeons removing a neurogenic tumor attached to the sacral plexus while minimizing neurological impairment. However, this technique may only show the neurological defect after it has occurred during the surgery.

To conclude, the field of nerve imaging guiding surgery still need to be investigated and both radiologic and surgical techniques still need improvements to show their theoretical asset in the management of patients presenting pelvic pathologies. The first step of this process is to explore the state of the art of PNN anatomy, which is complex and not well well known by both radiologic and surgical communities. This point will be the subject of the next subsection.

2.1.4 Pelvic nervous network (PNN) anatomy

In this section we describe the global structure of the pelvic peripheral nervous system, with the main functions of the somatic and autonomous trunks. The detailed anatomy of each nerve is developed in Section 5.4, as it is directly used in the proposed tractography segmentation method in Section 5.5.

Pelvic innervation can be divided into somatic and autonomic systems that are partially mixed within specific anatomic structures. The normal pelvic functions, such as digestive and urinary continence, or later in life sexual function, require the interconnection of both somatic and autonomic systems. During childhood, continence learning assumes the transition between conscious sensations (coming from the somatic system connected to the cortical encephalic level) and unconscious ones (coming from the autonomic system connected to the subcortical encephalic level). Voluntary motion control may only be efficient if controlled and regulated by extra-pyramidal paths connected to the cerebellum, thalamus and basal ganglia. The emotional aspects from pelvic sensations are handled by the cingulate gyrus, the fornix and the hypothalamus that elaborate autonomic and hormonal responses [61].

2.1.4.1 Somatic system

The role of the somatic system consists of the innervation of voluntary pelvic striated muscular groups linked to the cortico-spinal tract. The nature of transported nervous information is voluntary motricity of the pelvic muscles and sphincters, and both superficial and proprioceptive pelvic sensations. Normal pelvic functions, such as continence, require these sensations and reflect the learning process starting from conscious sensations to unconscious ones. This process requires the myelinisation of the fibers that occur for the pelvic nervous network after the age of two. The main anatomical structures are the sacral plexus and its principal terminal branch, the pudendal nerve innervating the perineum 5.16. They tightly relate to surrounding bony, ligament and muscular structures as seen in Figures 2.18, and 2.19: sacral foramen, greater and lesser sciatic foramen separated by ischial spine, ischio-pubic branch; sacrospinous and sacrotuberous ligaments; piriform, obturator and levator ani muscles.

2.1.4.2 Autonomous system

The autonomous system gathers sympathetic and parasympathetic systems, as seen in Figures 2.21 and 2.22. Both systems are mixed at the pelvic level with a lot of connections within the inferior hypogastric plexus surrounding the pelvic organs: rectum, bladder and ureter, hypogastric vessels, and genital system. These nervous systems ensure the normal neuro-vegetative functions of these organs, like defecation, urination, fertility, or sexual arousal for example.

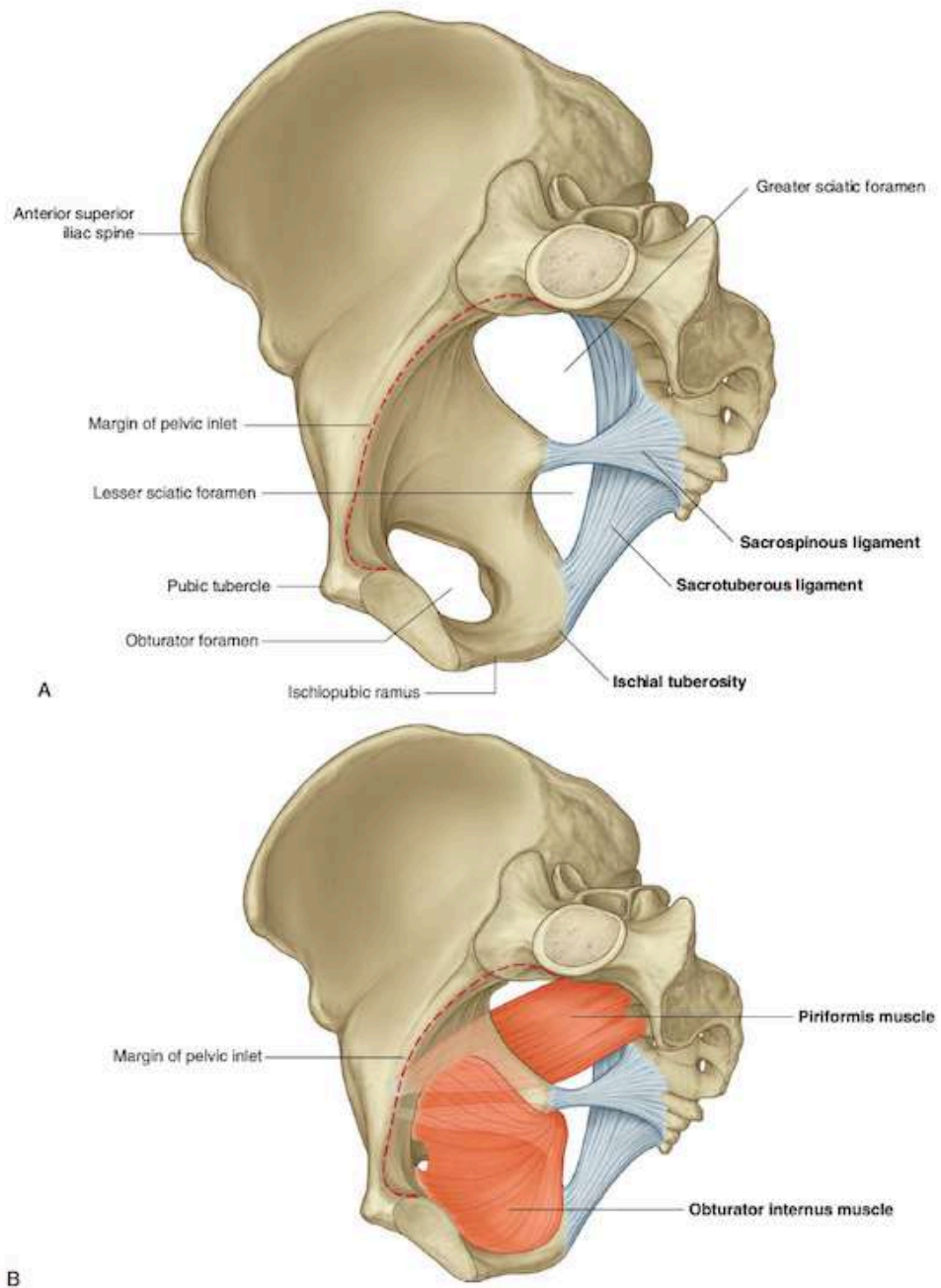


FIGURE 2.18: Pelvic walls. A: Bones and ligaments of the pelvic walls B: Muscle of the pelvic walls [71].

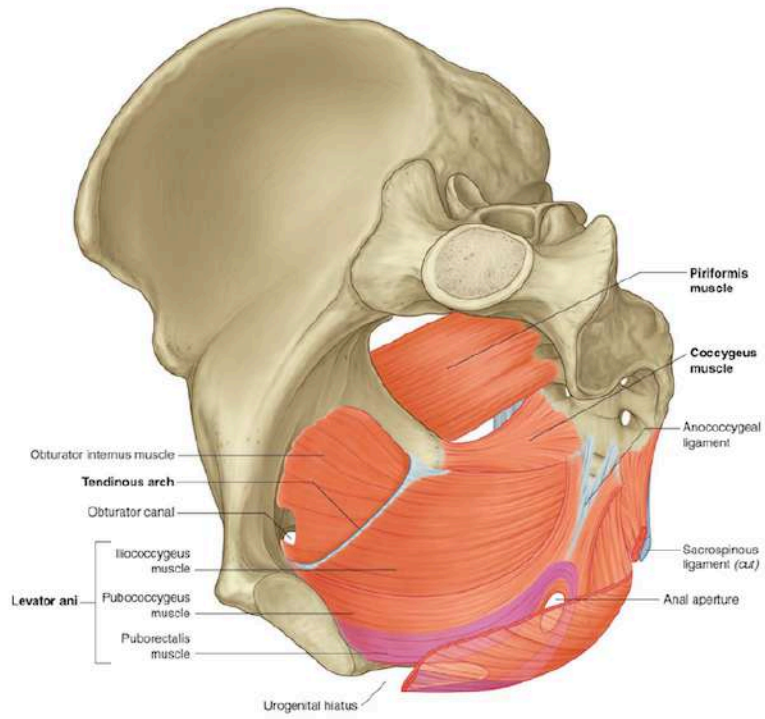


FIGURE 2.19: Pelvic diaphragm [71].

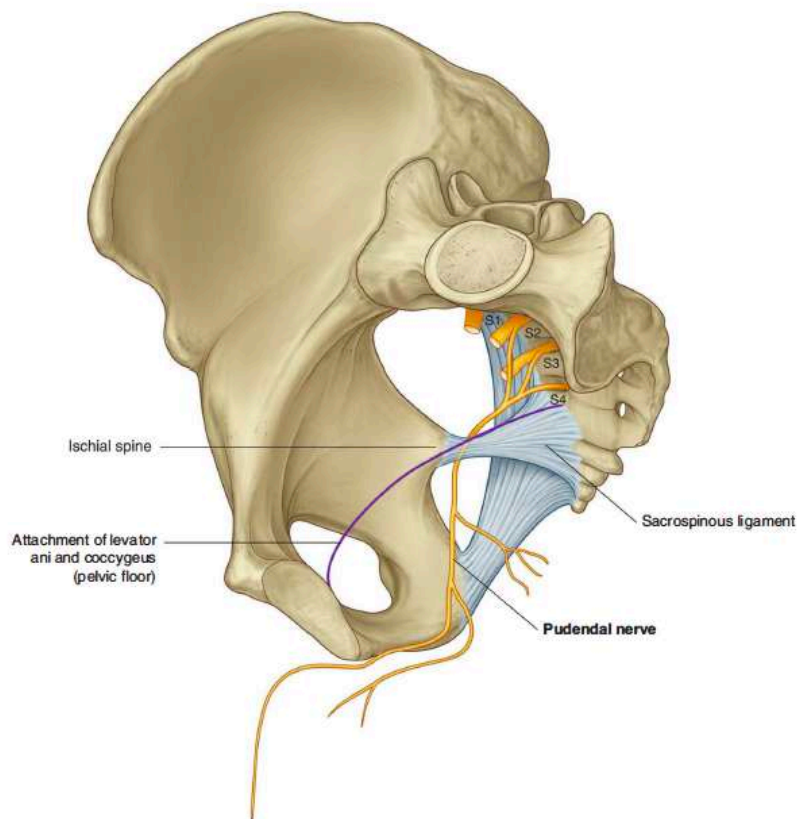


FIGURE 2.20: Pudendal nerve. [71].

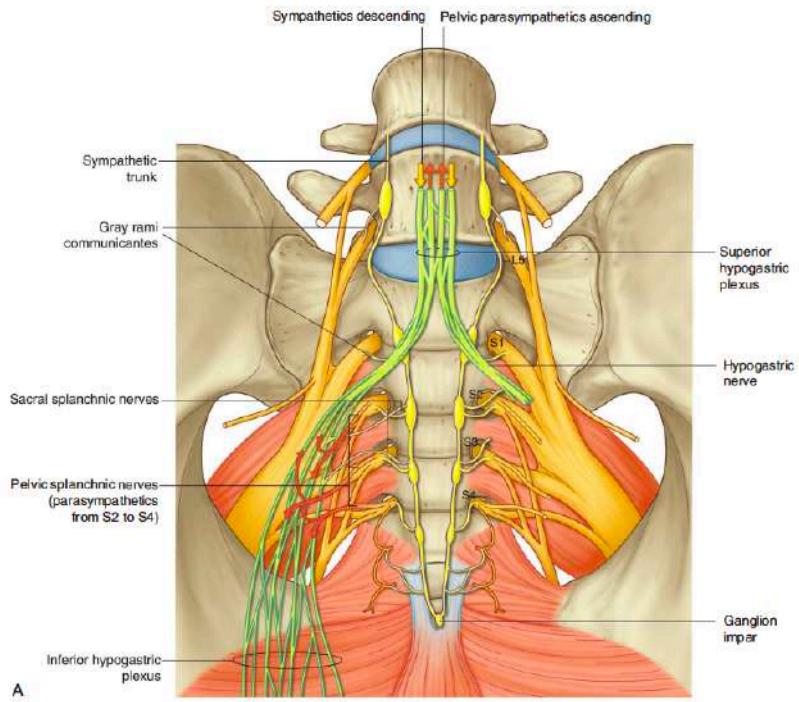


FIGURE 2.21: Pelvic autonomic system. Frontal view [71].

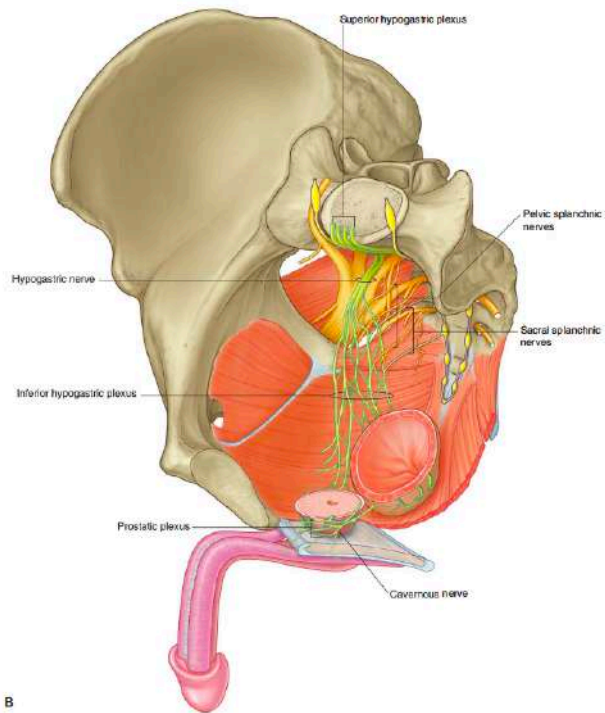


FIGURE 2.22: Pelvic autonomic system. Oblique view [71].

2.2 Pediatric MRI

MRI is the radiological tool of choice for both the pelvic area and to investigate children, thanks to its absence of radiation. In this section, we will consecutively detail the state of the art in pelvic MRI (with some examples in the pediatric field), with a specific focus on both anatomical and diffusion sequences.

2.2.1 Pelvic MRI

In this section, we focus only on the pelvic area, excluding the spinal chord that requires specific MRI sequences and which is out of the scope of the thesis. Nowadays, MRI has become the gold standard for imaging both the pediatric pelvis and the pelvic floor musculature [187]. MRI is an *in vivo* non-radiant radiological tool particularly well suited for soft tissue imaging. The indications for abdomino-pelvic MRI are numerous [170]: tumors, digestive and genito-urinary malformations such as ARM [3] (see Figures 2.23 and 2.24), or extrophy-epispadias complex with assessment of pelvic floor musculature [187, 192] (see Figure 2.25), and gynecologic pathologies (see Figure 2.26). MRI is also able to investigate the major abdomino-pelvic vessels with MR-Angiography, both in vascular malformations and thrombosis or aneurysm. Finally, MRI may be the best option in post-traumatic and inflammatory complications evaluation [170].

From a technical point of view, high field MRI (1.5 or 3 Teslas) provides a high signal to noise ratio (SNR), and a body coil is suitable for children because it allows for high tissue spatial resolution and multidimensional imaging [190]. As a consequence, high-resolution T2-weighted sequences, both 2-D and 3-D, are very useful in the evaluation of the pediatric pelvis. 3D volumetric T2-weighted imaging allows for the acquisition of isotropic or near-isotropic images that can be reconstructed into any plane during post-processing without the need for additional acquisitions. This sequence is advantageous because it provides a good T2 signal, especially at 3 Tesla. We used such sequences in our radiologic protocol as described in Chapter 3. In some pelvic pathologies in adults, some authors even conclude that volumic sequences may shorten imaging time by reducing the need for acquisition of multiple multi-planar 2D sequences [126, 165, 167, 182]. The widespread use of MRI however brought some challenges for the pediatric radiologist. A large number of children are scanned awake, with fewer and fewer studies being performed under general anesthesia. It resulted in more artifacts due to patient motion, difficulties with breath-holding and intolerance to long imaging time [58].



FIGURE 2.23: Intermediate or high ARM with a recto–urethral bulbar fistula in a boy. (a) Image from colostography showing a rectourethral fistula (arrows) at the level of the bulbar urethra. (b) Sagittal T2-weighted MR image showing the rectal pouch (white arrow) ending at the level of the levator ani muscle and the fistula (black arrow) extending anteriorly to the bulbar urethra. (c) Axial T2-weighted MR image at the pubococcygeal level showing an anteriorly located anorectum (white arrow) with an asymmetric and underdeveloped puborectalis muscle (black arrows)[3].

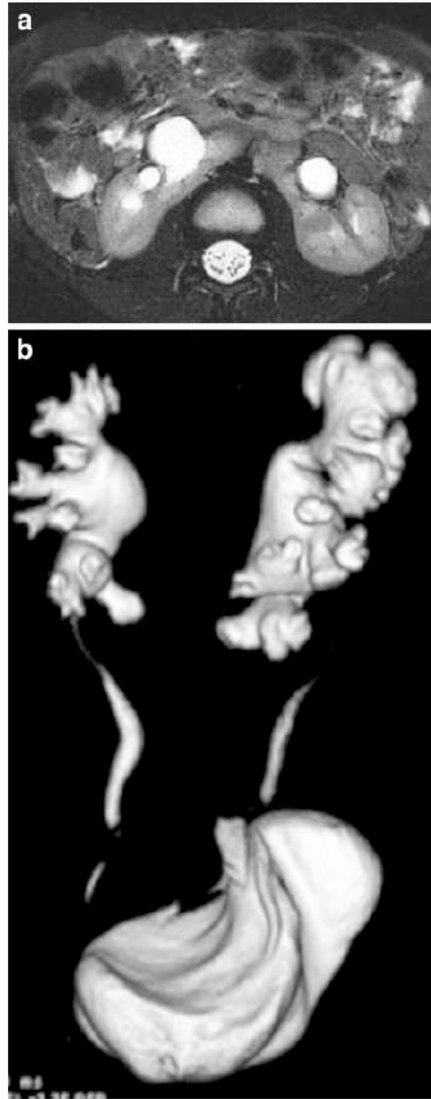


FIGURE 2.24: 2-year-old boy with a horseshoe kidney and ureteropelvic junction (UPJ) obstruction in the right-side renal moiety. MR urography was performed to identify the course and insertion of the right moiety ureter. (a) An axial high-resolution T2-weighted MR sequence with fat suppression shows the horseshoe configuration with dilatation of the right-side moiety and UPJ. (b) A posterior projection of a shaded surface display created from a 3-D T2-weighted volumetric acquisition shows the horseshoe configuration with dilated collecting system and the ureters from each moiety inserting orthotopically into the bladder [58].

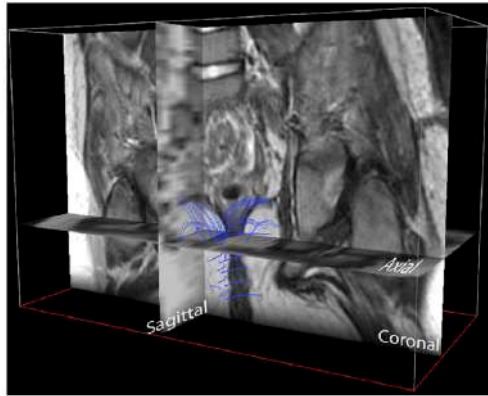


FIGURE 2.25: Patient with bladder extrophy. The contours of levator ani muscle are drawn bilaterally on several sections as far as the muscle groups can be identified in axial, coronal, and sagittal planes [192].

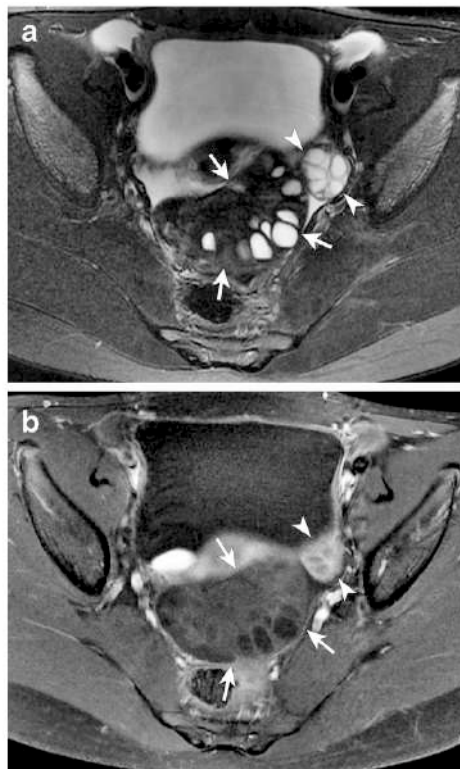


FIGURE 2.26: Torsed ovary in an 11-year-old girl who presented with periumbilical pain and vomiting, with findings of a pelvic mass by US (not shown). (a) Fat-suppressed T2-W axial MR image reveals a strikingly asymmetrical appearance of the ovaries. The normal left ovary (arrowheads) has intermediate to mildly hyperintense stroma with multiple sub-centimeter follicles. The right ovary (arrows) is significantly larger and relatively hypointense. The follicles are arranged peripherally, and some even have fluid levels. (b) Axial contrast-enhanced T1-W fat-suppressed MR image through a similar plane shows no enhancement of the right ovary (arrows). There is normal enhancement of the left ovary (arrowheads) for comparison. The right ovary was dusky at laparoscopy with no improvement after surgical detorsion and was therefore removed [59].

2.2.2 Diffusion weighted imaging (DWI)

The main goal of this thesis being the development of a DWI-based tractography segmentation method for pelvic nerves, a good understanding of this complex radiologic technique is mandatory. It is important to note that most of the work on diffusion MRI have been performed on brain imaging, and later applied to other anatomical areas. That's the reason why the references within the following paragraphs mainly concern the brain. Moreover, this thesis being the work of a medical practitioner, we will not go too far into the physical and mathematical principles.

For the detailed physics of diffusion imaging, see [203].

Besides conventional sequences, MRI offers specific acquisition sequences that can give functional or tissue specific information, like DWI. It is a variant of conventional magnetic resonance imaging based on the tissue water diffusion rate [116]. Molecular diffusion in tissues is not free, but reflects interactions with many obstacles, such as macro-molecules, fibers, and membranes. Water molecule diffusion patterns can therefore reveal microscopic details about tissue architecture, either normal or in a diseased state [218]. In brain imaging, DWI is now a standard in diagnosis of ischemic stroke, and may also be used in epilepsy and neuro-toxicity [50]. Another major application is brain oncology [203]. DWI may also be of use in a wide range of tissues, such as the grading of prostate lesions and differentiate them from benign prostatic hyperplasia or hemorrhage. It is also more and more widely used in breast cancer, genito-urinary diseases, thoracic malignancies, head and neck malignancies, muskulo-skeletal system, liver, pediatric brain development and aging, bowel disorders, and also as whole-body imaging [16, 50].

2.2.3 Diffusion tensor imaging (DTI)

Introduction

DWI refers to the contrast of the images and DTI is a type of post-processing of the DWI data sets. The idea is that water molecules diffuse differently (anisotropy) along the tissues depending on the type, integrity, architecture, and presence of barriers within these tissues. The analysis of water molecules diffusion directional pattern therefore may give information about these tissues and their quantitative anisotropy. For example in the brain, diffusion is less restricted along the axons of white matter tracts and tends to be anisotropic, compared to the cerebro-spinal fluid, where diffusion goes equally in all directions (isotropic). For the mathematical basis of DTI, see [23, 25, 49, 117, 140, 162].

Diffusion tensor imaging is one of the major applications of DWI in the neurological field. DTI studies focus on multiple pathologies such as acute stroke, brain tumors, neuro-degenerative disorders, epilepsy, Alzheimer disease, schizophrenia, autism, Parkinson's disease, and changes in white matter micro-structure during development and aging [183]. It is also more and more often included in image guided neurosurgery methods to enhance pre-operative planning and post-operative evaluation of nerve injury [76].

DTI presents a complex post processing process, that is well summarized by Soares et al [183], (see Figure 2.27). It requires the knowledge of imaging artifacts, MRI acquisition parameters definition, neuro-anatomical complexity, and both hardware and software limitations. These issues are addressed by a multitude of pre-processing and analysis methods in several software packages. An abundant literature describes the main technical issues and pitfalls [102, 157], which are complemented by available neuro-anatomical atlas of the brain [40, 209].

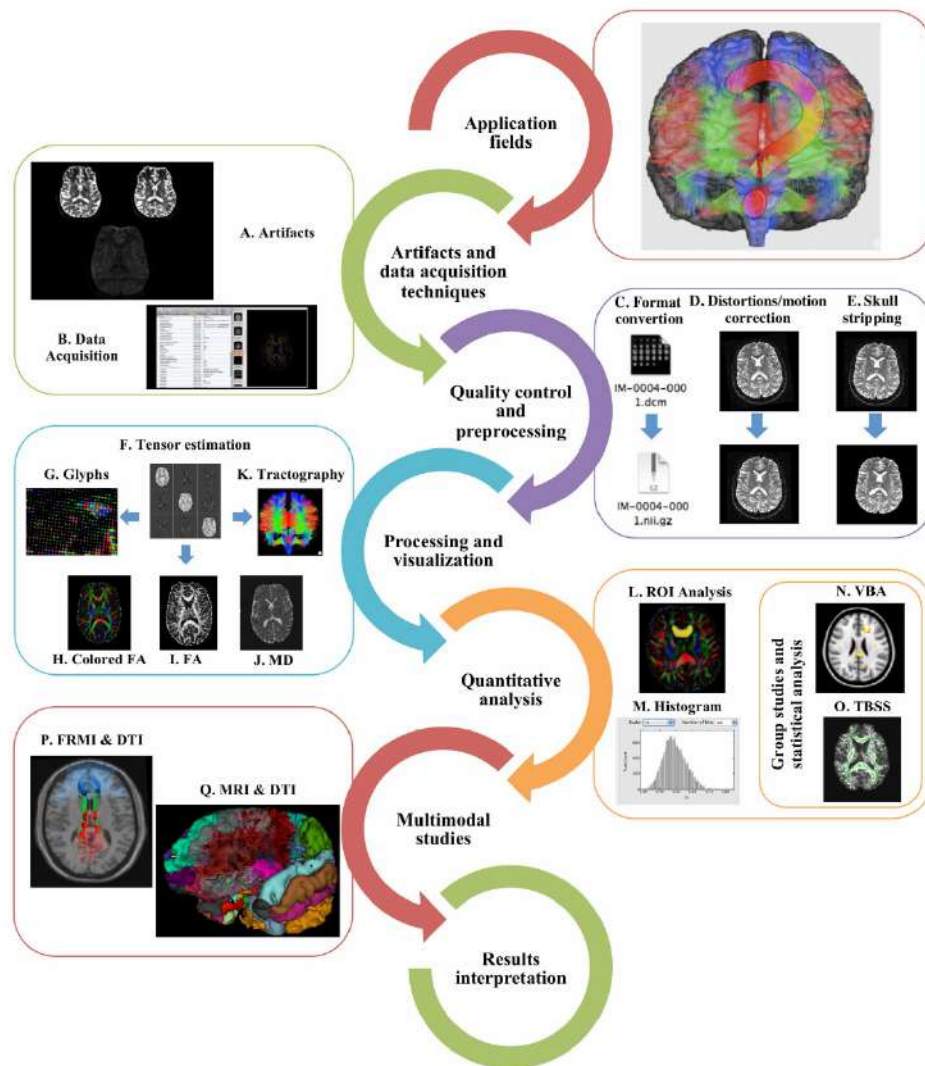


FIGURE 2.27: Typical DTI work flow. In order to perform a DTI study, researchers need to understand its main application fields, recognize the main artifacts (A) and what acquisition protocols can be used (B). The data should undergo quality control, pre-processing, including format conversion (C), distortions and motion correction (D), and skull stripping (E). Before further analysis, tensors need to be estimated (F) and the resulting data can be visualized as glyphs (G), scalar indices such as colored FA (H), FA (I), MD (J) or as tractography (K). ROI (L), histogram (M), VBA (N), or TBSS (O) analyses may be performed and the results can be incorporated with fMRI (P) or structural MRI (Q) in multimodal analysis. Finally, results interpretation should be made with extreme caution [183].

Processing and visualization

After data pre-processing using state of the art methods, the next stage in DTI analysis comprises the tensor estimation at each voxel. A wide range of free and commercial DTI software tools are available for that task, such as Explore DTI, MedINRIA and 3D Slicer. These software allow then for calculating the two main diffusion measures that are Fractional Anisotropy (FA) and Mean Diffusivity (MD).

While MD corresponds to molecular diffusion rate (packing density of the fibers), FA is a normalized measure of the fraction of the tensor's magnitude due to anisotropic diffusion and ranges from 0 (isotropic diffusion) to 1 (anisotropic diffusion). FA itself has no information about the orientation. This can be shown by color-coded FA maps in which the color of each voxel shows its main diffusion direction. In these maps, red color represents left-to-right orientation, green posterior-to-anterior and blue inferior-to-superior diffusion. Typically, MD is higher in damaged tissues due to an increased free diffusion. In contrast, FA decreases due to the loss of coherence in the main preferred diffusion direction.

The main challenge is then to visualize and present the tensor information in an intuitive and easily interpretable way, using either tensor glyphs, scalar indices or tractography in 3 dimensions. The latter is the more visually intuitive, and projects 3D trajectories of nervous fibers between different part of the nervous system [24, 140, 215]. Tractography processing can be divided in three main stages: seeding, propagation, and termination.

Seeding consists in defining the points from which the fiber bundles will be drawn and start; one of the most common methodologies is based on defining Regions Of Interest (ROIs) and placing one or more seeds in each voxel of the ROI. The ROIs can be manually drawn or extracted from other MRI modalities. A second popular approach consists of using automatic seeding for the whole brain, producing a whole brain tractogram. The selection of the tracts of interest then relies on specific segmentation methods of the whole brain tractogram, that will be discussed in Subsection 2.2.4.

During the propagation process the fibers are gradually generated. Fiber tracking can be performed with different algorithms divided in two main categories: deterministic and probabilistic [68, 196]. Deterministic tractography aims at modeling the data and reconstructs one fiber from each seed. On the other hand, probabilistic approaches take into account the uncertainty of the estimation, which results in probability maps representing the likelihood of a voxel being part of a fiber and provides the multiple possible fiber directions starting from each seed.

The last tractography step is termination of the fiber tracking procedure. The termination aims at avoiding the propagation of the fibers in voxels where the robustness of the tractogram is not sure. The common termination criteria are minimum FA thresholds (typically 0.1–0.3 in adult brain and 0.1 in infant) and turning angle threshold (typically 40–70°, depending on the pathway).

Quantitative analysis and results interpretation

Among all the methods to extract fiber bundles of interest in the brain, evaluation of the quality and reliability of fiber bundle identification remains a significant challenge. Several measures can be performed in that purpose, as reported in [89, 188].

First are geometric measures such as volumetric overlap, normalized tract volume, tract length, Jaccard coefficient, Dice coefficient, or point cloud divergence. These measures aim at being robust to biases, providing physical intuition, and focus on the global shape of the fiber bundle.

Second are the functional measures that describe the differences in the diffusion parameters sampled by the fiber bundles. It requires the computation of parametric maps of FA and MD, that are used to extract summary measures from specific tracts. FA and MD measurements may either be realized on the whole tract, giving a mean FA or MD value of the tract, or be performed based on ROI analysis. However, the main problems of ROI analyses include: the influence of the image intensity on ROI boundaries by direct segmentations on the map of interest (typically FA or MD); the difficulty to co-register diffusion with typical anatomical images (T1 or T2 weighted) when using anatomical ROIs; performing analysis in smaller/thinner tracts.

Interpreting tractography maps can be problematic due to the intrinsic unrealistic assumption of a homogeneous unidirectional population inside the voxels. Specific regions containing two or even more differently oriented fiber bundles within the same voxel (crossing, diverging, or kissing fibers) lead to incorrect estimations of fiber directions and pathways and abrupt terminations of tracts. This can be overcome by using more complicated approaches such as multi-tensor models, High Angular Resolution Diffusion Imaging (HARDI), Q-Ball Imaging (QBI), or Spherical Deconvolution Model (CSD). Recently, these methods have gained interest, and aim at replacing the DTI model for tractography [215]. However, the methods often require longer acquisition time and an even more complex post-processing work flow, which prevent them to spread to a larger community of researchers. For these reasons, we performed all our tractograms in this thesis using DTI and a deterministic algorithm, as described in Chapter 5, despite their inherent limitations.

These measurements can however be used to both evaluate the robustness of tract identification, and thus the reliability of the tractography method, but also to perform individual or group statistical analysis, what usually researchers and clinicians are interested in. In this thesis, we will perform these two types of quantitative analysis, the first one on a healthy adult subject to test the reliability of our tractography segmentation method, and the second one on pediatric patients harboring different types of pelvic malformations. But the virtual nature of tractography must never be forgotten, along with the limitations of DTI tractography, especially in crossing fibers, that affect more FA than MD [196]. This point will be discussed further taking into account the subject of the thesis, the pelvic nervous network, that comprises very straight fiber tracts like the sacral plexus, but also complex networks with a lot of crossing fibers like the inferior hypogastric plexus.

2.2.4 Tractography segmentation

In brain tractography, most of the methods for identifying the tracts of interest start with the computation of a whole brain tractogram, by simultaneously placing seed points through out all voxels in the brain. The next step consists then in choosing a method to identify and extract the tracts of interest from the whole brain tractogram. Three methods are commonly employed to accomplish this [188]:

- **Manually placing ROIs around the most compact portions of fiber bundles** [40, 141, 208]. It involves identifying and drawing inclusive and exclusive ROIs on FA or DTI maps, using methodologies established in the literature, or by a neuro-anatomist expert. This method is very time-consuming, and can only be used to delineate previously identified nerves with well known trajectories.

This fact is an obvious limitation in pathological cases, and even more in the pelvic area where even the normal nervous anatomy is well known only by very few anatomists. The other pitfall is the noisy nature of pelvic diffusion images, where the nerve signal is buried in the middle of numerous non nervous structures such as muscles (excellent candidates for false positive thanks to their similar tract structure), pelvic organs, vessels and lymphatics. Manually drawing the perfect starting, ending or exclusive ROIs on these type of images is quite impossible. The difficulty obviously grows even more in pediatric rare diseases such as pelvic tumors and malformation, where the anatomical variations may be numerous. This first approach will however be the subject of a first exploratory study developed in Chapter 5, as it is the only method used in the literature about tractography of the pelvic nerves (see Subsection 2.2.5).

- **Atlas-based methods** [115, 212, 222, 224]. These automated methods have been developed to address issues of time, labor, and reproducibility. They require anatomical atlases and diffusion images co-registered before the tractography segmentation process.

However, they are not suitable for the purpose of this thesis, because of the absence of available peripheral nerve atlas to date, both in adult and pediatric patients. However, anatomical constraints such as described by [212] in the White Matter Query Language (WMQL) may be part of a solution to identify the peripheral pelvic nerves within the pelvic DTI. The principle of WMQL will be detailed in Chapter 5 before the description of our proposed method of tractography segmentation.

- **Grouping streamlines into clusters based on fiber similarity properties** [153]. This alternative automated method groups streamlines that follow similar anatomical pathways into distinctive clusters, and recognize them among a group of subjects.

This is not achievable in pediatric DTI data sets without the presence of age atlases, and due to the noisy nature of DWI pelvic images, that would provide a lot of clusters of non nervous structures.

2.2.5 Tractography of peripheral nerves: state of the art

- **Introduction**

All the previous subsections dealing with DWI pre/post-processing methods, and tractography methods, were documented on studies on the brain. This field of research has indeed been richly explored since more than twenty years now. However, diffusion MRI associated with tractography algorithms may also be used to evaluate the peripheral nervous system. It is a promising tool for surgical planning because it allows for the visualisation of nervous tracts, which may not be visible on conventional imaging [41]. It is still an emerging field of research, and a lot of the considerations about the pre and post-processing methods of DW imaging, and the DTI tractography generation in brain, stay valid. DTI studies on the peripheral nervous system raise even more challenges related to imaging artifacts, because of the small caliber of peripheral nerves showing low levels of FA. Advances in MRI hardware and software have though made it possible to provide data about altered functional measures, caused by pathological processes on peripheral nerves [148].

- **Applications**

Outside the pelvis

The applications of DTI imaging of peripheral nerves outside the pelvis mainly focus on acute nerve injuries, compression neuropathies, inflammatory neuropathies, and peripheral nerve tumors [41, 148].

The median nerve has become a clinical target for DTI studies because altered diffusion measures may help in the diagnosis of the carpal tunnel syndrome [41].

Others studies on the anatomy and diffusion characteristics of the facial nerve in patients presenting with vestibular schwannoma [47, 51, 191] or parotid gland tumors [9] showed a good correlation between tractography and surgical findings, with an interesting input in the pre-operative planning of the tumor resection, and the anticipation of the nervous post-operative morbidity.

The same conclusions were brought by Kasprian et al [?] in soft tissue tumors of the lower limb and Schmidt et al [178] in peripheral nerve sheath tumors of various locations. They emphasized the fact that the MD values of the tract in close contact with the tumor was usually higher, and the FA lower, with a good correlation with pathological examination showing nerve infiltration below a certain value ($FA < 0.3$).

Vargas et al [200] study focused on the brachial plexus endangered by various types of tumors, with again a good correlation between tractography results and surgical findings in terms of nervous tract disorganization on both macroscopic and pathological levels.

In studies on acute nerve injuries of the brachial plexus [87, 189], the authors also conclude that DTI tractography is a reliable tool to evaluate nerve damage and/or disruption compared to surgical findings. The advantage of unilateral disease impairing bilateral nervous structures relies on the possibility of using the subject as its own control for DTI measures such as FA and MD. However, all these studies aiming at image guided surgery do not represent the tractograms within their 3D anatomical environment, with the need for the surgeon to mentally extrapolate classical 2D anatomical sequences, as seen in Figure 2.28.

The studies focusing on chronic neuralgia mostly concern adult's pathologies like cervical [48, 175] and lumbar discopathy [15, 37, 52, 75]. In these works, FA values of L5 and S1 roots range from 0.2 to 0.3 and MD from 1.7 to 4. These variations are obviously linked to the variety of MRI sequences parameters, and hard and software used for pre- and post-processing of the data sets. Despite the lack of normalized values of the sacral plexus according to sex and age, the more suitable FA threshold to start tractography seeding is commonly accepted to be between 0.1 and 0.15. Balbi et al [15] also conclude to a higher inter individual variations in MD than in FA measurements. In cervico-brachial neuralgia, FA values seem to be less correlated to the clinical assessment of pain than MD [48].

In their work on peripheral nerve tractography of the upper and lower limb, Hiltunen et al [96] advise to use a higher FA threshold for tractography seeding in order to eliminate false positives of muscles and tendons. This is however only achievable in these types of peripheral nerves that bear a much higher mean FA value around 0.4 and 0.6. This latter finding may be explained by histological differences: spinal root nerve endoneurium contains five times less collagen than peripheral nerve endoneurium. In addition, the spinal nerve roots have no perineurium, as opposed to peripheral nerves, and a less developed epineurium [15].

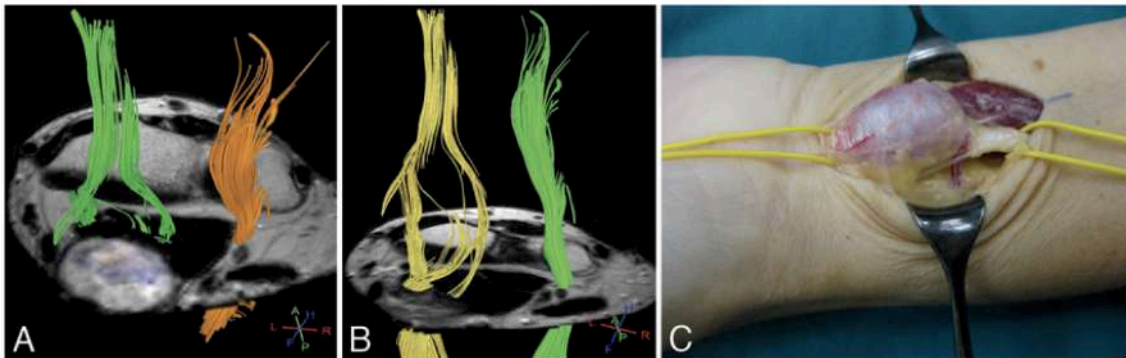


FIGURE 2.28: A: Three-dimensional diffusion tensor tractography (DTT) scan of a wrist schwannoma. The median (green) and ulnar nerves (orange) are visualized. The main trunk of the median nerve is split by the tumor into 2 fascicle groups that pass the tumor mass dorsally and radio-laterally, respectively. B: The fascicles of the median nerve are separated by the tumor and rejoin each other at the level of the wrist joint. The tumor mass is left out by the nerve fibers, and its location can thereby be estimated. C: Intra-operative photograph of the tumor of the left median nerve at the wrist. The radio-lateral fascicle group and the second fascicle group, which passes the tumor mass dorsally, can be seen (the left side of the picture is distal) [178].

Pelvic tractography

The sacral plexus from L4 to S4 has been explored in a series a male healthy volunteers by Van der Jagt et al [199], using a very low FA threshold (0.001) but multiple ROI placements along the nerves, and a very straight angle threshold of 30°. They reported no differences between left and right sides across the subjects in terms of FA and MD values, that S1 and S2 are the thicker nerves, and failed to reliably track S4 roots. The very beginning of the pudendal nerve was found in one subject. Some significant changes in the architecture of the sacral plexus and FA values were also observed in patients with endometriosis [128] (see Figure 2.29).

The only reported pediatric cases are spina bifida patients with sacral nerve roots agenesis [92] (see Figure 2.30). The authors report similar FA values but lower MD values of the spinal roots L5 to S3 in spina bifida patients compared to controls. The pudendal nerve was supposedly observed in one patient. They also advocate to reiterate the study in other pathologies of the caudal pole such as ARM, and fuse both anatomical and DTI information to improve the analysis at each level of the sacral roots.

More medial and distal pelvic innervation has been very little explored by tractography. Some studies in the field of prostate cancer to evaluate the impact of nerve sparing surgery techniques showed promising results [82, 109] (see Figure 2.31), even if a more recent report doubts that the current DTI technique actually enables a realistic representation of peri-prostatic fibers [?]. There is no study to date of DTI exploration of the inferior hypogastric plexus or the pudendal nerve.

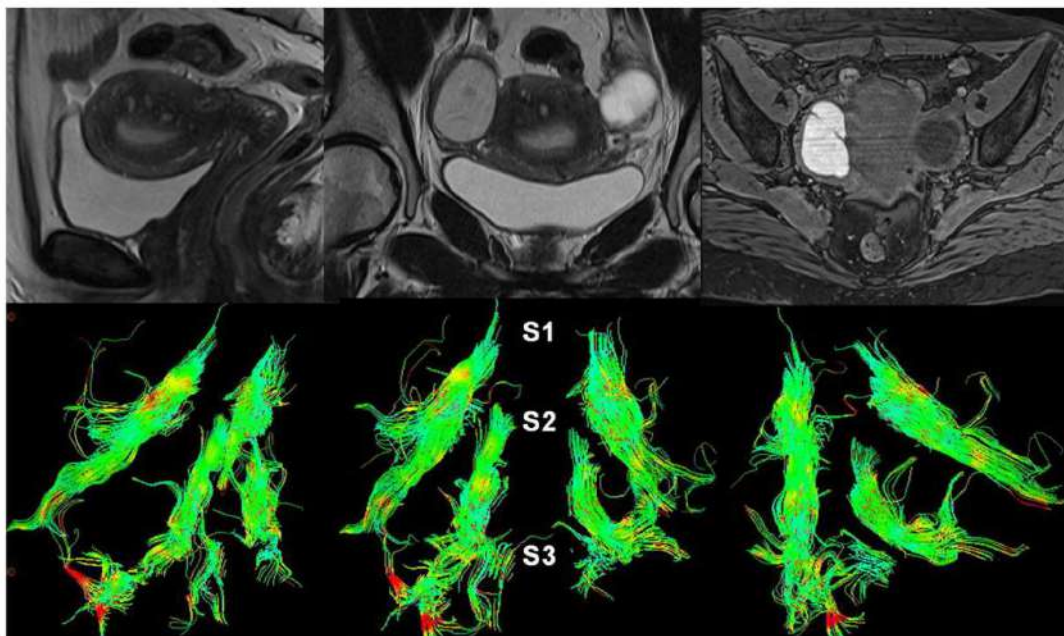


FIGURE 2.29: Fiber tracking reconstruction in a woman affected by endometriosis and adenomiosis. The fiber bundles in all 3 cases are short, stubby and have lots of branches [128].

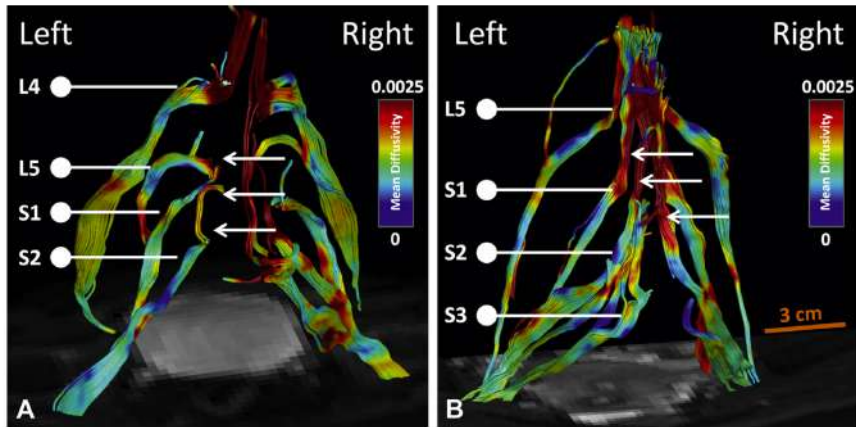


FIGURE 2.30: Lower lumbar and sacral nerves. A: healthy control. B: patients with SB and myelomeningocele from L5 level to caudal. On the left side L5 root (1) could not be reconstructed [92].

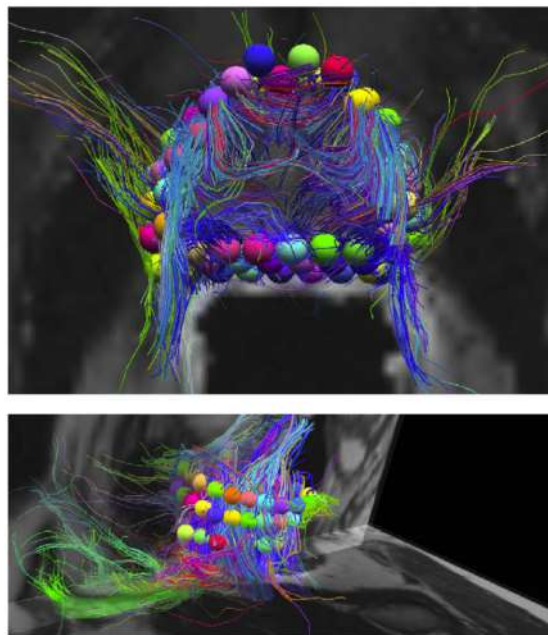


FIGURE 2.31: Peri-prostatic tractography images. Up: Near axial T2W image demonstrating ROI placement with fiber tracts visualized. Down: Oblique T2W image demonstrating ROI placement with fiber tracts visualized. [82]

2.3 Conclusion

While exploring the current state of the art methods of tractography processing, we highlighted an important unexplored field of research associating peripheral nerve tractography, tractography segmentation methods, the pelvic area and pediatrics. For now, published pelvic tractography results remain partial, showing only the origins of the sacral plexus roots, in both adult and in the few reported cases of pediatric patients. However, injuries linked to surgical dissection usually involve more distal and medial nerves: for instance, the pudendal nerve, in charge of the somatic perineal motor function and sensitivity; the inferior hypogastric plexus, in charge of the pelvic autonomic function of digestive, urinary and genital systems.

We must state that the physics behind diffusion image acquisition assumes perfect field homogeneity, infinitely flat gradient changes and perfectly shaped radio-frequency pulses. However, in reality, this is impossible because of power requirements and hardware limitations, which limit DWI accuracy and result in lower image quality and artifacts. The maximum resolution achievable by optimizing matrix size, field of view, and slice thickness is limited by the hardware specifications of the scanner. A 3 Teslas scanner can achieve a DW image with an acquisition matrix of 128 x 128 voxels and an isotropic voxel size limited to 2 mm. In anisotropic scans, in-plane resolution can be improved to 1 mm, but with a lower SNR. Moreover, DWI images are subject to artifacts like distortion due to field inhomogeneity and differences in the region being imaged, especially at 3 Teslas. DWI images are also subject to motion, either microscopic or macroscopic, resulting in motion artifacts like ghosting or blurring of the image. Even if precaution can be taken to minimize voluntary patient movement, involuntary movements due to breathing, blood flow and mechanical vibrations of the MRI table are still unavoidable. The approaches to counter the inherent challenges associated with DWI are hardware upgrading, usage of contrast agents, optimizing acquisition parameters, and software based post-processing techniques, so that the gap between current state of the art imaging and ideal diffusion imaging is reducing [50].

We therefore concluded that we had to use some of the existing classical methods of pre- and post-processing diffusion MRI such as DTI, and to adapt the MRI acquisition parameters to our population. We also mainly needed to develop an original method of tractography segmentation suitable for the pelvic region, in order to provide a more complete representation of the PNN.

Moreover, none of the existing works include the 3D tractography results within the 3D model of the patient. The reason is the need for the tedious task of manual segmentation of all the pelvic organs on volumic T1 or T2 sequences MRI sequences, that are not quite systematically included yet in pelvic MRI protocols. As a consequence, we therefore contributed to develop semi-automatized methods for MRI segmentation.

Thereby in this thesis, we aim at enhancing the tractography results by working on diffusion sequence refinements and designing an original tractography segmentation method, detailed in Chapter 5. We will test this method on patients included in a database detailed in Chapter 3, and present the results in ARM patients in Chapter 6. We will also integrate the nervous anatomy within the patient specific 3D model including the other pelvic organs, in our scope of pediatric image guided surgery in the IMAG2 laboratory, as detailed in Chapter 4. Keeping in mind the inevitable biases of tractography, we will also test our tractography processes with a comparative human fetal model in immunochemistry, which stands for the gold standard in anatomical studies, as detailed in Chapter 7.

Chapter 3

Clinical data characteristics and MRI acquisition

In this chapter we describe the relevant data which are analyzed in this thesis.

In Section 3.1 we present the clinical characteristics of all the patients such as their age, sex, pathology type and associated syndromes, along with a 2D MRI pelvic illustration.

In Section 3.2 we detail the MRI parameters used in all the patients of the series, for both anatomical and diffusion sequences.

In Section 3.3 we provide the organization of the segmentations and the tractograms within the database.

3.1 Patients and pathologies

Since 2016, patients from 3 months to 18 years of age presenting pelvic tumors or malformations have been included in the study, after ethic board committee agreement (Reference number of CPP = Comité de Protection des personnes Ile de France III = 2015-AO1705-44). Clinical and radiological data, surgical photos and videos are collected in an anonymous and prospective database, available online, designed in collaboration with the Imagine Institute's Data Science team, as shown in Figure 3.1. The relational database is Oracle and access is provided through a web interface developed in PHP. The diagram of the base is presented in Figure 3.4. The interface makes it possible to enter information on patients, malformations, tumors, surgery, clinical follow-ups and state of 3D reconstruction, as seen in Figure 3.2. The interface also gives access to aggregated data, as seen in Figure 3.3.

Until now, 94 patients met the inclusion criteria and were included in the study: 39 tumors, 50 malformations and 5 controls (median age in months (min-max): 156 (84-192)). These control patients underwent a pelvic MRI that happened to be normal. Tumor and malformation types are reported in Table 3.1.

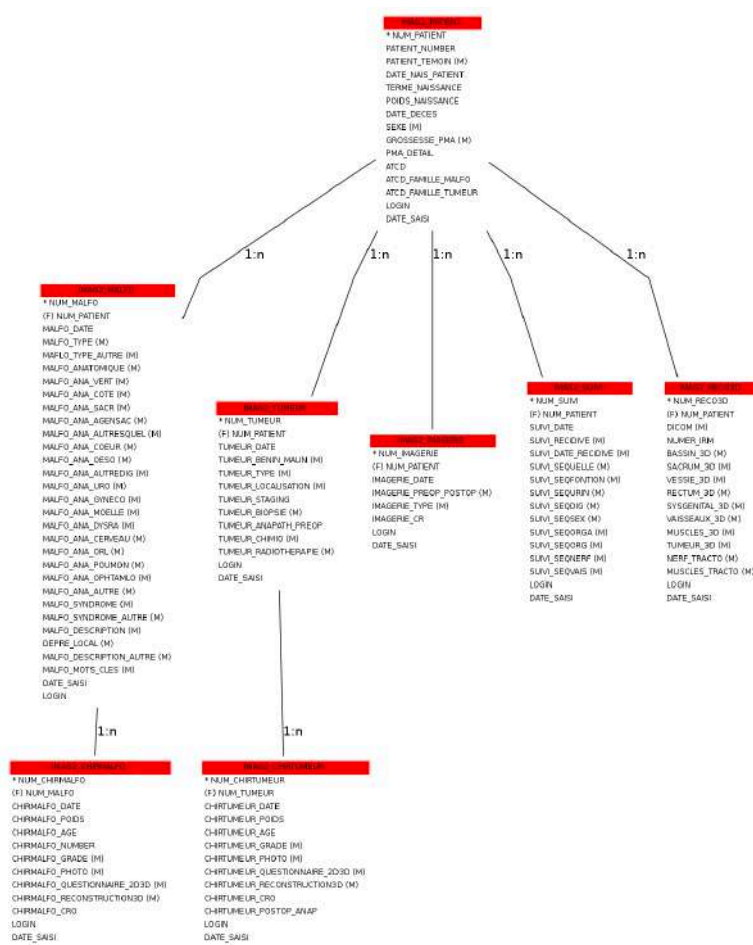


FIGURE 3.4: Database diagram.

TABLE 3.1: Patients' pathologies.

Tumors	39 cases	Median age ¹ in months	Malformations	50 cases	Median age ¹ in months
Ovarian tumor	15	156 (5-192)	Anorectal malformation	32	6 (3-156)
Sacro-coccygeal teratoma	6	11 (0-44)	<i>High</i>	7	6 (3-84)
Pilonidal cyst	1	192	<i>Low</i>	22	6 (3-156)
Lipoma of the buttock	1	36	<i>Cloaca</i>	3	108 (36-120)
Ganglioneuroma	2	120 (60-180)	Urogenital sinus	2	44.5 (5-84)
Ganglioneuroblastoma	1	36	Gynecological malformation	3	156 (132-180)
Neurofibroma	3	144 (96-144)	Urological malformation	5	24 (6-60)
Bladder tumor	2	114 (60-168)	Sacral agenesis	2	72
Urogenital rhabdomyosarcoma	5	60 (12-61)	Sacro-coccygeal dimple	2	42 (24-60)
Kystic lymphangioma	2	84 (60-108)	Vascular malformation	2	108 (96-120)
Burkitt lymphoma	1	62	Rectal duplication	1	60
			Rectocele	1	168

¹ median age (min-max)

3.1.1 Tumors

The ovarian tumor group comprises simple cysts (n=6), teratoma (n=6), cystadenoma (n=1) and cystic lymphangioma (n=1), as seen in Figures 3.5 and 3.6.

A malignant component was present in 2 out of the 6 cases of sacro-coccygeal teratoma, as seen in Figure 3.7. All 3 cases of pelvic neurofibroma happen in the context of NF1 as seen in Figure 3.8. Two other neurogenic tumors are illustrated in Figure 3.9.

The bladder tumor group comprises 1 case of papillary tumor of low grade and 1 case of veino-lymphatic malformation of the bladder wall, as seen in Figure 3.10. The urogenital RMS group comprises prostatic RMS (n=3), urachal RMS (n=1) and vaginal RMS (n=1), as seen in Figure 3.11.

The case of pelvic Burkitt lymphoma, as seen in Figure 3.12 happened in the context of a Nijmegen syndrome, which is a rare autosomal recessive congenital disorder causing chromosomal instability, and characterized by a microcephaly, a distinct facial appearance, a short stature, an immunodeficiency, a radiation sensitivity and a strong predisposition to lymphoid malignancy. Some MRI views will not be displayed because they have only be performed post-operatively with no signs of tumor anymore.

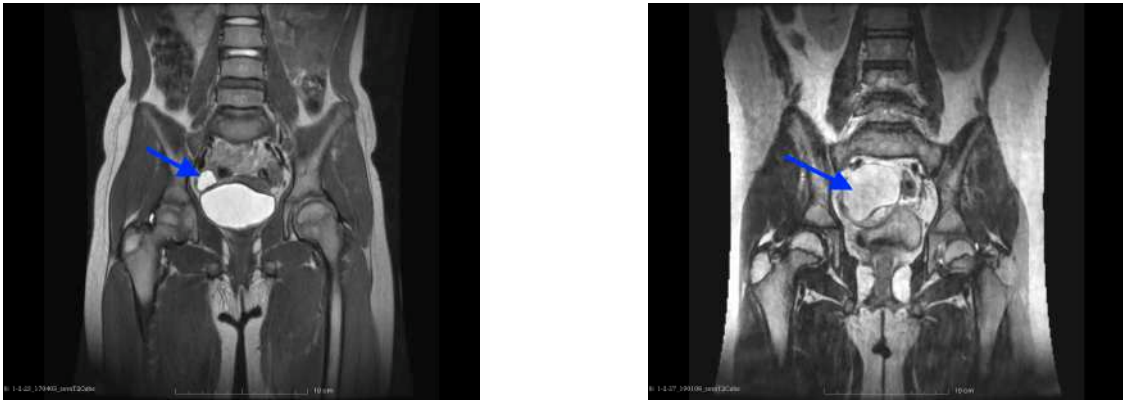


FIGURE 3.5: Simple right ovarian cyst on the left, right ovarian teratoma on the right.



FIGURE 3.6: Right ovarian cystadenoma on the left, right ovarian cystic lymphangioma on the right.



FIGURE 3.7: Benign SCT on the left, malignant SCT encasing the last sacral pieces on the right.



FIGURE 3.8: Pelvic neurofibroma on the left and abdomino-pelvic neurofibroma on the right.

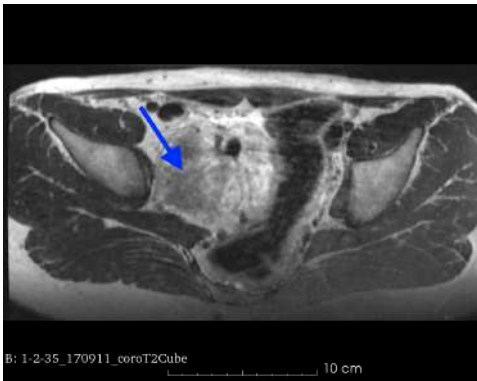


FIGURE 3.9: Pelvic ganglioneuroma on the left, ganglioneuroblastoma on the right.



FIGURE 3.10: Veino-lymphatic malformation of the bladder.

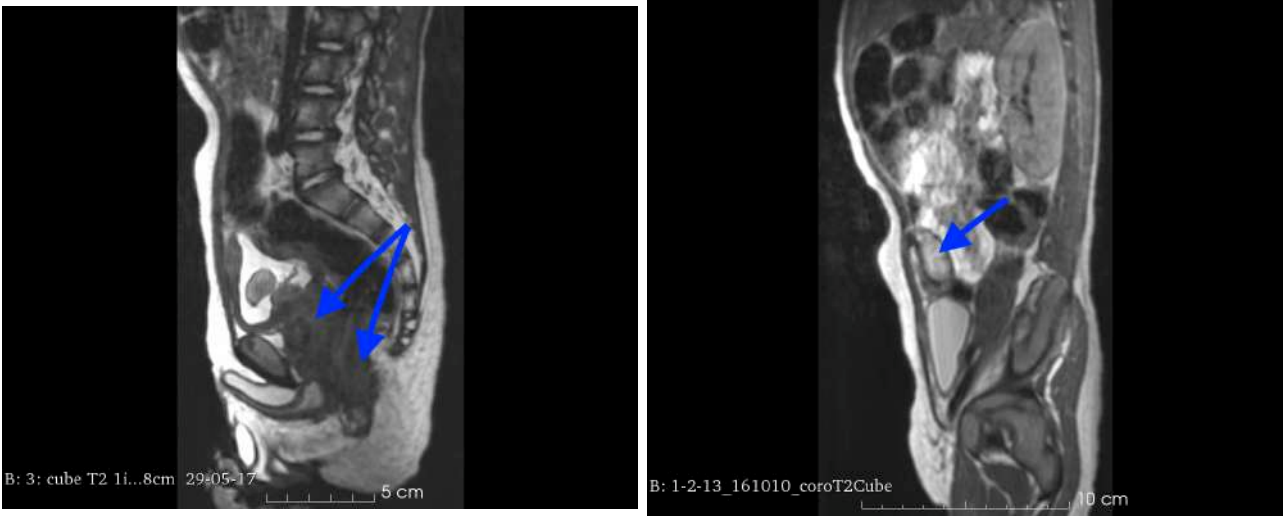


FIGURE 3.11: Prostatic RMS on the left, urachal RMS on the right.



FIGURE 3.12: Abdomino-pelvic Burkitt lymphoma.

3.1.2 Malformations

In this thesis, the radiological evaluation of the pelvic nervous network focuses on the largest group of patients, hence the **ano-rectal malformation (ARM) group (n=32)**, including 16 girls and 16 boys.

As expected, low malformations were more frequent (n=22), including perineal fistula (n=10), vestibular fistula (n=5), recto-bulbar fistula (n=2), no fistula (n=4), rectal stenosis (n=1) as seen in Figures 3.13, and 3.14. High malformations, as seen in Figure 3.15, included recto-prostatic fistula (n=4), recto-vesical fistula (n=1), recto-vaginal fistula (n=1), and caudal duplication (n=1). The series includes also 3 cases of cloaca patients. The occurrence of associated congenital malformations in both ARM sub-groups is reported in Table 3.2.



FIGURE 3.13: Perineal fistula on the left, vestibular fistula on the right.



FIGURE 3.14: Rectal stenosis with colonic dilatation.



FIGURE 3.15: Caudal duplication on the left, cloaca on the right.

TABLE 3.2: Occurrence of associated congenital malformations in both subgroups of ARM.

Associated congenital anomalies	Low ARM n=22	High ARM n=7
Vertebra	3 (13%)	4 (57%)
Ribs	1 (4%)	1 (14%)
Other skeletal	8 (26%)	4 (57%)
Heart	6 (27%)	2 (28%)
Oesophagus	0	2 (28%)
Other intestinal	5 (22%)	3 (43%)
Urinary system	6 (27%)	4 (57%)
Gynecological system	3 (13%)	0
Lung	1 (4%)	1 (14%)
Brain	1 (4%)	0
Head and Neck	7 (32%)	1 (14%)
Eyes	4 (18%)	0
Others	1 (4%)	0

Regarding the status of both spine and sacrum, their association is described in Table 3.3, as well as the level of sacral agenesis, above or below the 2nd sacral vertebra (S2), and the type of dysraphisms encountered, as illustrated in Figures 3.16 and 3.17.

TABLE 3.3: Association between sacral agenesis and spinal dysraphism in ARM patients.

Isolated Sacral Agenesis	3
below S2	3
above S2	0
Sacral Agenesis and Spinal Dysraphism	4
below S2	4
above S2	0
Filum lipoma	1
Short spinal chord	1
Low lying conus	2
Isolated Dysraphism	4
Filum lipoma	4



FIGURE 3.16: Isolated sacral agenesis below S2 on the left, Tethered chord with filum lipoma and sacral agenesis below S2 on the right.



FIGURE 3.17: Low lying conus with vertebral and sacral agenesis below S2 on the left, short spinal chord on the right.

Most of the ARM patients underwent the pelvic MRI **before** the surgical repair of the malformation. However a few patients (n=5) underwent both a pre AND post operative pelvic MRI. This could get us some insight into the consequences of the pelvic surgery on both the muscular and the nervous networks. Some patients (n=9) also only underwent a pelvic MRI after the ARM primary repair, as Necker Hospital is a referral center for difficult ARM cases. These cases will be excluded in the anatomical description of the native nervous anatomy, so that changes cannot be the consequence of surgery. They may however bring some other insights, as they are often very complex and interesting cases.

The gynecological malformation group comprised one case of isolated Müllerian duplication, one case of hydrosalpinx, and one case of vaginal atresia as seen in Figure 3.18.

The urological malformation group comprised one case of ureterocele, one case of ureteral duplication, one case of female epispadias, one case of bladder extrophy, and one case of retro-caval uretere (for examples see Figure 3.19).

The vascular malformation group comprised one case of rectal vascular dysplasia as seen in Figure ??, and one case of dermal perineal vascular dysplasia.

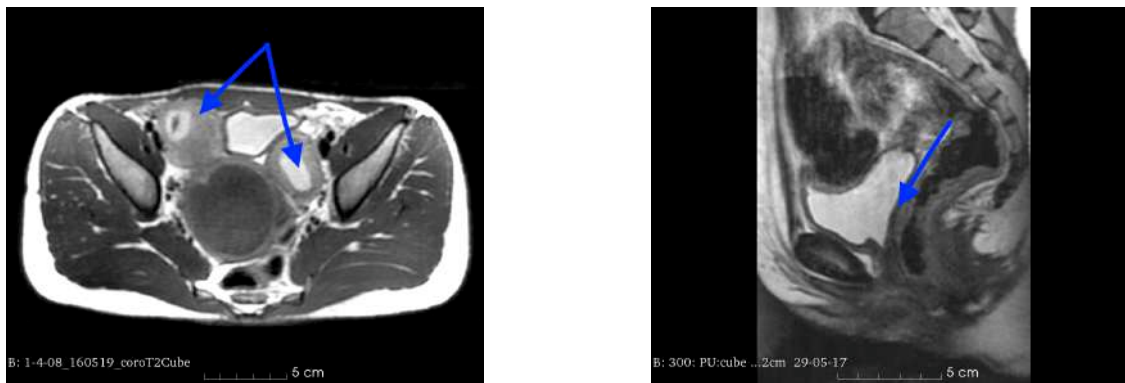


FIGURE 3.18: Müllerian duplication on the left, vaginal atresia on the right.

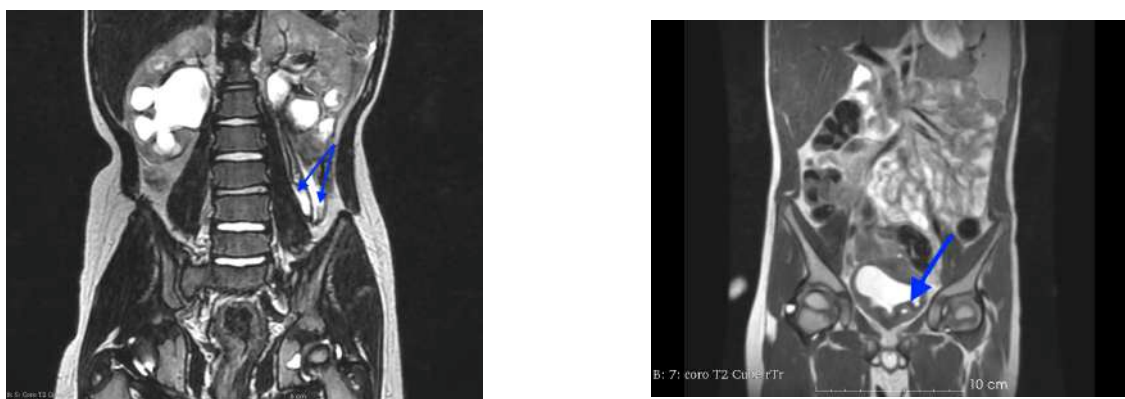


FIGURE 3.19: Ureteral duplication on the left, ureterocele on the right.

Among the malformations group (n=48), 14 patients (30%) present with a poly-malformative syndrome.

The high occurrence of the rare Currarino syndrome (4 cases in our series of ARM) is a consequence of the MAREP rare disease center, which manages one of the largest cohort of patients with this syndrome. Most of the patients also presented with a tumor of the caudal pole such as a pre-sacral teratoma, as seen in Figure 3.20.

VACTERL syndrome (3 cases) is an abbreviation that stands for vertebral defects, anal atresia, cardiac defects, tracheo-esophageal fistula, renal anomalies, and limb abnormalities.

The Cat-eye syndrome (1 case) is a rare chromosomal disorder gathering multiple malformations affecting the eyes (iris coloboma), ears (pre-auricular pits and/or tags), anal region (anal atresia), heart and kidneys.

The PELVIS syndrome (1 case) is a congenital condition characterized by perineal hemangioma, external genitalia malformations, lipomyelomeningocele, vesico-renal abnormalities, imperforate anus, and skin tag.

One patient presented with both Hirschsprung's and Pallister-Hall syndrome, the later being a pleiotropic autosomal dominant malformative disorder, characterized by hypothalamic hamartoma, pituitary dysfunction, bifid epiglottis, polydactyly, and, more rarely, renal abnormalities and genitourinary malformations.

Hunter disease (or mucopolysaccharidosis type II, 1 case), is a lysosomal storage disease caused by a deficiency of the lysosomal enzyme iduronate-2-sulfatase, which first symptoms in early childhood may include abdominal hernias as in this patient in our series.

The Townes-Brooks syndrome (1 case) is an autosomal dominant genetic disorder characterized by the absence of the anal opening (imperforate anus), abnormal ears associated with hearing impairment and thumb malformations.

The Rapp-Hodgkin syndrome (1 case) is a type of anhidrotic ectodermal dysplasia, characterized by anhidrotic ectodermal dysplasia, cleft lip, cleft palate and others features, including genito-urinary malformations.

T21 or Down syndrome (1 case) is a genetic disorder caused by the presence of all or part of a third copy of chromosome 21, which is typically associated with physical growth delays, mild to moderate intellectual disability, and characteristic facial features, including duodenal atresia, pyloric stenosis, Meckel diverticulum, and imperforate anus regarding the intestinal tract.



FIGURE 3.20: Pre-sacral teratoma in a Currarino case.

3.2 Definition of the MRI image acquisition parameters

The MRI device used in this work is a 3T MRI, General Electrics. A cardiac coil with 32 channels is used for the children under the age of 10 years old, and a standard abdominal coil for the children above the age of 10. The MRI research sequence protocol has been initially designed by the pediatric radiologists and the GE application engineer, according to their expertise and the existing literature. These were added to the standard clinical protocol of pelvic imaging for a child presenting a pelvic tumor or a malformation.

The **coronal T2-w 3D sequence** (coro T2 cube GE) has the following parameters: TR 2609 ms; FA 90°, TE 68 ms, with pre-defined protocols registered in the MRI console with fixed FOV according to the child's age (22 cm for babies, 25.6/26.8/32/35 cm for children) matched with corresponding matrices in order to obtain a constant isotropic acquisition (voxel size of $1 \times 1 \times 1 \text{ mm}^3$) for all patients (duration around 7 minutes on average). The aim was to obtain the best quality of images in the 3 planes required for segmentation and 3D modeling.

Respiratory triggering on pediatric patients leads to longer acquisition time that was not acceptable for both the child and the MRI schedule. This is due to high respiratory frequency of the children, and respiratory trigger was therefore not used.

Filtering tests on a healthy voluntary female subject according to GE protocols were also performed: PURE (2 coils calibration based filter, cardiac coil and MRI coil) and SCIC (surface coil integrity correction based on signal compensation according to the distance between the voxels and the surface coil). SCIC filter showed the best image quality and was chosen for the final optimal protocol. Examples of the anatomical sequences are shown in Figure 3.21.



FIGURE 3.21: Anatomical sequence: coro T2 cube with voxel size of $1 \times 1 \times 1 \text{ mm}^3$ (isotropic) in a 13 years old girl with ovarian teratoma on the left, and in a 12 months old girl with ano-rectal malformation (perineal fistula) on the right.

The parameters of the **axial T2-w diffusion sequence** required for tractography were set as follows:

- TR = 6000 ms and TE = 53 ms;
- 25 directions: this choice is the result of a compromise between quantity of directional information and time acquisition. In central nervous system studies, it has been suggested that at least 20 directions are needed for the precise measurement of anisotropy [148];
- 2 NEX : it is the number of acquisitions which are averaged to improve the SNR;
- b 600 seconds/² : the range in peripheral nerve DTI studies for b value usually ranges from 400 to 1000 seconds/mm² [148]. This low value has been chosen to limit artifacts due to bowel movements;
- non-isotropic resolution with a voxel size of $1.5 \times 1.5 \times 3.5$ mm³. The isotropic resolution was not reached for duration reasons and SNR issues especially with the abdominal coil. Lowering the voxel size in all directions would lead to a low SNR. This could be compensated by an increased NEX number, but at the price of an increased duration of the acquisition. This could not be acceptable both for the child, leading to more movement artifacts, and for tight MRI schedule during clinical hours;
- matrix 96×96 pixels and FOV adapted to the size of the patient.

Example of the diffusion sequences is shown in Figure 3.22 in the same patient with an ovarian teratoma.

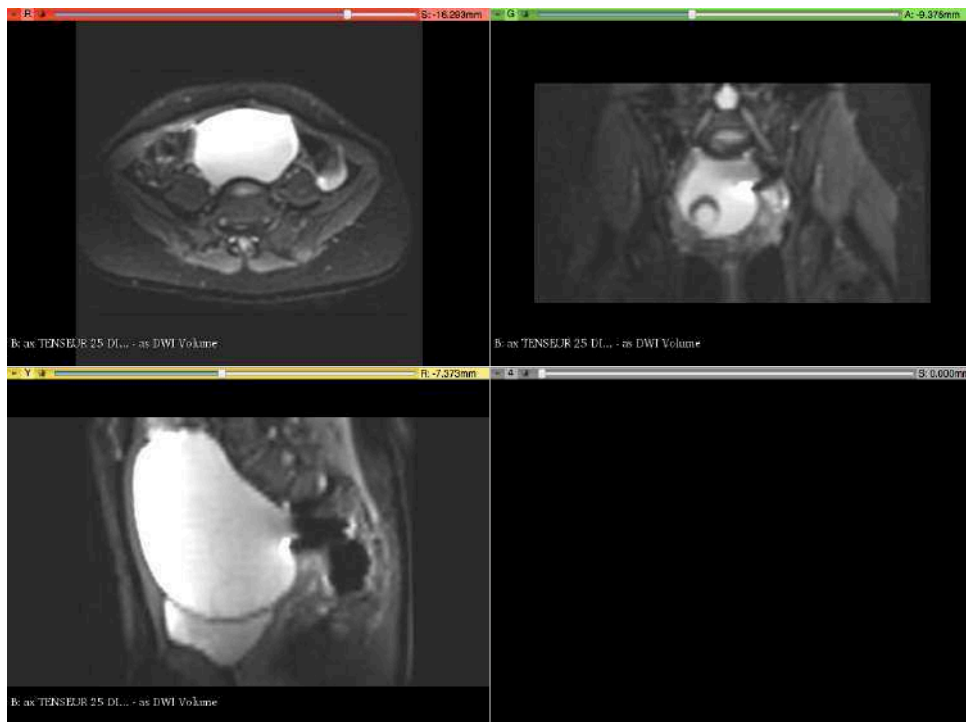


FIGURE 3.22: Diffusion sequences in a 13 years old girl with ovarian teratoma.

3.3 Database organization

Once the patient undergo the pelvic MRI, the DICOM images are directly extracted from the MRI console on an external device and saved in the laboratory database. This database is organized as shown in Figures 3.23 and 3.24, and shall be respected to ensure the absence of loss of information. The Slicer environment, and the modules we used will be described in Chapter 4, as we used this software as our main visualization tool.

Both anatomical image (coroT2cube) and label file were saved in .nii.gz format, as they are meant to be used by the team to semi-automatize the segmentation process with machine learning methods in the near future.

The segmentation process was done mostly manually with the Slicer Segment Editor, within a home-made segmentation template that comprises 61 different structure/labels, as shown in Figure 3.24. Each symmetrical structure has a distinct label for each right and left sides, plus a third label gathering the two sides. This aims at performing symmetry studies based on this database.

The sacral canal is drawn from L5 to coccyx when possible. The sacral holes and the ischial spine are spheres placed in the optimal locations. The genital label means the prostate in male and both vagina and uterus in female patients. The miscellaneous label is used to add a structure specific to the pathology of the patient, such as the common channel in a cloaca for example.

An entire 3D patient's specific model was computed for 70 patients, using in-house semi-automatic methods for the pelvic bones and bladder, and manual segmentations for the other organs (digestive, genito-urinary, vessels and muscles), using the existing tools in 3D Slicer.

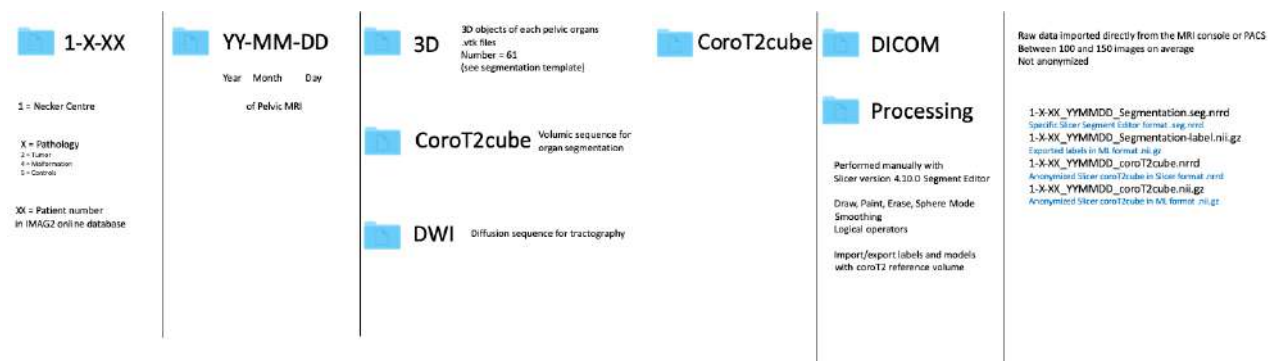


FIGURE 3.23: Main folders of the database on the left, and CoroT2cube sequence analysis on the right.

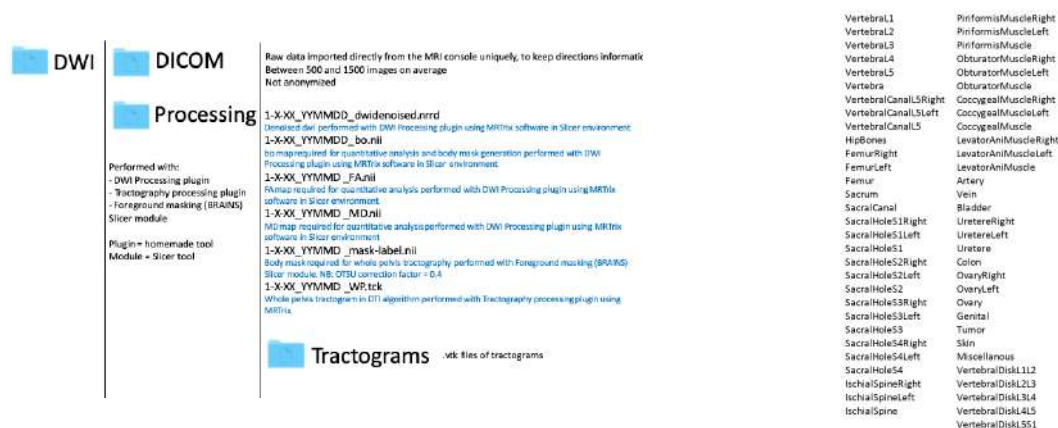


FIGURE 3.24: DWI sequence analysis on the left, and 61 Labels list on the right.

3.4 Conclusion and Discussion

During this thesis, we managed to build a database of nearly a hundred cases of pelvic tumors and malformations in children, highly representative of the pathologies distribution within the pediatric population, as described in the state of art section 2.1. This is both due to the high income of patients in Necker Hospital pediatric surgery department and a good inclusion rate by the surgeons within the department. Even if including a hundred pediatric patients with rare diseases is already a real achievement, we could have even more enrich this database with one of the most frequent pediatric pelvic pathology being Hirschsprung's disease. Its classical management does not include a pelvic MRI, except in cases of severe post-operative complications. However, they would have been well suited for the control group regarding the macroscopic PNN anatomy, especially because the diagnosis is often made at very early ages. They would also have been well suited for pre- and post- operative studies focusing on the consequences of the surgery on the PNN anatomy. Indeed, several surgical techniques are still debated among surgeons, and tractography of the PNN would be a great tool to evaluate them and adapt our practice accordingly.

We could also add more pelvic tumors to the database, especially in the scope of pre- and post-operative comparison studies, as illustrated in our case report [146]. Voluminous tumors endangering proximal nervous structures are ideal cases regarding our current hardware and software limitations in pelvic tractography. It should be more easy to highlight significant changes in these patients rather than in pelvic malformations where the nervous abnormalities are certainly more distal and therefore less easily traceable. From the practical point of view, these children definitively require repeated imaging during their follow-up. However in Paris, oncological centers perform the global follow-up of the patients and they are separated from surgical centers, which makes it difficult to coordinate the MRI planning. An official clinical study on the subject in direct collaboration with those centers would be mandatory to achieve this goal.

Regarding the control group, studying healthy children is a difficult goal to achieve in pediatrics in general, and in our case, the MRI, even if not really invasive, still stays a unpleasant moment for a child. In the future, more pediatric specialties may be involved to implement the database, such as orthopedics, gastro-enterology etc. It would require to collaborate with them in order to identify which child needs a pelvic MRI for his/her classical clinical management, and add the adequate sequences for pelvic tractography.

However, this database still allowed us for studying high quality and homogeneous pelvic MRI data sets in rare disease such as ARM, and use it for both qualitative and quantitative comparisons of their nervous phenotype, as presented in Chapter 6. For both sequences, the quality of the images in pediatric cases allowed to perform both qualitative manual organ segmentations and pelvic tractography. Pelvic pediatric diffusion images are very sensitive to movement artifacts, but it remained possible to register them on the anatomical sequence when required, to draw the ROIs on the main nervous structures on denoised DTI maps, and to obtain coherent tractography results, as detailed in Section 5.1.

The diffusion MRI parameters were set by the radiologic team at the beginning of the thesis according to literature data, and maintained throughout it, in a purpose of consistency. However, in a pure research context with less acquisition time constraints, more work has been performed for fine tuning of the diffusion sequence parameters in a healthy adult subject, with a pelvic MRI performed 3 times consecutively. This work will be detailed later in Section 5.3. As a consequence, the MRI protocol for pediatric patients should be modified now to take advantage of our results and adapt it accordingly. It most probably imply more directions (50), higher resolution, and isotropic voxels. This will consecutively lengthen the MRI acquisition time, which must be discussed with the radiologic team, in terms of benefit-constraint balance, and will require another evaluation by the ethical board.

The on-line prospective database was very useful and easy to use, especially in the scope of clinical studies where we always have to go back to the clinical characteristics of the patients in order to make the best out of our results and design relevant further research hypothesis. The next step would be to incorporate the patient's imaging data, once enough space on the Imagine Institute servers is available: indeed, 1 Gigabyte is necessary for each patient, including DICOM images, and post processing files. It would provide within a sole environment a unique vision on every single patient, with the clinical characteristics matched with radiologic raw data and 3D models. Knowing that all data are anonymized, giving access to this database to other research centers would be a great way to valorize this work and spread IMAG2 expertise on the subject. However, managing intellectual property issues based on medical data is a challenging goal at the moment.

Chapter 4

Segmentation, 3D visualization and portability work-flow

This chapter presents the collaborative work with Alessio Virzi during his PhD, and the Master students Jean-Baptiste Marret, Eva Mille, and Quoc Peyrot.

Section 4.1 presents the software benchmark, the evaluation of semi-automatic segmentation methods and the 3D visualization process.

Section 4.2 presents the portability work-flow that enables to use the 3D patient specific models in a clinical context.

4.1 Segmentation and 3D visualization

4.1.1 Software benchmark

Our specific need of 3D modeling of abdomino-pelvic tumors and malformations in children led us to perform a software benchmark [207]. Several existing software tools for image processing were analyzed according to seven main criteria (automation degree, segmentation time, usability, 3D visualization quality, image registration, tractography and potential plugins). In the literature, few papers reviewed the various software tools able to read DICOM images with the aim of integrating clinical research and medical imaging [91, 125, 198]. In these studies, the authors made the difference between open source, free and commercial tools, and analyzed them according to several general criteria such as usability, interface, data management and 2D and 3D viewing tools. In another study, Presti et al. [127] focused on the issues of image-guided surgery, by reviewing different software tools taking also into account the possibility of their integration in a portability work-flow till the operating room.

However, none of the previous studies considered the segmentation performances of the different software tools. Thanks to our study we quantitatively demonstrated that none of the analyzed software meets the time criteria for segmentation needed in clinical practice. This clearly justifies the need of developing dedicated segmentation methods for pelvis structures in pediatric MRI. Finally, this study led us to choose 3D Slicer as the core software platform ¹ for the development of compatible in-house semi-automatic plugins to perform 3D patient specific models.

¹ <https://www.slicer.org/>

3D Slicer 3D Slicer is a free, multi-platform, and open- source software for image analysis and visualization written in C++, Python, and Qt. The origin of this software was a project between different laboratories of the Brigham and Women’s Hospital and the MIT in 1998. In the past years, several improvements of the software capabilities were achieved through the support of the National Institute of Health (NIH). The main interface of 3D Slicer appears as a typical radiology workstation, allowing for a large number of different visualization configurations to analyze 2D, 3D, and 4D images [104]. Indeed, 3D Slicer presents several advantages: gratuity, open-source nature, large set of manual segmentation tools, a reasonable time of manual segmentation (10 hours on average for a whole pelvis including bones, organs, vessels, muscles and nerves), a good quality of 3D visualization, registration tools, efficient tractography module, and an accessible developer interface enriched by many tutorials and an active community. 3D Slicer thus allows us to represent within the same interface 3D models issued from classical 2D or 3D segmentation and tractography results, which has not been published elsewhere to our knowledge, as seen in Figure 5.2. This work is the subject of a joint publication with Alessio Virzi during his PhD, published in Journal of Digital Imaging [207].

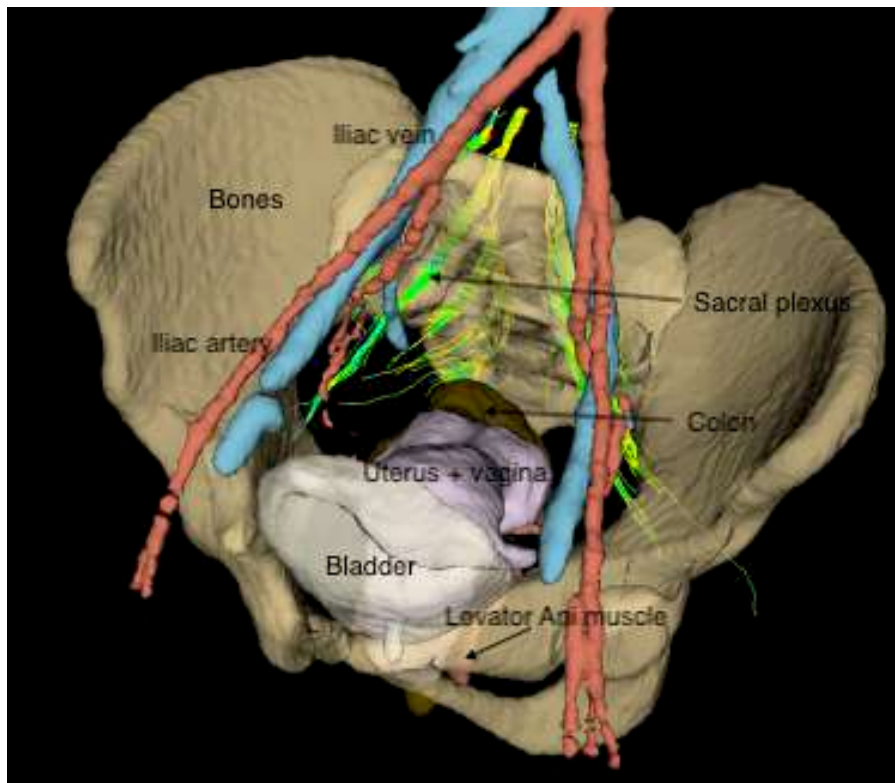


FIGURE 4.1: 3D model of normal adult female pelvis including sacral plexus tractography. The nerves are in light green and yellow, the bones in beige, the urinary system in white, the digestive system in brown and the genital system in purple systems, the vessels in blue for veins and red for arteries, and pelvic muscular complex in dark red.

4.1.2 Semi-automatization of the segmentation process

The work of Alessio Virzi at LTCI / Télécom Paris Tech was dedicated to the development of specific segmentation methods of pelvic organs. He developed new methods for segmenting the pelvic bones, the bladder and the vessels, and implemented them as semi-automatic plugins within the 3D Slicer platform, delivering a powerful and user friendly segmentation tool to the clinicians.

The semi-automatic method for the segmentation of the pelvic bones in T2-weighted images consists of two main steps: first a semi-automatic registration of age-specific bones templates with the target MRI, and secondly the segmentation refinement, based on deformable models, that takes into account the local curvature of the pelvic bones. My collaboration to this work allowed evaluating these tools for user-interaction friendliness and anatomical precision. The quantitative evaluation of the results was realized by Eva Mille during her master thesis. The comparison between manual and semi-automatic segmentation methods, validated by two experts (one professor of anatomy and one pediatric radiologist) led to the following results: significant reduction of segmentation time for both pelvic bones (8282%) and bladder (77%), with a lower clinical relevance for the semi-automatic method. The discrepancies may be explained by the presence of growth cartilaginous areas that are not included in the CT bone template used to guide the segmentation, and the bladder filling degree difficult to standardized in pediatric patients without bladder catheter use. This work led to a joint publication [206]. This methods presents one important drawback: the templates used are extracted for CT scan images, that do not take into account cartilages, that are an important part of the bony structure in a growing child. For this reason, we performed all the bone segmentations manually in this thesis, because correcting the semi-automatized segmentation actually takes longer that doing it manually. We are currently replacing the templates by manual ones extracted from MRI images in order to obtain more accurate results in the pediatric population of our study.

Further work has been performed on bone segmentation by the Master 2 student Quoc Peyrot, using a deep learning approach based on the 3D convolutional network named LiviaNet [70], enriched with a spatial localization information. The performance of the deep neural network was quite satisfactory, with a DICE correspondence index compared to manual segmentation of 0.80 [0.74 ; 0.85], and a calculation time of 30 seconds with an NVIDIA graphic card. Despite these encouraging preliminary results, this methods still needs to be implemented within the Slicer 3D environment to be usable by medical practitioners. The sacrum segmentation for example was therefore performed manually.

The semi-automatic method for bladder segmentation in T2-weighted MRI images is based on a modified version of the Chan-Vese level-set model [43], aiming to obtain a robust pre-segmentation inside the bladder region, and on a parametric deformable model for the final segmentation refinement [39]. The performances of the proposed approach, validated on a set of 25 T2-w MRI volumes of pediatric patients, were quantitatively and qualitatively appreciated by medical experts. This method was very useful for most of the patients, provided the patient does not present an empty bladder, which forces to perform the segmentation manually.

The semi-automatic method for vessel segmentation consists of a patch-based deep learning approach to segment pelvic vessels in 3D MRI images of pediatric patients. For a given T2-weighted MRI volume, a set of 2D axial patches is extracted using a limited number of user-selected landmarks. In order to take into account the volumetric information, successive 2D axial patches are combined together, producing a set of pseudo RGB color images. These RGB images are then used as input for a convolutional neural network (CNN), pre-trained on the ImageNet dataset, which results into both segmentation and vessel labeling as veins or arteries. The performances of the proposed method, validated on a dataset of 35 T2-w MRI volumes of pediatric patients, were quantitatively and qualitatively appreciated by medical experts. This work has been published in [205].

4.2 Portability work-flow

3D patient specific models may be used all along the surgical management process, during the pre-operative phase: surgical planning within the medical staff and patient/parents information and communication, during the per-operative phase to guide the surgery, and during the follow-up phase in parallel to clinical evolution: monitoring both potential complications and natural healing evolution.

Taking into account the difficulty of handling 3D models in a medical imaging post-processing software on regular hospital computers, portable devices appeared to be the best option to build a usable portability work-flow. Tactile devices such as iPad® and iPhone® may display applications where the surgeon must be able to rapidly load the 3D model of the patient, navigate within the 3D scene, zooming on the organ of interest, and playing with transparency. The 3D visualization happens to be very useful to the entire medical team to enhance the surgical planning in complex cases, where the 2D classical black and white radiological images may some times stay obscure. But even in more straightforward cases, the communication with the patients and their parents is greatly improved by the visualization of the organs in bright and different colors, as they do not possess our medical anatomical knowledge. Seeing the large tumor with their own eyes and apprehending the inevitable difficulties of the surgery certainly ease for them the acceptance and the adhesion to the medico-surgical management and its inherent risks.

As a first attempt, we used an application called KiwiViewer developed by Kitware, working on IOS et compatible with 3D models generated by 3D Slicer. To this end, KiwiViewer extension has to be uploaded in 3D Slicer to convert all the segmentations in one sole ZIP file compatible with the application. Taking into account the data confidentiality requirements, these 3D models cannot be stored on any type of external server or cloud. The ZIP file needs to be registered within the anonymous database. The data base access is ID and password secured (HTTPS protocole). The ZIP file URL address up-load in KiwiViewer application allows for the vizualisation of the patient's specific model on a tablet or smartphone, the navigation within the 3D scene, zooming on the organ of interest, and playing with transparency as seen in Figures 4.2 and 4.3. This solution however could not be further developed because of the absence of 64bits version update of Kiwiviewer to match the evolution of tactile devices.

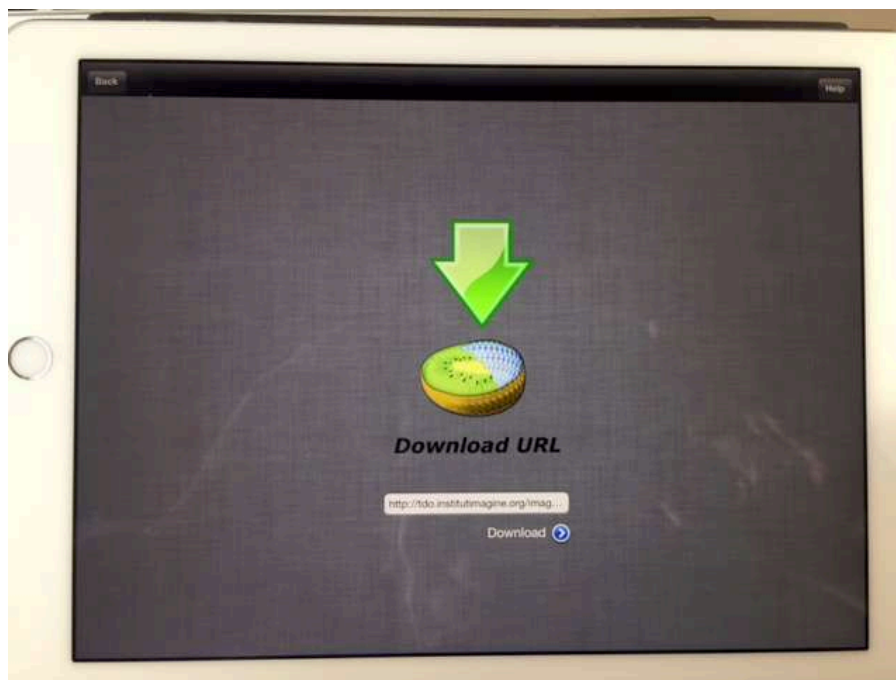


FIGURE 4.2: Kiwi viewer interface for downloading the url link to the 3D patient specific model stored in the anonymous database.

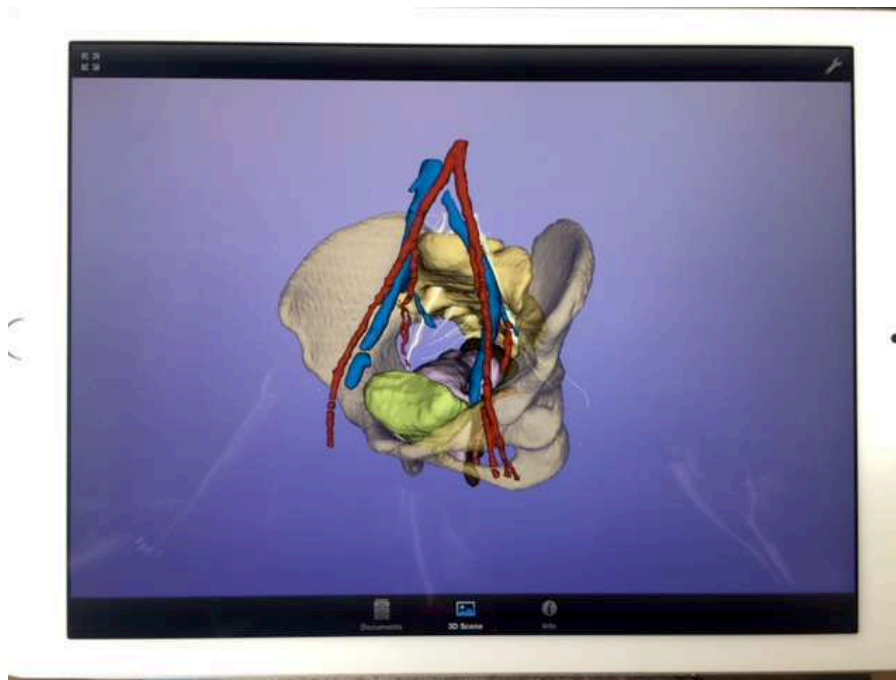


FIGURE 4.3: Kiwi viewer interface for visualization of 3D patient specific model.

Next, Alessandro Delmonte designed the IMAG2 specific visualization software to fulfill the surgical team requirements. The utilized framework was Unity 3D, and C# language. A very simple, elegant and user friendly interface allows for a magnified visualization of the 3D models, compared to Kiwiviewer or 3D Slicer 3D scene. It also provides the usual features of rotation, translation, zooming, explode mode to separate 3D objects, and transparency levels to enable the best comprehension of the patient's anatomy, as seen in Figures 4.4, 4.5 and 4.6.

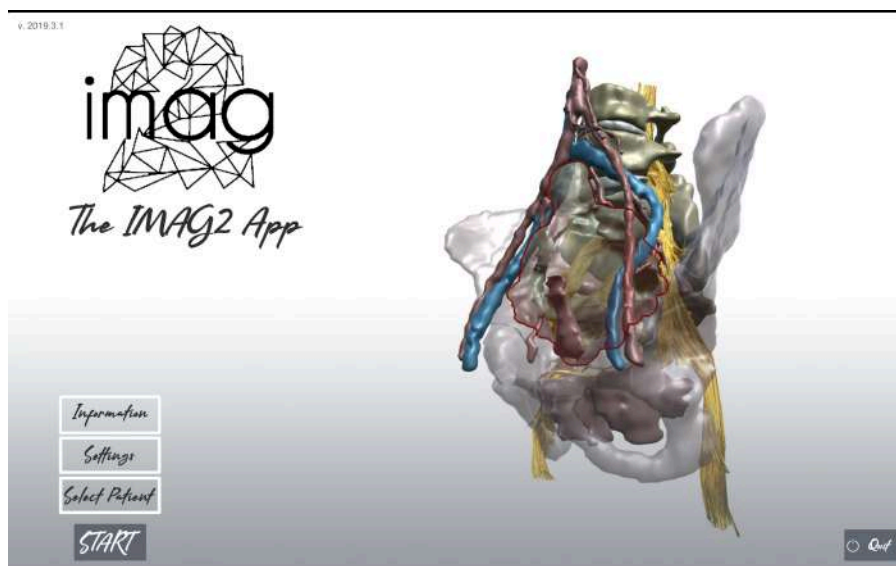


FIGURE 4.4: Welcome page of IMAG2 visualization software.



FIGURE 4.5: Pelvic bony, muscular, nervous and vascular anatomy of a 2 years old girl with low anorectal malformation on the left, with a zoom on the right L5 root on the right.

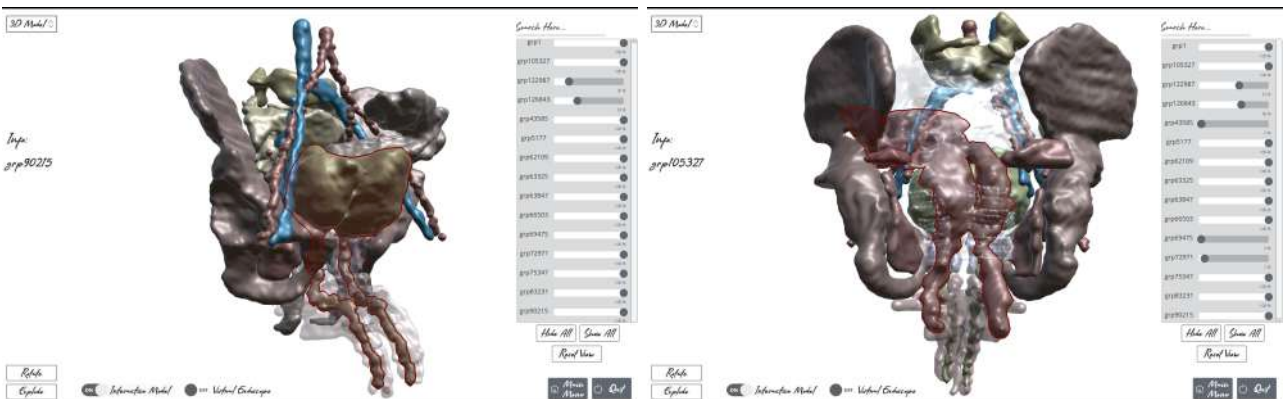


FIGURE 4.6: Rare case of caudal duplication in a 3 months old boy, with the visualization of the double bladder, urethra and penis on the left and the double rectum and colon on the posterior view on the right.

4.3 Conclusion

All the work performed by Alessio Virzi during his PhD, the master students, and Alessandro Delmonte supported my personal work on pelvic tractography segmentation. Indeed, their work on methods to semi-automatize the process of pelvic organ segmentation was of great help in order to lower the time required to perform it. It is a mandatory step, as the tractography segmentation method we developed is based on the anatomy of pelvic organ segmentation, as presented in Chapter 5. The work on the semi-automatization process of pelvic organ segmentation is still on-going. The Master student Quôc Peyrot will spend his PhD starting next year on deep learning methods for image segmentation. This is a very promising field, and we have provided now for nearly a hundred of manual segmentations of the whole pelvis, that was mandatory to train these algorithms. Shortening the pelvic organ segmentation time will also increase the performance of our anatomy tractography segmentation method.

All these methods were embedded into plugins for the Slicer 3D environment. Despite its long learning curve, this software is usable for medical practitioners without any mathematical or coding background, and allows them to test patients' data sets of images and perform statistical studies as developed in Chapter 6. This every day collaboration between research engineers in medical image processing developing new methods and medical practitioners having the anatomical and clinical knowledge and a direct access to patients data is the key to a successful translational research, that can improve our knowledge and generate an impact in our medical practice.



Chapter 5

Pre and post-processing methodology for DTI tractography of pelvic nerves

This chapter is the first part of the main contribution of this thesis with Chapter 6. We aim here at developing a method for pre- and post-processing DTI images with tractography in order to explore the anatomy of the PNN, including both the somatic and autonomous systems.

In Section 5.1 we detail a preliminary approach of classical ROI-based tractography performed on a control adult female subject, the corresponding results, and its limitations along with possible solutions.

In Section 5.2 we detail our pre- and post-processing work-flow for pelvic diffusion images, regarding denoising, registration issues, tractography software used for tractograms generation, and tractography parameters. This workflow is summarized in Figure 5.5.

In Section 5.3 we detail the work performed to optimize the acquisition parameters of the diffusion sequence, using 3 consecutive MRI acquisitions of the same healthy adult female subject, with variations of b value, number of directions and number of NEX.

In Section 5.4 we detail the anatomy of the pelvic nervous network according to the existing literature in a much more extensive manner as in Chapter 2, and adding highlights on the main surrounding structures such as bones, muscles, vessels and organs along with their relationships with the PNN.

In Section 5.5 we develop an original method for anatomy-aware tractography segmentation, using the description of each nerve in natural language, and transformed into mathematical language. This method is tested on the same healthy adult female subject used in the preliminary ROI-based approach of Section 5.1. The resulting nerve bundles were analyzed from a qualitative and quantitative point of view.

5.1 DTI ROI based tractography: preliminary study

5.1.1 Introduction

The classical ROI based method used in the literature in both brain and peripheral nerve imaging (see Chapter 2) consists in manually drawing one or several ROIs along the nervous track of interest to guide the tractography. These ROIs are usually placed where the fiber bundle is more visible, along its path, and also at its end (inclusive ROIs), and in other strategic places where the fiber bundle is surely known not to pass through (exclusive ROIs) [208]. However, the noise of the pelvic diffusion image itself and the numerous non-nervous structures within the pelvic area prevent from identifying clearly the pelvic nervous network along all its path. For this reason, a manual multi-ROI approach placing several ROIs from its beginning to its end, remains quite unachievable. The only place where the pelvic nerves can surely be identified on a diffusion image is their very beginning, within the sacral canal and the sacral holes. This approach is tested next on an adult healthy subject.

5.1.2 Method

To perform this preliminary study, we used the volumic sequence for the sacrum segmentation (as detailed in Chapter 3), and a diffusion sequence which parameters were: 25 directions, b600, 2 NEX. No denoising was performed of the diffusion images in this first exploratory study. The tractography was carried out using the Slicer Tractography ROI Seeding module (DTI deterministic algorithm), with the following parameters: seed threshold(FA)=0.1, cutoff(FA)=0.05, angle(fibers)=45°, length(fibers): 50 - 800, according to the existing literature on pelvic nerve tractography [199].

Our ROI-drawing method consists in manually draw the ROIs only at places where the pelvic nerves are clearly visible and surely go through, meaning within the sacral canal and the sacral holes, on each slice of the b0 image (see Figure 5.1). We chose this method in order to avoid muscle or ligament tracking (false positives), that may occur when drawing other ROIs inside the pelvis.

As a consequence, in order to identify the level of the sacral roots and recognize them according to their contact with the bones, the first mandatory structures to manually segment are the pelvic and sacral bones on the volumic anatomical sequence. Then comes the placement of the ROIs themselves, the sacrum canal, the vertebral canal L5 and the sacral holes, on the same sequence. No registration was performed between anatomical and diffusion sequences, as the subject did not move during the acquisition. The registration of the organs was checked visually.

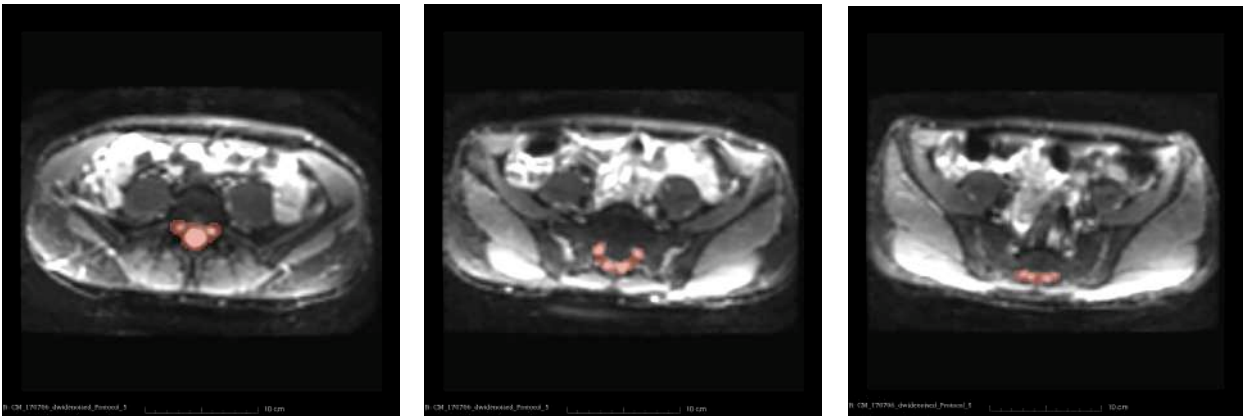


FIGURE 5.1: Manual ROI drawing (in red) within the sacral canal and the sacral holes on axial diffusion images, slices left to right going in a caudal direction, from the level of vertebra L5 to the coccyx.

5.1.3 Results

Using this ROI-based method, we obtained the representation of the proximal part of the sacral roots from L5 to S3, as seen in Figure 5.2. This sacral plexus tractogram was similar to the ones presented in the literature on pelvic tractography [199], in terms of localization, global shape, thickness of the tracts, and the number of sacral roots (L5 to S3), as seen in Figure 5.3.

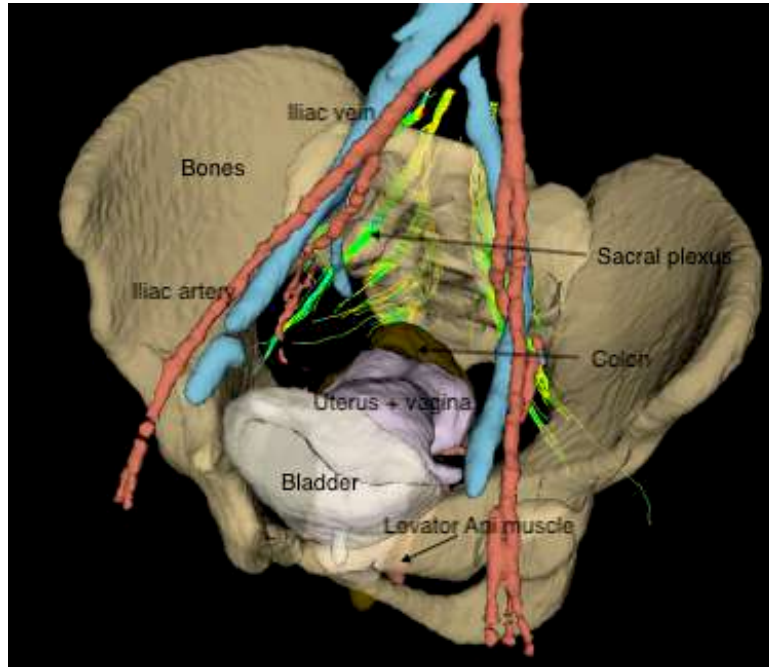


FIGURE 5.2: Tractography of the sacral plexus included in the 3D model of the pelvis of an adult healthy female subject.

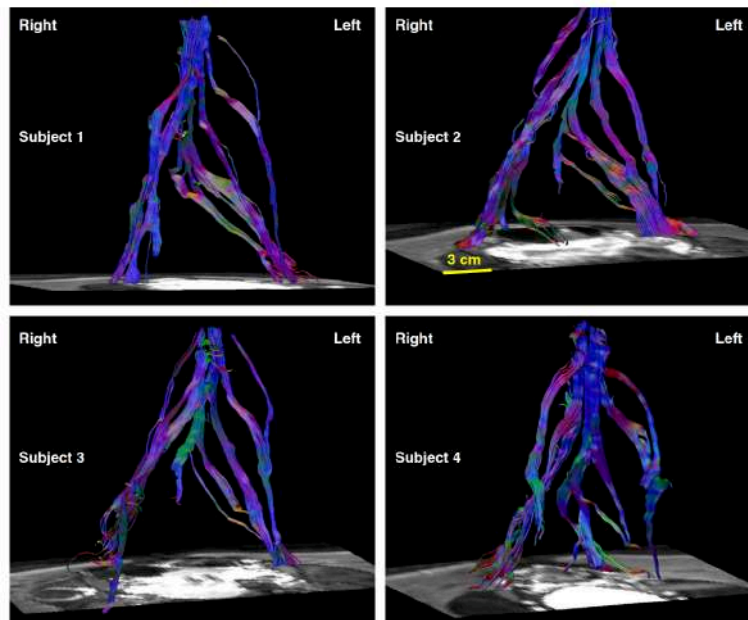


FIGURE 5.3: Feasibility of tractography of the normal sacral plexus demonstrated in four different volunteers presented in the work of van der Jagt et al. [199].

A critical analysis of these preliminary results leads to the following observations:

- there are "noise" fibers belonging to the posterior inter-spinous ligament and to the muscles of the hip, due to the lack of precision during manual ROI drawing within the sacral canal till the coccyx. Several attempts of placing the ROIs within the sacral canal led to similar noisy results. Indeed, the distal inner part of the sacral canal may be difficult to correctly distinguish from the bony and ligament structures surrounding it, due to its small size and the quality of the diffusion images;
- we failed to find the entirety of distal nerves like the pudendal or obturator nerve. These are very thin nerves (around 1-3 mm of diameter), that may have a very low FA. However, when lowering the FA beginning threshold, the result is far too noisy. Moreover, the resolution of the acquisition may be too low (3.5x3.5x3.5 mm³) to see them;
- we cannot investigate the anatomy of the hypogastric plexus with this method, because the precise ROI drawing of this complex, thin and very variable nervous network is impossible. It is located more medially within the pelvis compared to the sacral plexus, surrounding the ureters and iliac vessels. It is somehow connected to the somatic sacral plexus but with very small fibers, showing myelinisation variations, that may prevent the tractography algorithm to find them using a sacral canal ROI based approach.

5.1.4 Conclusion on the preliminary study and proposed solutions

To summarize, according to the known anatomy of the pelvic nervous network, these preliminary results showed missing fibers (false negatives) and some unwanted fibers (false positives). To improve these results, we designed in parallel our own pre- and post-processing work-flow of diffusion images using existing tools for brain analysis and an original tractography segmentation method.

One step consists in pre-processing the diffusion data sets using state of the art methods available in the literature and on-line, as detailed in Section 5.2. The goal is to obtain the cleanest data set as possible, to increase true positive tracts and to reduce false positives. However, software such as MRTrix are not easy to use by non engineers, due to the need of command lines to be launched through the computer terminal. The implementation of such tools via several plug-ins developed by Alessandro Delmonte allowed to exploit these state-of-the art tractography tools in a user-friendly interface. Another step consists in working on the diffusion sequence acquisition parameters, as detailed in Section 5.3, in order to increase true positive tracts. Regarding our constraints of using a clinical 3 Teslas MRI scanner, this step was performed on an adult voluntary healthy female subject, during a restrained slot (one hour) devoted to research acquisitions. Moreover, despite our target of pediatric patients, an hour spent within the MRI machine for research purposes is hardly achievable for a healthy child.

With the aim of finding more true positive tracts, including the inferior hypogastric plexus, the main idea is to compute a whole pelvis tractogram, in analogy to whole brain tractography, and lower the FA stopping threshold to 0.01 in order to track even small and thin fibers presenting a low level of FA. Then the next step is to use the surrounding pelvic organ segmentations to filter this tractogram and identify our nerve targets. The first attempt in that sense consisted in computing the whole body tractogram using a body mask from which we subtracted all the segmented pelvic organs. The result was however still too noisy, with a lot of fibers which nature could not be recognized with certainty as distal sacral plexus nerves, hypogastric plexus or muscles, as seen in Figure 5.4.

Willing to continue to explore the hypothesis that an anatomy-aware tractography segmentation method may be the solution to improve our results, we designed the Pelvic Query Language (PQL), as detailed in Section 5.5. This method requires a thorough understanding of the pelvic nerves anatomy, that will be detailed in Section 5.4.

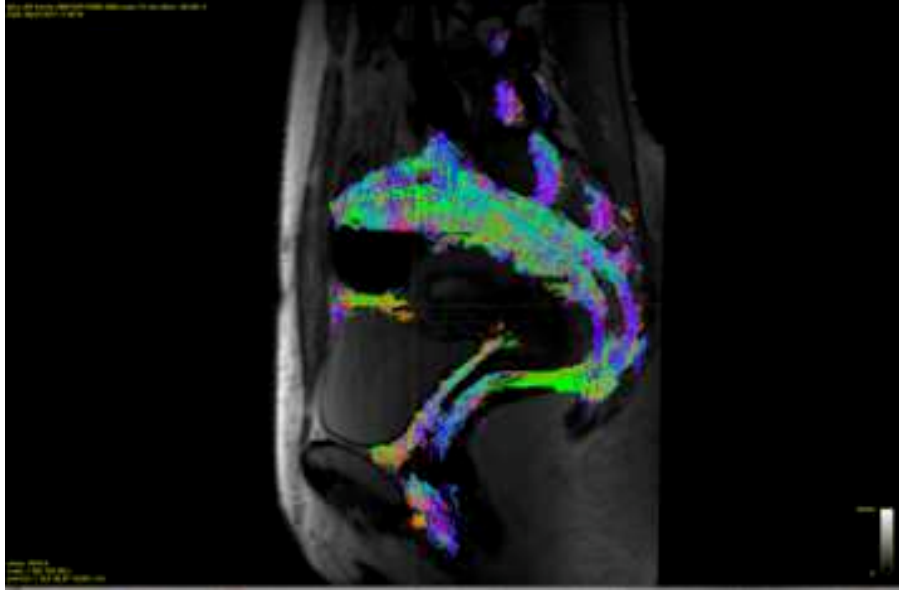


FIGURE 5.4: Whole body tractogram computed using the MRTrix software after the subtraction of the pelvic organs from the body mask.

5.2 Pre and post-processing work-flow for pelvic diffusion images

Our pre- and post-processing work-flow of diffusion images is represented in Figure 5.5.

5.2.1 Pre-processing

We performed the pre-processing of diffusion images using a plugin developed and integrated in the 3D Slicer environment by Alessandro Delmonte. This plugin uses methods and software packages from MRTrix for denoising [201, 202], correcting frequency/phase shifts, spatial non-linearities and field inhomogeneities [185], as well as the Gibbs artifact [107].

Registration

Giving that we aim at merging post-processing results from the volumic sequence (organ segmentations) and diffusion sequence (tractograms), both images must be well aligned. If they are not, the final 3D model of the patient will be anatomically incoherent. We visually evaluate the difference of alignment between the two images in the Slicer 3D viewer. This process is qualitative and depends on expert anatomical knowledge. The quality of registration is assessed as: minor, medium or major misalignment. The misalignment was judged minor if there was no major rotation and/or translation and no deformations. The misalignment was judged medium if there was more than one centimeter in translation and/or more than 20° in rotation angle, and no deformation. The misalignment was judged major if there was important deformations combined with scaling issues. The anatomical landmarks used are the base of the proximal (promotoire) and distal (coccyx) sacral limits in the three planes.

If the misalignment has been judged minor, we can correct it by manually applying an affine transformation on the anatomical image using the diffusion image as a reference. The output image is linearly interpolated. This transformation is manually applied by using the Transforms module of Slicer 3D allowing us to verify in real time the applied transformation. The optimal transformation was chosen by visually verifying the alignment of the previously mentioned anatomical landmarks (promontoire and coccyx).

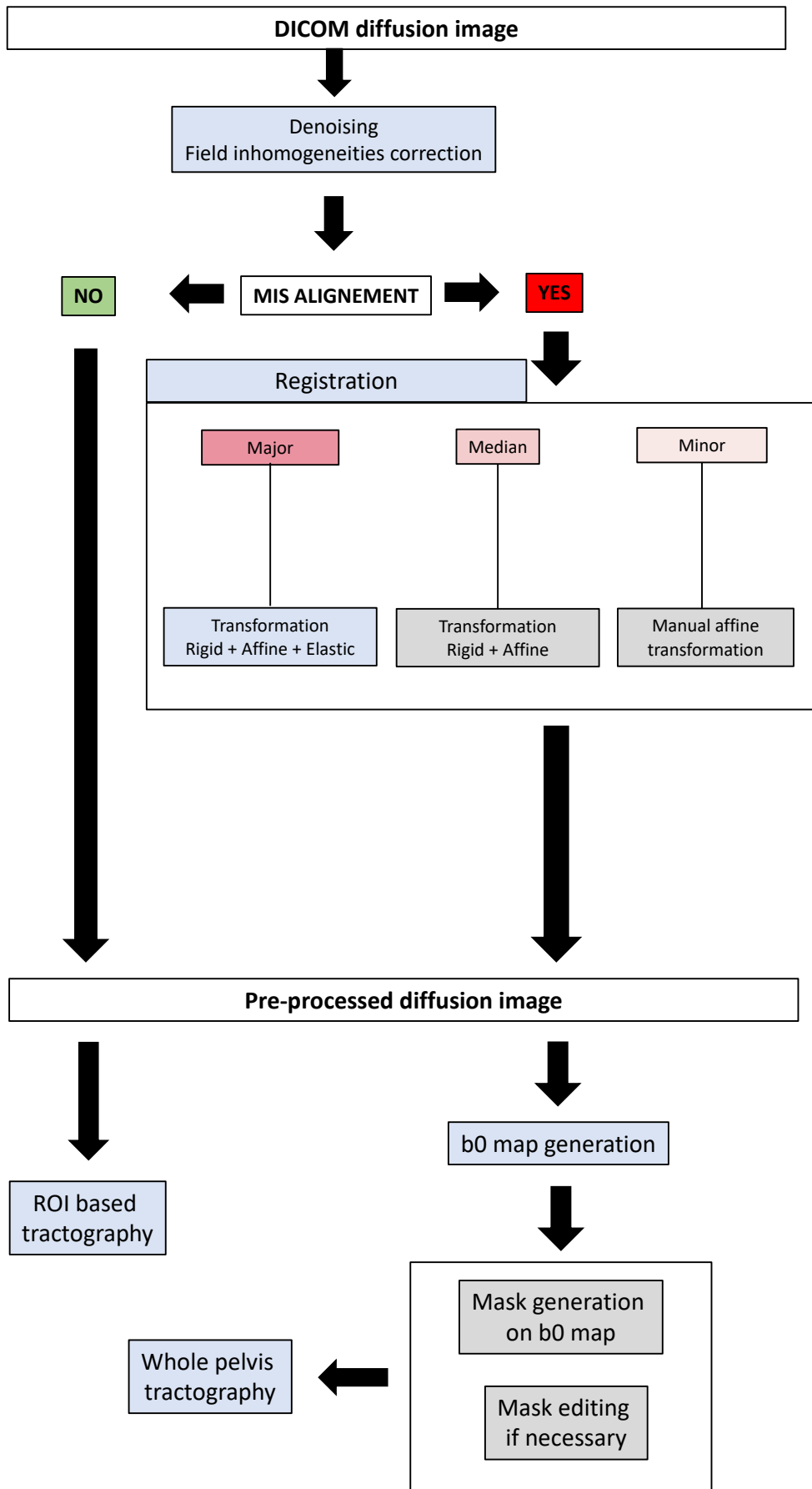


FIGURE 5.5: Pre and post-processing work-flow of diffusion images. In blue = home-made plugins; in grey = 3DSlicer modules.

If the misalignment has been judged medium, we chose to use the General registration (BRAINS) module of Slicer 3D to avoid inaccuracies of a manual registration and keep a low computing time. In this process we combine multiple transformations: first rigid transformation, translation and rotation with 6 degrees of freedom and then an affine transformation with 12 degrees of freedom. The first rigid transformation is used to perform a global alignment between the two images, and then the affine transformation finely completes the registration process. In both phases we chose a linear interpolation method. Both transformations are automatically computed in order to maximize the mutual information between the volumic image and the diffusion image [134], which is well suited for images of different natures. The optimization algorithm is based on gradient descent (<https://www.nitrc.org/projects/multimodereg/>).

If the misalignment has been judged major, a more complex registration method is necessary, since we must be able to find the corresponding information between the two images. In this scope, we decided to perform a registration process that uses consecutively rigid, affine and then elastic transformations. The corresponding algorithms are implemented in the software suite called ANTs (Advanced Normalisation Tools) (<http://stnava.github.io/ANTs/>). To achieve proper registration we need non-linear registration algorithms: we chose SyN, one of the top performing algorithms present in ANTs [110]. Beside going through registration algorithms, ANTs improves the registration within each algorithm gradually at different resolutions. The idea is to start with "blurry" images (low resolution, highly smoothed), register those to each other, then go to the next iteration, at a higher resolution, and so on. We registered the lowest resolution image (diffusion image) on the highest one (volumic image). For the first two steps (affine and rigid transformations), the interpolation was linear, and the similarity measure was the mutual information. For the third step (elastic transformation), the similarity measure was the cross-correlation measure, as a consequence of better experimental results. This latest registration takes a long computing time (between 3 and 4 hours), and was therefore used with parsimony.

5.2.2 Post-processing

If there is no misalignment and the two sequences are already well aligned, tractography post-processing is possible either with a ROI based method as described in Section 5.1, or using a method based on whole pelvic tractography.

When the chosen method is based on whole body tractography, a mask on the b0 image may first be generated. The whole pelvis tractography does not need to be performed on the whole DWI image, so generating a body mask of the region of interest of the inner pelvis may be of use for noise filtering, computing time saving and file size reduction. The Foreground masking BRAINS module of 3D Slicer is then used to create a mask over the most prominent foreground region of the image. This is accomplished via a combination of Otsu's thresholding [156] and a closing operation, performed using a cubic structure of 9x9x9 voxels. If the result is not completely satisfying, with a few missing voxels within the pelvic area, this mask may eventually be modified through the Slicer3D segment Editor.

The body mask is then used to generate the whole body tractography .tck file, using tckgen MRTrix software package. It uses a DTI deterministic algorithm. It contains a maximum of 1 million fibers departing from 3 seeds per voxel and weighs 6 Gigas on average. The parameters are: Seeds Threshold (FA) = 0.15; Cutoff (FA) = 0.01; Admissible angle = 45°; Length = 50-800 mm. The parameters have been modified compared to the one used in subsection 5.1: the FA seeds threshold have been elevated at 0,15 instead of 0,1 in order to minimize false positive tracts; the FA cutoff has been lowered to 0.01 instead of 0.05 in order to give the opportunity to continue the tracking of even small distal fibers with a low FA; angle and length have not been modified.

5.3 Choice of the parameters of the diffusion sequence

Ideal diffusion MRI acquisition parameters is a difficult goal to reach, especially with a tractography purpose. They must be adapted to objective of the study, to the anatomical area that is investigated, and to the used MRI hardware. A lot of work on the subject has been done in the brain area [210], but very few in the field of peripheral nerve imaging, and none in sacral plexus tractography. Moreover, there is always a necessary trade-off between the acquisition time, the SNR and the expected results. Once the parameters has been chosen arises also the question of reproducibility along time with the need of a longitudinal study with the same subject and identical parameters.

5.3.1 Method

Data sets

In order to improve the pelvic tractography results while maintaining an acceptable acquisition time, we performed three times consecutively a pelvic MRI on the same healthy adult female subject. All MRIs included the same coronal T2-weighted volumic sequence with isotropic voxels $1 \times 1 \times 1 \text{ mm}^3$ (acquisition time = 7 minutes), and a diffusion sequence with fixed TE (57), TR (6550), matrix (96x96), FOV ($32 \times 32 \text{ cm}^2$) and voxel size ($3.5 \times 3.5 \times 3.5 \text{ mm}^3$) for an acquisition time of 15 minutes. The first MRI also included different diffusion sequences modifying the following acquisition parameters:

- number of acquisitions (NEX=1 vs NEX=2), in order to evaluate if we could reduce the acquisition time without losing too much SNR;
- number of directions (50 vs 25), in order to evaluate the influence of the increase of the number of directions on the tractography result;
- b value (1000 vs 600), for the same purpose;
- acquisition axis (oblique vs strictly axial), for the same purpose, according to the global orientation of the sacrum and the sacral plexus.

This led us to six different diffusion protocols:

Protocol 1 = 25 directions, b600, 2NEX

Protocol 2 = 25 directions b600 1NEX

Protocol 3 = 50 directions b600 1NEX

Protocol 4 = 50 directions b600 2NEX

Protocol 5 = 50 directions b1000 2NEX

Protocol 6 = 50 directions b600 oblique axis 1NEX

The second MRI included two different diffusion sequences, one with 50 directions corresponding to protocol 5 of the previous MRI and the other one with the same parameters but 100 directions. For scanning time reasons, no further variations in the protocol were possible. It should be mentioned that the subject gave birth between the first and the second MRI. Some changes in the pelvic anatomy may be induced by this event.

The third MRI only included one diffusion sequence (protocol 5).

Pre and post-processing

The pre-processing method followed the work-flow detailed in Section 5.2. The tractography was performed using a ROI based approach, the ROIs being manually drawn on the sacrum canal and the sacral holes.

Quantitative analysis of tractography results

We performed a quantitative analysis of fibers bundles through the generation of various evaluation measures. For each sacral plexus root, the values representing the mean, median and standard deviation are computed, as well as the maximum and minimum boundaries. In the scope of a symmetry study, each side (left and right) of the sacral roots were computed separately. To study the characteristics of each sacral root in this control patient, we chose the following measures, according to the existing literature [89]:

- Geometrical measures

Length of the fiber bundle: Total length of the fiber (in mm) is computed by adding up all the streamline segments. Each streamline segments has a length that is computed using the Euclidean distance between two consecutive points.

Mean Turning angle of the fiber bundle: For every triplets of points along the fiber, the local angle was computed in the reference of the plane formed by the triplets. The mean of all the angles is then calculated to give the mean turning angle of the fiber bundle. It is expressed in degrees. In order to take into account the length of the fiber bundle, we then calculated the mean turning angle/length of the fiber bundle, expressed in degrees/mm.

Volume of the fiber bundle: To compute this volume in mm^3 , the tracts must be converted into a volume using the Slicer 3D module Tractography to MaskImage. This module converts fiber bundles to volumes by filling pixels in the volume where fiber points are located, an operation called rastering. The volume in mm^3 will then be calculated using the 3D Slicer module Label Statistics. The count of filled pixels is the number of pixels in the volume that have this value. The volume mm^3 is the product of this count times the resolution of the image.

- Diffusion measures

Mean FA value of the fiber bundle: this measure is computed by calculating the mean between FA values at every point of the streamline on the FA map.

Mean MD value of the fiber bundle: this measure is computed by calculating the mean between MD values at every point of the streamline on the FA map.

Additionally, the 3DSlicer integration enables an interactive and immediate fiber analysis, complemented by graphs, as seen in Figure 5.6. If the box 'Plot distribution' is ticked the scene will switch automatically to a layout with a plot window containing the profile of the selected evaluation measures along the fiber lengths. Each fiber is divided in twenty portions. In every fiber portion the measure values are mapped for all the points composing them. The section score is then computed as the mean of the measure values.

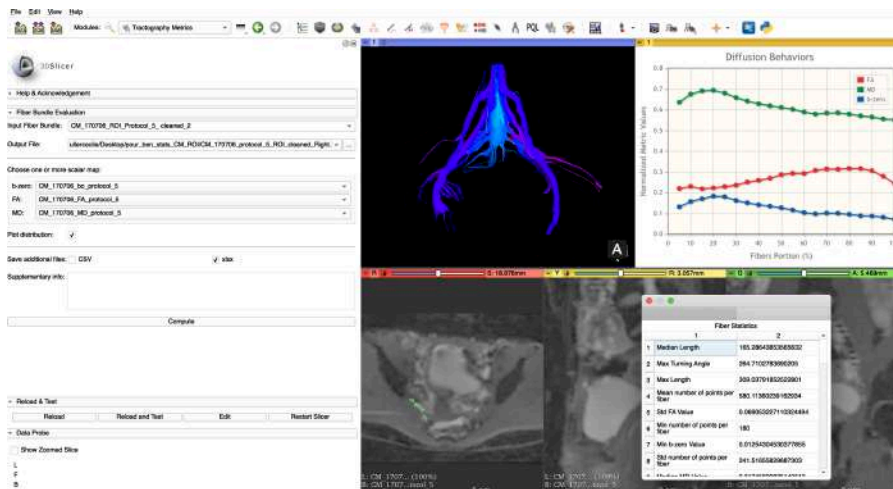


FIGURE 5.6: 3D Slicer interface for fiber properties.

5.3.2 Results

Qualitative and quantitative analysis

The qualitative analysis is performed by visual appraisal and the sacral plexus tractograms together with the 3D bony structures (hip bones and sacrum) are presented in Figures 5.7 for protocols 1 and 2 of MRI N°1, Figure 5.8 for protocols 3 and 4 of MRI N°2, Figure 5.9 for protocols 5 and 6, Figure 5.10 for MRI N°2, and Figure 5.11 for MRI N°3. The quantitative analysis detailing ROI based tractograms measures is presented in Table 5.1. In the table, results separate left and right sides of the sacral plexus, but in the following analysis, we will consider either the sum (for geometrical measures such as volume and length) or the mean value (for functional measures such as FA and MD) of the two right and left sacral plexus tracts.

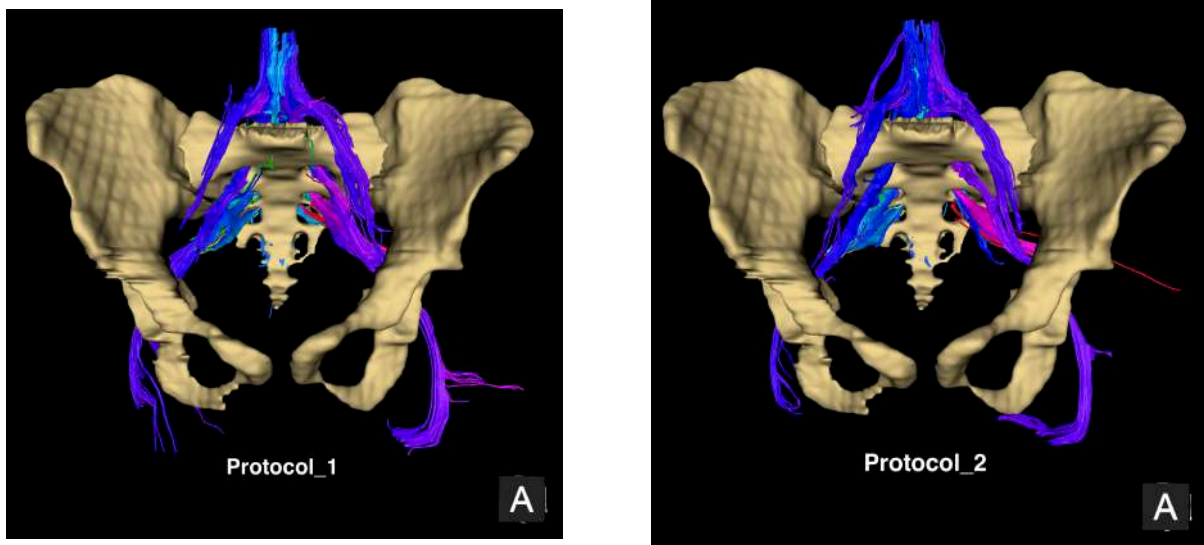


FIGURE 5.7: Sacral plexus obtained with the ROI-based method on the first MRI using protocol 1 on the left and protocol 2 on the right.

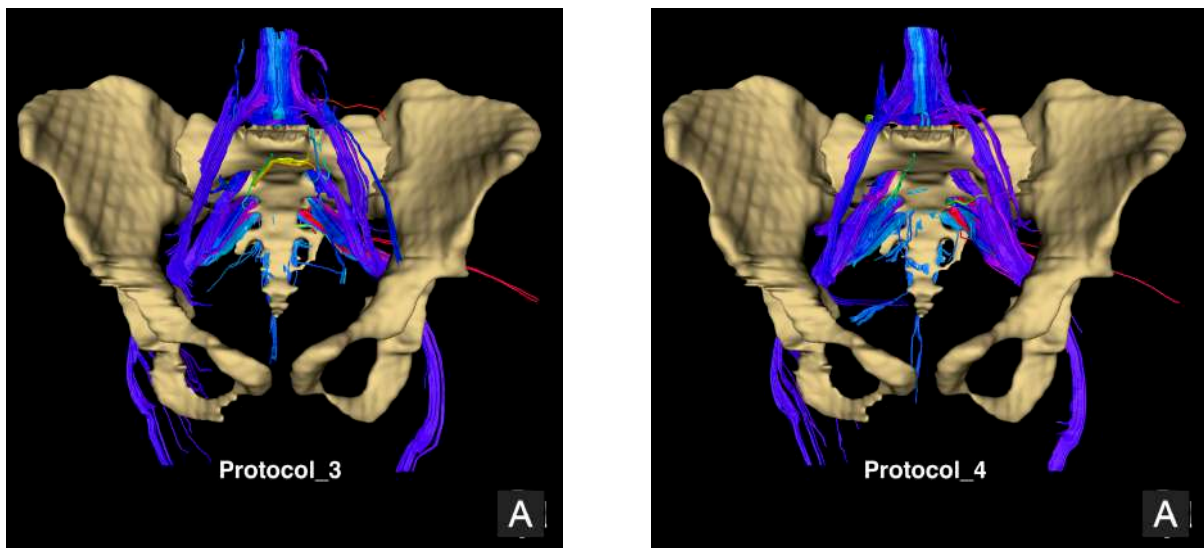


FIGURE 5.8: Sacral plexus obtained with the ROI-based method with MRI N°1 using protocol 3 on the left and protocol 4 on the right.

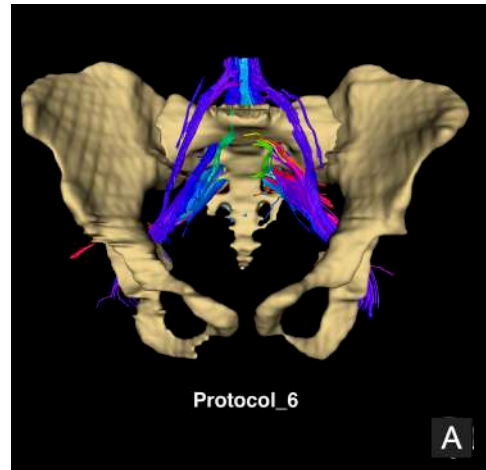
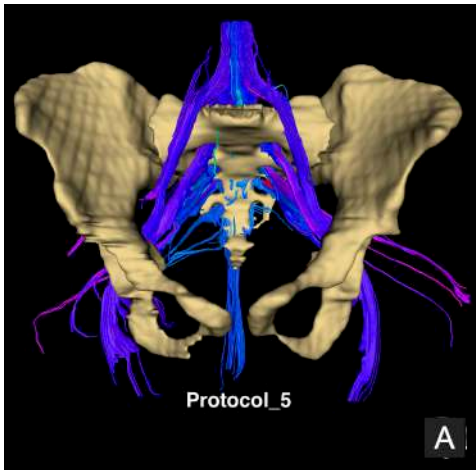


FIGURE 5.9: Sacral plexus obtained with the ROI-based method with MRI N°1 using protocol 5 on the left and protocol 6 on the right.

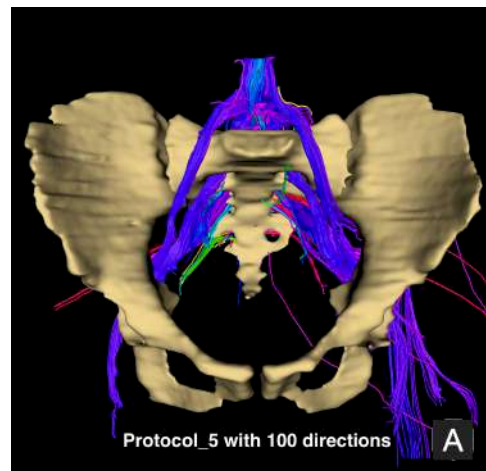
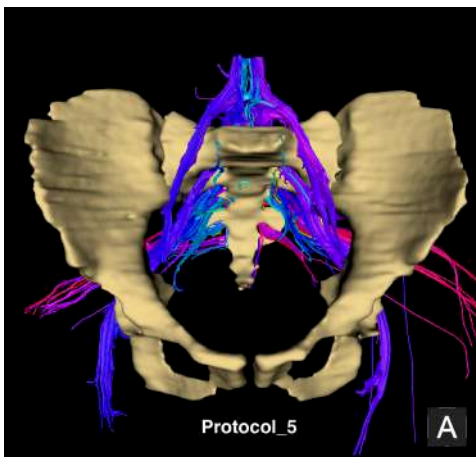


FIGURE 5.10: Sacral plexus obtained with the ROI-based method with MRI N°2 using protocol 5 on the left (50 directions) and protocol 5 with 100 directions on the right.

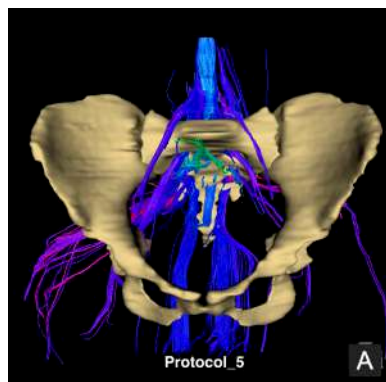


FIGURE 5.11: Sacral plexus obtained with the ROI-based method with MRI N°3 using protocol 5.

TABLE 5.1: Metrics of sacral plexus tractograms obtained with ROI based method in MRIs N°1, 2 and 3. Grey lines highlight the 3 acquisitions with identical parameters. Volume is expressed in mm³ and length in mm.

IRM	Acquisition	N° directions	b value	N° NEX	Axis	Volume Right	Volume Left	Length Right	Length Left	FA Right	FA Left	MD Right	MD Left
1	protocol_1	25	600	2	axial	24911	21969	85.89	108.87	0.27	0.29	0.53	0.52
1	protocol_2	25	600	1	axial	23499	17784	92.70	106.98	0.28	0.30	0.72	0.71
1	protocol_3	50	600	1	axial	34254	24982	124.74	123.23	0.28	0.25	0.86	0.86
1	protocol_4	50	600	2	axial	34347	28895	115.33	128.94	0.26	0.26	0.51	0.50
1	protocol_5	50	1000	2	axial	41544	31932	161.88	137.76	0.27	0.23	0.61	0.63
1	protocol_6	50	600	1	oblique	23623	20655	87.18	115.31	0.25	0.27	0.83	0.83
2	50DIR	50	1000	2	axial	30823	30599	110.86	123.54	0.29	0.27	0.60	0.61
2	100DIR	100	600	2	axial	29097	35073	139.12	97.38	0.33	0.29	0.84	0.84
3	50DIR	50	1000	2	axial	46737	28645	130.41	104.38	0.31	0.31	0.52	0.51
Mean						32092	26726	116	116	0.28	0.27	0.67	0.67

Influence of NEX number:

When visually comparing the results of protocols 1 (2 NEX) versus 2 (1 NEX), and 3 (1 NEX) versus 4 (2 NEX) in MRI N°1, we noticed that the sacral plexus presented more fiber bundles with 2 NEX compared to 1 NEX, either with 25 or 50 directions. This was confirmed by the quantitative analysis presented in Table 5.1: the global volume of the sacral plexus was bigger with 2 NEX (46880 mm³) than with 1 NEX (41283 mm³). The global length of the sacral plexus was also bigger with 2 NEX (199.68 mm) than with 1 NEX (194.76 mm). Mean FA value did not seem to be impacted by the number of NEX (0.28 with 2 NEX, 0.29 with 1 NEX), but MD values were higher with 1 NEX (0.715) than with 2 NEX (0.525). Similar results on NEX variations were obtained when comparing protocol 3 and 4 with 50 directions.

The FA value does not vary because we add similar fibers with similar trajectories. The MD value is increased because of the increase of the SNR, including in the area of the sacral holes. This means that within a voxel, the increase of NEX number does not change the angular resolution but enhances the packing density of fibers. This all taken together leads to select more fibers that lead to an augmented global volume and length of the tracts. Increasing the number of NEX improves the SNR, and therefore allows a higher qualitative diffusion image that provides better tractography results with the identification of more true positive tracts.

Influence of number of directions:

When visually comparing the results of protocols 2 versus 3, 1 versus 4 in MRI N°1 versus 100 directions in MRI N°2, we noticed that the sacral plexus presented more fiber bundles with an increased number of directions, independently of the NEX number. This was confirmed by the quantitative analysis (see Table 5.1), showing a bigger volume and a longer global length of the sacral plexus with 25, 50 and 100 directions 2 NEX protocols: global volume = 46880, 63242 and 64170 mm³ respectively; global length = 194.76, 244.27 and 236 mm respectively. We must note the shorter length of sacral plexus with 100 directions compared to 50 directions, but still more compared to 25 directions. Mean FA and MD values seemed to present the same pattern of evolution: relatively close values for 25 and 50 directions: 0.28 and 0.26 respectively for FA, 0.525 and 0.514 respectively for MD, and higher values with 100 directions: 0.31 for FA and 0.84 for MD.

Increasing the number of directions improves the angular resolution of the diffusion image that is used to perform the tractography, brings more information within the voxel, and enhances the probability to find more fibers. The consequence is the production of a tractogram with more tracts, a bigger global volume and a longer length. The visual analysis allows to define these additional fibers as true positives. With 100 directions, we found too many different fibers, that can be defined as false positives and therefore led to a worse qualitative tractography.

Influence of NEX number versus variation of number of directions:

This comparison is justified by the fact that the acquisition time is strictly equivalent when we divide the number of directions by two and double the number of NEX, or the other way around. When visually comparing results of protocols 1 versus 3 in MRI N°1, we noticed that the sacral plexus presented more fiber bundles with 50 directions and 1 NEX than 25 directions with 2 NEX. This was confirmed by the quantitative analysis (see Table 5.1), showing a bigger volume (59236 versus 46880 mm³) and a longer global length (247 versus 194 mm) of the sacral plexus with 50 directions. This experiment led us to conclude that the increase of the number of directions outranks the increase of NEX number while aiming for increasing the number of true positive tracts. This is concordant with the results in the literature [210].

Influence of b value

When visually comparing results of protocols 4 versus 5 in MRI N°1, we noticed that the sacral plexus presented more fiber bundles with $b = 1000$, especially for the distal sacral roots S3 and S4, that were only obtained with protocol 5. This was confirmed by the quantitative analysis (see Table 5.1), showing a bigger volume (73476 versus 63242 mm³) and a longer global length of the sacral

plexus (299,64 versus 244,27 mm) with $b = 1000$. This is concordant with the usual b value used in brain diffusion imaging. However, this study was performed on a cooperating subject, with minimum movement artifacts. In pediatric patients, this value shall be lowered to $b = 600$, in order to minimize the noise of the image.

Influence of acquisition axis

On a sagittal anatomical view, the sacrum presents an oblique axis, and so do the sacral roots. For this reason, we made the hypothesis that changing the acquisition plane for an orthogonal plane to the sacral axis would provide better results by lowering partial volume effect. However, when visually comparing results of protocol 3 and 6 in MRI N°1, we noticed that the sacral plexus presented more fiber bundles with a strict axial plane, which was confirmed by the quantitative analysis (see Table 5.1), and invalidated our hypothesis.

The reason is that the sacral plexus roots change direction along their path from the spine to their end in the gluteal region, and it is difficult to find the optimal acquisition plane. In fact, a strict axial plane leads to less partial volume effect than an orthogonal plane to the global sacral axis.

Symmetry study

Taking into account that these results only concern one healthy adult subject with its own specificity among the general population, it was however interesting to compare the right and the left sides of the sacral plexus. This subject showed a clear asymmetry in terms of volume in favor of the right side: mean volume on the 9 acquisitions = 32092 versus 26726 mm^3 for the left side. Regarding the length, in 4 acquisitions on 9, the right side was longer than the left side, with a similar overall mean length of the 2 sides on the 9 acquisitions (116 mm). Mean FA and MD values were similar for the both sides (see Table 5.1). A right-left asymmetry in volume does not affect the functional value of the tracts.

Longitudinal acquisitions

All three MRIs included the protocol N°5, which presented the most satisfactory qualitative and quantitative result, in terms of volume and length of the sacral roots. The three MRIs presented similar results in terms of volume and length of sacral plexus tractograms: volume = 73476, 61422, and 75382 mm^3 respectively; length = 299, 234, 234 mm respectively. FA and MD values were quite similar between MRIs N°1 and 2, but higher for FA and Lower for MD in MRI N°3 (see Table 5.1). In order to further quantitatively compare the sacral plexus tractography results of the 3 MRIs within the same 3D space, we manually registered MRI N°2 and MRI N°3 on MRI N°1 using the 3D model of the sacrum and the Transforms module of 3DSlicer, as seen in Figure 5.12. The generated transformation was then applied to the sacral plexus tractograms of MRIs as seen in Figure 5.13. This allowed for a visual appraisal of a good global concordance of the sacral plexus tractograms, claiming for a relative robustness of the ROI-based DTI tractography. In order to quantify the degree of concordance, we calculated the Dice index between MRI N°1 and N°2, and between MRI N°1 and N°3. It required to first convert the tractograms into a mask image using the Tractography to Mask Image module of Slicer 3D. Denoting X and Y the volumes to be compared, the Dice index is computed as:

$$SD = \frac{2|X \cap Y|}{|X| + |Y|} \quad (5.1)$$

where $I.I$ denotes the cardinality. The Dice index between MRI N°1 and N°2 was 0.42, and of 0.25 between MRI N°1 and N°3. These very low results are explained by the fact that we are comparing several tracts, which are very fine tubular structures. The exact discrepancy between the tracts registered in the same reference volume (which is calculated by the Dice Index), does not really reflect the actual similarity of the tracts, in terms of volume, shape and direction. Moreover, the third MRI showed aberrant false positive tracts for S3 and S4 roots, despite the same methodology of ROI drawing on the sacral holes. This might be linked to acquisition artifacts and also explain the very low Dice coefficient.

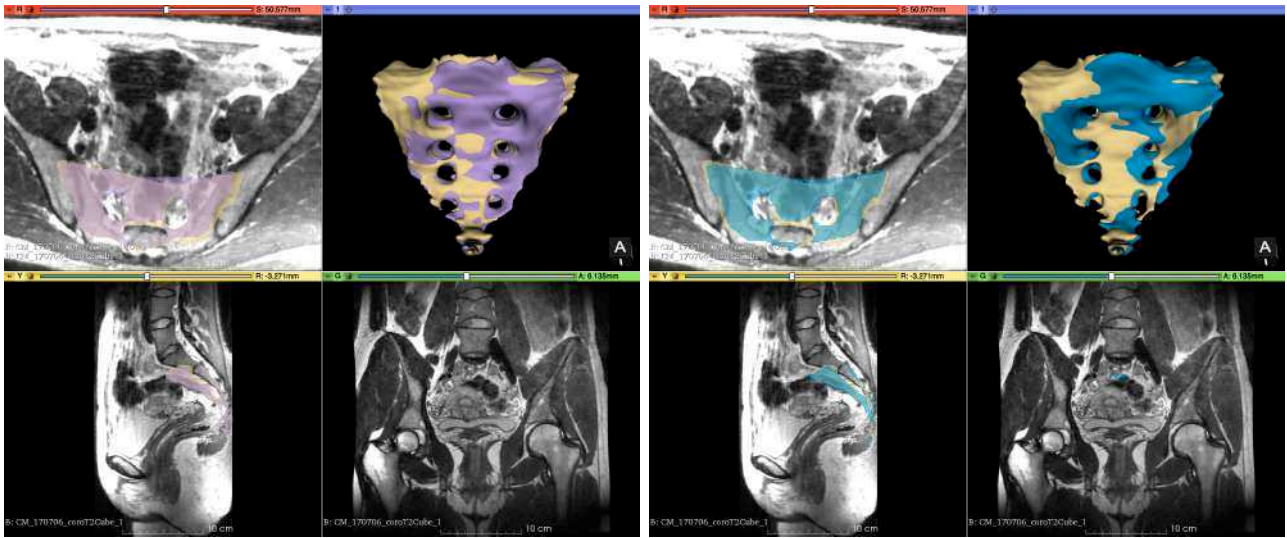


FIGURE 5.12: Manual registration of IRM N°2 (sacrum in purple) on the left and IRM N°3 (sacrum in blue) on the right on IRM N°1 (sacrum in beige), using the Transforms module of Slicer 3D. The overlapping sacral 3D views show how the MRIs were manually registered together by visual appraisal.

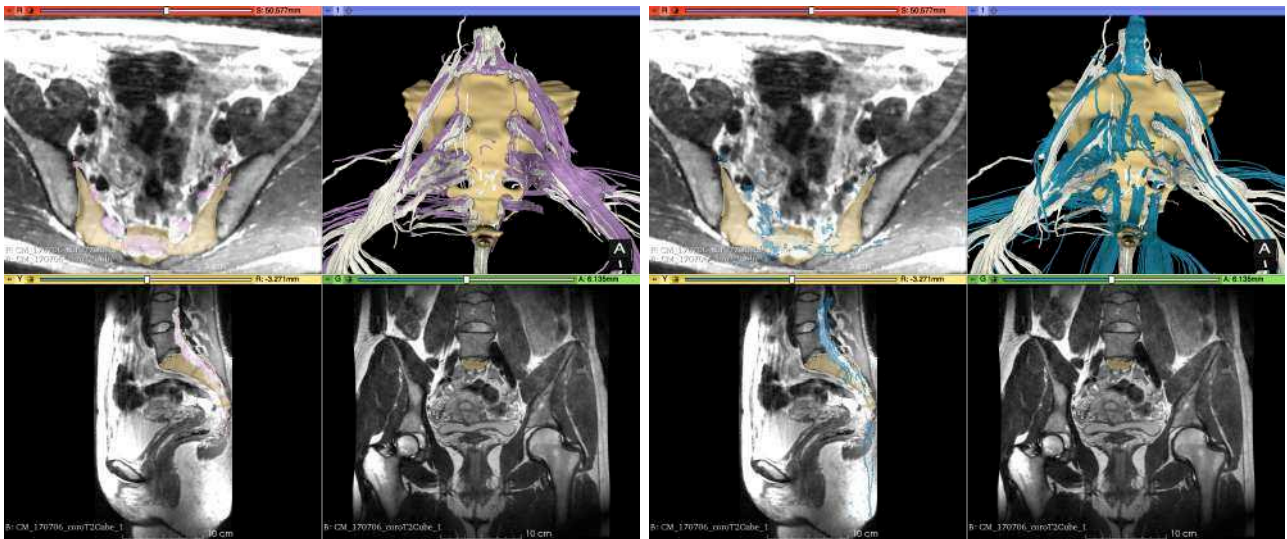


FIGURE 5.13: Merge of sacral plexus tractograms of MRI N°1 (in white) and N°2 (in purple) on the left, N°1 and N°3 (in blue) on the right.

To conclude, the most satisfying result was obtained, as expected according to the literature, with 100 directions, 2 NEX, $b = 1000$ and a strict axial plane, especially regarding the S3 and S4 sacral roots bifurcation below the ischial spine, and showing the beginning of the pudendal nerve (Protocol 5). However, while these parameters allowed us to obtain more fiber bundles and so more true positive tracts according to the known anatomy of the sacral plexus, it also increased the number of false positives, such as the ones visible along the middle axis of the sacrum, most probably being ligament tracts of the posterior inter-spinous ligament. Moreover, even if the hypogastric plexus is connected to the sacral plexus, we failed to identify it with a classical ROI drawing method. These results lead us to conclude that we still required a better methodology to generate more true positive tracts (hypogastric plexus, pudendal nerve) and to filter out the false positives ones (ligament and muscular tracts). This is addressed in the next two sections.

5.4 Design of specific description of the pelvic nervous network (PNN) anatomy

5.4.1 Introduction

The existing literature consists of anatomical books considered as references, such as the well known Netter's human anatomical atlas [150], Kamina's Clinical Anatomy Tome 4 [105] and Gray's Anatomy [71]. Netter's human anatomical atlas is made of very detailed drawings with some explanation notes, while Kamina's and Gray's anatomy books also present detailed written descriptions in natural language. Some discrepancies have been noted in the nomination of pelvic nervous tracts. For example, pelvic splanchnic nerves may correspond to either sympathetic rami coming from para vertebral ganglia afferent to the inferior mesenteric plexus, or to hypogastric nerves efferent from that plexus, or even parasympathetic tracts issued from S2 to S4 and being part of the sacral plexus far below. This latest entity also has a synonymous name: *nervis erigentes* in Latin or *nerfs érecteurs d'Eckart* in French.

The updated Gray's anatomy book [71] has been chosen as a reference for the names of the nerves, because it is the most recent anatomical book and therefore reflects the most widely used denominations nowadays. However in this section, the different nerves and plexuses will be illustrated by all three authors, because they are all complementary: Gray's anatomy [71] is the more schematic, understandable at the first sight and then useful to get the big picture in volume of the pelvic nervous network. Kamina's work [105] displays more detailed sagittal views of the pelvic innervation that are more likely comparable to radiological views. Finally Netter's drawings [150] are detailed, artistic and realistic: they allow us to really understand the complexity of the pelvic area and dive into anatomical details.

5.4.2 Description methodology

Based on these works, the PNN is here divided into tracts of interest, according to: global shape and location, connections, nature (somatic, sympathetic (S) or parasympathetic (paraS)), function: sensitive, motor or neuro-vegetative, and specific interest for the surgeon. Their description in natural language entails a lot of spatial relationships, which are presented here to provide a precise understanding of the anatomy of the pelvic nervous network. This thorough knowledge is mandatory to quickly analyze the tractography results as false or true positives, or identify the missing tracts (false negatives), no matter which tractography method is used. However, all the elements of the description cannot be part of its further transformation into mathematical language and algorithms. The description have therefore to be simplified and restrained to the main relationships that will be underlined in the text, along with the closest surrounding anatomical structures which will be in **bold**. These elements are the basis of our anatomy aware tractography segmentation method as detailed in Section 5.5. The choice of the most useful anatomical structures and relationships relies on different parameters:

First, the anatomical structures part of the description must be clearly visible on the anatomical MRI sequence, relatively easy to segment, and meaningful for the description of the pelvic nerves.

Second, some of these structures will not be segmented because they are outside the inner pelvic area such as the muscles of the hip. The manual segmentation time of all the pelvic structures is already quite high, around eight hours on average, so that we do not want to add the segmentation of structures that are not useful for inner pelvic surgery.

Third, some of these structures are impossible to segment in a reproducible way because they are fuzzy areas with no defined boundaries such as the lesser sciatic foramen, or the pelvic wall for example.

Fourth, the addition of several relationships may be useless to define one nervous tracts in mathematical language, and so would lead to a waste of computing time. As useful as they can be in natural language

to create a clear view of the anatomical situation, some relationships may cover the same space within the radiological image and therefore be redundant.

Fifth, we are not going to use nervous structures obtained with a tractography algorithm to describe another nervous tract in order to not amplify possible inadequacies: use the result of L5 tractography to help defining the sciatic nerve for example.

Sixth, the entire pelvic network will be described here, till its very end near all the pelvic organs and the pelvic skin, because it is directly linked to its function, its interest for the surgeon and therefore contributes to the overall comprehension. However, very distal nerves such as the perineal nerve for example, will not present anatomical structures in bold text or underlined relationships because our preliminary tractography tests emphasized that very thin nervous structures with a low FA buried within noisy diffusion pelvic images are hardly traceable given our current hardware and software limits.

5.4.3 Somatic System

- **Sacral Plexus** (see Figure 5.14)

The sacral plexus gathers the anterior rami of S1 to S4, and the lumbo-sacral trunk. The sacral roots coming from the conus medullaris go through the anterior **sacral foramina** and courses laterally and inferiorly down the pelvic wall, in relation to the anterior surface of the **piriformis muscle**.

The lumbo-sacral trunk, formed by the anterior ramus of L4 and all rami of L5, goes through the **vertebral L5 foramina**, courses in a vertical manner into the pelvis from the abdomen and pass anterior to the sacro-iliac joint.

Branches of the sacral plexus include the sciatic nerve and gluteal nerves, innervating the lower limb, and the pudendal nerve, innervating the perineum.

Smaller nerves originating for the sacral plexus supply the pelvic and lower limb muscles. They leave the pelvic cavity by passing through the greater sciatic foramen inferior to the **piriformis muscle**, to end in the gluteal region of the lower limb [71].

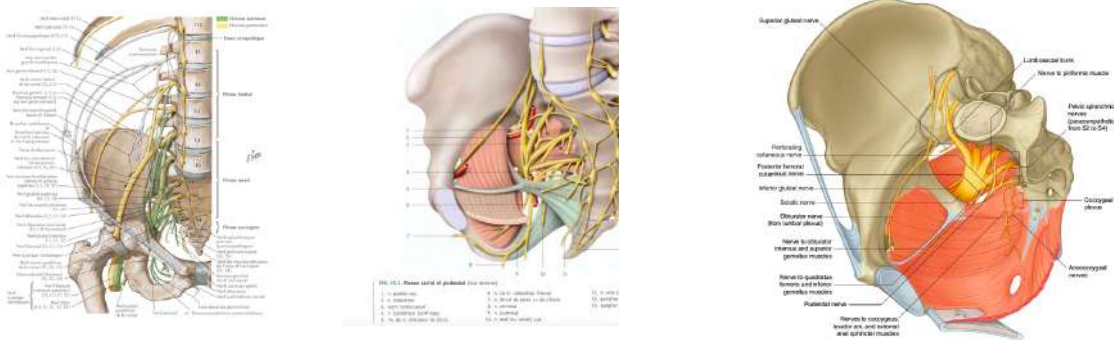


FIGURE 5.14: Sacral plexus by Netter, Kamina and Gray, respectively [150, 105, 71].

L5 root

L5 root is always described as part of the sacral plexus, but there is no precise definition of its specific course to refer to. It is the largest spinal nerve coming from the spine, going through the **L5 vertebral canal**, continuing in tight contact with the promontory and anterior to the 1st sacral vertebra. It connects with the S1 root to form the superior part of the sacral plexus when going out the pelvic area through the greater sciatic foramen, anterior to the **piriformis muscle** and posterior to the **ischial spine**. It is in continuity with the sciatic nerve. On a transversal view, its course is in a global posterior location compared to **ureter**, **iliac vessels**, **obturator muscle** and **ovary** in the female subject.

S1 root

S1 root, as L5, is also always described as part of the sacral plexus. Coming from the spine, it goes out from the sacrum through the **sacral hole S1**, with a global lateral and caudal direction, at the anterior surface of the 2nd sacral vertebra. It connects with both L5 and S2 roots, goes out of the pelvic area through the greater sciatic foramen, anterior to the **piriformis muscle** and posterior to the **ischial spine**. It is in continuity with both the sciatic nerve and the pudendal plexus.

S2 root

S2 root, as L5 and S1, is also part of the sacral plexus. Coming from the spine, it goes out from the sacrum through the **sacral hole S2**, with also a global lateral and caudal direction but more horizontal than S1, at the anterior surface of the junction between the 2nd and the 3rd sacral vertebra. It connects with S1 and S3 roots, goes out the pelvic area through the greater sciatic foramen, anterior to the **piriformis** and posterior to the **ischial spine**. It is in continuity with both the sciatic nerve and the pudendal plexus.

S3 root

S3 root, as L5, S1 and S2, is also part of the sacral plexus. Coming from the spine, it goes out from the sacrum through the **sacral hole S3**, with a global lateral and even more horizontal direction compared to S2, at the anterior surface of the 3rd sacral vertebra. It connects with S2 root, goes out the pelvic area through the greater sciatic foramen, anterior to the **piriformis**, and posterior to the **ischial spine**. It is in continuity with both the sciatic nerve and pudendal plexus.

S4 root

S4 root, as L5, S1, S2 and S3, is also part of the sacral plexus. Coming from the spine, it goes out from the sacrum through the **sacral hole S4**, with a global lateral and horizontal direction, at the anterior surface of the 3rd sacral vertebra. It connects with S3 root, goes out the pelvic area through the greater sciatic foramen, between the **piriformis** and **coccygeal muscles**, and posterior to the **ischial spine**. Its major contribution is for the pudendal plexus.

Sciatic nerve

The major terminal branch of sacral plexus (roots L5 to S3) is the sciatic nerve, which is the largest nerve of the body. It begins on the anterior face of the **piriformis muscle** and goes through the greater sciatic foramen inferior to the **piriformis**. It goes through the gluteal region, where it divides into its major terminal nerves, the common fibular nerve and the tibial nerve. It innervates muscles of the thigh, leg and foot and carries sensory fibers from the skin of the foot and lateral leg. It does not participate to the innervation of the pelvic organs but is an important landmark when interpreting the tractograms.

Other branches of sacral plexus

Other branches of the sacral plexus include nerves innervating muscles of the gluteal region, pelvic wall and floor: the superior and inferior gluteal nerves, the nerve to obturator internus, the nerve to quadratus femoris, the nerve to piriformis muscle and the nerve to superior gemellus, as seen in Figure 5.15. We are only detailing the path of the nerves involved in the inner pelvis innervation and not the ones innervating the external muscles of the thigh:

- Nerve to obturator internus muscle: it originates from roots L5 to S2, leaves the pelvis through the greater sciatic foramen inferior to the **piriformis muscle**. Like the pudendal nerve, it passes around the **ischial spine** and through the lesser sciatic foramen to re-enter the pelvis and innervates the obturator internus muscle on the medial side of the muscle, inferior to the **levator ani muscle** [71];
- Nerve to piriformis muscle: it originates from the sacral roots and innervates the muscle directly without leaving the pelvis.

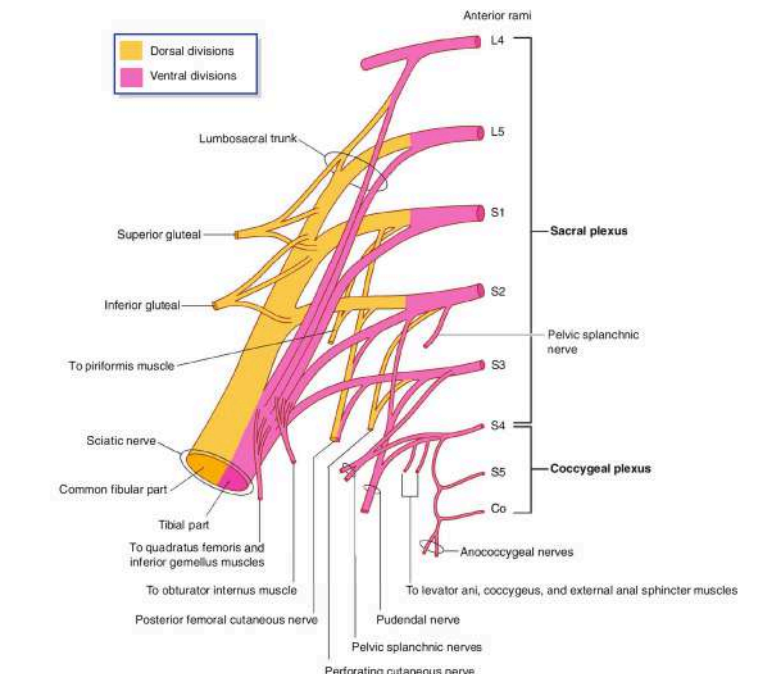


FIGURE 5.15: Components and branches of the sacral and coccygeal plexuses [71].

• Pudendal plexus

The pudendal plexus is in tight relation to the sacral plexus, and innervates muscles, skin and perineal organs, but also muscles and pelvic viscera, except for ovaries and testicles. It is made of fibers coming from **S2, S3 and S4 roots**. Its termination is the pudendal nerve. It lies against the antero-medial face of sacral plexus and **coccygeal muscle**, near its insertion on **sacrum bone**. It is covered by the pelvic parietal fascia, which constitute the separation with the lateral sacral artery. It goes around the **ischial spine**. Its collateral branches are: the pelvic splanchnic nerves (parasympathetic), the levator ani muscle nerve, the coccygeal muscle nerve, the rectal superior nerve, and the perforating cutaneous nerve [105].

Levator ani muscle nerve

It originates from S3, sometimes S4. Its global direction is anterior and caudal, goes above the **ischial spine** and ends on the top of the **levator ani muscle** with three or four branches. It may be double in some individuals [105].

Coccygeal muscle nerve

It originates from S4 and penetrates the medial face of the **coccygeal muscle**. In some individuals, it may be double and originates from levator ani muscle nerve [105].

Rectal superior nerve

It originates from S3 and S4, below the **piriformis muscle**, then around the **ischial spine** and then goes through the lesser sciatic foramen; it penetrates the ischio-rectal fossa to innervate the external sphincter muscle of the anus and the perineal skin. In some individuals, it may be double [105].

Perforating cutaneous nerve

It originates from S3 and S4, goes out the pelvic cavity by perforating the sacro-spinous ligament, goes under the gluteus maximus muscle to innervate the medial gluteal skin region. In some individuals it may originate from the pudendal nerve [105].

• **Pudendal nerve**

The pudendal nerve (see Figures 5.16 and 5.17) is the terminal branch of the pudendal plexus, that leaves the pelvis going through the greater sciatic foramen, inferior to the **piriformis muscle**; it comes back into the pelvis by going around the **ischial spine**, and through the lesser sciatic foramen; it is associated with internal pudendal vessels within the pudendal canal in close contact to the **obturator muscle**. Its path continues along the ischio-pubic branch until the perineal membrane and becomes the dorsal nerve of penis or clitoris. It innervates the skin and skeletal muscles of the perineum, and also the external anal and external urethral sphincters. Its collateral branches are the rectal inferior nerve and the perineal nerve [71, 105].

Rectal inferior nerve

It originates within the pudendal canal, goes through the ischio-rectal fossa to innervate the external sphincter muscle of the anus. In some individuals, it may be double or may originate from the sacral plexus. It may go through the sacrospinous ligament [105].

Perineal nerve

It originates from the pudendal nerve at its exit from the pudendal canal, goes down to the uro-genital perineum, and divides itself into two branches, one superficial and one deep. The superficial branch goes anteriorly and innervates the scrotum and the inferior face of the penis or the magnus labia. The deep branch goes on the transversal superficial muscle, innervates the deep transversal muscle of the perineum, urethral sphincter ischio-cavernous and bulbo-spongial. It terminates in the bulbo-urethral nerve [105].

Dorsal nerve of penis or clitoris

It goes above the perineal transverse ligament and goes through the infra-pubic hiatus. It crosses the lateral face of penis or clitoris ligament, follows the dorsal face of penis or clitoris till its end. It innervates the lateral face of the penis skin in men, and the superior part of the minor labia in women [105].

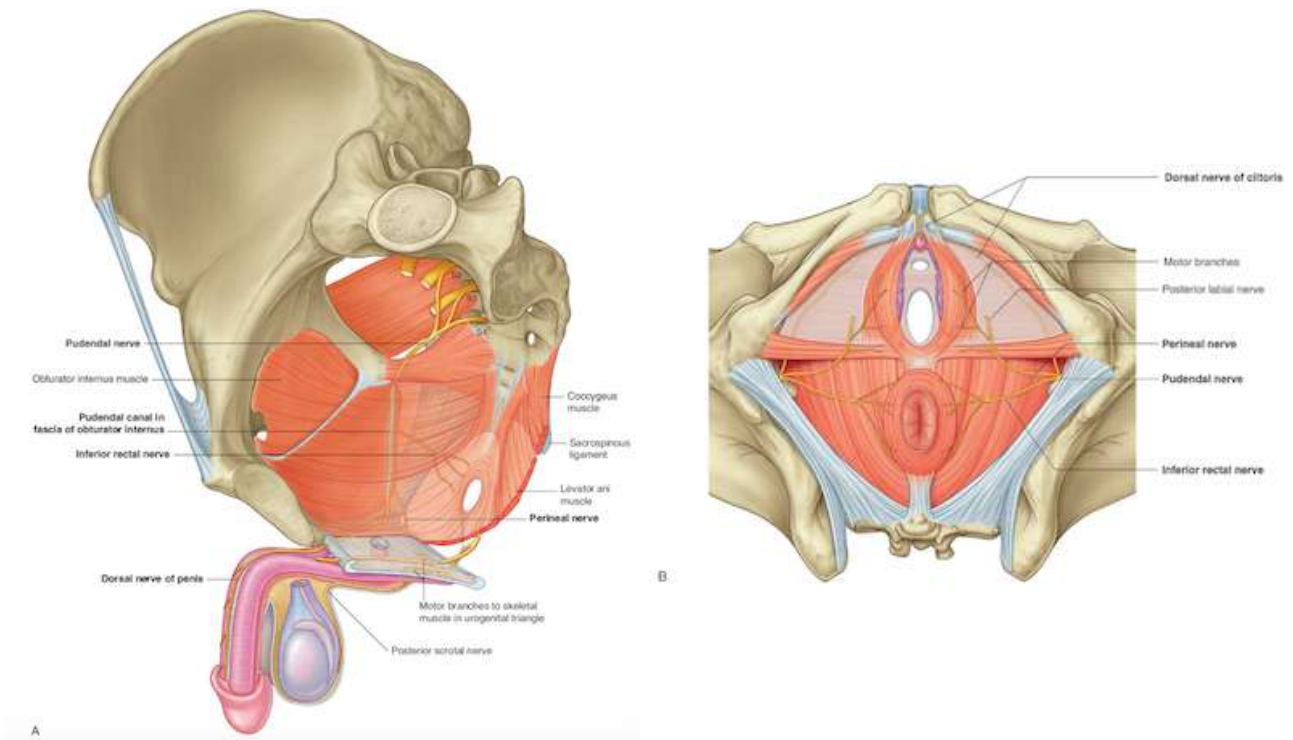


FIGURE 5.16: Pudendal nerve according to Gray [71]. A: In men. B: In women.

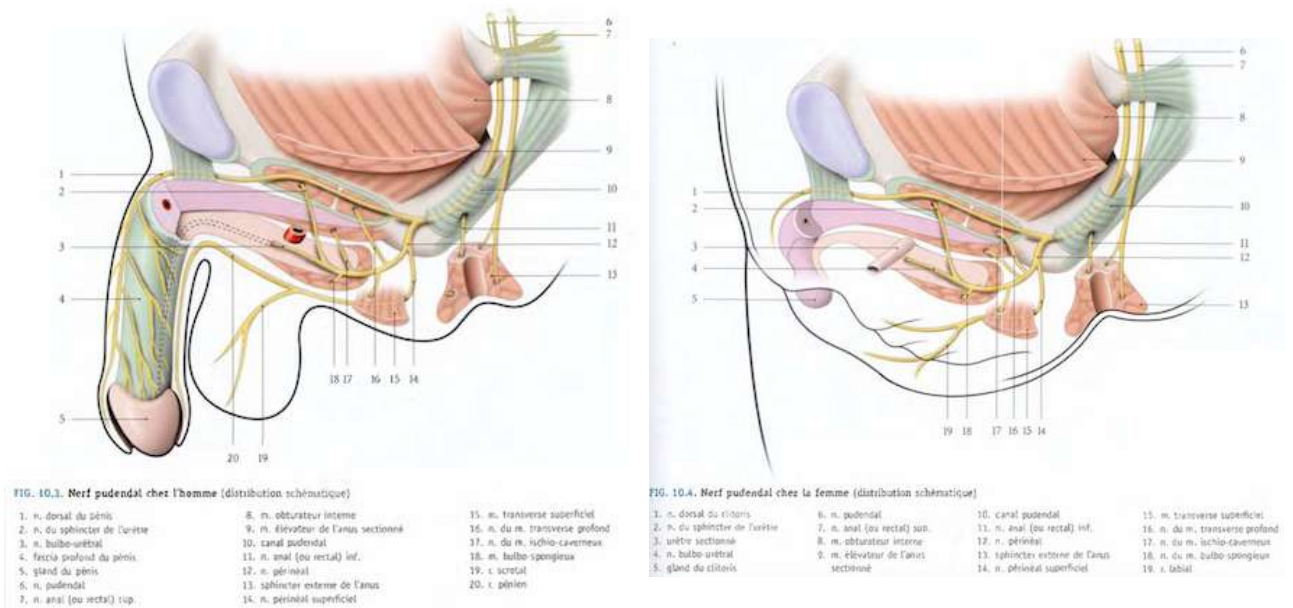


FIGURE 5.17: Pudendal nerve according to Kamina in men and women [105].

- **Coccygeal plexus**

The small coccygeal plexus is formed by the anterior rami of S5 and coccygeal rami, which originate inferiorly to the pelvic floor. They penetrate the coccygeal muscle to enter the pelvic cavity and join with the anterior ramus of S4 to form a single trunk, from which small ano-coccygeal nerves originate to innervate skin in the anal triangle of the perineum [71].

5.4.4 Autonomous system: S = Sympathetic and ParaS = Parasympathetic.

For illustrations, see Figures 5.18, 5.19, 5.20 and 5.21.

Sacral para-vertebral sympathetic chain (S)

The para-vertebral part of the autonomous nervous system is formed in the pelvis by the inferior ends of the sympathetic trunks. Each trunk enters the pelvis coming from the abdomen by passing over the ala of the **sacrum** medially to the lumbo-sacral trunks and posterior to the **iliac vessels**. The trunks path goes inferiorly on the anterior surface of the **sacrum**, medially to the **anterior sacral foramina**. Four ganglia are placed along each trunk. Anteriorly to the coccyx, the two trunks join to form the ganglion impar.

Superior hypogastric plexus or SHP (mix of S and paraS)

The SHP is anterior of the **L5 vertebra** between the promontory of the sacrum and the bifurcation of the **aorta**. It is formed by the abdominal aortic plexus and the 3rd and 4th lumbar splanchnic nerves. Below the sacral promontory, it divides itself into the right and left hypogastric nerves.

Hypogastric nerve (paraS)

The two hypogastric nerves run medially to **sacral foramina** and the **pelvic vessels**, crossing the lateral faces of the **rectum** and connect the superior to the inferior hypogastric plexuses.

Inferior hypogastric plexus or IHP (mix of S and paraS)

The IHP (right and left sides) is formed by the hypogastric nerves and the pelvic splanchnic nerves (described below). It is a thin network of little ganglia connected by short nervous tracts. It carries a global inferior direction, medial to **pelvic vessels** and somatic nerves. In men, it is situated within the genito-sacral ligament, and in women, within the utero-sacral ligament. Its anterior part reaches the seminal vesicles in men and the lateral **vaginal fornix** in women. Its inferior part touches the pelvic fascia. Its internal face is in relationship with the lateral faces of the **rectum, bladder and uterus** in women. Its external face is covered by visceral venous plexuses. It gives origin to the rectal, utero-vaginal, prostatic and vesical plexuses, which innervate the pelvic viscera.

The rectal plexus is divided into mean and inferior plexuses. The mean rectal plexus comes from the upper part of the IHP and accompanies the mean rectal artery. It innervates the rectum and the internal anal sphincter muscle. The inferior rectal plexus comes from the inferior part of the IHP and accompanies the inferior rectal artery to innervate the anal canal and also the internal anal sphincter muscle.

In men, the prostatic plexus comes from the antero-inferior part of the IHP and innervates the prostate, the seminal glands, the seminal duct, the urethra, and the bulbo-urethral glands. It also gives origin to the cavernous nerves of the penis. In women, the utero-vaginal plexus comes from the superior and inferior parts of IHP and gives origin to the uterine and vaginal nerves. Uterine nerves go behind uterine artery and innervates the uterus and the corresponding Fallopian tube. They give cervico-isthmical rami and fornix rami; they join at the end with ovarian plexus. Vaginal nerves accompany vaginal arteries and innervate the vagina, the urethra, the vestibular glands and the vestibular bulbs. They give origin to the cavernous nerves of the clitoris. In both men and women, the vesical plexus comes from the anterior part of the IHP; it innervates the bladder and the urethra.

Terminal branches of the inferior hypogastric plexuses pass through the deep perineal pouch and innervate erectile tissues of the penis and the clitoris in the perineum. In men, these nerves, called cavernous nerves, are extensions of the prostatic plexus. The pattern of distribution in women is not entirely clear, but they are probably extensions of the utero-vaginal plexus.

Splanchnic nerves

The **lumbar splanchnic nerves** (S) originate from the para-vertebral sympathetic trunks and associated ganglia to join the pre-vertebral plexus composed by inferior mesenteric plexus and the SHP.

The **pelvic splanchnic nerves** (paraS) does not originate from the para-vertebral sympathetic trunk but from the anterior rami of S2 to S4 and carries parasympathetic fibers that join the IHP. These nerves are vasodilatory on blood vessels, provoke bladder contraction, originate erection, and modulate activity of the enteric nervous system of the colon.

The **sacral splanchnic nerves** (S) originate from the sacral para-vertebral sympathetic trunks and also join the IHP. These nerves come from pre-ganglionic fibers that leave the spinal cord in the anterior roots, from T10 to T12. These fibers innervate blood vessels, provoke contraction of smooth muscle in the internal urethral sphincter in men and the internal anal sphincters in both men and women, initiate smooth muscle contraction associated with the reproductive tract, and are central during ejaculation.

Gray rami communicantes (S)

The principal function of the sympathetic trunks in the pelvis is to deliver post-ganglionic sympathetic fibers to the anterior rami of sacral nerves for distribution to the periphery, mainly to parts of the lower limb and perineum. This is accomplished by gray rami communicantes, which connect the trunks to the sacral anterior rami.

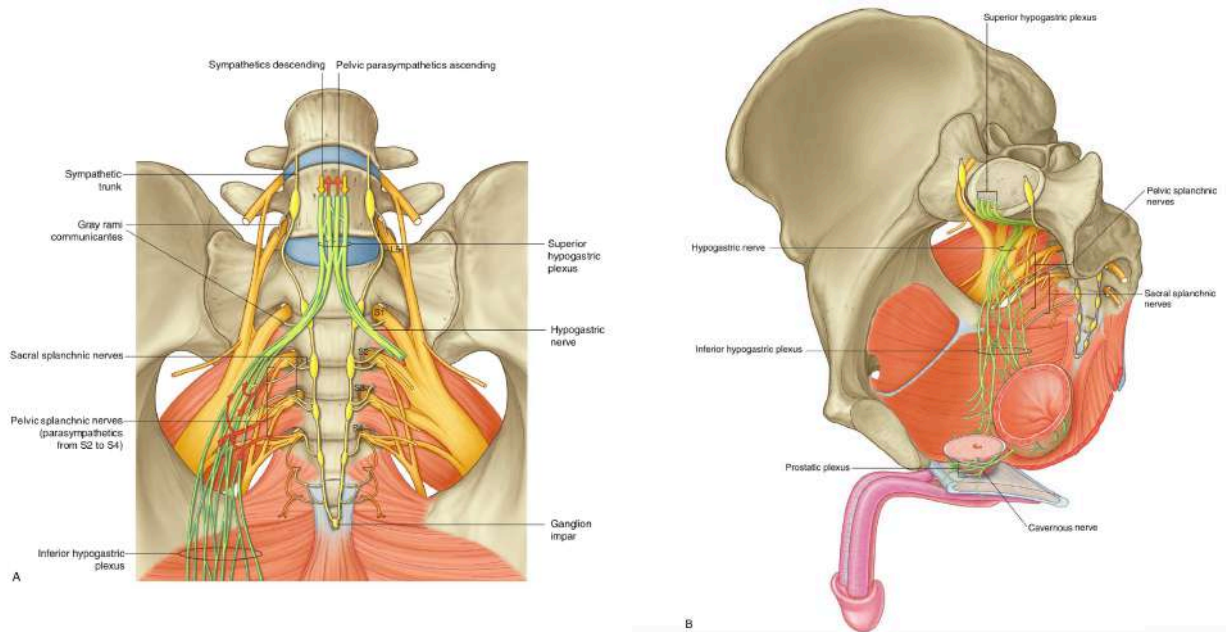


FIGURE 5.18: Pelvic autonomous system according to Gray's [71].

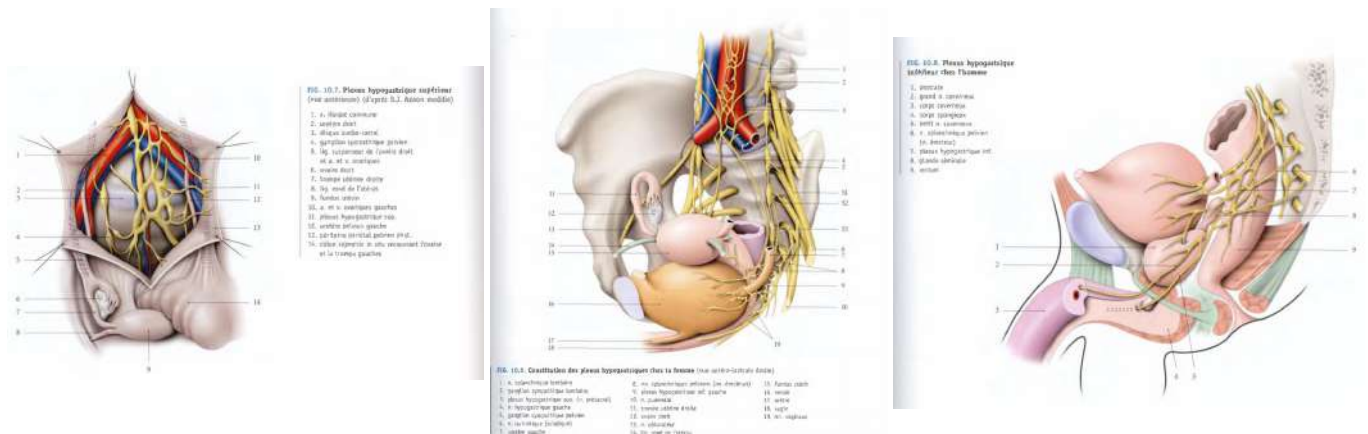


FIGURE 5.19: Pelvic autonomous system according to Kamina [105].

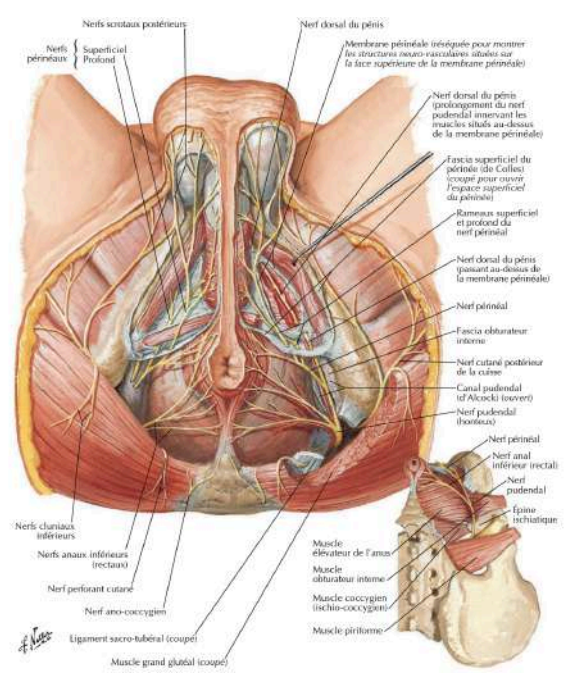
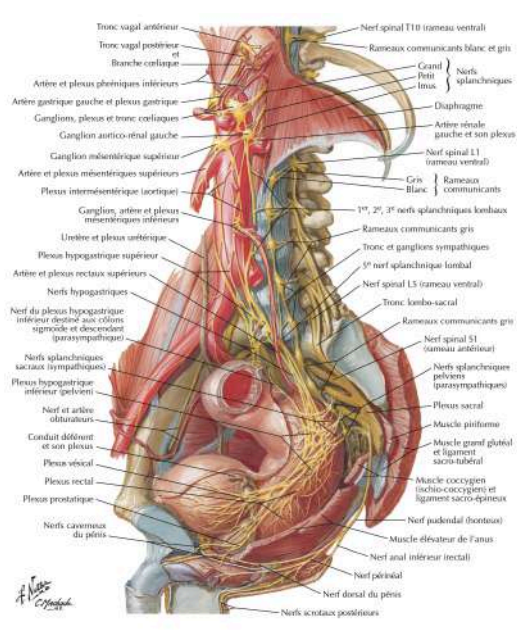


FIGURE 5.20: Pelvic autonomous system according to Netter [150].

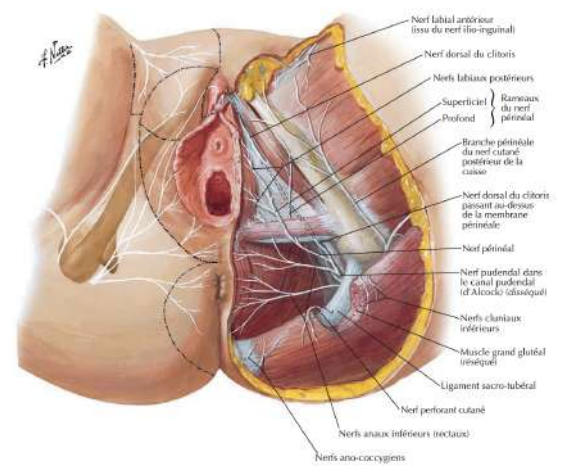
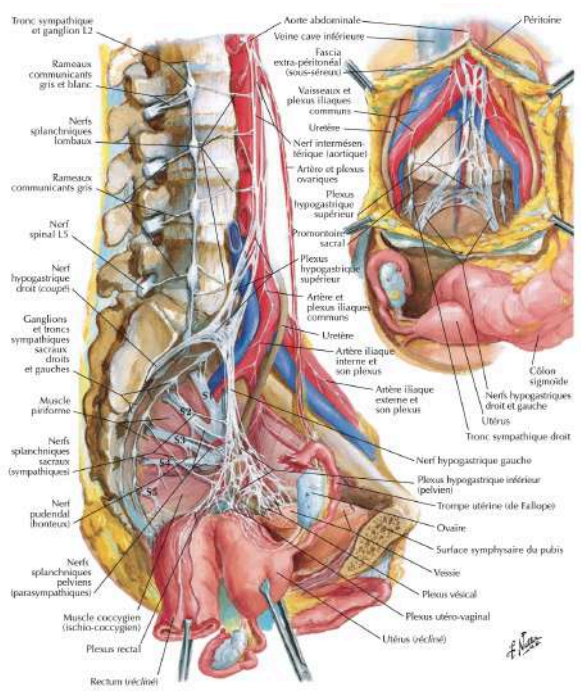


FIGURE 5.21: Pelvic autonomous system according to Netter in women [150].

5.5 Anatomy-aware tractography method: the Pelvic Query Language (PQL)

5.5.1 Introduction

Our goal is to develop an alternative method to ROI based tractography, that uses pelvic organ segmentation, the anatomical description of each nervous tract and allows for the recognition of each element of the pelvic nervous network. The aim is to improve pelvic tractography results and nerve recognition with a maximum of true positive tracts and a minimum of false positive tracts. The descriptions in natural language detailed in Section 5.4 are transformed into mathematical language, that will be used to perform an anatomy-aware tractography segmentation.

A.Delmonte took inspiration of the White Matter Query Language (WMQL) for brain tractography by Wasserman et al [213], and designed the Pelvic Query Language (PQL) for the pelvis, after a first work on brain white matter multi-resolution segmentation using fuzzy set theory [32, 67].

WMQL is a method that automatically extracts white matter tracts from diffusion MRI tractography, by using a syntactical definition of brain major white matter fiber tracts based on a neuroanatomist's expert knowledge. The framework is based on a query language with a near-to-English textual syntax. It makes it possible to construct a dictionary of anatomical definitions that include adjacent gray and white matter regions, and rules for spatial relations. These definitions are constructed in terms of different relationships between gyri, sulci, subcortical structures or white matter areas. To locate the anatomical structures used for the queries, the authors used existing neuroanatomical atlases. The operations of WMQL can be divided into three groups: (1) anatomical terms stating if a tract traverses or ends in a certain brain structure, (2) relative position terms indicating whether the tracts are, for instance, medial or frontal to a structure, and (3) logical operations such as conjunction, disjunction or exclusion of the previous two types of clauses. These three types of operations are represented in Figure 5.22.

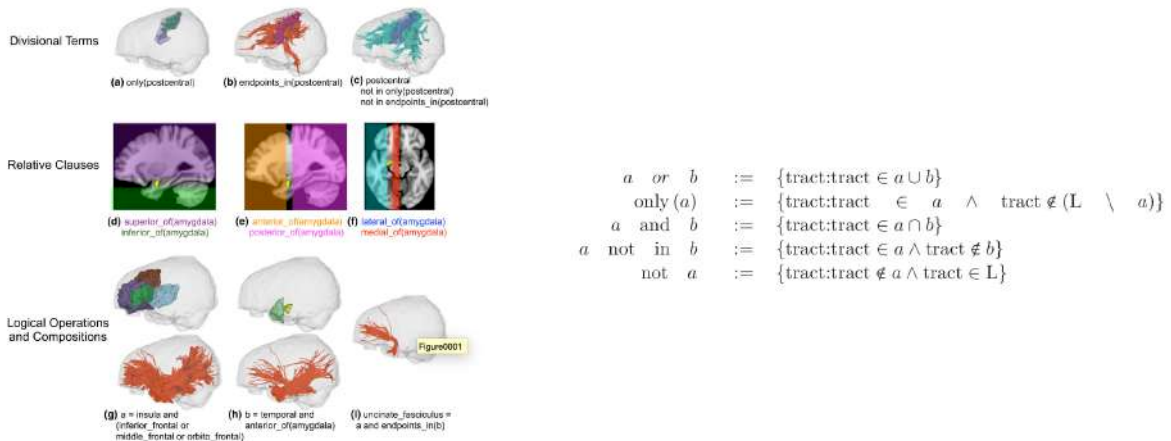


FIGURE 5.22: On the left: WMQL Terms (a–f) along with an example construction of a WMQL query (g–i). Regions in (g–i): insula (cyan); the orbito-frontal (purple), middle-frontal (brown) and inferior-frontal (dark green) convolutions. h The anterior temporal lobe (light green) defined as the section of the temporal lobe anterior to the amygdala (yellow). On the right: formalization of the WMQL logical operations, giving two WMQL sets a and b and the set of all streamlines L [212].

This method is fast and easy to use, and is based on binary relations and bounding boxes. However, a rectangular bounding box fails to accurately represent complex objects such as the sacrum for example, and it does impact the spatial relationships modeling. The binary relations also prevent from taking into account the intrinsic imprecision of numerous spatial relations.

To solve this issue, we propose in our PQL method to directly model qualitative anatomical definitions and use them into a segmentation algorithm, but within a richer framework, by representing the inherent imprecision of the anatomical definitions using the theory of fuzzy sets [32, 34, 67]. We use the manual segmentation of the subject’s pelvic organs instead of atlases, because such atlases simply do not exist in this anatomical area. Moreover, this allows for a direct recognition of the nerves from the subject’s data, without any registration with a prior model or atlas. Spatial relationships, connectivity and pathway operations are modeled, and may also be finely adapted thanks to tuning parameters. The whole PQL query design process is detailed in the next subsection.

5.5.2 PQL principle

Modeling spatial relations

Method

In order to model spatial relations between nerves and segmented anatomical structures, we rely on existing approaches based on fuzzy sets and mathematical morphology [33, 34] which has proved useful in several applications in the brain and thoraco-abdominal anatomical areas [38, 55, 84, 149].

Given a relation R to a reference object O , this method computes the region of the 3D space where this relation is satisfied. Since the spatial relations are inherently vague, this region is defined as a fuzzy set. Within a fuzzy region, the membership value of each point x is the degree to which x satisfies the relation R to O . It is generally computed as a fuzzy dilation of O with a structure providing the semantic of R . Here O is typically one of the segmented structures. The computation of the degree to which a fiber, or the point of a fiber, satisfies this relation R can be simplified as 0/1 if the fuzzy region is binarized.

Definitions: spatial relations, connectivity and pathway operations

The modeling of the six **directional relations: anterior_of, posterior_of, superior_of, inferior_of, medial_of and lateral_of** (see examples in Figure 5.23), enables the usage of spatial relations very often employed in anatomical textbooks to describe the location of the structure of interest compared to the other surrounding structures. As the pelvis presents several symmetric structures, we preferred to use the terms medial and lateral instead of right and left in order to be able to describe the spatial relations in the same way for both right and left sides. Moreover, in standard anatomical descriptions, associated spatial definitions are often used, such as antero-posterior etc. We therefore offer the possibility to combine with the boolean operator AND two standard relations such as anterior of and posterior of, as seen in Figure 5.24. For the mathematical definitions used for modeling the directional relations, see [31].

Modeling the **between** relation is also quite useful in the pelvic anatomical description, because a lot of nervous tracts run between the osteo-muscular encasing structure and the soft tissue organs situated on the mid-line of the pelvis. For the mathematical definition used for modeling the between relation, see [35].

The modeling of a region close to an anatomical structure (**in proximity of** in the PQL language), is based on the distance transform, providing for each background voxel its minimum distance to the object. For the mathematical definitions used see [30]. The distance transform has been converted in millimeters, taking into account also the possibility of anisotropic voxel sizes.

Spatial Relations

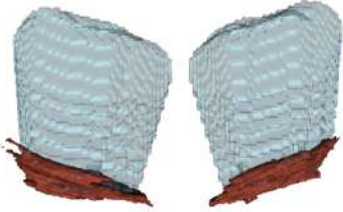
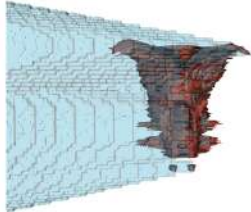
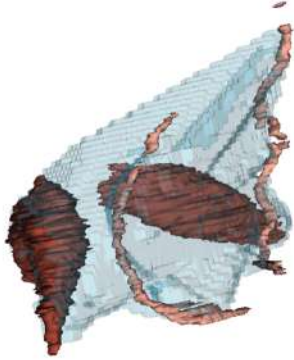

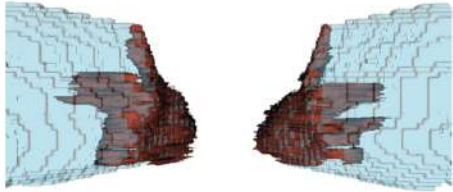
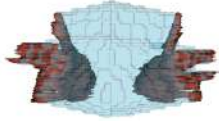
Relation	Spatial Representation	Relation	Spatial Representation
anterior_of (CoccygealMuscle)		left_of (LevatorAniMuscle)	
between (PiriformisMuscle, Uretere)		proximity_of (Ovaries)	
lateral_of (ObturatorMuscle)		medial_of (ObturatorMuscle)	

FIGURE 5.23: Examples of modeled spatial relations.

The modeled **connectivity and pathway operations** are: `crossing`, `only_in`, `not_in`, `endpoints_in`, `both_endpoints_in`, as seen in Figure 5.24. The `only_in` keyword selects the fibers that have 100% of their points in the chosen structure. The relationship "crossing" corresponds in the natural language to the expressions "going through", or passing "through". For the mathematical definitions used see [67]. This latest relation is very useful especially to describe the sacral roots, that all go through holes within the bony structure of the sacrum, coming from the sacral canal, and before entering the pelvic area. Representing these holes requires an additional segmentation, resembling a sphere placed just in front of the sacral holes.

Satisfaction degree of a spatial relation

When modeling fuzzy spatial regions, every voxel of an object of interest has a satisfaction degree regarding a spatial relation within the whole image. The advantage is to keep the uncertainty and stay valid even in case of inter individual variations for example. However, its usage is quite challenging when dealing with complex and combined spatial relationships. In the precise application of this method in pelvic anatomy, we therefore chose to add thresholds in order to binarise the relations.

For both directional and between relations, we can therefore adjust the degree of strictness of the definition, by tuning the **aperture** of the modeled area. This area may be represented as a cone, which angle has been normalized between 0 and 1, with 1 indicating a 180° angle, as seen in Figure 5.24.

Regarding the proximity relation, setting a distance in mm associated with it therefore allows for choosing the superior limit of distance where the object of interest (tractography fibers) does not satisfy the spatial definition anymore: the threshold in millimeters selects the portion of the space in proximity of the structuring element (organ) where the fibers must or must not pass through. A higher value provide a larger modeled space around the structuring element, but may also lead to the segmentation of some false positive tracts. Again, a compromise must be found using iterative testing and visualizing the results in 3D in real time. We must note that the resulting modeled space also includes the structure itself. When the threshold is low, around 1mm for example, using the proximity of relation nearly therefore equals the crossing of relation.

Satisfaction degree aggregation

Once we defined the satisfaction degree in each point of the image using these various thresholds, we then select the fibers of interest by associating to each spatial relation a percentage tuning: it allows choosing how many points of all the fibers (expressed with a % value between 0 and 100) must lie inside a volume of interest, in order, for the fibers themselves, to satisfy the relation. If only 1% of the tract belong to the volume of interest, it lowers the importance of the exactitude of the segmented structure, but the result may display a lot of false positive tracts. If we set the parameter at 100%, the segmentation must be very accurate in order to provide sufficient true positive tracts.

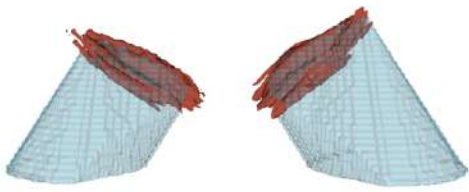
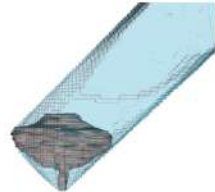
In the PQL environment, we set the tuning parameters defaults values as: `Aperture = 0.125`, `Percentage = 1` and `mm = 10`. Since pelvic organs present complex 3D shapes with multiple concave regions, and present a huge inter individual variability especially in pediatric patients, we chose a strict default value for aperture and mm tuning parameters in order to maximize the true positives tracts and mostly minimize the false positive ones. We chose a low value for percentage in order to lower the impact of the segmentation quality.

The influence on the results of the tuning parameters will be illustrated in the Figures of subsection 5.5.4.

Aperture Tuning

0.125 (default)	0.5	1
		

Definitions Combination

Relation	Spatial Representation	Relation	Spatial Representation
posterolateral_of (Coccygeal) { posterior_of() and lateral_of() }		laterosuperior_of (Bladder) { superior_of() and lateral_of() }	

Pathway Relations


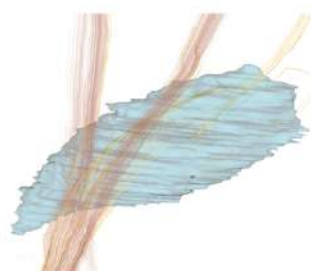
Relation	Spatial Representation	Relation	Spatial Representation
crossing (SacralHoles)		endpoints_in (PiriformisMuscle)	

FIGURE 5.24: Examples of aperture tuning, definitions combination and pathway relations.

Spatial relations combination = Query design

The pelvis being a complex environment, the definition of a nervous tract requires the combination of several spatial relations. Therefore, the description of the nerve (called "Query" in the PQL environment), is the combination of spatial relations using the Boolean operators: AND, OR and NOT. The spatial representations of the relations are combined accordingly.

Example of query structure: BundleName = (crossing(Structure) AND anterior_of(Structure, Aperture, Percentage) AND ((NOT between(Structure, Percentage)) OR proximity_of(Structure, distance=mm, Percentage)))

Implementation

This has been performed by A. Delmonte. A PQL query is a file containing the specification of the bundle to segment. It is formed by a combination of keywords and logical operators, and it is written in a near-to-English language in Python, that is suitable for the translation into machine operations. Writing the query is in the hand of the user and it is a process that involves an anatomical knowledge of the pelvic area.

Once the query is designed, PQL uses two files to perform the segmentation: the tractogram to segment (either a ROI based tractogram or a whole pelvis tractogram), and the segmentation file previously computed as detailed in the database organization section of Chapter 3. This latest file contains each of the segmented anatomical structures that can be used as a "Structure" in the queries. The computing time varies according to the size of the initial tractogram to segment, and the number of relations within the query: instantaneous with a ROI based tractogram, and till 5 minutes with a whole pelvic tractogram (1 million fibers) to segment and 12 relations to compute.

The result of the query is visualized as fiber tracts loaded in the 3D scene, also featuring the organs of importance for analysis and spatial recognition such as hipbones, sacrum, muscles etc. This 3D visualization is of utmost importance for the query design because the visual result in 3D guides the iterative testing which removes or adds directional relations, modify tuning parameters, etc.

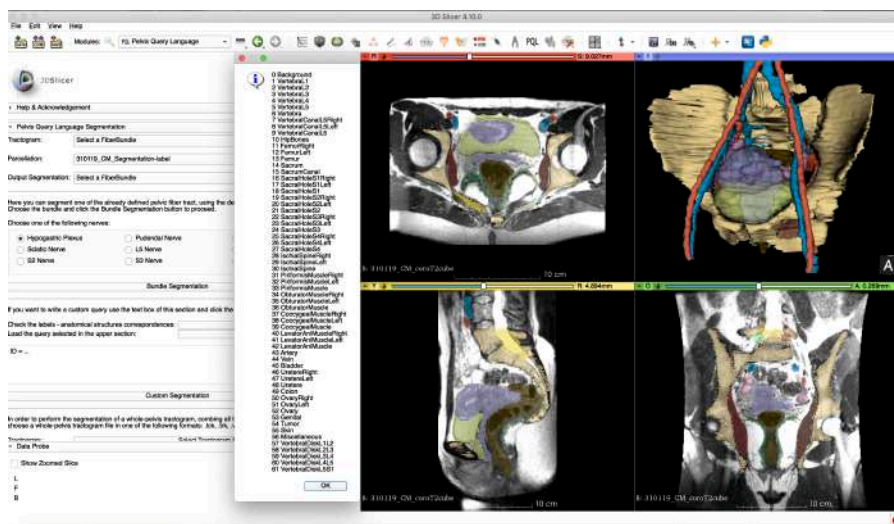


FIGURE 5.25: PQL interface and list of the anatomical structures.

5.5.3 PQL validity tested on a ROI based tractogram

Methods

In order to test the validity of our method, we used PQL to segment a sacral plexus tractogram, that presents all the roots from L5 to S4. Our aim was to design the optimum queries that were able to segment each root separately.

For this test, we used two MRI sequences (volumic for anatomical segmentation and diffusion for tractography) performed on a healthy adult female subject. The diffusion sequence parameters were those from protocol 5 in MRI N°1 of this subject, as detailed in Section 5.3. We chose this MRI because it gave the more accurate tractography results using a ROI based method as detailed in Section 5.3. The ROIs used were the vertebral canal L5, the sacral holes from S1 to S4 and the sacral canal.

Before performing the tests using the PQL method, here are some remarks about the ROI based sacral plexus tractogram, presented in Figure 5.26:

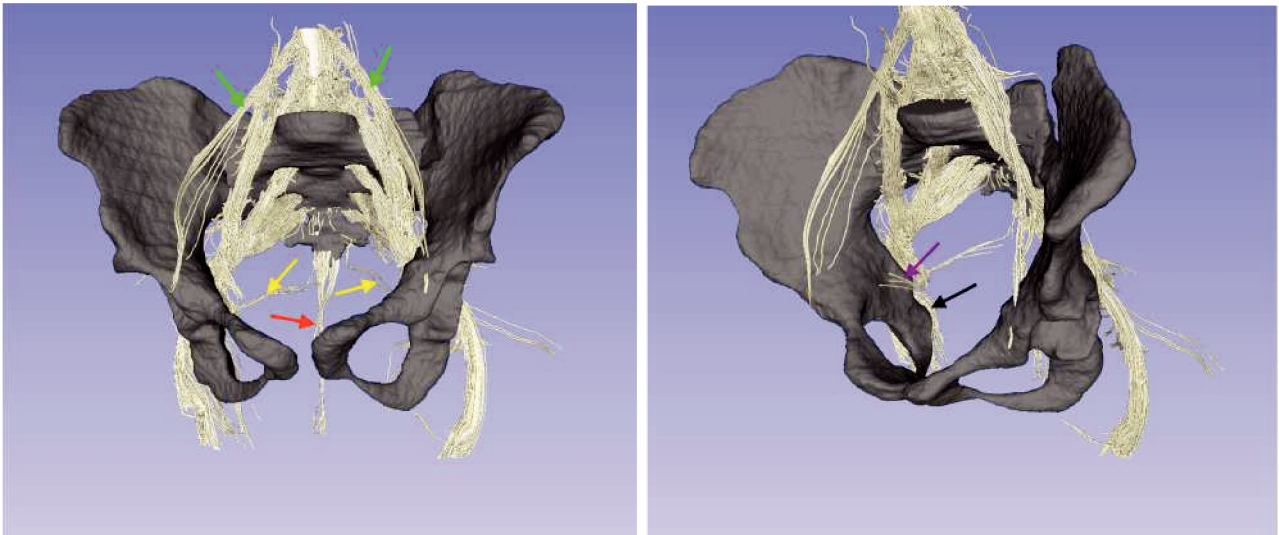


FIGURE 5.26: ROI based sacral plexus tractogram. Green arrows: L4 roots; Yellow arrows: may be S4 roots; Red arrow: noise fibers; Purple arrow: may be right obturator muscle nerve; Black arrow: may be right pudendal nerve.

- there is an uncertainty about the presence or not of sacral root S4. It may be false positive tracts from muscle of pelvic floor or fascia tracts coming from outside the spine;
- there is noise coming from ROI drawing outside the spine canal, representing fibers from the inter-spinal ligament and paravertebral muscles and fascias;
- L4 is represented, giving that the ROI drawing is made on an axial plane of the spine canal on all the slices of the acquisition, including the L4 vertebra region;
- it seems to represent the obturator muscle and pudendal nerves, but it is not sure where the fibers come from originally;
- it does not represent the pudendal plexus as a separate entity from the sacral plexus, meaning the reunion of S2 to S4 fibers to form the pudendal nerve when entering again the pelvic cavity under the ischial spine. Still, there are some fibers taking that route from S2 and S3 that resemble to obturator muscle and pudendal nerves;
- inter-individual variations must be taken into account. This manual ROI based tractogram is originated from only one example of a normal adult female specimen, which does not represent eventual inter individual variations.

During the translation from a natural language to the PQL language, attention must be paid to correctly identify all the functional information and to discard the relations that, while correct from an anatomical point of view, do not add any useful segmentation indication. First, we wrote first versions (V0) of the queries for each tract using extensively all the pelvic anatomical structures that may help to define the tract. Then we progressively removed the unnecessary arguments by visually comparing the results with the manual ROI based sacral tractogram used as a reference, in order to find the optimum query. Attention was paid to the thickness of the tracts (true positives) and the apparition of unwanted tracts (false positives).

Results

This is an example of the V0 query for L5 root:

L5 V0 = crossing(VertebralCanalL5) and (not posterior_of(Sacrum, aperture=0)) and posterior_of(Vein) and posterior_of(Artery) and posterior_of(Uretere) and proximity_of(Uretere, distance=20) and (posterior_of(Ovary) and proximity_of(Ovary, distance=20)) and anterior_of(PiriformisMuscle) and superior_of(IschialSpine, aperture=1) and anterior_of(IschialSpine, aperture=1) and posterior_of(ObturatorMuscle) and (not crossing(SacralHoleS1)) and (not crossing(SacralHoleS2)) and (not crossing(SacralHoleS3)) and (not crossing(SacralHoleS4)) and (not (anterior_of(LevatorAniMuscle, aperture=0) or posterior_of(LevatorAniMuscle, aperture=0)))

The computational time for segmenting the L5 root from this query was quite long (5 minutes). To find the optimal query, we kept the definition "crossing(VertebralCanalL5)" because this is the main defining structure for the L5 root, and progressively removed all the following definitions within the query one by one. A better result was obtained by replacing posterior_of(ObturatorMuscle) by not anterior_of(ObturatorMuscle), because it allows us to exclude fibers that go through the structure itself that may be false positives. The spatial relationships aim at eliminating the false positive fibers, and as they are situated posteriorily to that muscle, using not posterior_of(ObturatorMuscle) provides a more satisfying visual result. The same process process was used for all the sacral plexus roots and led to the final optimum queries:

L5 = crossing(VertebralCanalL5) and (not anterior_of(ObturatorMuscle)) and (not crossing(SacralHoleS1))

S1 = crossing(SacralHoleS1) and (not crossing(SacralHoleS2)) and (not crossing(VertebralCanalL5)) and (not (anterior_of(LevatorAniMuscle, aperture=0) or posterior_of(LevatorAniMuscle, aperture=0)))

S2 = crossing(SacralHoleS2) and (not crossing(SacralHoleS3))

S3 = crossing(SacralHoleS3) and (not crossing(SacralHoleS2))

The use of the **crossing** argument with the structure **sacral hole** is not surprising, because sacral plexus fibers are very well defined when they go out of the sacrum and penetrate the pelvis area. Adding a **not crossing** argument with an adjacent **sacral hole** allows for filtering some false positive fibers (regarding the tract of interest). Indeed, the presence of these tracts is explained by the segmentation of the sacral hole that may concern on its edges space where fibers from above or below sacral levels go through. This is not easily seen while performing the segmentation on the anatomical sequence.

On the one hand, the other more useful structures were surprisingly the obturator muscle for L5 and the levator ani muscle for S1, and not the piriformis muscle. This latest muscle however consists in the main anatomical relationship for the sacral plexus, but it may be too close to it (sometimes nerve fibers are even embedded within the muscle fibers) to be useful to discriminate true and false positives. The other two muscles may present appropriate shape and distance from the sacral plexus to perform this filtering, in association with a well-tuned spatial relationship modeling. On the other hand, soft tissue organs such as vessels or rectum were not discriminant in the sacral plexus query design. This

stays understandable as the sacral plexus roots main anatomical relationships are the bones and the muscles of the pelvis.

The concatenated query to obtain all the sacral plexus roots in one query was designed by using the query arguments for each root, removing the one that were conflicting, and adding the OR Boolean operator between the arguments corresponding to each root put in parentheses. For the visual result see Figure 5.27.

Sacral Plexus = (crossing(VertebralCanalL5) and not anterior_of (ObturatorMuscle)) or (crossing (SacralHoleS1) and not (anterior_of(LevatorAniMuscle, aperture=0) or posterior_of(LevatorAniMuscle, aperture=0))) or crossing(SacralHoleS2) or crossing(SacralHoleS3)

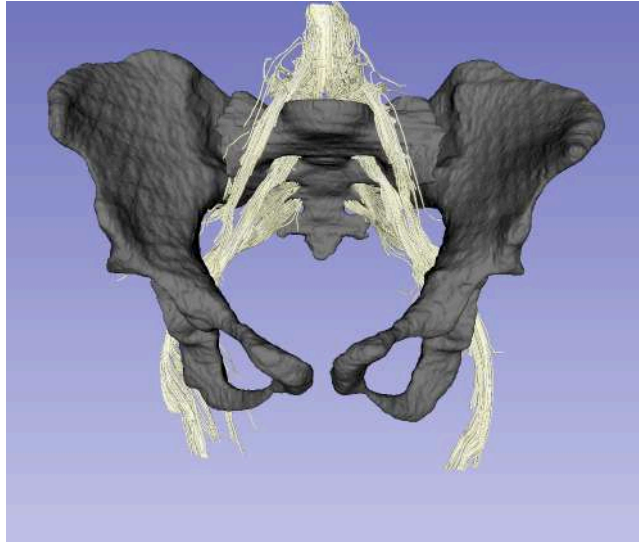


FIGURE 5.27: Concatenate PQL tractogram.

While visually comparing the ROI based tractogram and the concatenated PQL tractogram, we found that:

- PQL is able to find the main sacral roots from L5 to S3, with a good quality result, meaning keeping the right thickness of the tracts (true positives) going out the sacral holes, while removing the unwanted tracts (false positives), as the sagittal fibers from the inter-spinous ligament. This may be explained by the difference in the segmentation process: the ROI drawing method uses the sacrum canal till the coccyx, where it captures these false positive fibers. PQL only uses the segmentation of the sacral hole on the internal face of the sacrum materializing the way into the pelvis;
- PQL was not able to find the obturator muscle and pudendal nerves with the definition of the originating sacral roots of these nerves: L5 to S2 for obturator muscle nerve and S2 to S4 for pudendal nerve respectively. However, it could be because all these tracts are in continuity. However, these small nerves may bear a very low FA that prevents us from tracking them, and also they are in tight contact with muscle fibers that may interfere with the tracking algorithm;
- the queries of the following nervous structures were not designed, because these structures were missing from the manual ROI based tractogram: S4 root, pudendal plexus, levator ani, perineal, dorsal nerves of penis/clitoris, whole autonomous system.

5.5.4 PQL validity tested on a whole pelvis tractogram tractogram

Methods

Once we established the ability of the PQL method to segment fiber tracts of interest on a sacral plexus ROI based tractogram, we wanted to test it on a whole pelvis tractogram. Our aim was to explore the possibility of adding new tracts such as the hypogastric plexus in the pelvic nervous network tractograms using the PQL method.

We used to same subject and acquisitions as detailed in Subsection 5.5.3. The diffusion image was used to generate a whole pelvis tractogram as detailed in Subsection 5.2.2 about post-processing. The file weighting 11 Go, the computational time for each query is longer, around 15 minutes on average. For this reason, the testing strategy was inverted compared to the testing of the ROI based tractogram: using at first a one argument query using the closest structure from the tract results into a noisy but less heavy tractogram, that is used as the initial tractogram, similarly to the process of testing the PQL method on the ROI based tractogram. We then refined the segmentation by adding some useful spatial information in the query in order to filter the result and only obtain the tract of interest without any false positive tracts.

During the testing, we noticed that each plexus had a prominent direction for all its fibers: cranio-caudal for the sacral plexus and the pudendal plexus, and antero-posterior for the hypogastric plexus. If it was known and logical for the sacral plexus according to its global shape and direction, it was not anticipated for the hypogastric plexus. Because of its inherent complex organization, its usual description in anatomical text-books does not focus on the global direction of its fibers. We noticed that fact while using the Tractography Display Module of Slicer 3D that gives the possibility to visualize the tracts with a single color corresponding to their mean orientation: blue for cranio-caudal, green for antero-posterior and red for medial-lateral. This led us to design a specific post processing tool that filters the tractograms according to their mean orientation.

Results

- Query design on the control patient:

The process of query design is detailed and commented in the captions of Figure 5.28 for L5 root, Figure 5.29 for S1 root, Figure 5.30 for S2 root, Figure 5.31 for S3 root, Figure 5.32 for S4 root, Figure 5.33 for the pudendal plexus, and in Figures 5.34, 5.35, 5.36, 5.37, and 5.38 for the hypogastric plexus. These figures show the tracts that are either selected or removed by the arguments of the queries, and the final result, which will be commented in the conclusion of this subsection.

To better understand the various steps of iterative testing, Figures 5.39, 5.40, 5.41 5.42 5.43 represent the progressive segmentation of the whole pelvis tractogram, argument after argument within the whole query to obtain the hypogastric plexus. These figures appeared to be necessary regarding this plexus because of its complexity. The characteristics of the final result will be commented in the conclusion of this subsection.

Figure 5.44 represents the final result with the merge of the 3 plexuses: sacral, pudendal (red arrows) and inferior hypogastric (in green). This is the very first 3D representation of those three plexuses along with the 3D bony structure of the pelvis to our knowledge. It is also possible to add the pelvic organs within the 3D scene, but we did not represented it here because then the 2D static figures prevent from correctly visualizing the nerves.

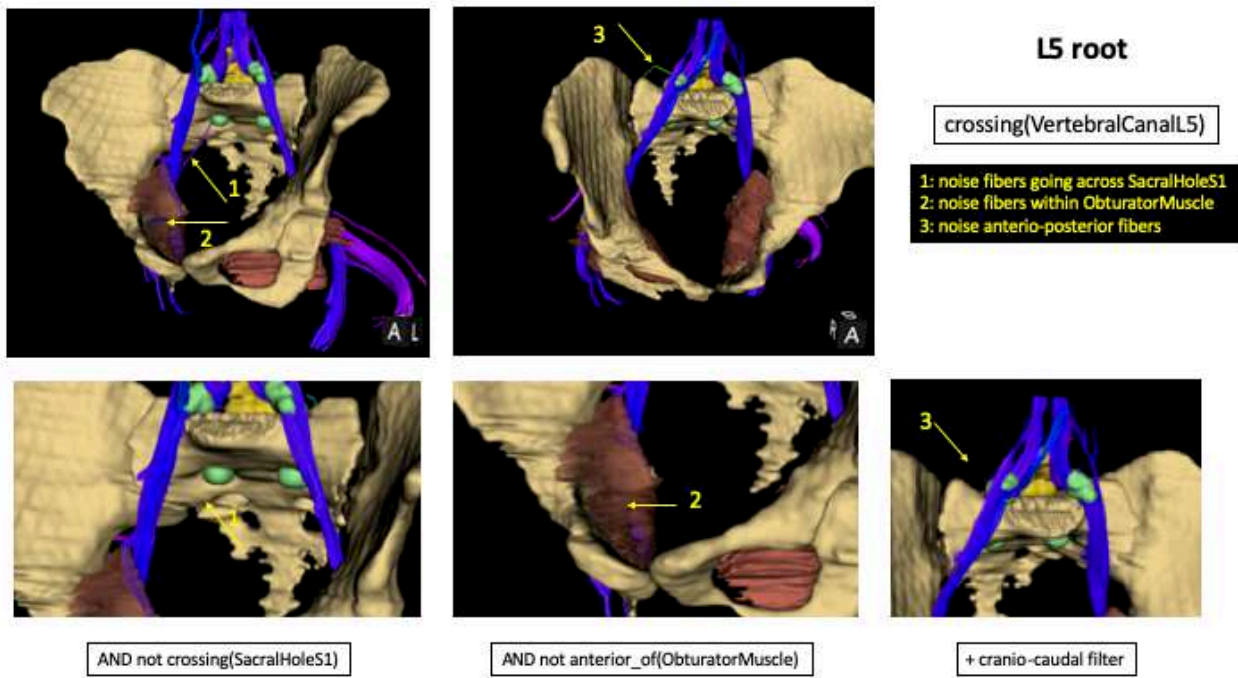


FIGURE 5.28: L5 root query design. The main defining spatial relation is crossing(VertebralCanalL5). False positives tracts namely 1 and 2 were progressively removed by adding to the query: AND not crossing(SacralHoleS1) AND not anterior of(ObturatorMuscle). These last fibers (2) were probably the obturator muscle nerve. The filtering was completed by adding the cranio-caudal filter to remove the green fibers that are antero-posterior false positive tracts (3).

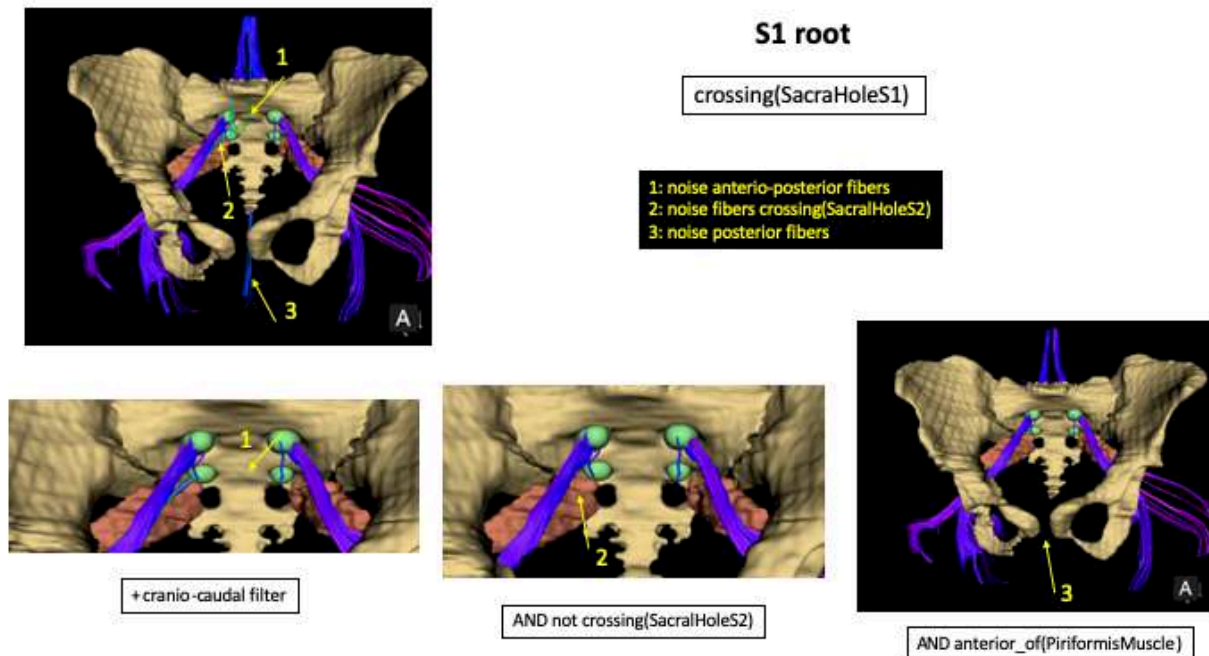


FIGURE 5.29: S1 root query design. The main defining spatial relation is crossing(SacralHoleS1). False positives tracts namely 2 and 3 were progressively removed by adding to the query: AND not crossing(SacralHoleS2) AND anterior of(PiriformisMuscle). The filtering was completed by adding the cranio-caudal filter to remove the green fibers that are antero-posterior false positive tracts (1).

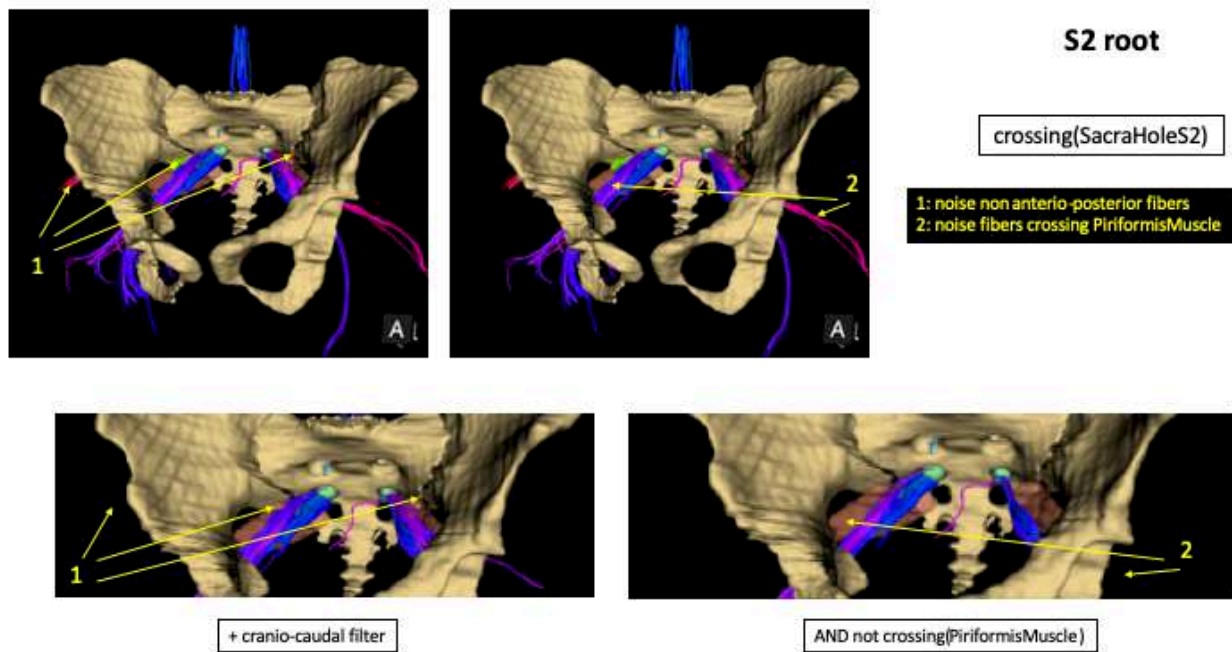


FIGURE 5.30: S2 root query design. The main defining spatial relation is crossing(SacralHoleS2). False positive tracts (2) were progressively removed by adding to the query: AND not crossing(PiriformisMuscle). These tracts were considered as false positives because of the unusual thickness of the S2 root on this result. This root is in very close contact with the piriformis muscle and make the difference between nerve fibers and muscle fibers may be challenging. The filtering was completed by adding the cranio-caudal filter to remove the green and red fibers that are antero-posterior and medio-lateral false positive tracts (1).

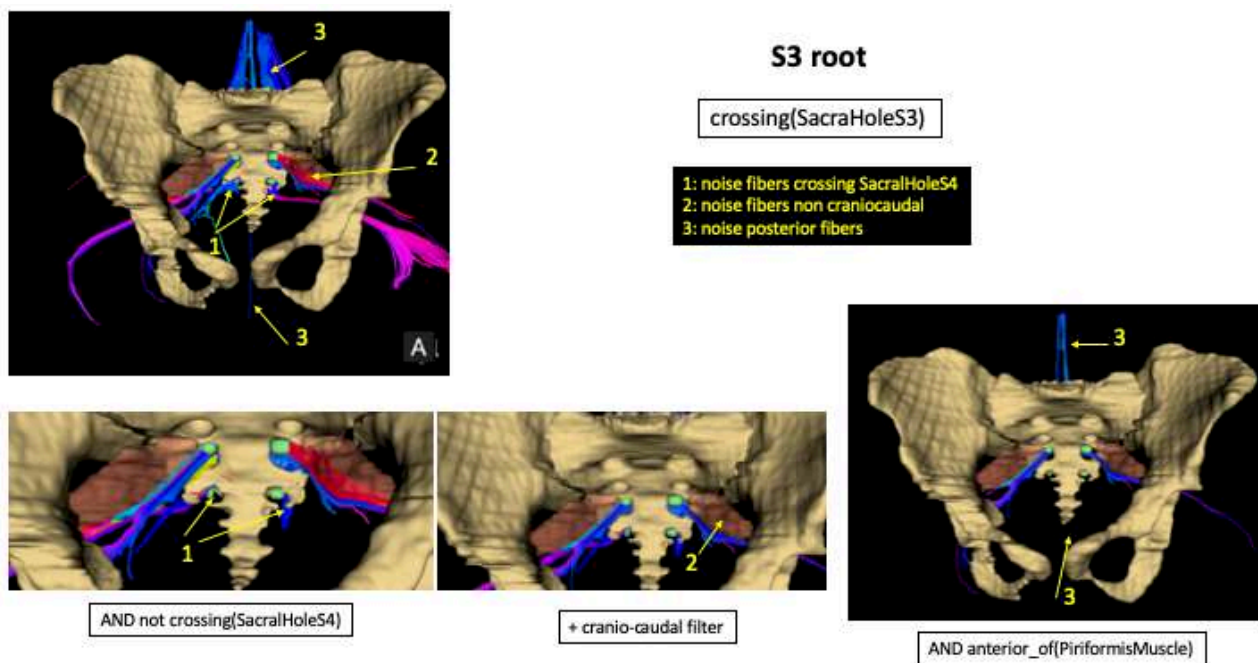


FIGURE 5.31: S3 root query design. The main defining spatial relation is crossing(SacralHoleS3). False positive tracts namely 1 and 3 were progressively removed by adding to the query: AND not crossing(SacralHoleS4) AND anterior of(PiriformisMuscle). The filtering was completed by adding the cranio-caudal filter to remove the red fibers that are medio-lateral false positive tracts belonging to the piriformis muscle (2).

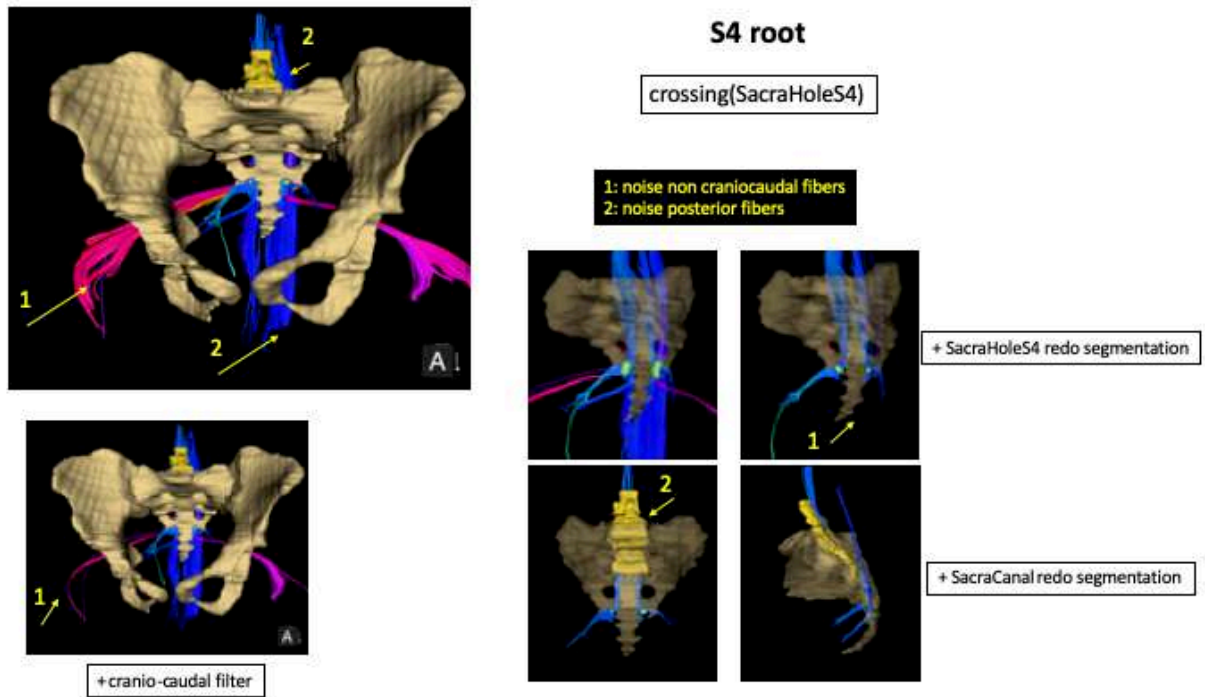


FIGURE 5.32: S4 root query design. The main defining spatial relation is crossing(SacralHoleS4). False positives tracts (2) belonging to muscular and ligament structures posterior to the sacrum were filtered by modifying the segmentation of both the Sacral Hole S4 and the Sacrum Canal. The sacral hole S4 is very small, and drawing a too much large sphere lead to these false positive tracts. The size of the sacral hole was therefore diminished. At first, the segmentation of the Sacrum Canal was done from L5 level till the coccyx. Again, in this same small caudal area (S4 hole, coccyx), any error in the segmentation lead to the selection of false positive tracts. We therefore decided to stop the sacrum canal segmentation at S1 level, where the boundaries between the sacrum and its surroundings is clearly possible to identify. This segmentation will help selecting only nerve fibers that pass through the sacrum canal and discard the posterior ones. The filtering was completed by adding the cranio-caudal filter to remove the red fibers that are medio-lateral false positive tracts belonging to the piriformis muscle and hip muscles (1).

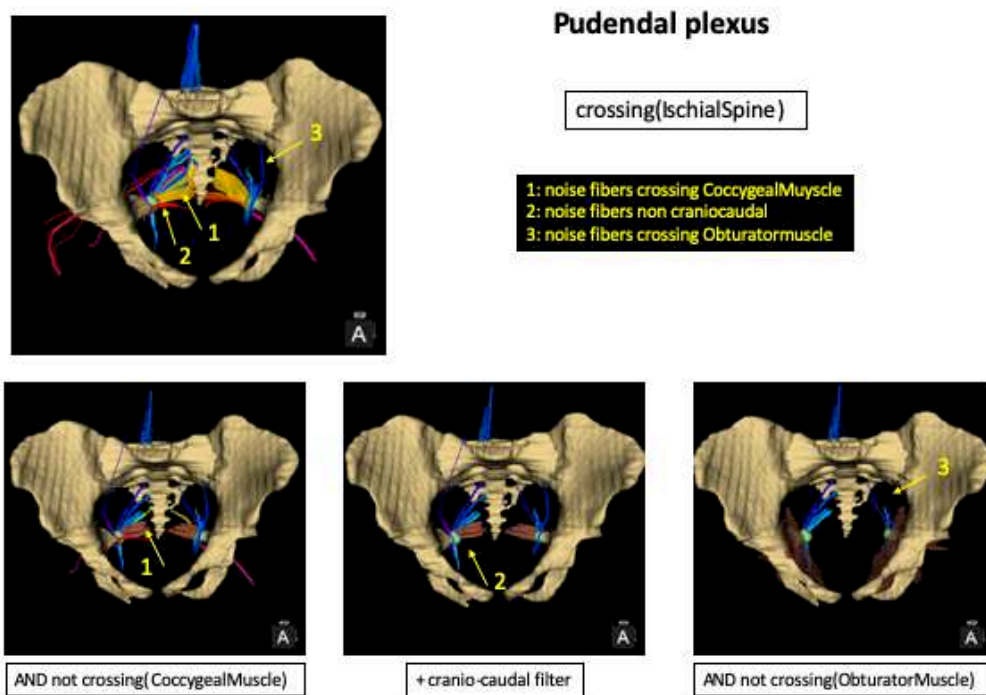


FIGURE 5.33: Design of pudendal plexus query.

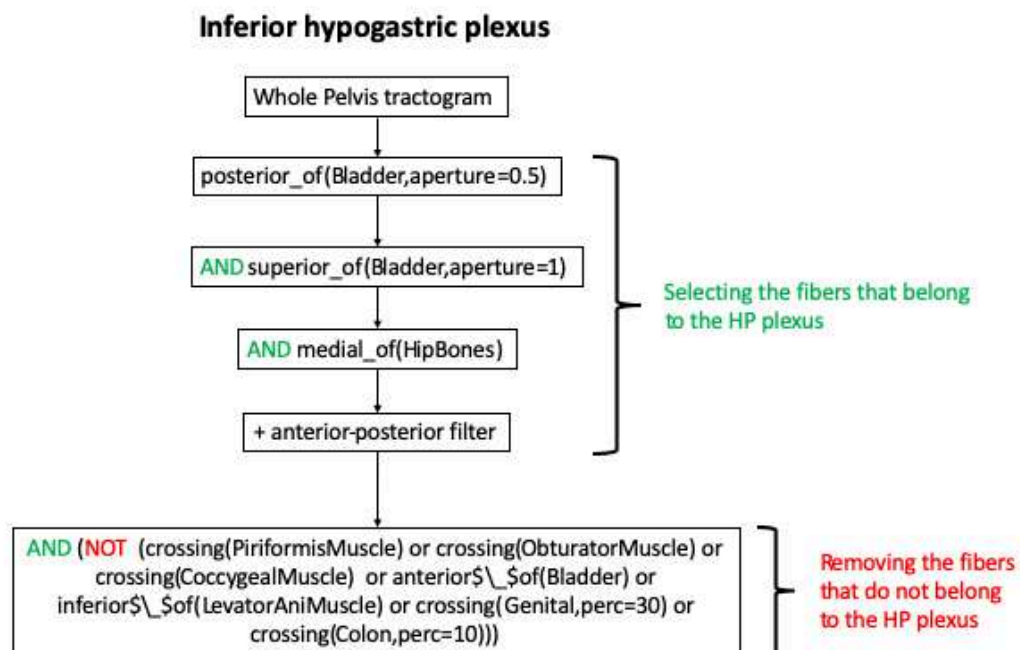


FIGURE 5.34: Overview of the design for the inferior hypogastric plexus

Inferior hypogastric plexus

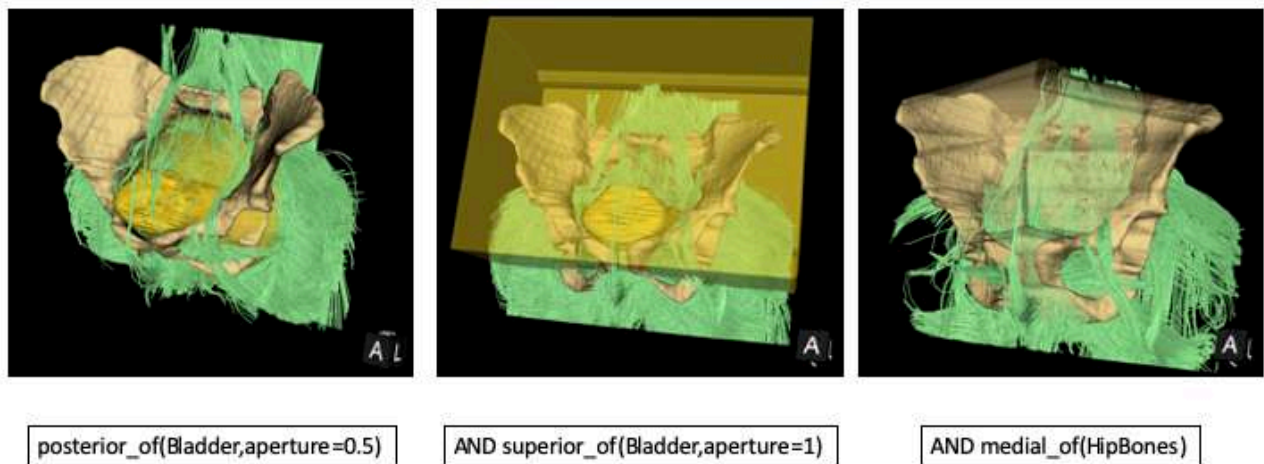


FIGURE 5.35: 3D view of the modeled spatial relations corresponding to the first three arguments arguments of the query. For each argument, the 3D view shows the segmentation of the whole pelvis tractogram corresponding to the query, independently from the previous argument within the query. This step allows to reduce the whole pelvic tractogram only to the fibers that are located inside the pelvic area and potentially belong to the inferior hypogastric plexus.

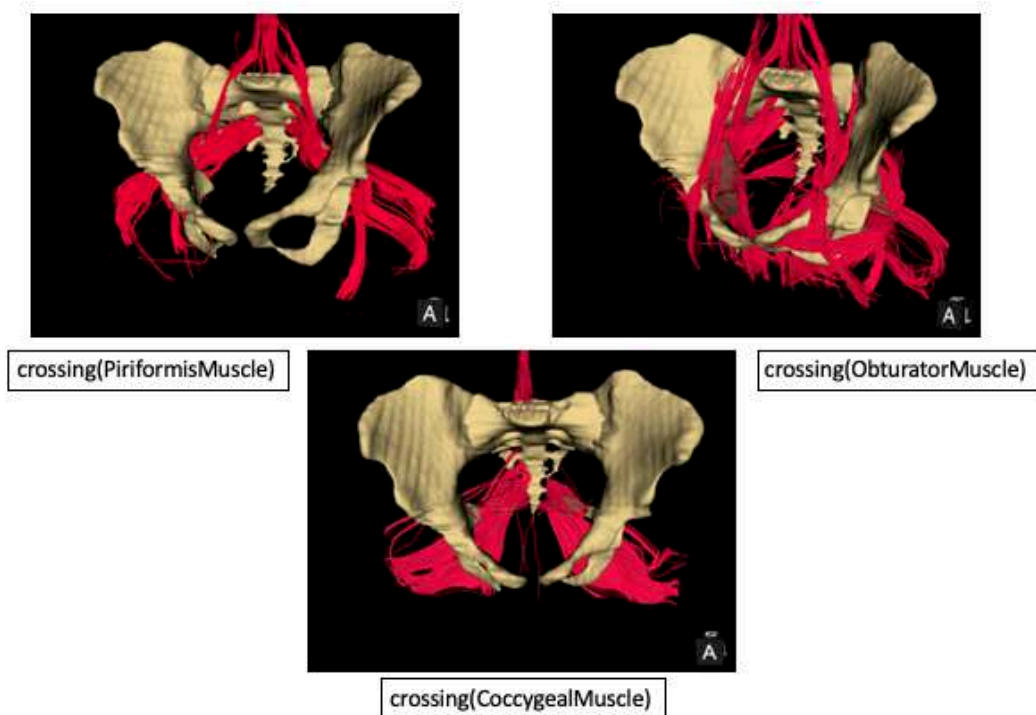


FIGURE 5.36: 3D view of the fibers that cross the piriformis, obturator, and coccygeal muscles, that will be removed by the NOT operator placed before the arguments of the query.

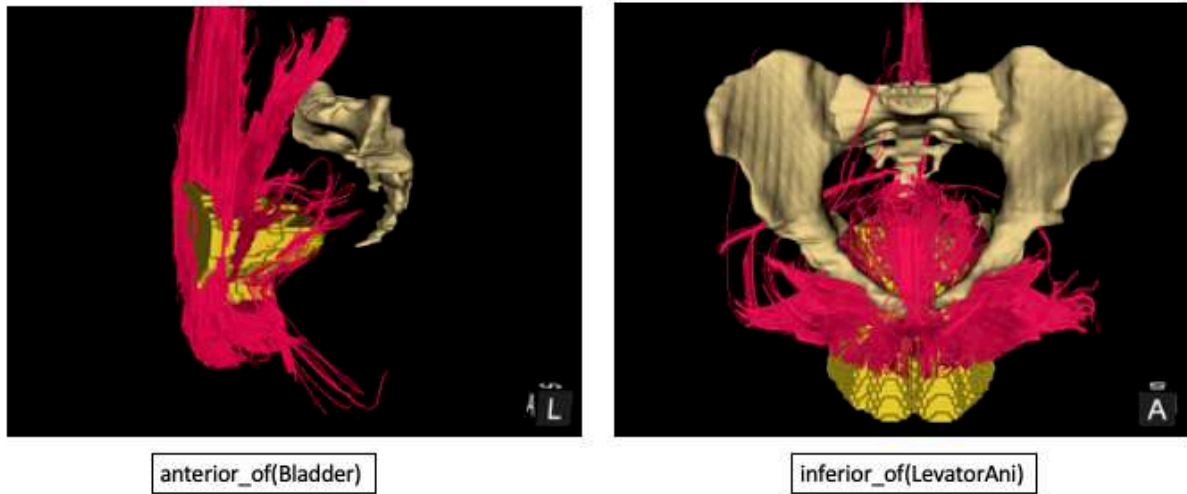


FIGURE 5.37: 3D view of the modeled spatial relations: anterior of Bladder and inferior of Levator Ani Muscle and the fibers that go through, which will also be removed by the NOT operator.

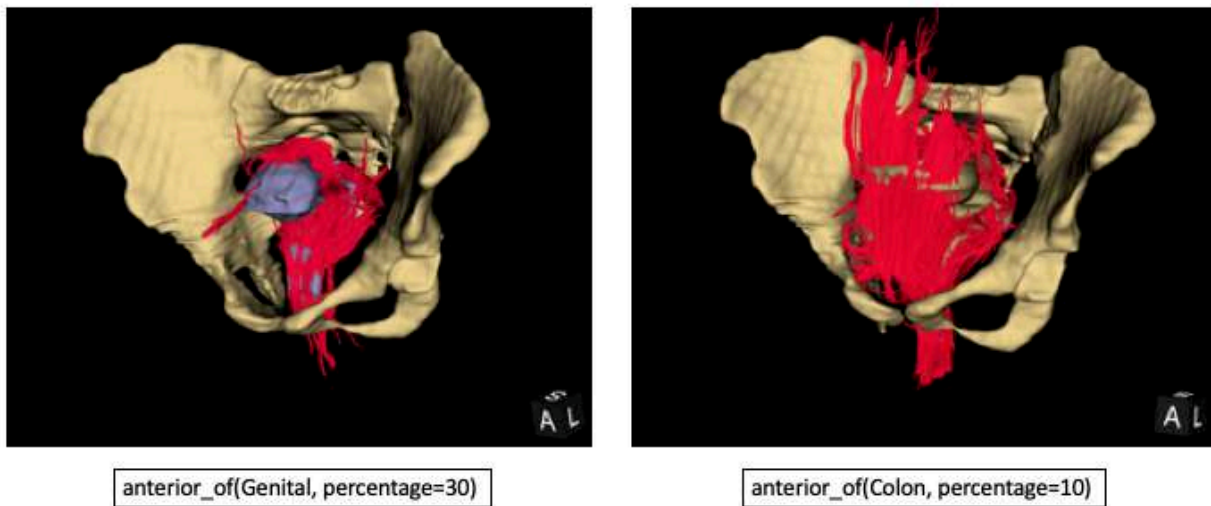


FIGURE 5.38: 3D view of the fibers that cross the genital and the colon. The percentage has been tuned with iterative experiments, while visually evaluating the 3D result in order to find a compromise between false positive tracts and missing true positives.

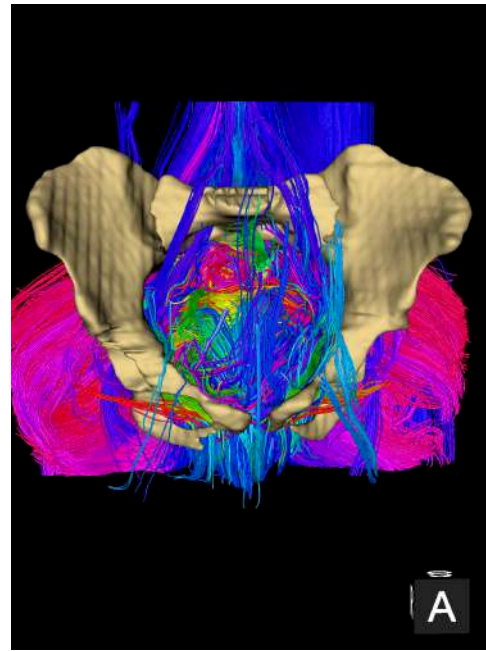
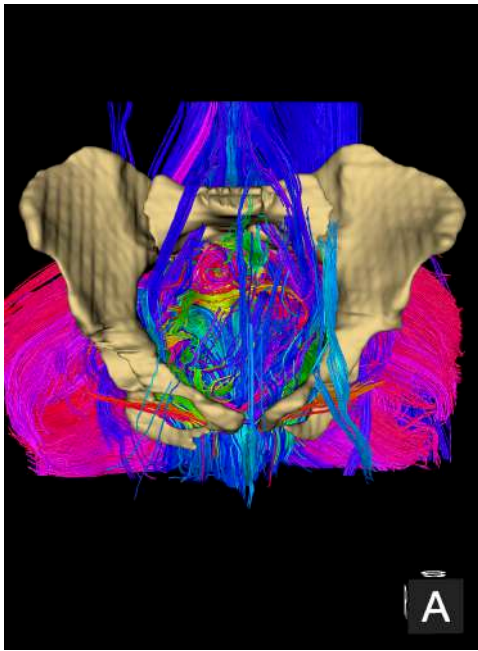


FIGURE 5.39: Progressive segmentation results. On the left: `posterior_of(Bladder,aperture=0.5)`. On the right: `AND superior_of(Bladder,aperture=1)`.

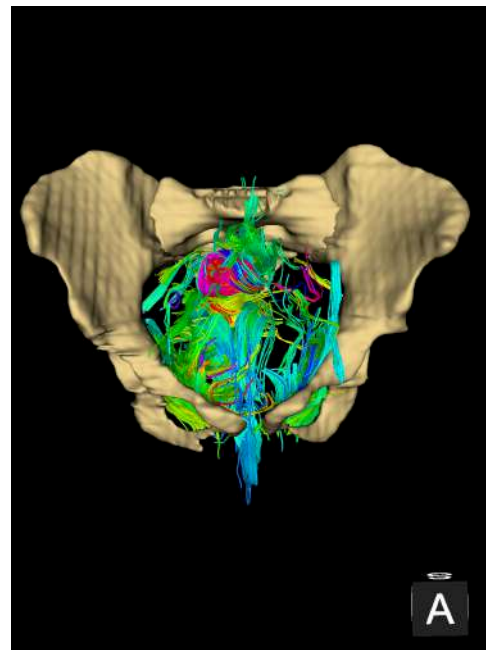
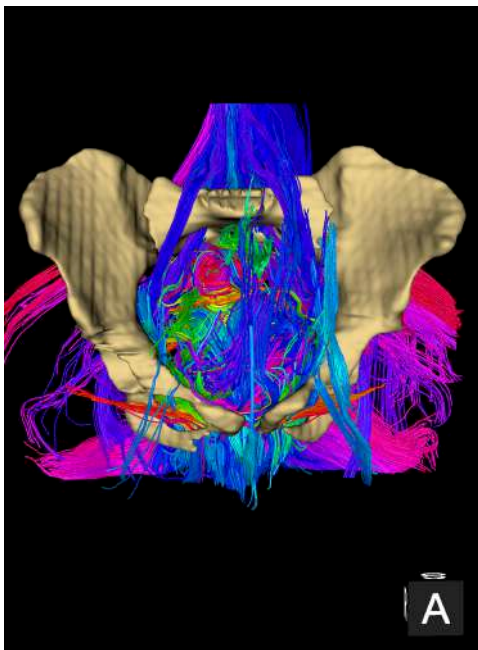


FIGURE 5.40: Progressive segmentation results. Left: `AND medial_of(HipBones)`. Right: antero-posterior filter. The first three arguments allow for a better first visualisation of the fibers that may belong to the IHP. Blue fibers seem to belong either to the sacral plexus, soft tissue organs or anterior abdominal wall. The fibers that seem to be located at the place of the IHP are green, meaning bearing a global antero-posterior direction. These fibers were selected by the application of the antero-posterior filter.

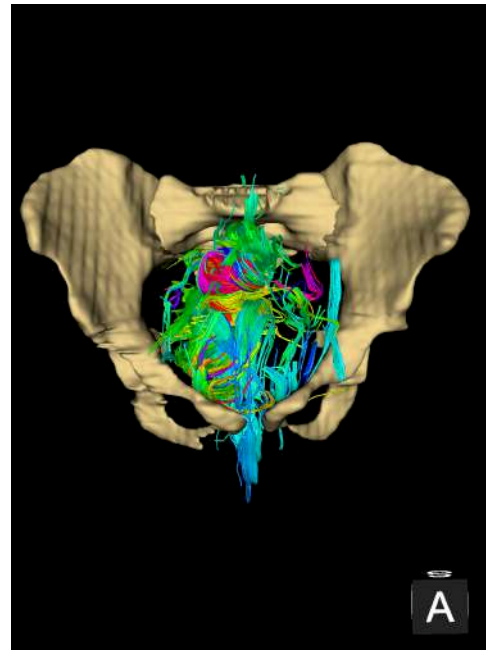
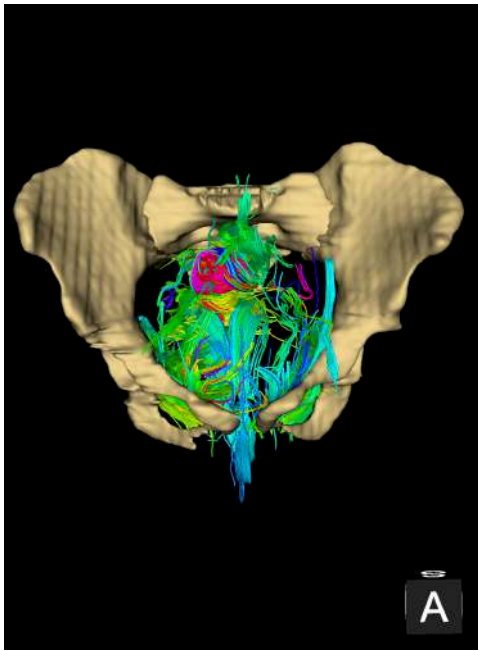


FIGURE 5.41: Progressive segmentation results. Left: AND not crossing(PiriformisMuscle). Right: AND not crossing(ObturatorMuscle). These two arguments aim at removing the fibers that go through these muscles and do not belong the IHP.

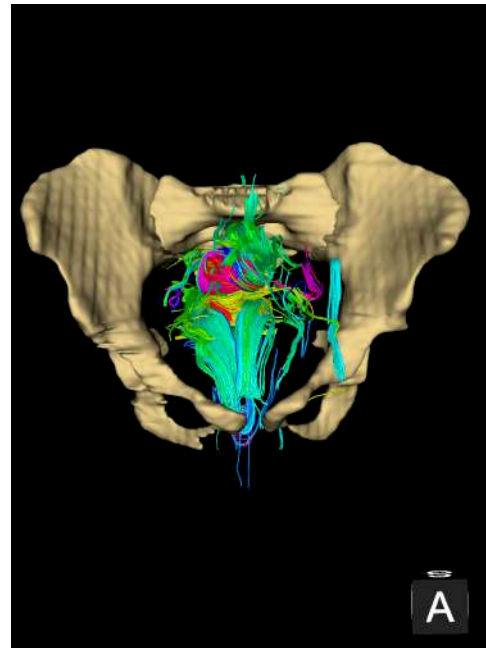
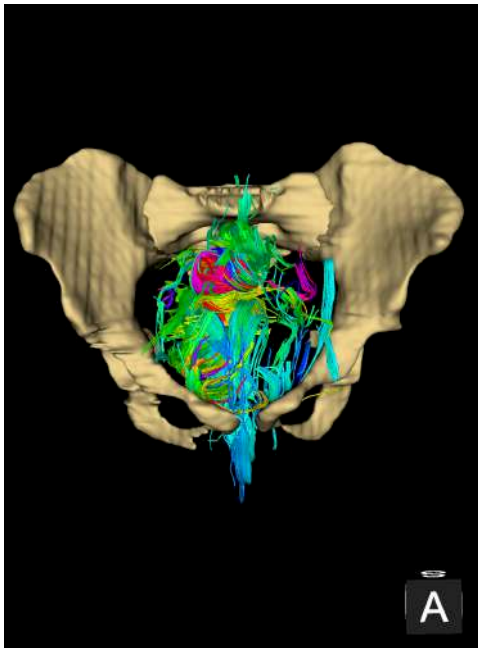


FIGURE 5.42: Progressive segmentation results. Left: AND not crossing(CoccygealMuscle). Right: AND not anterior_of Bladder. This latest argument aims at removing the fibers that are immediately posterior to the pubis and do not belong to the IHP.

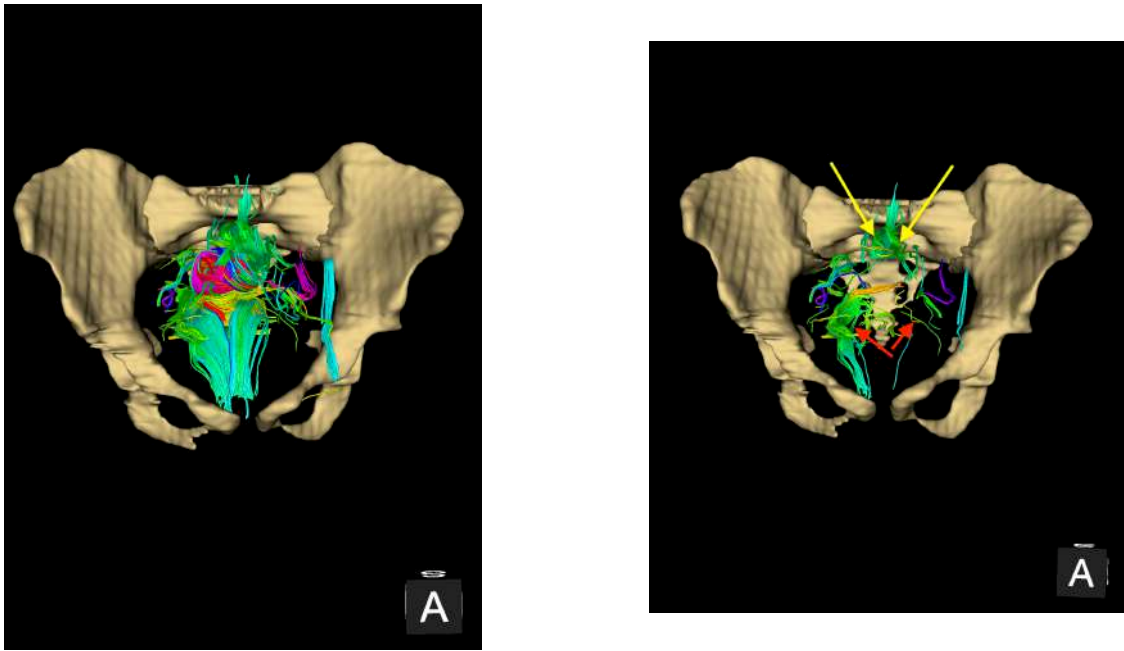


FIGURE 5.43: Progressive segmentation results. Left: AND not inferior_of(LevatorAniMuscle. Right: AND not (crossing(Genital, percentage = 30) or crossing(Colon, percentage = 10)). The percentage has been tuned with iterative experiments, while visually evaluating the 3D result in order to find a compromise between false positive tracts and missing true positives. Yellow arrows: right and left hypogastric nerves. Red arrows: right and left inferior hypogastric plexus. The right side presents more fibers. This may be due to the image itself and the pre and post processing treatment rather than to a true asymmetry in the subject.

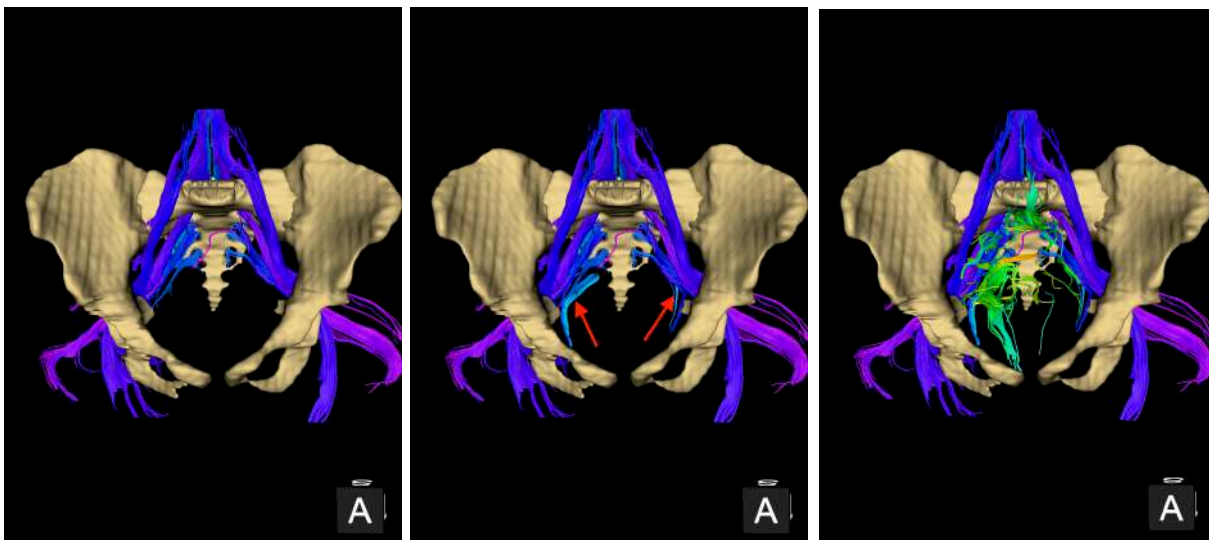


FIGURE 5.44: 3D views of the last version of L5 to S4 root (sacral plexus) on the left, the merge between sacral plexus and pudendal plexus (red arrows) in the middle, and the addition of hypogastric plexus on the right (green fibers). This latest image is the first to our knowledge to assemble iliac bones, sacrum, sacral, pudendal and hypogastric plexuses within the same 3D space using tractography.

- Queries modifications for an application in pediatric patients presenting an ARM

After designing the PQL queries on an adult healthy female subject, we tested them on 20 ARM patients. The qualitative and quantitative analysis of the results will be the subject of Chapter 6. We only acknowledge here the few modifications of the queries required to be more universal and overcome eventual inter-individual variations, especially in children.

The modified queries worked for the sacral plexus, but not for the pudendal and hypogastric plexuses. Regarding these last two, the results were not inaccurate with false positives, but negative, with no fibers at all, because there was probably not enough information within the diffusion image of these pediatric patients to be segmented by the PQL method and the corresponding queries.

Regarding the sacral plexus, some relationships were added in order to optimize the filtering of the whole pelvic tractogram. We added not crossing SacralHole S2 for L5 root query, not crossing VertebralCanalL5 for S1 root query, and not (crossing SacralHoleS1 or crossing SacralHoleS3) for S2 root query. The reason for that is that these patients were children, and their sacral area smaller, so while drawing the ROIs on the sacral holes, some of them may overlap on each other, bringing the need for more filtering.

We also changed the S2 query for the pediatric patients: we replaced the argument not crossing (PiriformisMuscle) by anterior of(PiriformisMuscle). Indeed, we noticed that the S2 roots in children is very often nearly completely enclosed within this muscle, and adding a not crossing argument would lead to the disappearance of the root in nearly half of the patients. We replaced it by the argument anterior of PiriformisMuscle in order to continue to filter false positive muscular horizontal fibers that go posteriorily into the hip region.

Figure 5.45 shows three examples of ARM pelvic tractograms. The tractography of the whole series of 20 patients with ARM will be the subject of Chapter 6.



FIGURE 5.45: Sacral Plexus tractograms of three patients with ARM.

Conclusion

The final optimum PQL queries for the sacral and pudendal plexuses, applying in all cases the cranio-caudal filter on the query result, were the following:

- **L5** = crossing(VertebralCanalL5) and not crossing(SacralHoleS1) and not anterior_of(ObturatorMuscle) and not crossing(SacralHoleS2)
- **S1** = crossing(SacralHoleS1) and not crossing(SacralHoleS2) and anterior_of(PiriformisMuscle) and not crossing(VertebralCanalL5)
- **S2** = crossing(SacralHoleS2) and anterior_of(PiriformisMuscle) and not crossing(SacralHoleS1) and not crossing(SacralHoleS3)
- **S3** = crossing(SacralHoleS3) and not crossing(SacralHoleS4) and anterior_of(PiriformisMuscle)
- **S4** = crossing(sacralHoleS4) and crossing(SacrumCanal)
- **Pudendalplexus** = crossing(IschialSpine) and not crossing(CoccygealMuscle) and not crossing(ObturatorMuscle)

These queries mainly include the crossing argument associated with the sacral holes and some more filtering using the three main muscles of the pelvic wall, namely the piriformis, the obturator and the coccygeal muscle. These queries seem to be relatively universal even with inter-individual variations and in pediatric patients. The S4 roots and the pudendal plexus are the most difficult to obtain, because they are very fine tracts surrounded by a lot of muscle fibers, which make them tricky to segmented according to the actual resolution of our diffusion images, associate with an entirely manual method of structures segmentation.

The final optimum PQL query for the hypogastric plexus was (with the addition of the antero-posterior filter):

- **Inferior hypogastric plexus** = posterior_of(Bladder,aperture=0.5) and superior_of(Bladder, aperture=1) and medial_of(HipBones) and (not(crossing(PiriformisMuscle) or crossing(ObturatorMuscle) or crossing(CoccygealMuscle) or anterior_of(Bladder) or inferior_of(LevatorAniMuscle) or crossing(Genital,perc=30) or crossing(Colon,perc=10)))

The IHP query was the most difficult to design, and required a lot of iterative testing and optimization to limit the number of arguments within the query. As expected according to the anatomical location of the IHP between the muscles and the pelvic organs, all these structures contributed to its segmentation process. The bladder was the most useful structure to perform a first filtering of the million fibers present in the initial whole pelvis tractogram. It is understandable because the bladder bears a quite regular shape and is located in the middle of the pelvis area, allowing for a simple and efficient spatial relationship modeling. The tuning of the percentage parameters of the structures named Genital and Colon was based uniquely on theoretical anatomical knowledge. Some of the fibers of the IHP are in fact extending till the sero-muscular envelope of these organs, in order to deliver their sympathetical and para-sympathetical balanced innervation. Setting a cut off which relies on a manual delineation of the organs limits may be difficult. The results of both the query design and the tractography results shall be taken with caution, with a need for comparative studies with gold standard pelvic nervous anatomy.

5.5.5 Qualitative and quantitative comparison between PQL and ROI based tractograms

Methods

As a final step to evaluate PQL accuracy in tractogram segmentation, we compared sacral plexus tractograms computed using the PQL method versus a ROI based approach. We have already demonstrated the ability of the PQL method to segment the inferior hypogastric plexus in the previous subsection, which is not achievable using a ROI based approach. However, we wanted also to evaluate its performances on the most easy to obtain pelvic tractogram: the sacral plexus.

In that study, we used the protocol 5 of the first MRI performed on the healthy adult female subject, which acquisition parameters were optimal as detailed in Section 5.3. We computed a sacral plexus tractogram with a ROI based method using the sacral holes and the sacral canal as seeding points. The segmentation of sacral holes and sacral canal was the same for both ROI and PQL method. The tractography parameters used to generate the whole pelvic tractogram were the same as the ones used for the ROI method: Seed Threshold (FA): 0.15; Cutoff (FA): 0.01; Angle: 45°; Length: 50 - 800mm. We computed a sacral plexus tractogram with the PQL method using the queries of L5 to S4 roots as detailed in the previous subsection.

Figure 5.46 shows the two versions of sacral plexus tractograms. The qualitative analysis of the ROI based tractogram already showed the presence of some false positives, absent from the one obtained with the PQL method. We must underline that the measures we used for quantitative analysis such as length, volume, angulation, FA and MD, do not allow us to make the difference between false and true positive tracts. So in order to compare both methods only on true positive tracts, we chose to manually edit the ROI based tractogram by removing the obvious false positive tracts; as shown in Figure 5.47. To edit the tractogram, we used the Tractography Display module of 3D Slicer.

As the ROI based tractogram uses seeding points located in the sacral canal, the tractogram obtained is global, gathering right and left sides of the sacral plexus. By contrast, the PQL generates separate left and right tracts for each root. In order to be able to quantitatively compare them, we chose to split in half the ROI based tractogram using a home made tool that uses the left or right sided segmentations of the sacral holes. Regarding the PQL tractogram, we merged all the roots from L5 to S4 from each right and left sides. This process resulted in 4 hemi sacral plexus tractograms for which we were able to compute the measures such as length, volume, angle, FA and MD.

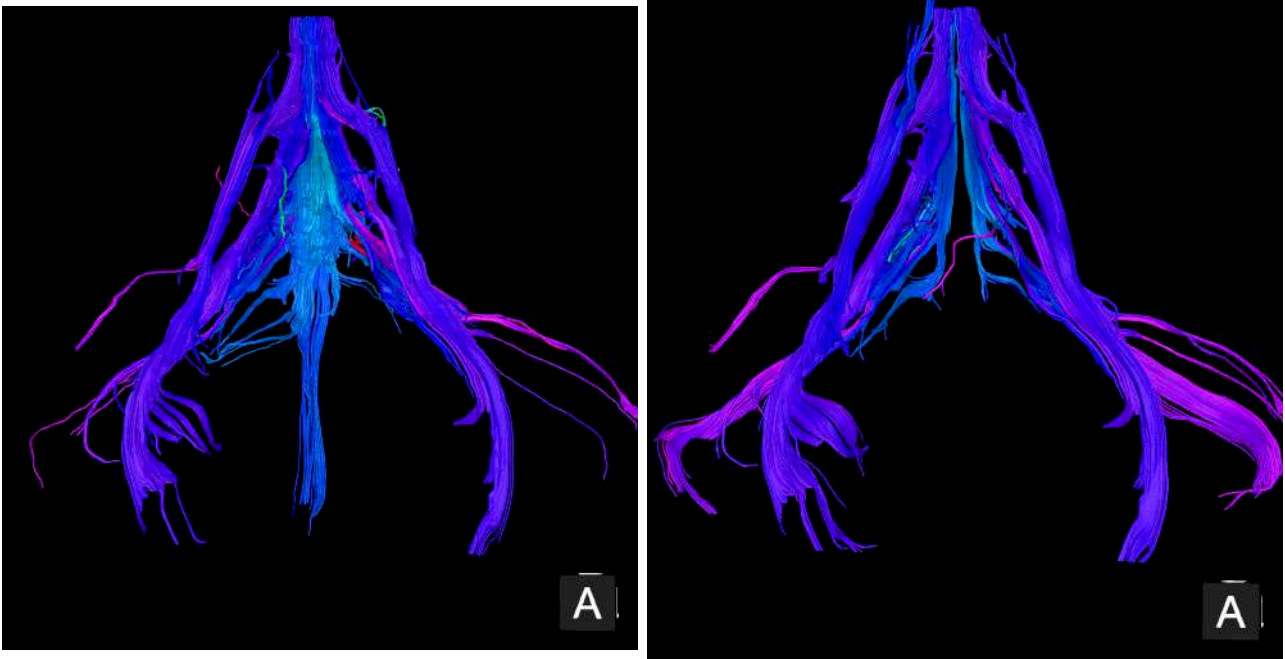


FIGURE 5.46: Sacral plexus tractograms, computed with a ROI based method on the left, and with the PQL method on the right.

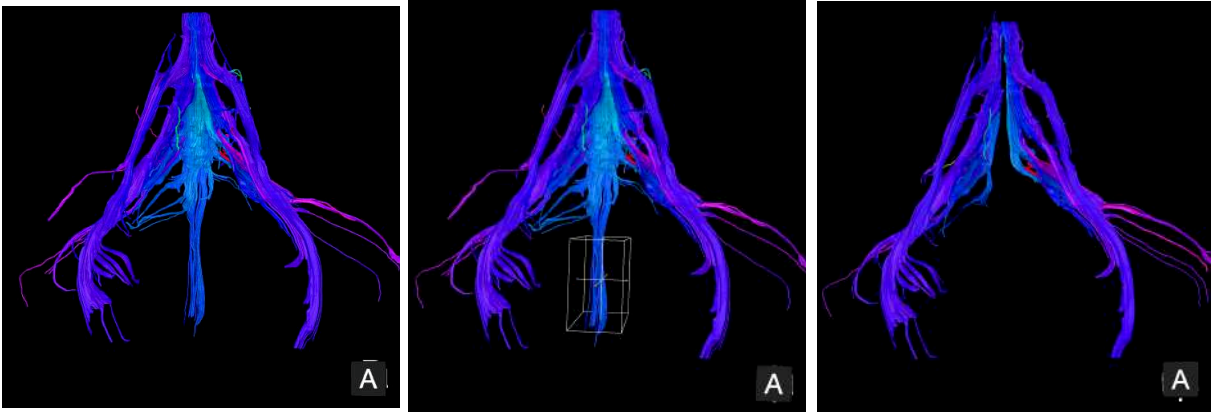


FIGURE 5.47: This figure illustrates the cleaning process of the ROI based tractogram using the Tractography Display module of Slicer 3D. We removed the obvious false positive tracts in the mid line (box in the middle image), resulting from seeding points placed within the sacral canal capturing fibers belonging to the posterior vertebral ligament.

Results

The comparison of the measures between ROI-based and PQL method is presented in Table 5.2.

TABLE 5.2: Comparison of measures between ROI based and PQL method applied on the 2 hemi sacral plexus right and left.

	ROI Right	ROI Left	PQL Right	PQL Left
Volume (in mm ³)	30660	25258	32968	25468
Length (in mm)	162	136	173	157
Mean Turning Angle (in °)	206	205	206	207
Mean FA	0.27	0.23	0.29	0.26
Mean MD	0.61	0.63	0.59	0.60

The qualitative evaluation by visual appraisal and the quantitative analysis using the measures computation lead to the following interpretation:

- Mean FA for both right and left side is higher using PQL method than ROI based. Assuming that the PQL method provide tractograms with more true positive tracts, meaning more fibers located within the same space of the image and having the same direction, a higher mean FA value was expected.
- Mean MD is similar between the two methods. This was also expected, as the additional true positive fibers bear the same diffusion properties, so the Mean MD value should not be impacted.
- Mean turning angle is similar between the two methods, which is understandable, because the global shape of the sacral roots is very similar using the two methods;
- Length is bigger using the PQL method , which means the method was able to select more fibers belonging to the sacral plexus compared to the ROI based method;
- Volume is bigger using the PQL method, which also means that the method was able to select more fibers belonging to the sacral plexus. The overall impression is that the sacral roots were also thicker using PQL, that means more true positive tracts. However, we must note that the result obtained using the PQL method displays more fibers extending till the muscle of the hip, which portion are no longer proper nerve tracts. The reason is that the tractography DTI algorithm is sometimes not able to discriminate the difference between fiber structures at the junction between nerve and muscle, where the FA value gets very similar. This fact may explain the difference in both length and volume between the two methods.

5.6 Conclusion and Discussion

After a preliminary study using methods already employed in the literature on PNN tractography, we identified several points to work on to be able to obtain a more accurate and complete visualization of the PNN anatomy.

We first design our own pre- and post-processing workflow for diffusion images, using both existing and in-house tools, but combining them and tuning their parameters in an optimum fashion for our purpose of PNN tractography. Our work-flow presented the advantage of being performed within the same software environment (3D Slicer) with a user-friendly interface, even using other software, thanks to the design of specific plugins. However, we did not solve all the registration issues, because sometimes the patient presented very distorted images, that we could not overcome even with an elastic transformation. Sequence registration still remains a challenge, that may benefit in the future from deep learning methods in image recognition.

In parallel, we also used a healthy adult female specimen in order to perform some testing on diffusion sequence parameters. The goal was to find the optimal diffusion parameters for PNN tractography, before their application on pediatric patients. We managed to find the optimal trade-off between resolution, number of directions, number of NEX, b value and an acceptable acquisition time for a clinical application. However, given the differences between an adult subject and pediatric patients, in terms of size and possible movement artifacts, we still have to find pediatric candidates to verify our preliminary results on acquisition parameters optimization. For example, we may have to lower the b value (from 1000 to 600) for SNR issues. Particularly, we will have to verify if performing an isotropic acquisition will allow us to better visualize the inferior hypogastric plexus in pediatric patients. But we can already conclude that we will need some improvements from the hardware (MRI machine and coils) in order to be able to track smaller fibers such as the pudendal nerve.

According to the fact that pelvic tractography is a quite new field and our focus being on pediatrics, with a large number of inter-subject variations due to age, rare malformations or huge tumors, a patient specific anatomy aware method seemed to be the more appropriate. We therefore computed a whole pelvis tractogram (in analogy with whole brain tractography) associated with an original segmentation method to identify the tracts of interest: the PQL method. This method based on fuzzy set theory and modeling of spatial relations allowed us for visualizing for the first time to our knowledge both sacral and inferior hypogastric plexuses using tractography. This method proved to be robust, accurate and slightly more efficient than the classical ROI based method. It also allowed for less manual post processing of tractography results, less need for expert knowledge in PNN anatomy, and less variability between operators. However, it stays highly dependent on the quality of manual pelvic organ segmentation which is still quite time consuming and subject to inter-operators variations. Moreover, the design of complex queries may be a difficult task: it requires a lot of iterative testing and a thorough understanding in 3D of the modeling of spatial relations, that are combined in order to select the tracts of interest. This was specifically the case for the tracts segmentation of the inferior hypogastric plexus, which query design was much more complex compared to the sacral plexus. It will surely also require further work for more distal nerves such as the pudendal nerve. We will also need validation studies regarding the numerous open challenges in tractography: no connections, length/size/shape/position bias, and invalid connections. Regarding the bias issue, some bundles are easier/harder to track, optimal tracking parameters vary across the pelvic nervous network, and bigger/longer/straighter bundles have more seeds in them and then may be over-represented. As a first step, the testing of this original PQL method on pediatric patients with ARM will be the subject of the next chapter.

Chapter 6

Exploring the pelvic nervous network using tractography in pediatric patients with ano-rectal malformations

6.1 Introduction

In this chapter, we used the anatomy-aware tractography segmentation method described in Chapter 5 to explore the anatomy of pelvic nerves in a series of 20 patients with ARM, and a group of 20 pediatric patients used as controls. The aim of this chapter is to use tractography to explore the pelvic nervous network anatomy of patients presenting ARMs, and to seek for phenotype differences that might help us to first better understand these malformations and then improve their surgical management.

In Section 6.2, we detail the clinical characteristics of the patients along with the applied imaging protocol, the objective of the study, the choice of the control group, the chosen measures for quantitative tractography analysis and our method to normalize them, and the used statistical tools.

In Section 6.3, we provide the statistical results of the quantitative analysis between the groups of ARM and controls, and between the groups of different types of ARM. We will also provide a qualitative analysis of the results when the low number of patients in each group prevents a reliable statistical analysis.

In Section 6.4, we discuss the results according to DTI tractography bias and summarize the necessary steps to achieve better results, in the various fields of MRI acquisition, pre and post processing methods.

In Section 6.5, we present a case report that illustrates the potential clinical application of pelvic tractography in the scope of image guided surgery. This case report also provides a clinical validation of the tractography results.

6.2 Methods

6.2.1 Population description and imaging protocol of the study

Clinical characteristics

The **clinical characteristics** of the control group and ARM patient group are presented in Tables 6.1 and 6.2, respectively. The age and weight were those at the moment of the pelvic MRI acquisition. Blood volume, L5 vertebra volume and L5 height are clinical and radiological characteristics useful for the normalization of the groups, as explained in Subsection 6.2.3.

We detail here the types of sacral agenesis (SA) and spinal dysraphism (SD):

- Patient 1#4#44 presented a SA below S2 in the context of a high cloacal malformation;
- Patient 1#4#10 presented a non operated filum lipoma in the context of a Pallister Hall syndrome with a low ARM, a vaginal atresia, a Hirschsprung disease, an hypothalamic hamartoma, a choanal atresia and a laryngeal diastema;
- Patient 1#4#20 presented a SA below S2 associated with a short spinal chord (conus medullaris terminating abruptly in L1) in a context of a low ARM;
- Patient 1#4#45 presented a SA below S2 associated with a tethered chord and a secondary syringomyelia, in the context of a very complex caudal pole malformation called a caudal duplication: diphalia, bladder duplication, rectal and colic duplication, thoracic vertebra malformation, and right club foot. These four patients will be compared to the other 16 ARM patients of the group.

Control group

The control group (n=20), that will be used to compare the radiological findings in ARM patients (n=20), was built by gathering patients with either a pelvic tumor or a malformation and included in the IMAG2 study, plus 1 control patient without any pelvic pathology, and presenting usable MRI data. These "control" patients did not *a priori* present any peripheral nervous abnormality due to neither a developmental cause occurring within the pelvic region nor a large tumor with possible deformation of the pelvic nervous network: small-sized ovarian tumor (n=9), vascular malformation (n=3), sacro-coccygeal dimple (n=2), low grade bladder papillary tumor (n=1), buttock lipoma (n=1), rectal duplication (n=1), retro-caval uretere (n=1), hydrosalpinx (n=1). None of the patients in the control group presented a sacral agenesis (SA) or spinal dysraphism (SD). Sixteen patients out of twenty were female.

The ideal situation would have been to use a proper control group with disease-free children but this is hardly achievable in the pediatric field from both ethical and practical points of view. Indeed, the hour spent within the MRI machine must be strongly motivated, taking into account the claustrophobia, the noise (especially in a 3 Teslas machine), the impossibility to move, and the glucagon sub-cutaneous injection.

The median age in months (min-max) of the control group is: 120 (24-192), which is higher than the median age in the ARM group (6 (3-156)), and has to be taken into account during the radiological analysis and the group comparisons. This fact led us to normalize the groups as detailed in Subsection 6.2.3, in order to try to compare controls with younger patients with ARM.

Imaging protocol

All the patients in this study underwent MRI investigation with a volumic sequence for pelvic organ segmentation and a diffusion sequence for tractography. The acquisition parameters were detailed in Chapter 3.

It is important to note that all the subjects underwent the MRI before any pelvic surgery. The other patients included in the database at the time of the MRI and that were already operated, were excluded from this study. The potential differences between the groups should therefore not be related to surgical modifications.

Post-processing

The segmentation was performed entirely manually. The sacral plexus tractograms were generated using the previously described PQL method using the optimum corresponding queries for roots from L5 to S4, as detailed in Chapter 5. Each side (right and left) was computed separately. This qualitative and quantitative study only concerned the sacral plexus tractogram, because the query results for pudendal and inferior hypogastric plexuses were not exploitable. The reasons for that will be discussed in Section 6.4.

TABLE 6.1: Clinical characteristics of the control group. PV malformation = pelvic vascular malformation. VL malformation = veino-lymphatic malformation.

Patient Number	Patient Type	Diagnosis	Age (in years)	Weight (in kg)	Sex	Blood volume (in mm3)	L5 vertebra volume (in mm3)	L5 height (in mm3)
1#2#01	control	ovarian teratoma	14	50	F	3750	36445	25
1#2#02	control	ovarian teratoma	14	45	F	3375	29910	24
1#2#04	control	ovarian teratoma	13	40	F	3000	35636	25
1#2#06	control	ovarian teratoma	15	55	F	4125	32863	23
1#2#12	control	ovarian teratoma	12	30	F	2250	28607	21
1#2#14	control	ovarian teratoma	8	20	F	1600	17283	16
1#2#19	control	ovarian teratoma	14	40	F	3000	31388	21
1#2#28	control	ovarian teratoma	16	50	F	3550	35434	24
1#2#37	control	ovarian teratoma	10	40	F	3000	17688	17
1#5#03	control	none	14	45	F	3375	28064	23
1#2#41	control	left buttock lipoma	3	15	F	1200	9450	13
1#4#28	control	hydrosalpinx	15	75	F	5325	33670	22
1#2#22	control	bladder tumor	5	15	F	1200	13280	16
1#4#01	control	sacro-coccygeal dimple	5	20	F	1600	10954	14
1#4#23	control	sacro-coccygeal dimple	3	15	F	1200	10510	16
1#4#46	control	retro caval uretere	2	13	F	1040	5966	13
1#4#09	control	rectal vascular dysplasia	10	47	M	3525	23589	21
1#4#24	control	rectal duplication	5	13	M	1040	9449	15
1#4#36	control	PV malformation	8	25	M	2000	20755	19
1#2#31	control	VL malformation	13	50	M	3750	31429	20

TABLE 6.2: Clinical characteristics of the ARM patients group. Cloaca is a special type of ARM as explained in Chapter 2.

Patient Number	Patient Type	Diagnosis	Age (in years)	Spinal/sacral status	Weight (in kg)	Sex	Blood volume (in mm3)	L5 vertebra volume (in mm3)	L5 height (in mm)
1#4#03	ARM	Low ARM	0,3	N	6	F	522	3639	10
1#4#04	ARM	Low ARM	0,4	N	10	M	870	3264	10
1#4#05	ARM	Low ARM	1,1	N	7	F	560	5138	12
1#4#10	ARM	Low ARM	2	SD	8	F	640	4313	12
1#4#11	ARM	Low ARM	0,5	N	5	F	430	1759	10
1#4#16	ARM	Low ARM	0,4	N	6	F	522	2172	9
1#4#19	ARM	Low ARM	0,3	N	6,5	M	565	3753	11
1#4#20	ARM	Low ARM	0,6	SA+SD	6,8	M	585	1844	9
1#4#21	ARM	Low ARM	4,1	N	15	F	1200	5798	14
1#4#22	ARM	Low ARM	0,3	N	6	M	522	2551	9
1#4#26	ARM	Low ARM	1,2	N	10	M	800	3496	10
1#4#29	ARM	Low ARM	4,6	N	15	M	1200	9740	15
1#4#34	ARM	Low ARM	13	N	40	F	3000	28003	18
1#4#38	ARM	Low ARM	1,25	N	9	F	720	4589	12
1#4#41	ARM	Low ARM	0,25	N	7,2	M	626	3883	11
1#4#06	ARM	High ARM	0,3	N	8	M	696	2406	8
1#4#27	ARM	High ARM	0,5	N	6	F	516	2731	9
1#4#33	ARM	High ARM	0,4	N	6	M	522	3987	10
1#4#45	ARM	High ARM	0,25	SA+SD	7	M	609	4359	11
1#4#44	ARM	Cloaca	9	SA	22	F	1760	14925	18

6.2.2 Objective of the study

The objective of the study is to explore the pelvic nervous network anatomy of patients with various types of ARM, associated or not with sacral agenesis or spinal dysraphism, compared to children with *a priori* normal pelvic nervous network. This improved knowledge should lead to better understanding, classification and surgical management of these patients. In this scope, we realized group comparisons based on the clinical characteristics of the patients:

The first groups comparison aimed at testing the hypothesis that ARM patients presented with a modified sacral plexus compared to patients without such a specific developmental disease of the caudal pole. In that purpose, we compared the tractography results of the control group (n=20) to the one of the ARM patients without sacral agenesis (SA) or spinal dysraphism (SD) (n=16). Assuming that a sacrum or a spine malformation can severely impair the development of pelvic nerves, we excluded the patients with a major additional malformation of the caudal pole such as SA and/or SD (n=4) from this statistical analysis.

The second groups comparison aimed at testing the hypothesis that SA or SD had an impact on the tractography results of the sacral plexus, within an homogeneous group of patients such as the ARM group. Four of them indeed presented a SA and/or a SD and will be compared to other 16 patients without any SA or SD (n=16).

The third groups comparison aimed at testing the hypothesis that the sacral plexus may present different features according to the level of the malformation, high or low. Indeed, we already know that a high ARM presents a more severe clinical prognosis and often requires a more complex surgical repair than a low form (see Chapter 2). The supplementary evaluation of the pelvic nervous characteristics would be of great help in surgical planning and patient follow up. ARM patients with SA or SD were excluded from this analysis. The group comparison therefore concerned Low ARM (n=14) and high ARM (n=4).

6.2.3 Evaluation measures and normalization for group comparison

Evaluation measures

All the tractograms were qualitatively evaluated by visual appraisal in the 3D Slicer 3D viewer, along with their surrounding bony and muscular structures such as the hip bones and the sacrum. The 3D visualization of the fiber bundles with the other pelvic structures was a key point to tractogram analysis.

We also performed a quantitative analysis of the fiber bundles through the computation of various measures. For each sacral plexus root, the values representing the mean, median and standard deviation were computed, as well as their maximum and minimum boundaries. In the scope of a symmetry study, each side (left and right) of the sacral roots was analyzed separately. To study the characteristics of each sacral root in ARM and control patients, we chose geometric properties such as length, mean turning angle, and volume, in order to appraise their size, global shape, orientation and development. We also computed diffusion properties such as FA and MD, in order to evaluate whether a pelvic malformation such as an ARM may have some consequences on the diffusion properties of the sacral plexus roots.

- **Geometrical Properties**

Length of the fiber bundle: The total length of the fiber (in mm) is computed by summing the lengths of all the streamline segments. The Euclidean distance is used for the length computation.

Mean Turning angle of the fiber bundle: For every triplet of points along the fiber, the local angle was computed in the plane formed by the triplet. The mean of all the angles is then calculated to give the mean turning angle of the fiber bundle. It is expressed in degrees. In order to take into

account the length of the fiber bundle, we then calculated the ratio mean turning angle/length of the fiber bundle, expressed in degrees/mm.

Volume of the fiber bundle: To compute this volume in mm^3 , the tracts must be converted into a volume using the Slicer 3D module Tractography to MaskImage. This module converts Fiber Bundles to Label Map Volumes by filling voxels in the label volume where fiber points are located, an operation called rastering. The volume in mm^3 is then calculated using the 3D Slicer module Label Statistics, which counts the number of voxels of the tracts, multiplied by the voxel size.

- **Diffusion Properties**

Mean FA value of the fiber bundle: this measure is computed by calculating the mean of FA values at all points of the streamline.

Mean MD value of the fiber bundle: this measure is computed by calculating the mean of MD values at all points of the streamline.

Normalization for group comparison

We already mentioned that the median age in months (min-max) between the two groups of controls and MAR patients was very different: 120 (24-192) versus 6 (3-156). In order to be able to perform comparisons of geometrical measures especially between these two groups, we decided to normalize the values by dividing them by the dimensions of another structure, also growing with the age of the child.

To normalize the volume of the tracts, we focused on two measurements: the volume of the L5 vertebra and the blood volume of the child (see values in Tables 6.1 and 6.2).

The volume of L5 vertebra for each patient was calculated by first performing a manual segmentation of the L5 vertebra, which volume was then automatically calculated in mm^3 by the 3D Slicer module Label Statistics as previously described for the calculation of fiber bundles volume. All the values according to age are presented in Figure 6.1. We could see that the L5 vertebra volume progressively increases with age, according to a linear regression line.

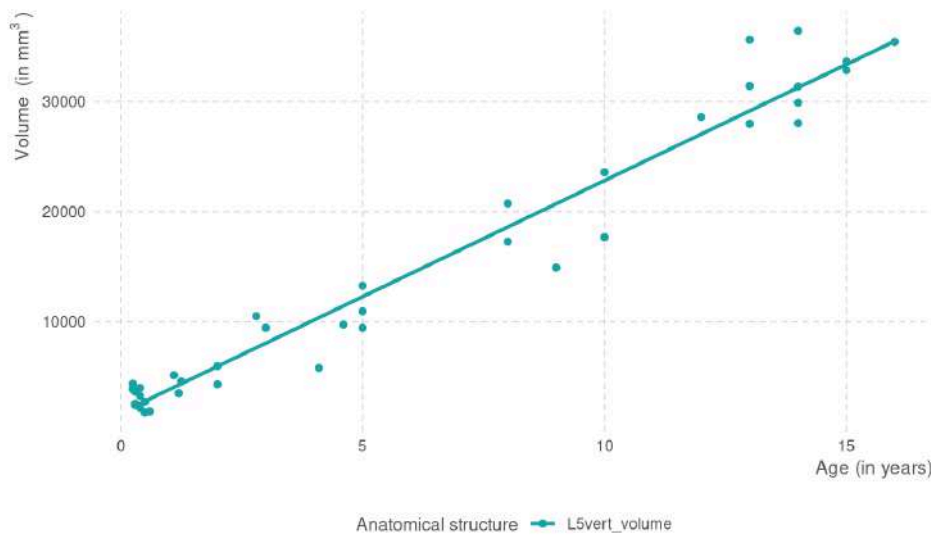


FIGURE 6.1: L5 vertebra volume according to age, computed by manual segmentation.

The blood volume for each child was calculated with the age of the child, his/her weight and standard values of mean blood volume according to age, following pediatric anesthesia guidelines [97], as shown in Figure 6.2. All the values according to age in our study are presented in Figure 6.3, and also follow a progressive increase with age according to a linear regression line.

Age	Mean blood volume per weight (mL/kg)
Newborn, 15-30 minutes of age	78.5
Newborn, 24 hours	83.3
Children, 3 months	87
Children, 6 months	86
Children, 1 year	80
Children, 8 years	80
Children, 10 years	75
Children, 15 years	71
Men	71
Women	70

FIGURE 6.2: Table of mean blood volume per weight (ml/kg) according to age. Blood volume = weight * mean blood volume per weight (mL/kg) [113].

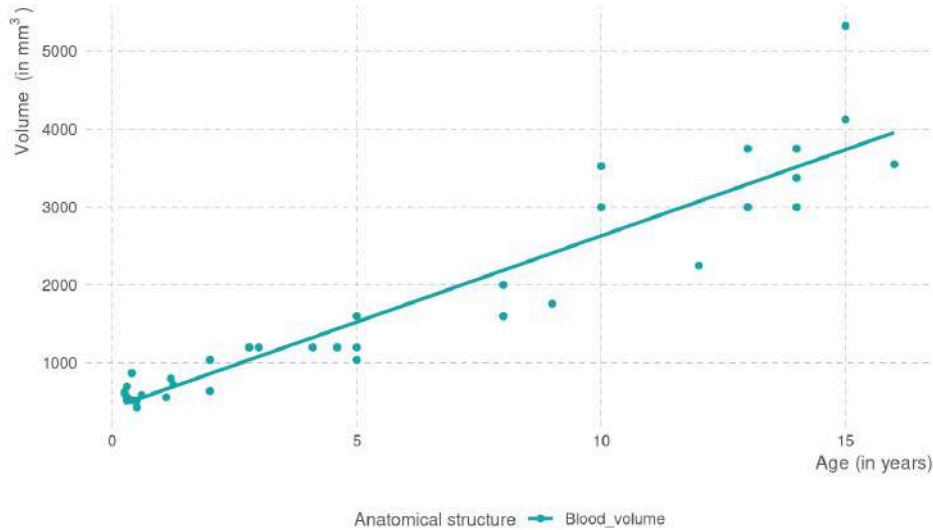


FIGURE 6.3: Blood volume according to age in our study.

The normalized values of sacral roots for each child were finally obtained by dividing their volume by either the L5 vertebra volume or the blood volume of the child.

On order to choose the best option for normalization between L5 vertebra volume and blood volume, we performed a Student test [219], where the t value means the percentage of chance to reject the hypothesis that the value is correlated to age. The dispersion of the values was represented by the residuals (difference observed between the sample and the model):

$$t \text{ value}(L5\text{vertvolume}) = 2.10-16, \text{ residuals: } -2.6; +2.7$$

$$t \text{ value}(\text{bloodvol}) = 2.10-16, \text{ residuals: } -5.5; +3.9$$

We concluded that even if both measurements were good candidates for normalization, the vertebral volume presented less scattered values (residuals) and was therefore chosen for the further statistical analysis.

To normalize the length of the tracts, we divided it by the L5 vertebra height (see values in Tables 6.1 and 6.2). The L5 vertebra height of each child was obtained by manually measuring it on a sagittal view of the volumic sequence as shown in Figure 6.4. Attention was paid to carefully take the measurement in the middle of the vertebra, excluding the disk. All the values according to age in our study are presented in Figure 6.5, following a linear regression line.

To normalize the mean turning angle/length of the tracts, we also used L5 vertebra height values. The mean turning angle value was divided by the normalized length (calculation described in the previous paragraph).

FA and MD are diffusion properties and we did not normalized these values, due to a lack documentation on their normal values within the pediatric population. Their evolution through age is not known for the sacral plexus roots.

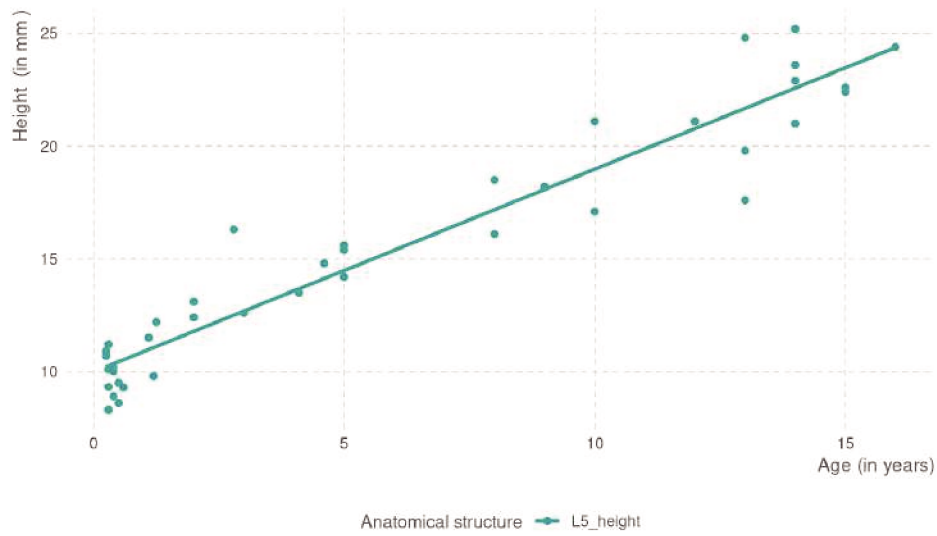


FIGURE 6.4: L5 vertebra height measurement (red line) on a coroT2 sagittal view. In this case, height = 22.5 mm.

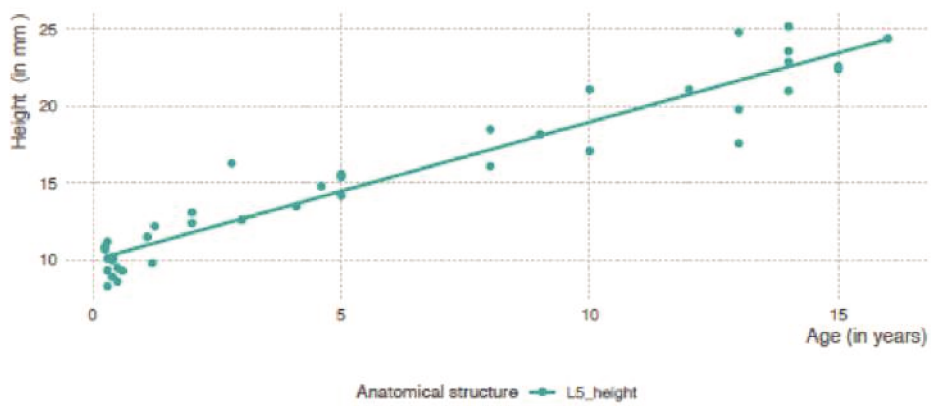


FIGURE 6.5: L5 vertebra height (in mm) according to age in our study.

6.2.4 Statistical tools

The statistical analysis was conducted in collaboration with B. Abt, data scientist and R software [83] specialist. R is a programming language and free software environment for statistical computing and graphics supported by the R Foundation for Statistical Computing.

Within the R environment, we performed a bio statistical test called the Wilcoxon test in order to compare median values of the chosen measures between the different groups of ARM and control patients. The Wilcoxon test is a non-parametric statistical hypothesis test used to compare two related samples, matched samples, or repeated measurements on a single sample to assess whether their population median ranks differ. It can be used as an alternative to the paired Student's t-test when the sample size is small and the population cannot be assumed to be normally distributed, which was the case in our population study.

6.3 Results

Visual examples of patient-specific 3D models including PNN tractography of control and ARM patients are displayed in Appendix.

6.3.1 Global description

Roots volume

As a first step to describe the pelvic nervous anatomy of our population, we present in Figures 6.6, 6.7, and 6.8 the evolution of the volume of each sacral plexus root from L5 to S4 according to age in 40 patients. We can see that the volume increases with age as expected, in a linear fashion for both right and left sides. It appears that the dispersion of values is more important for small children than for older children. This analysis must however take into account that most of the small children are ARM patients, and most of older children are control patients, and that these discrepancies may be due to the presence of a pelvic malformation. The results regarding the S4 root must be taken with caution, because it is a very small, thin root, with a low FA value, which is very difficult to find using tractography: the amount of values obtained for this root is greatly inferior to those obtained for the other roots.

However, when analyzing the volume only in the control group patient, we noticed that the regression linear line was nearly flat for all sacral plexus roots, after the age of 5 (see Figures 6.9, 6.10, and 6.11). This means that after this age, and till the age of 15 in our study, the roots seem to stop growing. This fact has implications for our normalization method which will be discussed with the results of the normalized volumes.

As a second step, we present in Figures 6.12, 6.13 and 6.14 the evolution of the normalized volume of the sacral plexus roots using the L5 vertebral volume, according to age, in 40 patients. The choice of the L5 vertebral volume to normalize the volume of the roots has been explained earlier in the methods section. We must note that we obtained a descending straight linear regression, instead of a flat one. This means that the L5 vertebra is a structure that grows and gain volume more faster with age compared to the sacral roots. Indeed, we know that the vertebra grows progressively from birth till the puberty. However, this does not seem to be the case for sacral plexus roots, which growth appears to be minimal after the age 5. This must be taken into account while interpreting the statistical results using normalized volumes.

We also noticed that the volume values are less scattered after the age of 5 years old. This fact could be explained by different reasons: the inter-individual variability may be bigger before this age, with a relative harmonization of the tracts volume with the growth. We could also imagine that the children are born with different amounts of nerve fibers, which are progressively reorganized with the growth of the child. Some of them may continue their development and growth, some others may regress in number and/or volume. It could also be explained by a better performance of the tractography to discern those peripheral nerves after the age of 5 years old. Another explanation could be the fact that after the age of 5, sacral plexus roots have gained a certain level of maturity, stop growing, and show diffusion properties that make them more discernible using tractography. This hypothesis may be concordant with our clinical knowledge of the establishment of the pelvic continence that occurs mainly between 2 and maximum 5 years of age.

Within the ARM group, we explored an eventual correlation between birth weight and sacral plexus roots volume. We did not find any correlation. This may be because all the MRIs were performed after the age of 3 months in our study, when most of the children have reached a weight closer to the mean according to that age. It is well known that most of the children presenting a low birth weight will catch up within a few months.

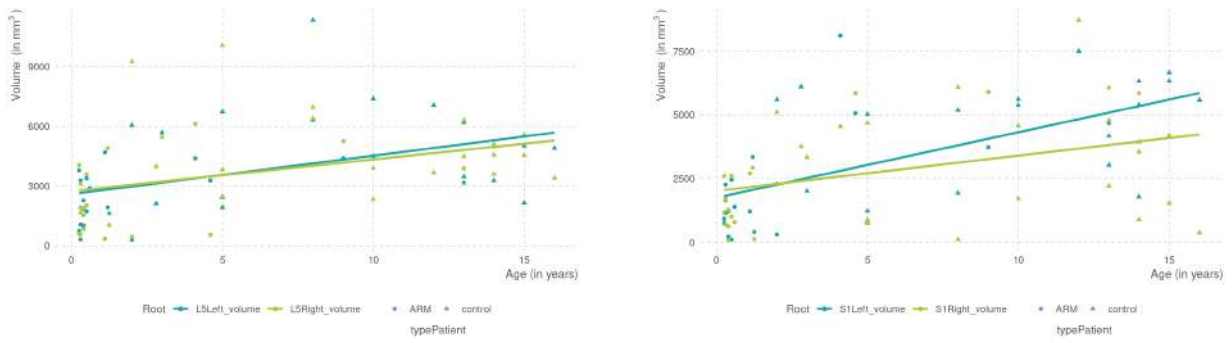


FIGURE 6.6: Volume evolution of roots L5 (left) and S1 (right) according to age in 40 patients.

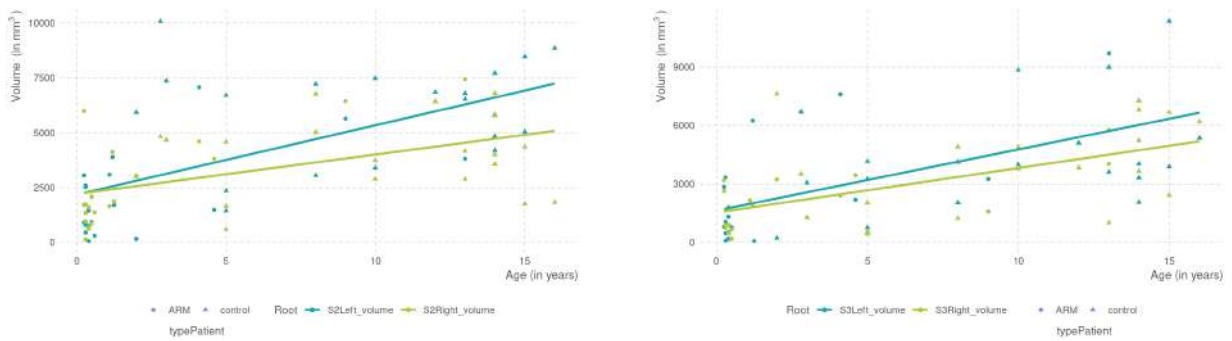


FIGURE 6.7: Volume evolution of roots S2 (left) and S3 (right) according to age in 40 patients.

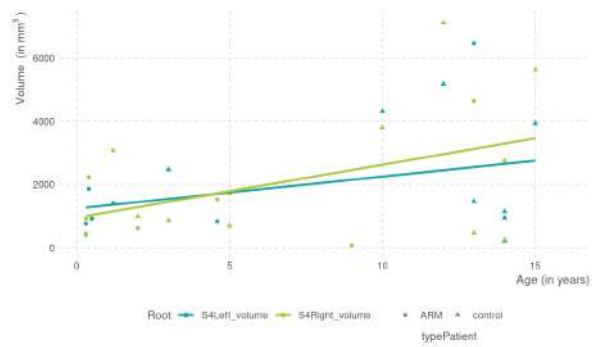


FIGURE 6.8: Volume evolution of root S4 according to age in 40 patients.

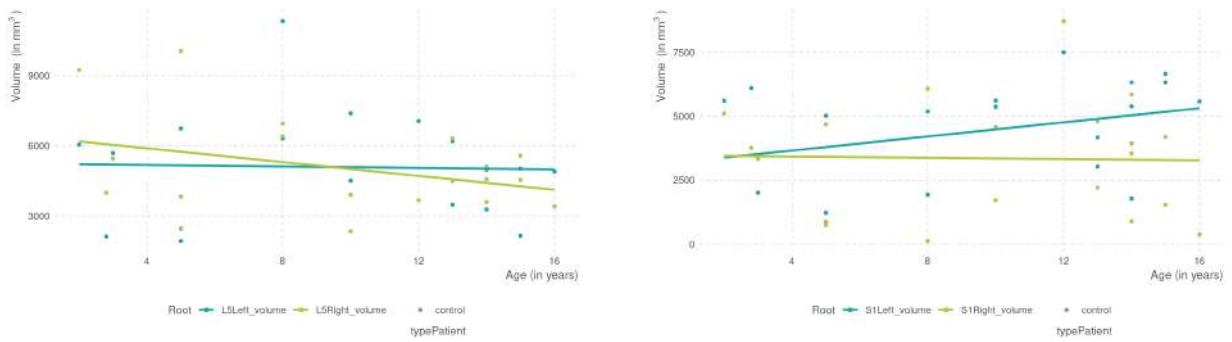


FIGURE 6.9: Volume evolution of roots L5 (left) and S1 (right) according to age in controls.

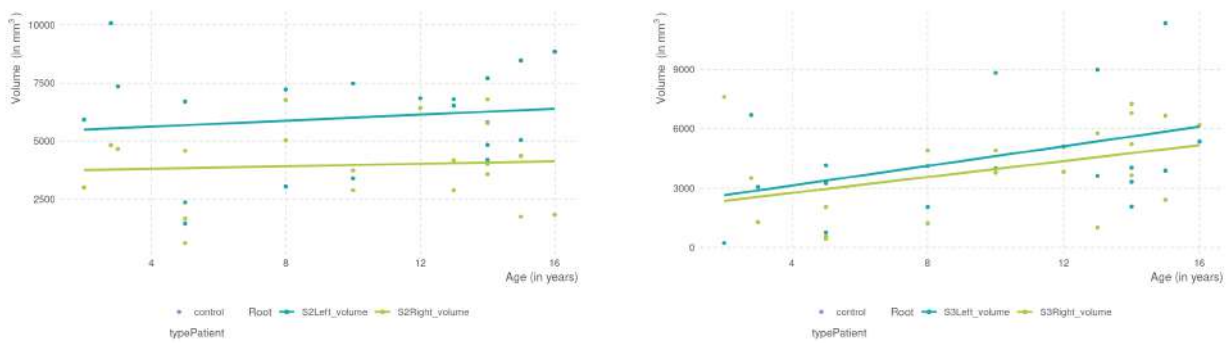


FIGURE 6.10: Volume evolution of roots S2 (left) and S3 (right) according to age in controls.

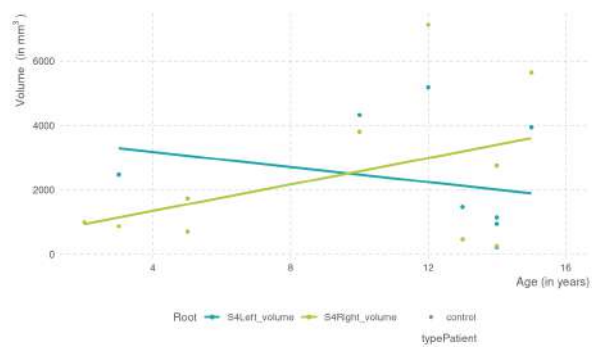


FIGURE 6.11: Volume evolution of root S4 according to age in controls.

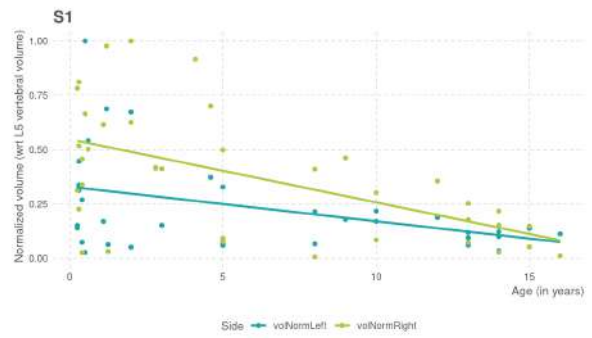
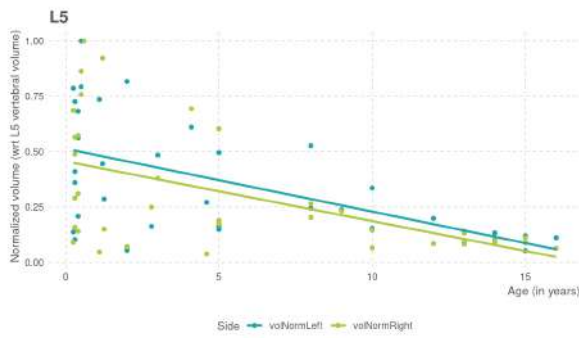


FIGURE 6.12: Normalized volume evolution of roots L5 (left) and S1 (right) according to age in 40 patients, using the L5 vertebral volume.

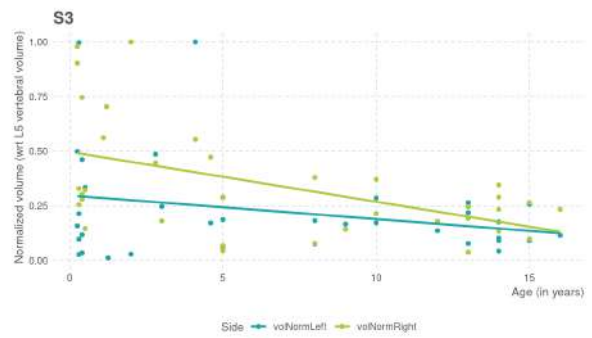
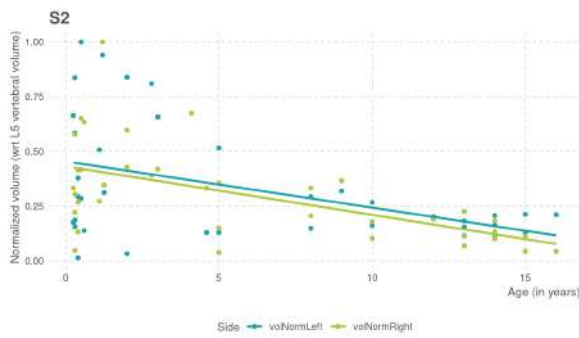


FIGURE 6.13: Normalized volume evolution of roots S2 (left) and S3 (right) according to age in 40 patients, using the L5 vertebral volume.

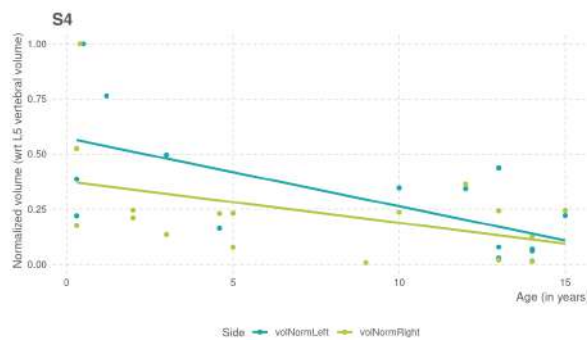


FIGURE 6.14: Normalized volume evolution of root S4 according to age in 40 patients, using the L5 vertebral volume.

Functional measures: FA and MD

We present in Figures 6.15, 6.16, 6.17, 6.18, 6.19, and 6.20 the evolution of the mean FA and MD values of each sacral plexus root according to age and side in 40 patients. The mean FA value in all roots seems to decrease with age, even after the age of 5, while the MD value appears to stay relatively stable with age. To our knowledge, this fact has not been described yet in the literature about tractography of peripheral nerves.

No significant differences were noted between left and right sides. We may conclude that even in cases of volume/length/shape differences between right and left, the diffusion properties stay similar on the two sides.

Regarding the FA values, we also noted that the values are more scattered in small children, likewise in the volume analysis. This may be linked to either less reliability of the tractography in these ages, to an inherent variability of the pelvic nerves diffusion properties before the age of 5, or linked with the ARM pathology. We must however underline that a similar pattern was not found about the MD values: the scattering was similar for all ages. If the pelvic malformation does impact the diffusion properties of the pelvic nerves, it appears to mostly concern their directional character and not their packing density.



FIGURE 6.15: Mean FA value evolution of roots L5 (left) and S1 (right) according to age in 40 patients.



FIGURE 6.16: Mean FA value evolution of roots S2 (left) and S3 (right) according to age in 40 patients.

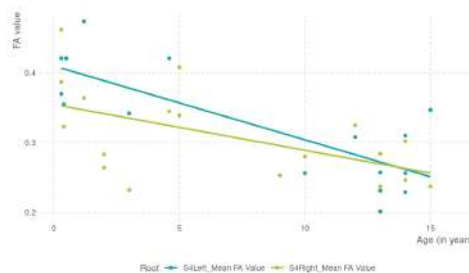


FIGURE 6.17: Mean FA value evolution of root S4 according to age in 40 patients.

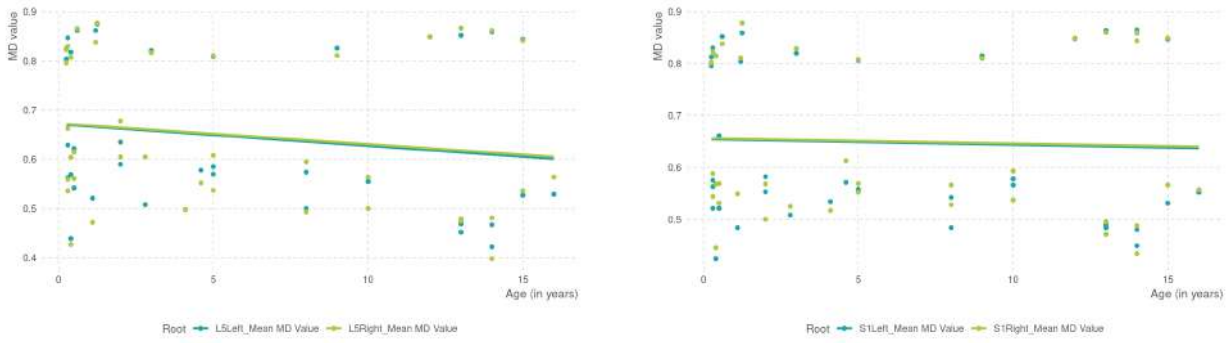


FIGURE 6.18: Mean MD value evolution of roots L5 (left) and S1 (right) according to age in 40 patients.

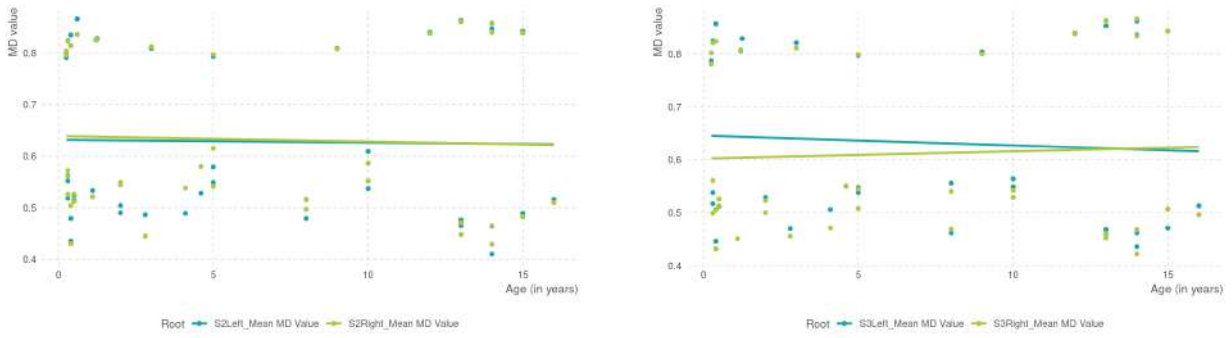


FIGURE 6.19: Mean MD value evolution of roots S2 (left) and S3 (right) according to age in 40 patients.

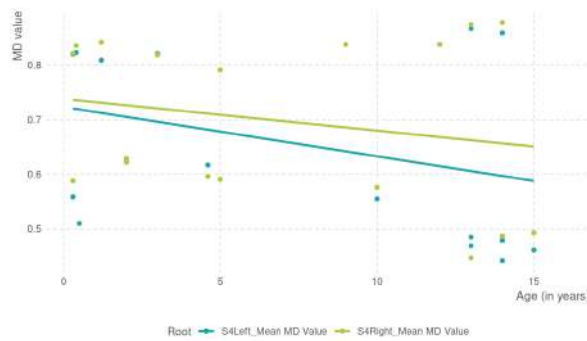


FIGURE 6.20: Mean MD value evolution of root S4 according to age in 40 patients.

6.3.2 Symmetry study

We chose to compute the right and left sacral plexus roots tractograms separately in order to be able to explore a potential of one side in the whole series of patients or in a specific group such as the ARM group. Figures 6.21, 6.22, 6.23 show the difference between right and left volume of the roots and its scattering around 0 in all patients and also in control and ARM groups (see Figures 6.24, 6.25, 6.26 and 6.27, 6.28, 6.29).

We then performed a comparison test using a paired Wilcoxon test in order to determine whether the scattering of the values between right and left sides was different in the whole series of patients, and also in both groups of control and ARM Patients, as seen in Table 6.3. None of the p values reach the statistical threshold of 0.05, and a lot of them are near 1. This means that in neither of the groups, we found a significant right-left asymmetry.

When looking at the raw data, we however noticed that half of the patients are symmetric, 25 percent show a prominent left side, and 25 percent a prominent right side. The settling of right left symmetry of the body does not rely on the same molecular mechanisms as the brain, and therefore the hand dominance, according to the literature [120]. Indeed, in the population, only 10 percent of the people are left handed. Our results are also concordant with the findings of Levin et al [120] regarding the organs that show a macroscopic symmetry such as the sacral plexus. A slight asymmetry may however be present, and is randomly scattered among individuals. The molecular determinants of this slight asymmetry have not been discovered yet.

However, the p values in the ARM group are clearly inferior and closer to the statistical threshold compared to those of the control group or the overall population of the study. This means that the existing slight asymmetry in ARM patients, even if not statistically significant, may show a tendency of a more prominent right size for all the sacral plexus roots, when looking at the scattering of the values on the histograms (see Figures 6.27, 6.28 and 6.29). This nervous phenotype in ARM patients has never been stated before to our knowledge. The hypothesis would be that the molecular determinants of ARM may also be involved in the setting of the slight right-left asymmetry of macroscopic symmetric organs, such as the sacral plexus.

	40 patients	Controls n=20	ARM n=20
L5	0.5	0.5	0.4
S1	0.8	0.9	0.1
S2	0.9	0.9	0.1
S3	0.9	0.8	0.7
S4	0.3	0.3	0.4

TABLE 6.3: P values of paired Wilcoxon tests performed for each sacral plexus roots in 40 patients, and in both groups of controls and ARM patients.

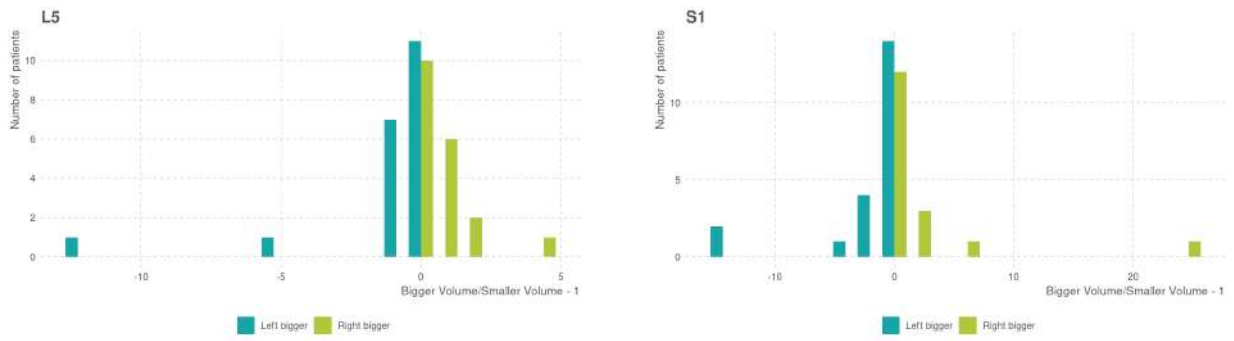


FIGURE 6.21: Normalized left-right prominence and scattering around 0 in all patients, for L5 and S1 roots.

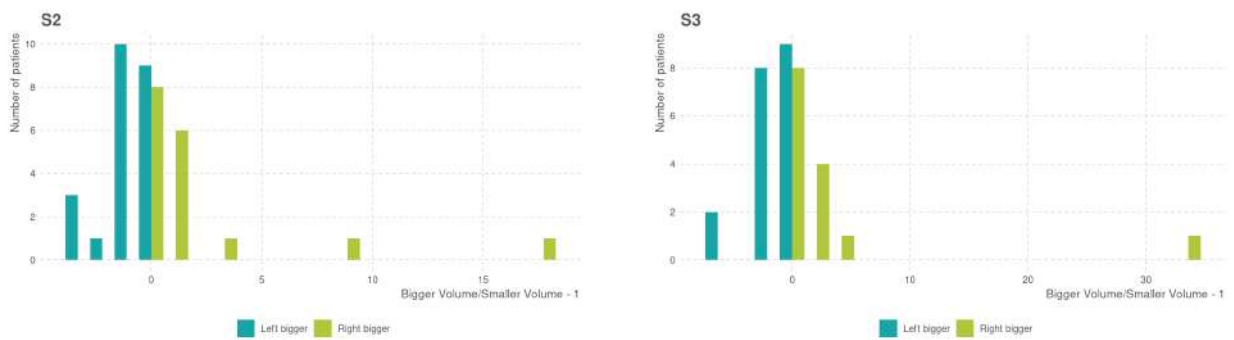


FIGURE 6.22: Normalized left-right prominence and scattering around 0 in all patients, for S2 and S3 roots.

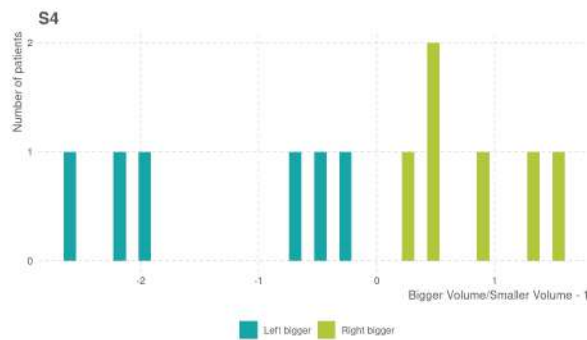


FIGURE 6.23: Normalized left-right prominence and scattering around 0 in all patients, for S4 root.

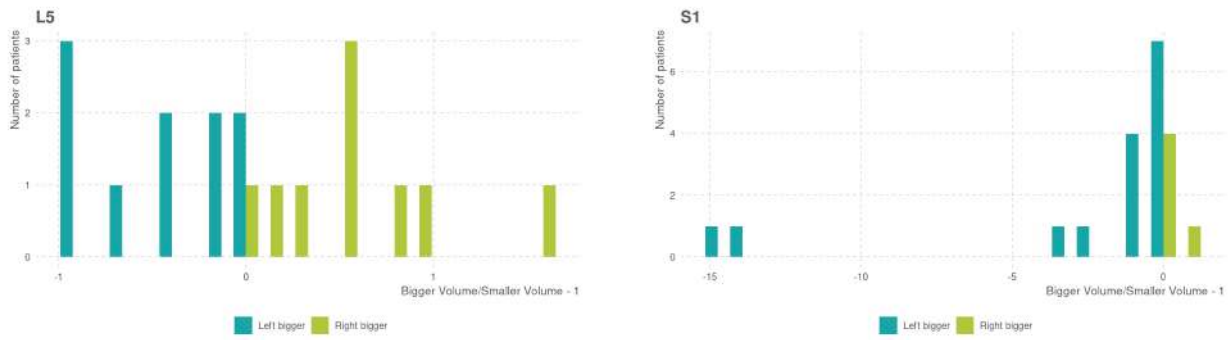


FIGURE 6.24: Normalized left-right prominence and scattering around 0 in the control group, for L5 and S1 roots.

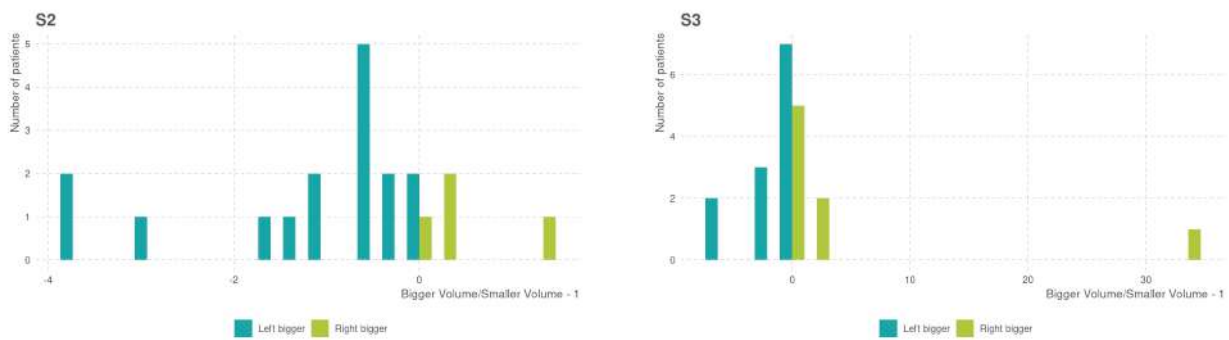


FIGURE 6.25: Normalized left-right prominence and scattering around 0 in the control group, for S2 and S3 roots.

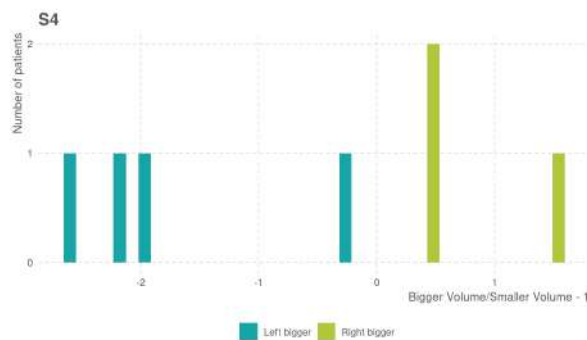


FIGURE 6.26: Normalized left-right prominence and scattering around 0 in the control group, for S4 root.

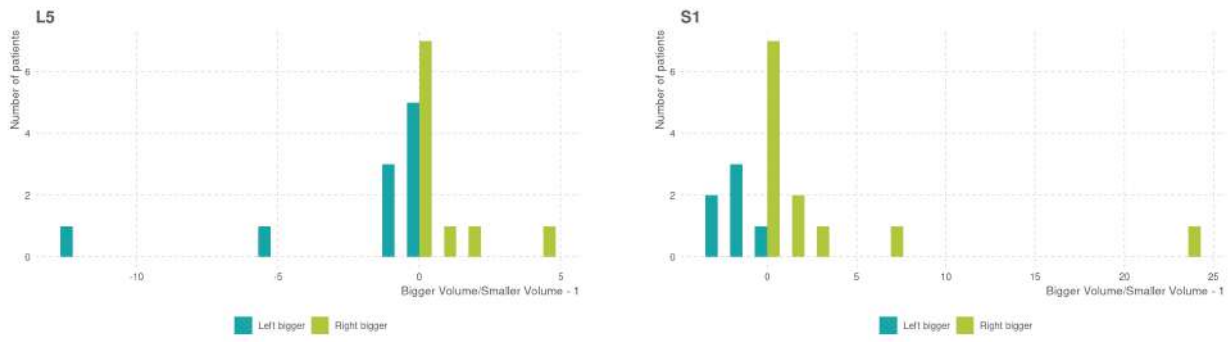


FIGURE 6.27: Normalized left-right prominence and scattering around 0 in the ARM group, for L5 and S1 roots.

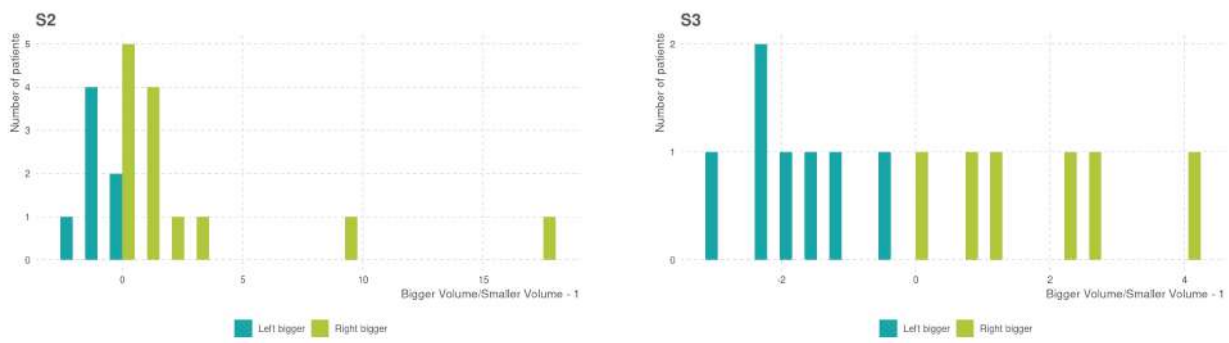


FIGURE 6.28: Normalized left-right prominence and scattering around 0 in the ARM group, for S2 and S3 roots.

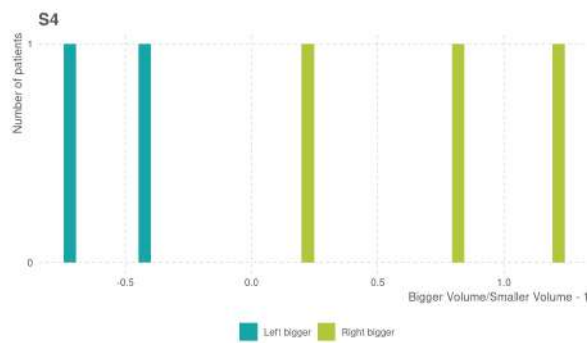


FIGURE 6.29: Normalized left-right prominence and scattering around 0 in the ARM group, for S4 root.

6.3.3 ARM vs control

As detailed in Section 6.2, the aim of this study was to compare the sacral plexus roots characteristics in MAR patients without SA or SD (n=16) versus the control group (n=20).

- Table 6.4 presents the comparison regarding the median volume in both groups for each root. As detailed in Section 6.2, the volume was normalized by the corresponding L5 vertebral volume for each patient. The results were statistically significant for roots L5 to S3. S4 root values were probably too few to allow for a reliable statistical analysis. The normalized volume in ARM patients appears to be higher than in the control group. Given the limits of the normalization process as detailed in Section 6.2, it is difficult to conclude. Indeed, the growth of L5 vertebra opposed to a steady volume of sacral plexus nerve may overestimate the difference between the groups, and be the reason why ARM patients seem to have larger nerves than controls. The scattering of the measures values is represented Figures 9.1, 9.2, 9.3, 9.4 and 9.5 in Appendix.

Roots	Median normalized volume		
	ARM (std)	Control (std)	p value
L5	1.07 (0.7)	0.37 (0.6)	0.003
S1	0.87 (0.6)	0.31 (0.4)	0.001
S2	0.92 (0.7)	0.37 (0.4)	0.01
S3	0.57 (0.6)	0.40 (0.2)	0.01
S4	0.39 (0.5)	0.28 (0.1)	0.14

TABLE 6.4: Wilcoxon’s test for comparison between ARM and control patients of the median normalized volume of sacral plexus roots. The p values in red are statistically significant. Std = standard deviation.

- Table 6.5 presents the comparison regarding the median length in both groups for each root. As detailed in Section 6.2, the length was normalized by the corresponding L5 height for each patient. The results were statistically significant for roots L5 to S3. S4 root values were probably too few to allow for a reliable statistical analysis. The normalized length in ARM patients appears to be higher than in the control group. Given the limits of the normalization process as detailed in Section 6.2, it is difficult to conclude, for the same reasons as for the volume analysis.

Roots	Median normalized length		
	ARM (std)	Control (std)	p value
L5 Left	7.5 (1.8)	4.26 (1.8)	7.10-5
L5 Right	6.7 (1.8)	4.4 (2.1)	0.001
S1 Left	7.6 (1.5)	5.5 (1.9)	4.10-5
S1 Right	7.8 (2.1)	5.1 (1.6)	4.10-5
S2 Left	7.9 (2.1)	4.6 (2.1)	0.0004
S2 Right	7.3 (2.5)	3.8 (1.5)	2.10-6
S3 Left	7.9 (1.8)	4.9 (1.6)	7.10-5
S3 Right	7.8 (1.5)	3.8 (2.1)	4.10-5
S4 Left	6.6 (1.2)	3.8 (1.7)	0,005
S4 Right	7.4 (3.2)	5.5 (2.6)	0.07

TABLE 6.5: Wilcoxon’s test for comparison between ARM and control patients of the median normalized length of sacral plexus roots. The p values in red are statistically significant. Std = standard deviation.

- Table 6.6 presents the comparison regarding the ratio median angulation/normalized length in both groups for each root. The results were statistically significant for roots L5 to S3. S4 roots values were probably too few to allow for a reliable statistical analysis. The normalized length in ARM patients appears to be higher than in the control group. Given the limits of the normalization process as detailed in Section 6.2, it is difficult to conclude.

Roots	Median angulation/normalized length		
	ARM (std)	Control (std)	p value
L5 Left	29 (7)	48 (16)	0.0001
L5 Right	32 (10)	45 (13)	0.009
S1 Left	26 (5)	36 (14)	0.0008
S1 Right	27 (7)	39 (15)	0.0002
S2 Left	27 (5)	44 (12)	0.001
S2 Right	30 (8)	53 (17)	1.10-5
S3 Left	28 (5)	44 (13)	9.10-6
S3 Right	28 (5)	54 (16)	3.10-6
S4 Left	33 (6)	53 (13)	0,005
S4 Right	26 (10)	39 (18)	0.1

TABLE 6.6: Wilcoxon’s test for comparison between ARM and control patients of the median angulation/normalized length of sacral plexus roots. The p values in red are statistically significant. Std = standard deviation.

- Table 6.7 presents the comparison regarding the median FA value in both groups for each root. A statistical difference was reached for S2, S3 and S4 roots. As we noticed earlier, the FA value seems to decrease with age, and MAR patients are younger, so this difference appears to be the consequence of the difference of median age of the groups.

Roots	Median FA value		
	ARM (std)	Control (std)	p value
L5	0.35 (0.06)	0.36 (0.06)	0.3
S1	0.39 (0.07)	0.36 (0.05)	0.07
S2	0.41 (0.07)	0.34 (0.05)	2.10-5
S3	0.44 (0.09)	0.28 (0.06)	5.10-6
S4	0.37 (0.07)	0.28 (0.05)	0,001

TABLE 6.7: Wilcoxon’s test for comparison between ARM and control patients of the median FA value of sacral plexus roots. The p values in red are statistically significant. Std = standard deviation.

- Table 6.8 presents the comparison regarding the median MD value in both groups for each root. No statistical difference was found. As MD does not appear to change during infancy, we may conclude that MAR patients do not present any difference in the density of their pelvic nerves.

Roots	Median MD value		
	ARM (std)	Control (std)	p value
L5	0.66 (0.15)	0.56 (0.14)	0.1
S1	0.58 (0.15)	0.56 (0.14)	0.3
S2	0.55 (0.15)	0.53 (0.15)	0.2
S3	0.55 (0.16)	0.53 (0.15)	0.4
S4	0.82 (0.13)	0.57 (0.16)	0.06

TABLE 6.8: Wilcoxon’s test for comparison between ARM and control patients of the median MD value of sacral plexus roots. Std = standard deviation.

6.3.4 ARM with SA or SD vs ARM without SA or SD

As detailed in Section 6.2, we aimed in this study at exploring the consequences of the presence of a SA or a SD on the characteristics of the sacral plexus roots. We therefore compared 16 patients with ARM with normal spine and sacrum (median age 5.4 months) and 4 patients with ARM associated with an abnormal spine (SD) and/or sacrum (SA) (median age 15.6 months). Giving the small amount of patients especially in the latter group, we did not performed the same Wilcoxon test as in Subsection 6.3.3. Figures 6.30, 6.31, 6.32, 6.33 and 6.34 present the scattering of the values for all the patients of the two groups. The observation of the box plots led to the following remarks:

It seems like MAR patients with normal spine and sacrum present bigger and longer sacral roots, which is coherent with the hypothesis that an abnormal spine leads to underdeveloped sacral plexus roots.

The presence of a dysraphism also seems to influence the median angulation of the roots: ARM patients with SA or SD present a wider angle of curvature of the sacral roots. The interpretation may be that the spine or sacral malformation induces an abnormal development of the roots that results in wider angulation. As a consequence, their termination may also be impaired, and therefore their functionality, which could explain the worse prognosis of an ARM patient with a SA or a SD.

Regarding the diffusion properties, ARM patients with SA or SD seem to present higher values of both FA and MD. We must underline that there was an heterogeneity within the type of abnormal spine and/or sacrum of the 4 patients, which may probably lead to differences in diffusion properties, that are not clearly identifiable because of the small number of patients.

We also noted that S4 root has been rarely found in patients with SA or SD. This root being the most distal and the finest one, this is understandable from an anatomical point of view. A caudal pole anomaly may impact more distal and thin structures than the proximal ones such as L5 root. This is also consistent with the clinical outcome of these ARM patients, that is known to be worse in the presence of SA or SD. Indeed, S4 root is a contributor to the pudendal plexus that handles both digestive and urinary continence. We must also note that when the S4 root was found, it was always the right one, which is consistent with the previous findings about the prominence of the right side of sacral plexus roots in ARM patients.

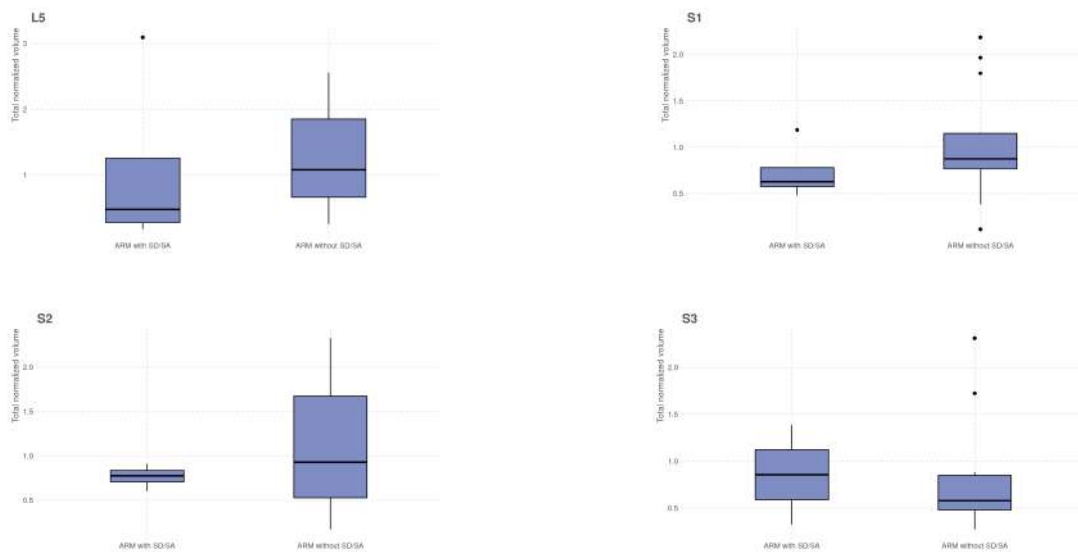


FIGURE 6.30: Scattering of total normalized volume values of sacral plexus roots in ARM patients with and without SA or SD.

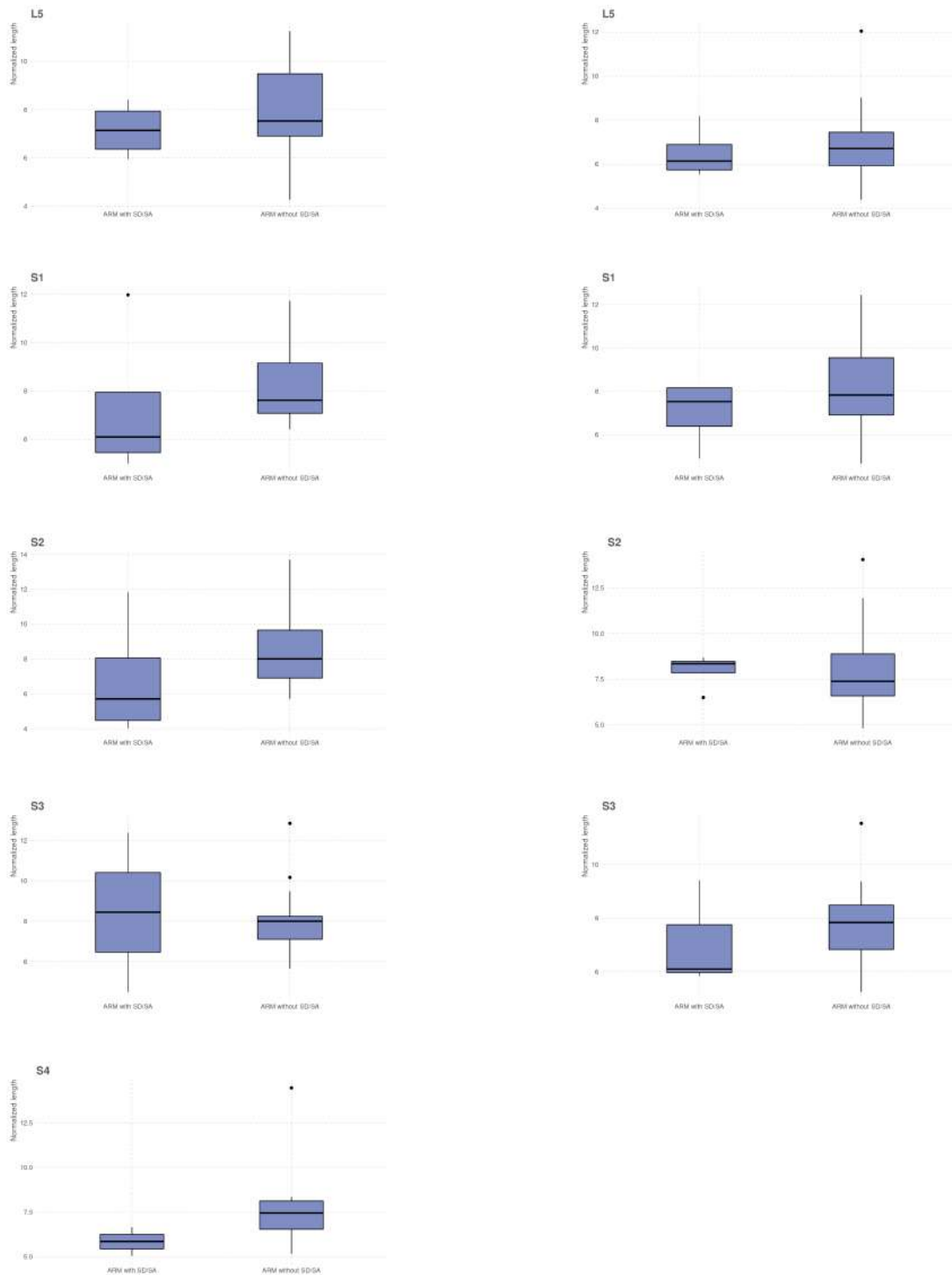


FIGURE 6.31: Scattering of normalized length values of sacral plexus roots in ARM patients with and without SA or SD. On the left are represented the left roots, on the right, the right roots.

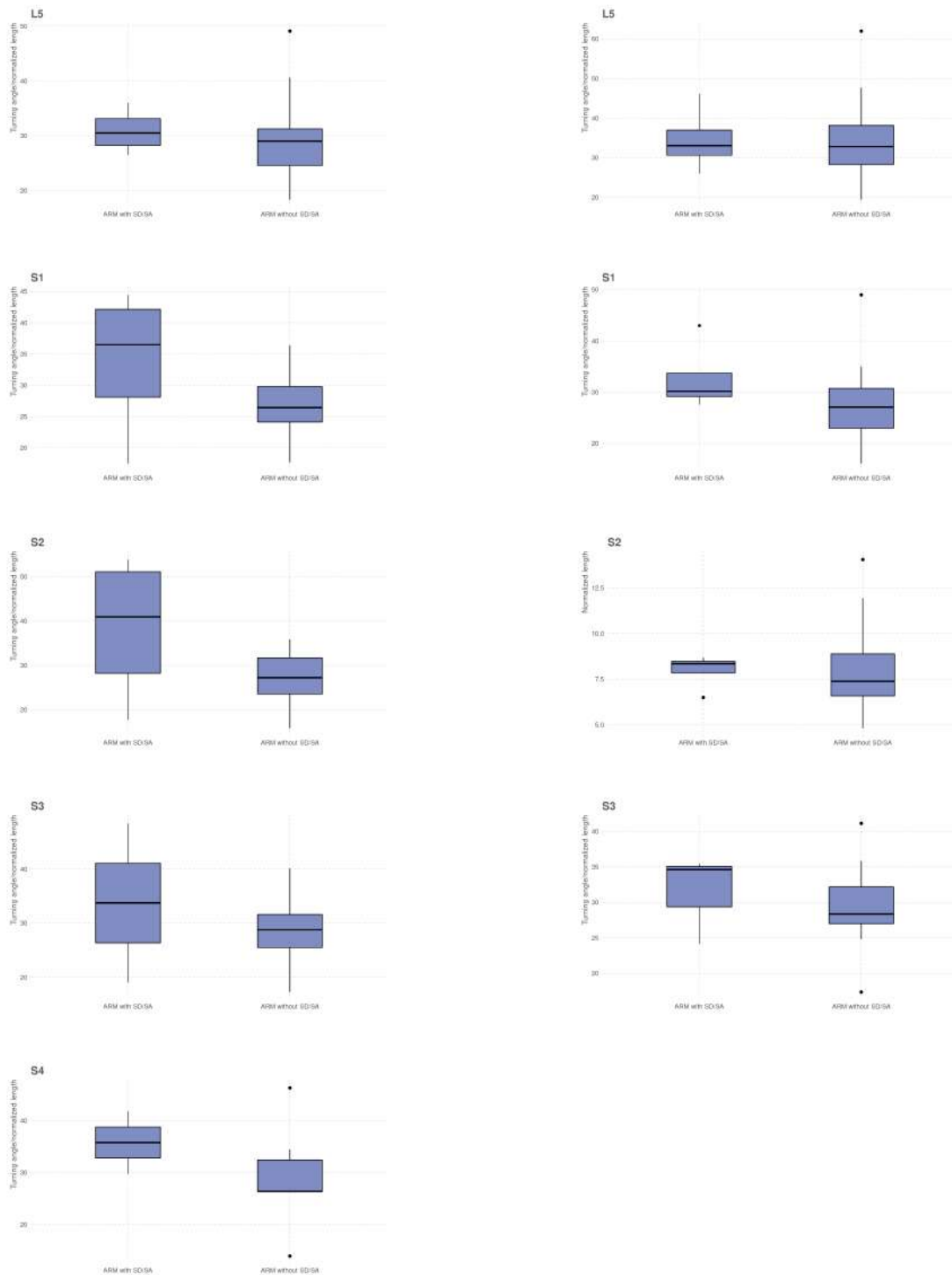


FIGURE 6.32: Scattering of angle/normalized length values of sacral plexus roots in ARM patients with and without SA or SD. On the left are represented the left roots, on the right, the right roots.

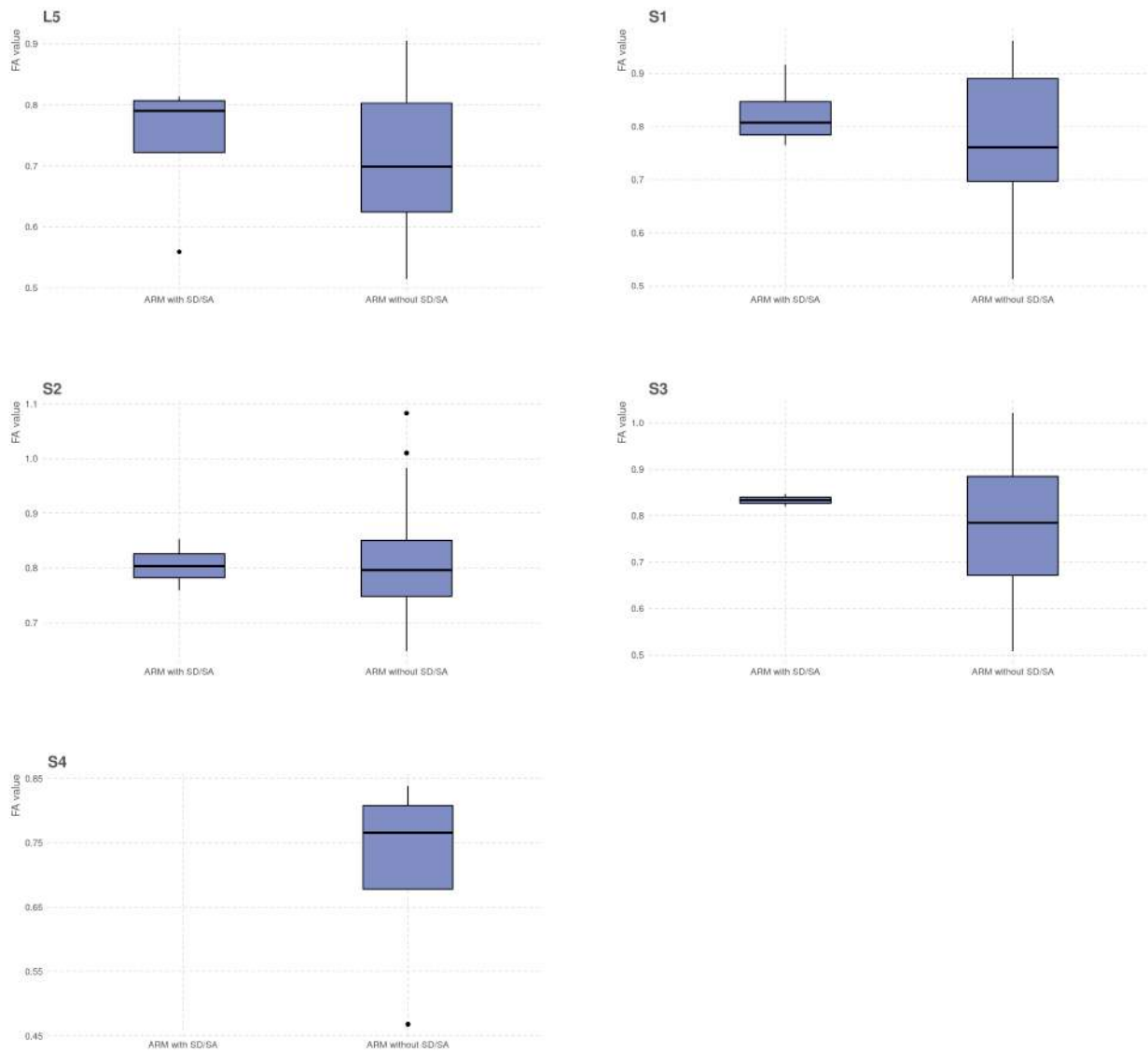


FIGURE 6.33: Scattering of mean FA values of sacral plexus roots in ARM patients with and without SA or SD.

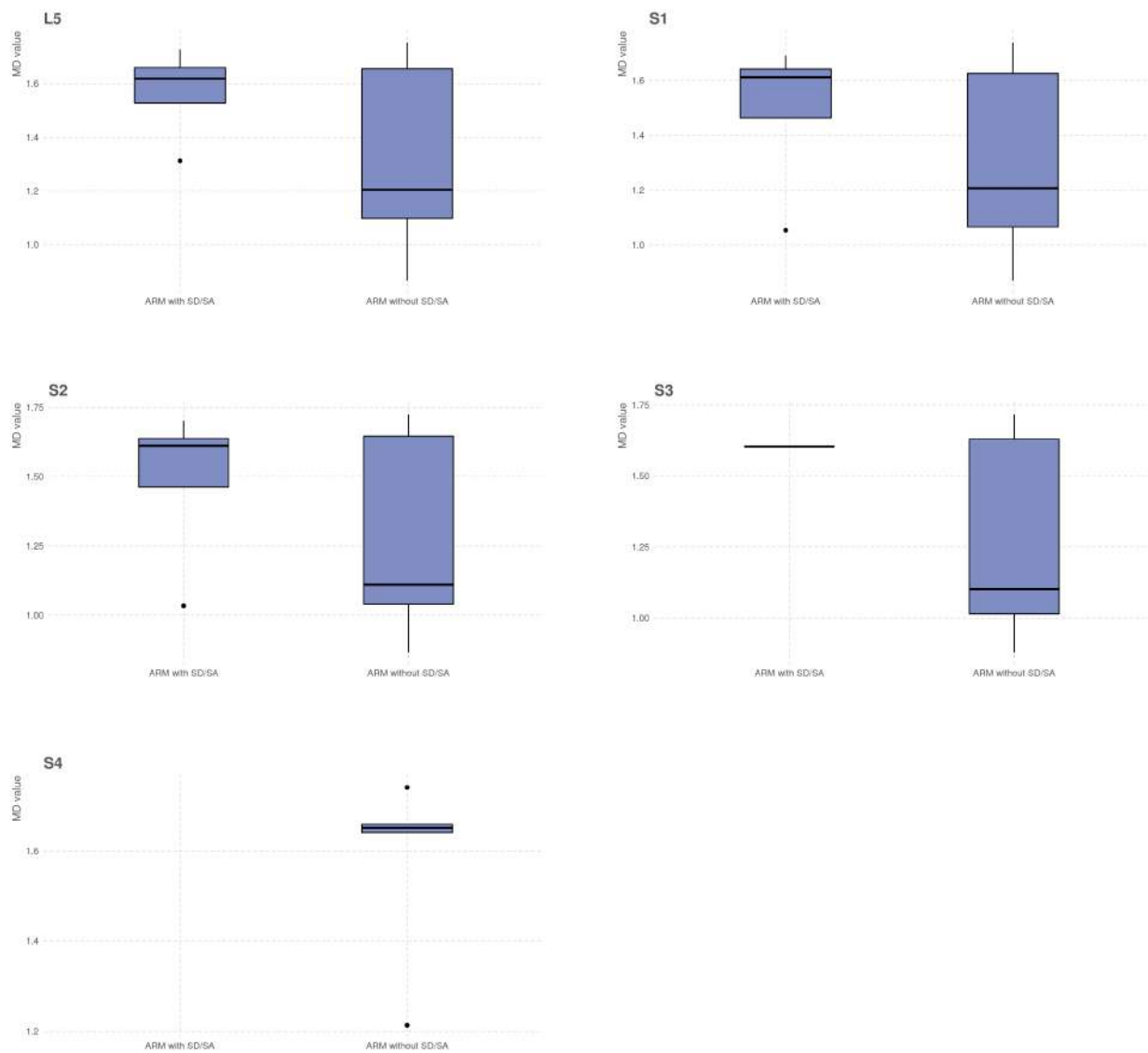


FIGURE 6.34: Scattering of mean MD values of sacral plexus roots in ARM patients with and without SA or SD.

6.3.5 Low ARM vs High ARM

As detailed in Section 6.2, we aimed in this study at enhancing the knowledge of the nervous phenotype of ARM patients, regarding the level of the malformation. We therefore compared 13 low ARM patients (median age: 6 months) with 3 high ARM patients (median age: 4.8 months). All 16 patients were free from SA or SD. Giving the small amount of patients especially in the latter group, we did not performed the same Wilcoxon test as in Subsection 6.3.3. Figures 6.35, 6.36, 6.37, 6.38 and 6.39 present the scattering of the values for all the patients of the two groups. The observation of the box plots led to the following remarks:

Low ARM patients present bigger and longer sacral roots, but no difference in FA and MD values, compared to high ARM patients. These findings are consistent with our knowledge of high ARM patients presenting a worse outcome in terms of continence. S4 roots was less often tracked in high ARM patients. Based on the same facts as detailed in the previous subsection, these findings are coherent with our current anatomical representation of these malformations. We can therefore assume that the tractography may be useful for a more precise assessment of the nervous phenotype in ARM patients.

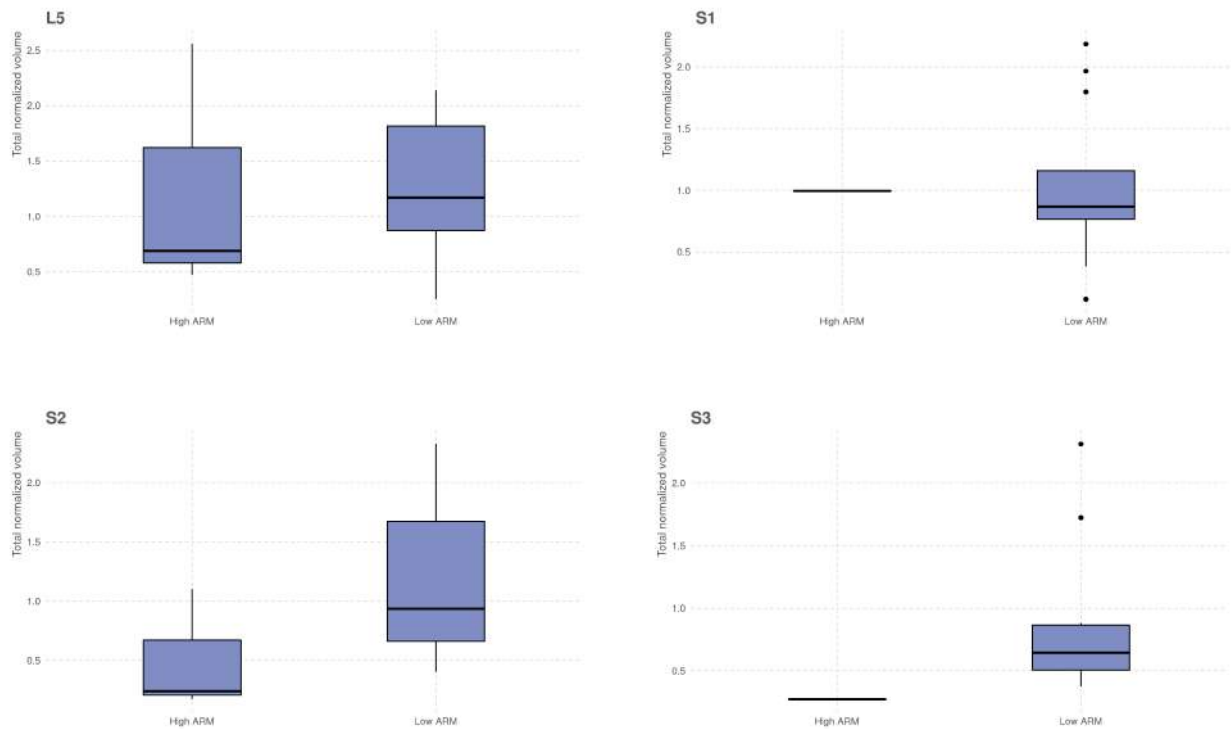


FIGURE 6.35: Scattering of total normalized volume values of sacral plexus roots in low and high ARM patients.

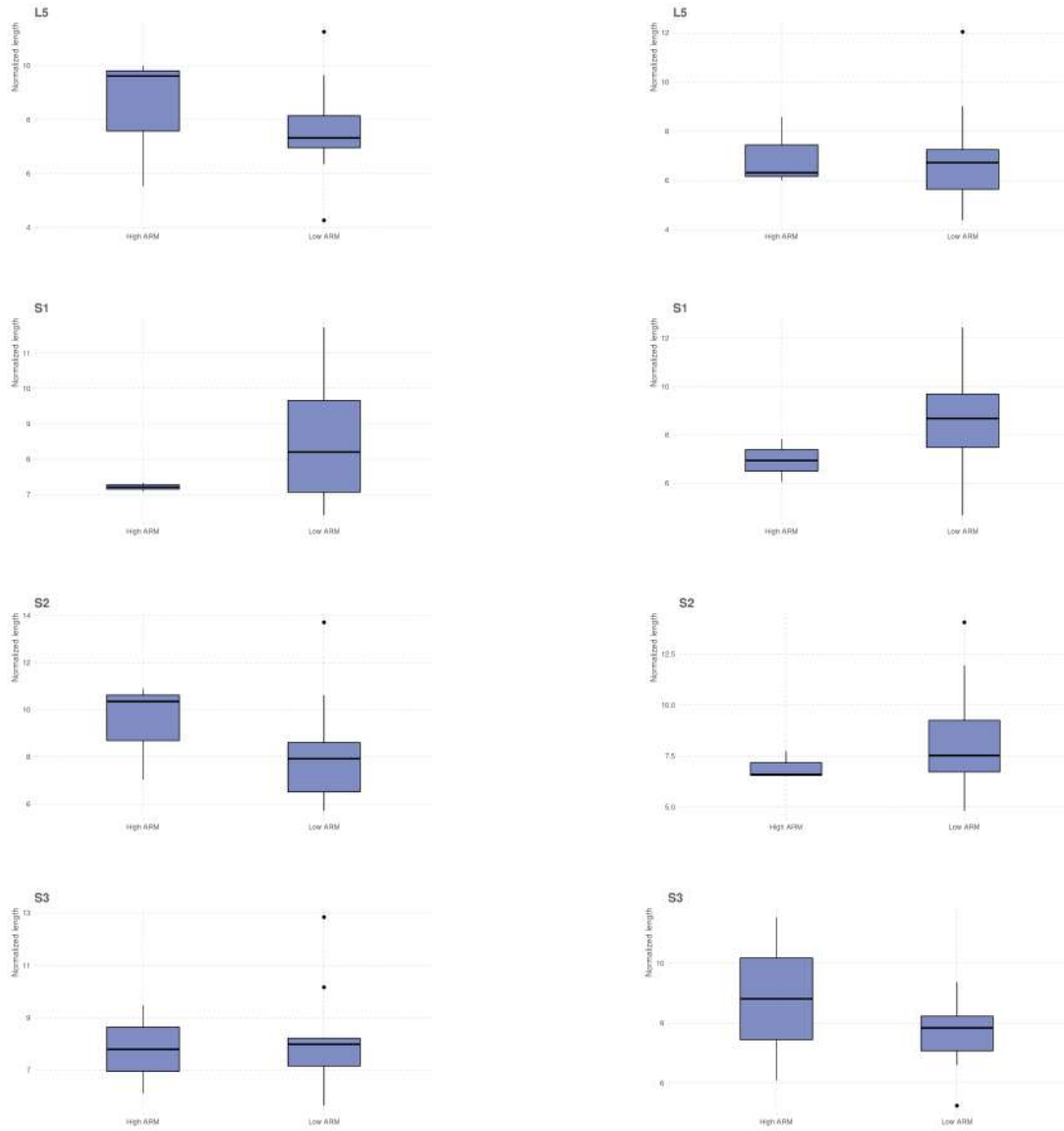


FIGURE 6.36: Scattering of normalized length values of sacral plexus roots in low and high ARM patients. On the left are represented the left roots, on the right, the right roots.

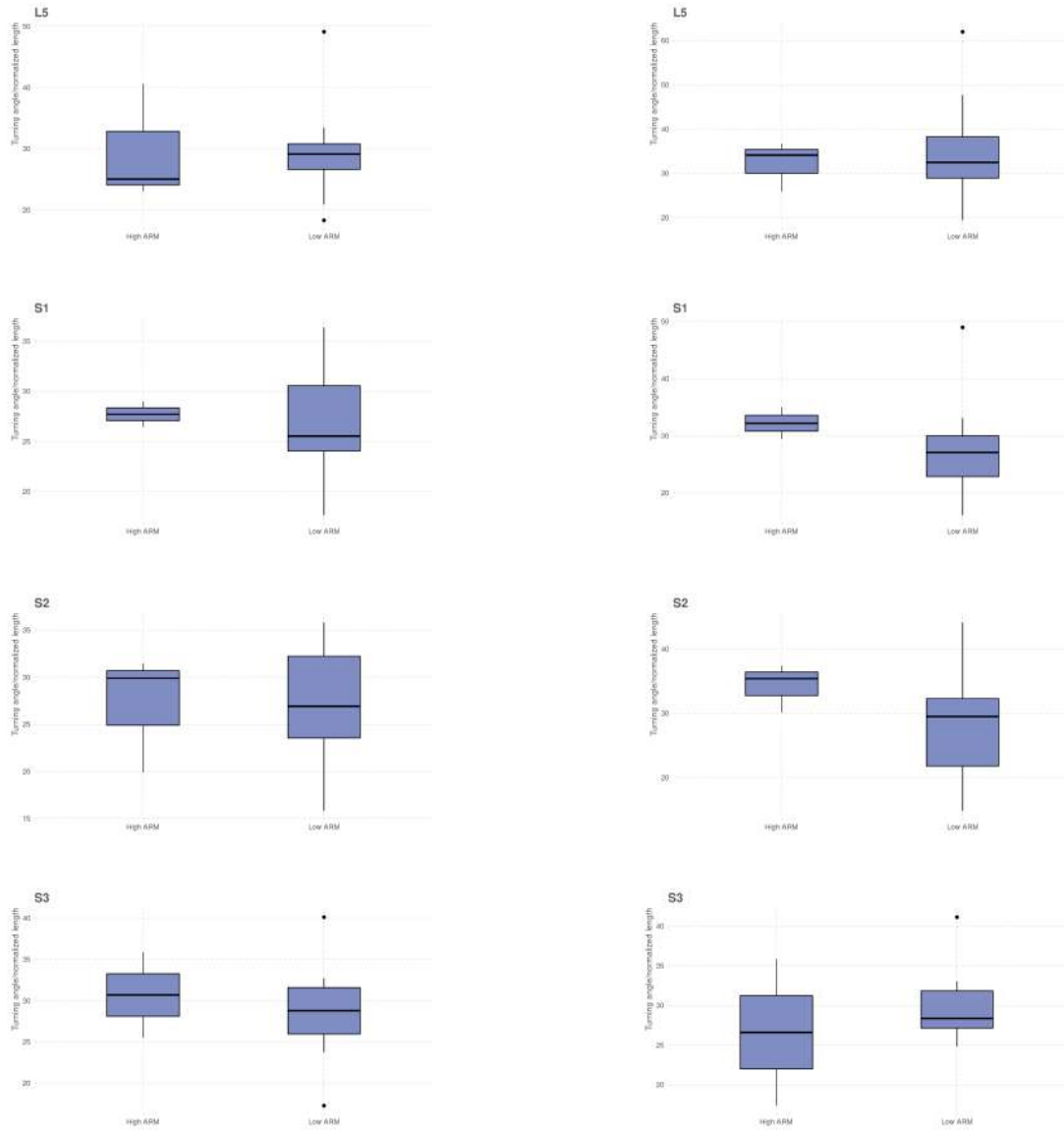


FIGURE 6.37: Scattering of angle/normalized length values of sacral plexus roots in low and high ARM patients. On the left are represented the left roots, on the right, the right roots.

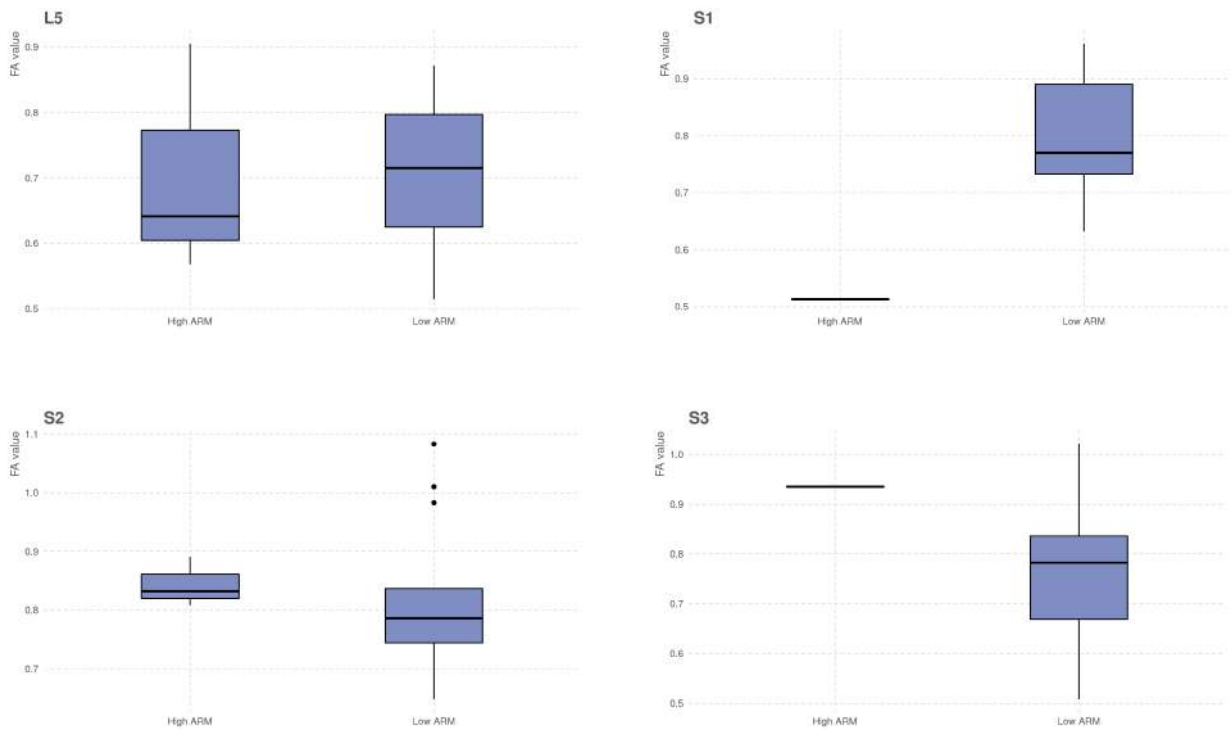


FIGURE 6.38: Scattering of mean FA values of sacral plexus roots in low and high ARM patients.

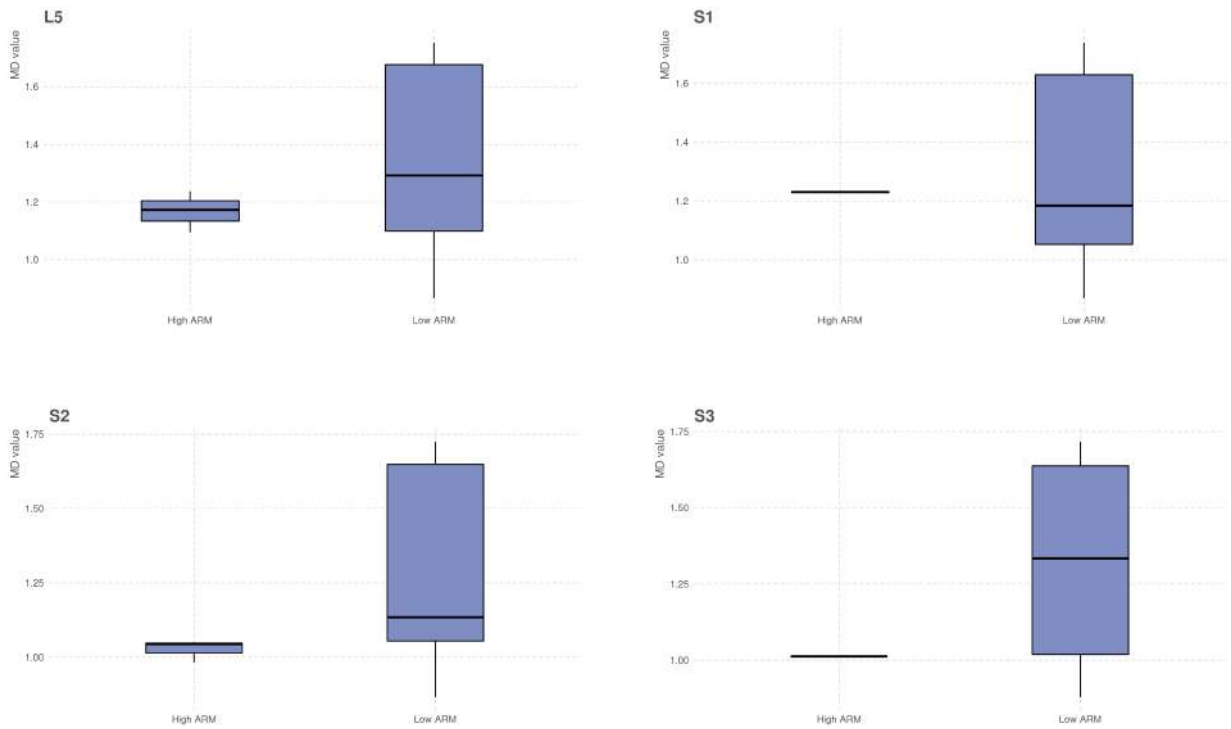


FIGURE 6.39: Scattering of mean MD values of sacral plexus roots in low and high ARM patients.

6.4 Conclusion and Discussion

In order to validate the PQL method from a clinical point of view, we used it in a series of 40 pediatric patients, half of them presenting an ARM.

Regarding the global description of the tracts of the whole series of patients, the most interesting finding was that after the age of five, the volume of the sacral roots seemed to reach a plateau, as if their growth really slows down after that age, in opposition to the other structures of the body. This fact has never been brought to our knowledge for now. Increasing the number of patients under the age of 5 would be of great help to investigate the evolution of the sacral plexus roots during this specific period of growth. It would probably yield less scattering of the results. In a specific focus on this age group, we could also design a specific diffusion sequence protocol, with increased directions and resolution. However, the limitation is as always the acquisition time and the movements artifacts, especially in small children who are not under general anesthesia. After confirmation of this finding, it would open interesting fields of research about nerve modeling, growth regulation and surgical management adaptation regarding continence issues. The other interesting finding in our clinical study was the tendency in ARM patients to present a prominent right side in the sacral plexus roots. If confirmed by further studies, it may lead to unveil common molecular determinants between ARM and left-right asymmetry set up.

More specifically, our analysis on the global volume of the roots did not bring any information about the evolution of the thickness of the roots. We did not performed this analysis because it would have been very difficult to reliably and robustly choose the exact same location to measure the cross section of the roots in all patients.

The main difficulty we encountered during the analysis of our results was the normalization method of the geometrical data, required because of the important median age group difference between ARM and control patients. We chose to perform it using the L5 vertebra height and volume, as it appeared to be well correlated with age and growth. However, our results showed that the growth of the sacral plexus roots is not linear, and seem reaches a plateau around the age of 5, in opposition to L5 vertebral volume and length. As there was no perfect solution to compare two groups with such a difference in median age, we chose to keep this normalization method. However, we are well aware that it may has interfered with the Wilcoxon comparison test and provided an altered statistical difference.

Other candidates for normalization were explored. One of the candidates that will possibly follow the same pattern of growth compared to sacral roots was the volume of the sacral canal. However, this structure is difficult to segment especially at its end near the coccyx because of noise and resolution issues of the volumic sequence. Moreover, some patients in this study present with a sacral agenesis, which makes it even more difficult to evaluate the sacral canal volume.

The solution would be to provide younger control patients to be able to match the ARM population. Indeed, we would be able to study in detail the evolution of both the geometrical and diffusion properties of the sacral roots. We may be able to confirm our hypothesis of a significant remodeling of the roots during this period of growth, and may lead to the constitution of a pediatric atlas of the sacral plexus. It would also confirm or infer the behavior of FA and MD values in our series. Indeed, studies about FA value evolution in the brain with aging showed that FA tend to rise till the thirties, and then decrease after that. All these studies were however performed in adults and not growing children [210], so there is still a gap between adolescence and adulthood to be explored in that field.

The main obstacle to increase the number of controls under the age of 5 is that few children of that age require a pelvic MRI except for ARM and urological malformations. The latest could also present ARM abnormalities of the sacral plexus roots. The solution would require to extend the field of pediatric specialties for inclusions, like pediatrics, gastro-enterology, or orthopedics. These specialities may however not have a direct interest in exploring the nervous system anatomy, which will make the inclusions more difficult but not impossible. We failed to correlate the roots volume to the birth weight, probably because the MRI was performed after the age of 3 months and not at birth. This

latest solution stays highly unethical, because there is rarely a medical reason for performing a pelvic MRI within the first days of life of a child, US being the gold standard.

Regarding the study on the influence of SA or SD, we found a tendency in patients with SA and/or SD to present smaller and shorter sacral plexus roots, in concordance with the hypothesis that an abnormal spine development would impair the sacral plexus roots development, especially in terms of volume and length. This is also coherent with our clinical knowledge about the worse continence outcome of the patients presenting SD and/or SA: these modifications in volume may be a sign of less effective pelvic innervation. However, the group of ARM patients presented a wide range of miscellaneous defects, going from a simple sacral agenesis below S2 till a major spine abnormality such as a short spinal chord. In order to conclude on the exact consequences of a these caudal pole defects, we should repeat the same study with the inclusion of patients coming from the pediatric neurosurgical department, presenting only various types of SA and SD, without any ARM. That would allow us to investigate the exact impact of the spinal malformation on pelvic nerve development.

Regarding the study on the influence of the level of ARM, our results were coherent with our clinical knowledge of high ARM bearing a worse continence prognosis than low ARM. However, more patients are needed to conclude, especially in cloaca patients, which management still stays very challenging for us. It is a separate type of ARM, that can be low or high, depending on the length of the common channel. We should also be able to compare male and female separately. Indeed, pelvic organs greatly differ between the two sexes, and so may the sacral plexus roots. However, adding more patients may stay challenging, because these are very rare and a lot of them happen to be already operated when they reach a tertiary center that is able to perform a 3T MRI. Moreover, high ARM often present an associated SA or SD that may interfere with our findings, as detailed in the previous paragraph.

Unfortunately, we were not able to explore the inferior hypogastric plexus in pediatric patients. The reason was probably a matter of resolution, voxel isotropism etc. This could be overcome by using our results in the healthy adult subject in the pediatric diffusion MRI protocol. Another interesting hypothesis would be that as the inferior hypogastric plexus is a complex network of crossing fibers, better results may be achieved using other tractography algorithms such as CSD or Q-Ball imaging as mentioned in Chapter 2. They however require a longer acquisition time and more directions, so we would have to modify the MRI protocol accordingly, which may be difficult using a clinical MRI scanner.

To conclude, the limitations of our clinical study is obviously the small number of patients, especially in sub-groups of malformations, which prevent us from performing adequate statistics. Our findings however suggested interesting paths of research, but still need an implementation of the database to lead to a clinically relevant analysis and therefore have a potential impact on the surgical management of ARM patients. A last interesting study would be to include more patients with pre- and post-operative pelvic MRIs, in order to evaluate the consequences of different surgical techniques on the PNN, once we have established the "normal" 3D anatomy using tractography.

6.5 Clinical validation of tractography: a case report

This article was published in the Journal of Pediatric Surgery Case Reports [146].

6.5.1 Introduction

According to the virtual nature of tractography, researchers aim at validating its results, either using clinical or pathological correlation. We report here the case of a 12 years girl with Neurofibromatosis type 1 (NF1) presenting a presacral neurofibroma where a prophylactic surgery was proposed to avoid the risk of transformation to a malignant peripheral nerve sheath tumor (MPNST). Pre-operative pelvic tractography combined to robotic surgery allowed for a precise definition of the neurofibroma origin and anticipation of potential complications. Post-operative tractography confirmed the validity of this imaging technique and underlines its potential benefit in pelvic surgery.

6.5.2 Clinical history

A 12 years old girl was followed for NF1 when she was diagnosed with a pelvic neurofibroma. The MRI showed a slowly growing lesion of 50 x 45x 53 mm, extending within the 2nd left sacral foramina. A PET-scan revealed a SUV max index of 2.83 with a tumor/liver ratio of 1.6. A per-cutaneous biopsy was performed, that showed a neurofibroma with cytological abnormalities but without any sign of malignancy, and no upraise of the mitotic index. The surgical resection of the neurofibroma was scheduled with a robotically assisted approach (Da Vinci Xi robot, Intuitive Surgical ®).

6.5.3 Imaging protocols

A pre-operative and a post-operative pelvic MRI were performed on a 3 Teslas machine (General Electrics®), according to the classical protocol for children's pelvic MRI used in the radiology department. After ethical board committee agreement, two additional sequences for research purposes were added, with an overall duration of 45 minutes and without general anesthesia: - Coronal T2-weighted volumic sequence: isotropic acquisition with a voxel size of 1x1x1 mm³, duration=7minutes. - Axial diffusion sequence: 25 directions, b600, quasi-isotropic resolution with a voxel size of 3.2x3.2x3.5 mm³, duration=5minutes. Anatomical images were segmented in order to build a 3D individual model of the patient using Slicer 3D 4.6.1 software. Results from tractography were then added to this model.

6.5.4 Results

see Figure 6.40

Pre-operative imaging with tractography showed that the lesion was arising from the left S2 root. During surgery, a voluminous tumor was found, displacing both the rectum and the colon to the right (A). The tumor was clearly attached to a nervous structure coming from the sacral roots, which needed to be sectioned for removal (B). Tumor extraction was done within a bag after partition through the umbilical port. No blood transfusion was required. The surgery length was of 15 minutes. The pathology report showed a typical plexiform neurofibroma without malignancy. The patient was discharged at day 3. Post-operatively, the clinical examination showed paresthesia and dysesthesia of the left leg calf and of the plantar vault (left S1-S2 territory), without any motor deficit. These symptoms spontaneously disappeared within the following weeks. The 3D patient specific model, the analysis of the pre- and post-operative tractogram are shown in Figure 6.40 C, D, E and F respectively. MRI performed 8 months post-operatively did not show any tumoral residue and apparently normal sacral roots S2 and S3 while viewing standard T1 and T2-weighted sequences. Diffusion tensor imaging

with tractography however showed a thinning of S2 left root (purple arrow, D), where the tumor was supposedly attached, in agreement with post-operative clinical symptoms.

6.5.5 Discussion

This case report demonstrates the interest of integrating tractography in a pediatric case of pelvic neurofibroma and support its wider use in pelvic surgery with neurological concerns. The surgery was indicated because of the high risk of transformation to a malignant peripheral nerve sheath tumor (MPNST) suggested by the results of the Pet Scan with an index above 2 and a tumor/liver ratio above 1.5 [56]. MPNST are highly aggressive sarcomas associated with a poor prognosis, for which the treatment of choice remains surgery [72, 73]. The robotic assisted technique was chosen because of its advantages in pelvic surgery [98, 164], and in order to avoid scar and preserve muscle in a patient whose disease is known to expose to iterative surgeries. The use of tractography integrated in a patient specific 3D model helped to better identify the connection of the tumor with the sacral plexus and to inform properly the patient and her family of the potential neurological risks. The thinning of the S2 sacral root on the post-operative sacral plexus tractogram and the disappearance of aberrant nervous tracts probably resulted from the section of these components to remove the tumor. These results must be taken with caution due to the absence of quantitative measurements and available normal values in tractography parameters of the sacral plexus especially in children. They are however in agreement with reports about tractography and peripheral nerve sheath tumors surgery [178, 123], mentioning the thinning of the involved peripheral nerve. Tractography is a post-processing tool applied on diffusion tensor MRI images, using mathematical algorithms and work remains to be done to prove its actual accuracy, especially for peripheral nerves. The correspondence between the clinical symptoms that occurred during the post-operative course and the nerve lesion identified on post-operative imaging validates a posteriori the clinical relevance of tractography.

6.5.6 Conclusion

In this case report, we combined the latest surgical and imaging technologies to offer the best management for prophylactic surgery in the frame of a genetic predisposition syndrome to cancer. To our knowledge, it is the first report showing in the same 3D scene the peripheral nerve tractogram, the tumor and the surrounding organs. We are currently working to optimize and automatize both segmentation and tractography processes in order to use it in daily clinical practice.

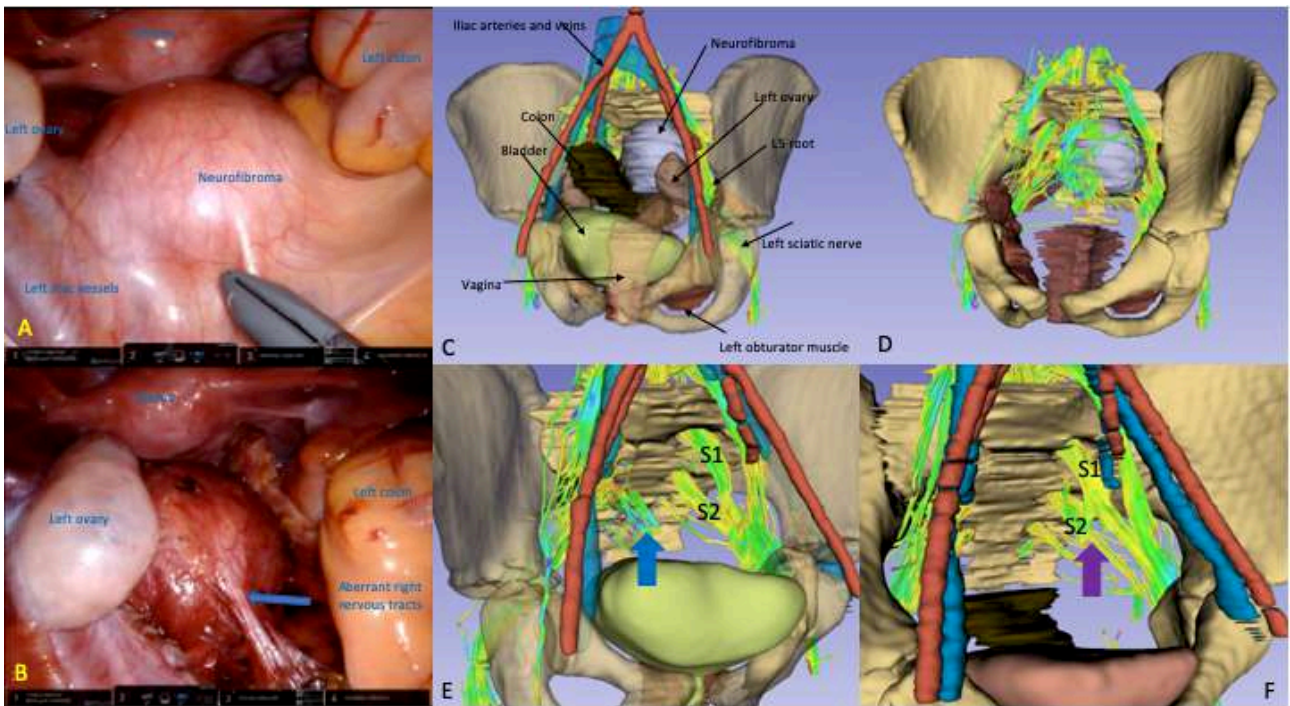


FIGURE 6.40: A= Robotic surgical view of the pelvis inspection before the dissection of the pre-sacral tumor. B= Robotic surgical view during the dissection, showing the nervous tracts linking the sacral plexus and the tumor and that were sectioned for tumor removal (Figure 1E). C= 3D model of the pelvis performed on the pre-operative MRI, with manual delineation of each organ using Slicer 3D 4.6.1 Segment Editor1 and including the sacral plexus tractogram and the pre-sacral neurofibroma (in purple). D= Merge of both manual segmentation and tractogram of the neurofibroma, in contact with the left part of the sacral plexus. E= Pre-operative tractogram without the representation of the neurofibroma. Note some aberrant fibers coming from the right side of the sacral roots (blue arrow) and reaching the tumor (blue arrow). S1=sacral root S1. S2=sacral root S2. F= Post-operative tractogram. Note the thinning of S2 root (purple arrow), where the tumor was supposedly attached, in agreement with the post-operative clinical findings of the lesion of sensitive S2 territory. It also shows the disappearance of the aberrant nervous tracts coming from the right side of the sacral plexus. S1=sacral root S1. S2=sacral root S2.



Chapter 7

Validation of tractography by Light Sheet Fluorescent Microscopy in a human fetal model

In this chapter, we describe our attempt to validate pelvic tractography results, by comparing them to Light Sheet Fluorescent Microscopy (LSFM) of the pelvic nervous network in a human fetal model.

Section 7.1 explains the need for a correlation between tractography and the anatomical reality, that can be explored by an immunochemistry study using LSFM.

In Section 7.2 we detail the methods used for fetal MRI imaging, pathological examination and LSFM protocols.

In Section 7.3 we present the tests performed on 7 fetuses, which have been conducted in collaboration with the Master 2 student Pierre Meignan for the last two fetuses. The results in terms of post-processing the LSFM imaging and registering with tractography results was the product of his work during his Master thesis.

Section 7.4 concludes on these preliminary results, gives some perspectives and also brings some supplementary information about the early development of the pelvic nervous network in the human fetus.

7.1 Introduction

Tractography presents the advantages of being the only in vivo non-invasive method to visualize in 3D the nervous anatomy. However, this technique bears several biases due to the current hardware and software limitations of diffusion MRI, and also relies on mathematical algorithms to represent the nerve fibers. There is currently no robust method to ensure its reproducibility and reliability based on the comparison to the anatomical reality [193].

All the existing works on tractography validation were carried out on the central nervous system. Johansen-Berg et al [103] described an effective thalamus segmentation using tractography based on general atlases of histology and anatomy. Fernandez et al [79] compared cerebral tractograms of patients with brain tumors to anatomical dissections of human brains, the purely visual comparison seeming to validate the tractography method. These works however did not allow for an effective comparison of two different techniques performed on the same subject, and therefore heavily rely on the examiner's interpretation.

Dyrby et al and Knösche et al [74, 112] used the same animal model (pig brain) to compare DWI images enhanced by manganese injection (specific tracer for white matter tracts), with tractography results. Despite an overall good correlation for the main white matter tracts, different tractography methods showed different results in terms of missing or aberrant tracts, especially in regions with crossing fibers and high curvature.

Few comparative studies using standard brain histology have been performed both on adult or fetal brain. The pathological representation considered as the gold standard however only showed the global architecture of the brain, which was manually aligned slice by slice with FA maps [139, 181, 197]. There is therefore no existing comparative work using the 3D structure of nervous networks.

Outside the brain anatomical area, 3D reconstruction of immuno-stained 2D slices (Computer Assisted Autonomic Dissection (CAAD)) has already been carried out in the fetal pelvic region [142, 143, 152], but it is a very tedious and time consuming process. It was never compared to tractography results.

LSFM is an ex-vivo revolutionary technique because it allows for a very detailed study of any anatomical area, while preserving its 3D structure, and therefore being very close to in-vivo techniques. It is a growing field of interest to better understand fetal development, a goal pursued by A.Chedotal's team in Institut de la Vision, Paris [26, 27]. The principle of this technique is to clear the sample to make it transparent before immuno-staining. It will then be imaged by a sheet of laser light within the microscope box which will directly deliver a highly qualitative 3D fluorescent imaging, as illustrated in Figure 7.1). The whole process will be detailed in Section 7.2.

Working on pediatric pathologies, and having the opportunity to work in close collaboration with gynecology and fetopatology departments in Necker Hospital and A.Chedotal's team of Institut de la Vision, we designed a comparative human fetal model between fetal tractography and LSFM.

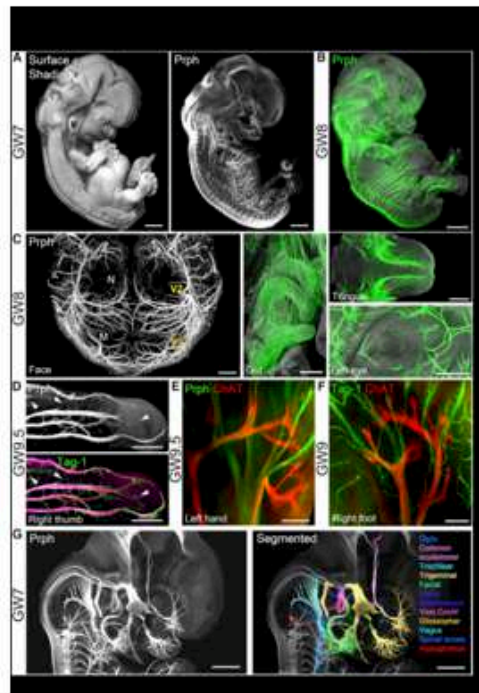


FIGURE 7.1: Nervous system (in green) in a 7 weeks of gestation whole fetal body in LSFM [26].

7.2 Methodology

All fetuses between 18 and 36 weeks of gestation (WG) scheduled for a termination of pregnancy were potentially eligible, if they did not present any pelvic pathology on prenatal US scan. The parental agreement was collected through a written consent form allowing the autopsy of the fetus, the performance of all exams required for diagnosis, and samples for scientific purposes (Assistance Publique des Hôpitaux de Paris: AP-HP/DAJDP-15-02).

The overall study for one fetus lasts 3 months on average, including the following steps: 1) MRI acquisition (in collaboration with the pediatric radiologists D.Grévent and N.Boddaert), 2) foetopathological examination and pelvic dissection (in collaboration with the foetopathologist B.Bessières), 3) LSFM process (in collaboration with M.Belle and A.Chedotal from l'Institut de la Vision), 4) post-processing and analysis of the images (N. Goudin, Institut Imagine).

The optimizations of MRI acquisition, dissection and clearing process are detailed in Section 7.3.

7.2.1 MRI

As soon as possible after the termination of the pregnancy in the gynecology department (ideally before 12 hours, to avoid dessication and maceration), the fetus was scheduled for the MRI acquisition on the 3 Tesla machine of the pediatric radiology department. At the beginning of the study, we placed the fetuses in a dorsal position, wrapped in a moisturized tissue. For the last two, we put them in a ventral position within a box filled with physiological serum to improve the SNR.

The parameters of the volumic and diffusion sequences were identical at the beginning of the study to those applied to the pediatric patients as described in Chapter 3. There were then progressively refined to improve the tractography results, as detailed in Section 7.3. The final fetal imaging protocol included a T2 weighted volumic sequence with the following parameters: TR 2500, TE 53, voxel size = $0.8 \times 0.8 \times 0.8 \text{mm}^3$, Matrix = 512×512 ; and a T2 weighted diffusion sequence with the following parameters: 60 directions, b1000, TR = 4149, TE = 62, voxel size = $0.47 \times 0.47 \times 1 \text{mm}^3$, 6 NEX.

7.2.2 Pathological examination

The pathological examination was performed in collaboration with B. Bessières, foetopathologist. The pelvic dissection occurred after the standard pathological examination and lasted an hour on average.

General inspection: it estimates the maceration state and notify the presence of a dysmorphism of the face or of the limbs.

Cutaneous incisions: this follows the standard abdominal approach in fetal pathology examination, with additional incisions in the inguinal and lumbar region in order to access both the coxo-femoral articulation and the spine with the purpose to remove the entire pelvic bloc and leaving the skin untouched (see Figure 7.2).

Standard samples for foetopathology examination: heart, lung, diaphragm, kidney and suprarenal glands (preserving the ureters), liver, small bowel and colon (sigmoid section), spleen, dudodenum-pancreas, stomach, ovaries, spine (lumbar section above the iliac crests).

Steps of the pelvic dissection, see pictures in Figure 7.2:

- The dissection starts with the the peeling of the skin and of the sub-cutaneous tissues above the pubic bone, genital organs, inguinal fossa, and iliac crests towards the lumbar fossa with muscle section till the psoas muscle, in order to reach the lumbar vertebrae;
- The umbilical and external iliac vessels must be dissected and ligated;
- The abdominal vessels (aorta and inferior veina cava) must be peeled to reveal the vertebral ligament;
- The vertebral section must be performed at the L3-L4 level, 2 cm above the aorta bifurcation;
- The spinal muscles must be cut;
- A careful cutaneous peeling above the sacrum towards the coccyx must be performed;
- The coxo-femoral desarticulation is performed;
- The distal section of digestive, urinary and genital channels must be done above the perineal skin, which last step frees the pelvis from the rest of the fetal body;
- We then irrigate the aorta with a solution of Phosphate-Buffered Saline (PBS) + Paraformaldehyde (PFA) 6 x 20 ml;
- The urinary, genital and digestive channels are removed;
- The pelvis is cut into two hemi-pelvis following a medial sagittal plane.

This pelvic dissection method is an original work issued from this study. It allows for the preservation of the entire 3D structure of the whole pelvis, including bones and soft tissues such as nerves. It also allows for the conservation of the external integrity of the fetus, meaning the cutaneous surface. This fact is particularly important in the view of restoring an acceptable cosmetic aspect of the fetal body before giving it back to the parents if they claim for it. The precise and neat sagittal section in two hemi-pelvis combined with the careful removal of the urinary, genital and digestive tracts aims at two goals: to reduce the size of the sample in order to fit into the microscope box, and to maximize the contact surface between the pelvic nerves (they run between the pelvic bones and the organs) and the solution containing the antibodies, and therefore enhance both fixation and immunostaining. However, these steps must be very carefully performed by an experienced surgeon or foetopathologist: if the sagittal section is not accurate, the reconstruction of both left and right sides of the pelvis may be impaired during the post processing of LSFM images. In the same way, if the dissection of the organs is not delicate, it may injure or displace the pelvic nerves, which 3D organization may therefore be impaired, and lead to inaccurate LSFM results. The aorta irrigation aims at obtaining an optimized fixation of the whole sample through the arterial network, complementary to the immersion of the sample into the fixation solution. This step directly impacts the quality of both immunostaining and clearing, because these latest steps only work on well deeply fixated tissues.

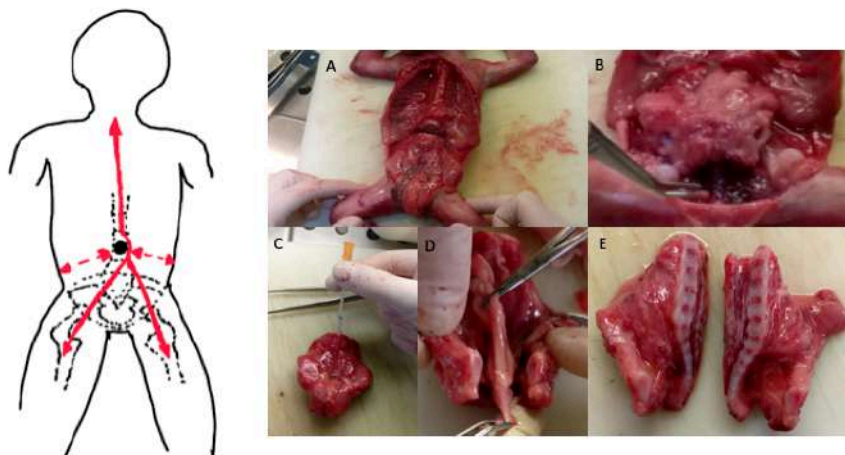


FIGURE 7.2: Cutaneous incisions on the left. A: Vertebral section. B: Coxo-femoral desarticulation. C: Irrigation of the aorta. D: Removal of urinary, genital and digestive channels. E: Sagittal section of the pelvis in two hemi pelvis.

7.2.3 Light Sheet Fluorescent Microscopy (LSFM)

Clearing and immunostaining processes that prepare the sample before LSFM acquisition were designed by A.Chedotal's team in Institut de la Vision for smaller samples from fetus below the age of 15 WG. Our bigger samples required modifications of the protocol, with essentially a longer fixation time in PFA (3 weeks against 3-5 days), and a longer incubation time (3 weeks instead of 2 weeks).

Sample fixation

The two hemi-pelvis were immersed in a 4 % PFA solution during 21 days at 4°C. PFA solution were changed twice at 24h and 48h, with the addition of 0.1g/l azide solution (anti fungal) at 72h. The samples were then stored in PBS at 4°C until the next step (see Figure 7.3).

Dehydration/Bleaching/Dehydration

Samples were then dehydrated in successive solutions of Methanol/PBS of increasing concentration: 50% MeOH, 80%MeOH, 100%MeOH (2h for each step with agitation at room temperature). Samples were then transferred in a solution of MeOH+6% H2O2 to bleach the sample, with an overnight incubation at 4°C, protected from the light. The samples were then re-hydrated in successive solutions of Methanol/PBS of decreasing concentration: 100% MeOH x2, 80% MeOH, 50%MeOH (2 hours for each step with agitation at room temperature). This step lasted 48h and led to a total depigmentation of the sample. Post-dissection hematomas may also be removed by H2O2 (see Figure 7.3). The samples were then stored in PBS at 4°C until the next step.

Blocking and Permeabilisation

The samples were then placed in a solution of PBSGT for 4 days with rotation at room temperature (PBSGT = 0.2% gelatin, 0.5% Triton 100X in PBS, thimerosal 0.1g/L). This step aims at making the sample permeable and saturating aspecific sites before immunostaining.

Antibody incubation

This step took three weeks. The first two weeks concerns the incubation with primary antibodies in a modified solution of PBSGT + 5% Triton 100X + 0.1% saponin at 37°C with rotation (70rpm). The primary antibodies used were antibodies against Peripherin that is a specific protein of peripheral nerves (AB1530, Sigma Aldrich, dilution 1/1000). Samples were secondarily flushed in PBSGT 0.5% 6 times in 24h during 15 minutes at room temperature with rotation in order to get rid of non fixed primary antibodies. Samples were then immersed in a PBSGT +0.1% saponin (10microg/mL) solution at 37°C with secondary antibodies during one week. The solution was filtered through 0.22 micrometer filter in order to prevent the precipitation on secondary antibodies. Secondary antibodies (donkey anti-rabbit A647, Jackson Immunoresearch, 711-605-152, dilution 1/500) specifically target the species of used primary antibodies (rabbit). They are also marked with fluorochromes which wave length is 546 nm. Finally, the samples were flushed in a PBSGT solution 6 times at room temperature during one day, and stored in a PBS solution at 4°C until the next step.

Clearing iDISCO+

The clearing process lasted 3 days according the iDISCO+ modified protocol [169]. The samples were immersed in solution of progressively increasing concentration of Methanol: 20%MeOH, 40%MeOH, 60%MeOH, 80%MeOH, 100%MeOH, 100%MeOH (room temperature, one hour each step, with agitation at 12 Rpm). This step aimed at the tissue dehydration. The samples were then transferred in a 2/3 Dichloromethane (DCM) + 1/3 MeOH solution during 12 hours. To eliminate the rest of MeOH, the samples were flushed during 1 hour in a solution of 100 % DCM. This step aimed at the delipidation of the tissue.

The final step of the clearing process consisted of the immersion of the samples in a 100% solution of pure Benzyl Ether (DBE), which allows for the homogenization of the refraction index of the tissue. DBE is a very lipophilic solution which penetrates the membranes of the dehydrated and delipidated tissue. Another couple of hours was necessary for the DBE to penetrate the whole sample and provide a transparent sample. The samples were then stored in DBE at room temperature, protected from the light (see Figure 7.3).

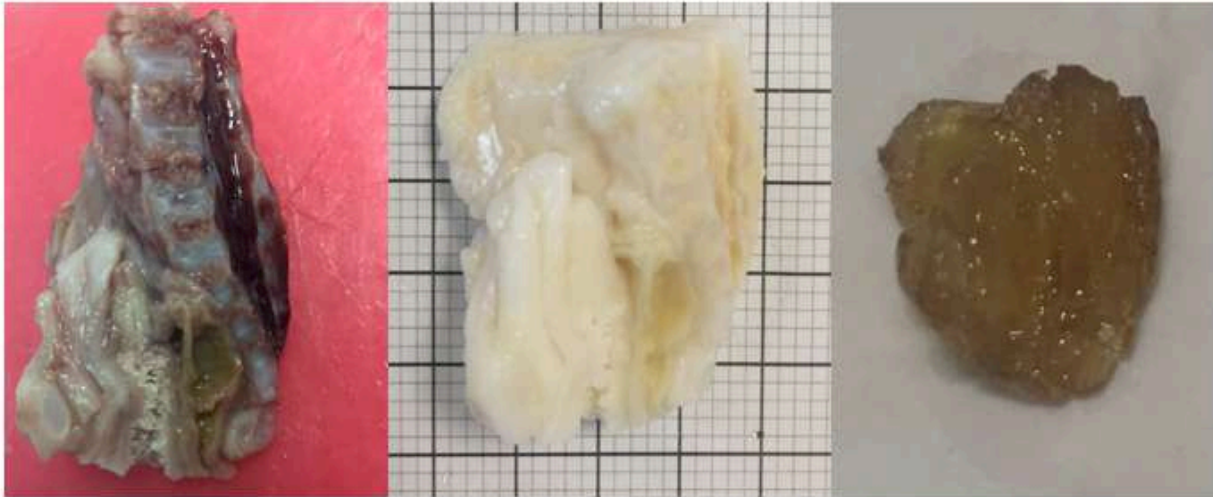


FIGURE 7.3: Right hemi-pelvis of fetus 2 after fixation in PFA, bleaching and clearing respectively.

Microscope acquisition

LSFM is an innovative technique of fluorescence microscopy with the use of a laser light illuminating the part to be analyzed in an axial plane very precisely (see Figure 7.4). The signal detection path is located in a plane orthogonal to the illumination path, which decreases the photo toxicity and maximizes the quality of the information [214]. The advantage is the maintenance of the integrity of the sample and the possibility of a reacquisition.

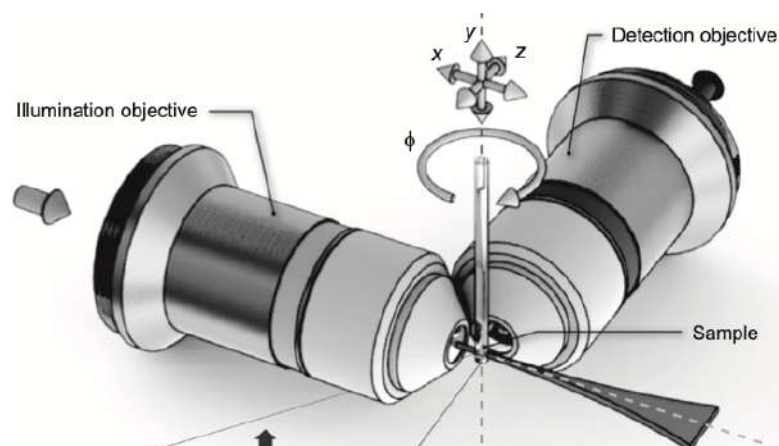


FIGURE 7.4: LSFM principle: both illumination and detection paths are orthogonally oriented with the sample located at the intersection of the two planes. [214].

The challenge during the acquisition was to successfully highlight the fetal pelvic network. The first problem was the size of our specimens compared to the size of the microscope box that was used routinely for smaller samples. The positioning of the sample in the microscope chamber could take from 30 minutes to several hours depending on its size and shape (see Figure 7.5). The resolution was of $5.16 \times 5.16 \times 2 \mu\text{m}^3$, dependant of the square microscope box dimensions (width and depth) and the minimum zoom allowed by the microscope optical system. Indeed, our samples being of a big size and having difficulties to fit into the microscope box, we had to use the minimum zoom in order to capture the maximum volume of the sample. The acquisition was carried out plane by plane, the laser light beam moving in z-axis at specific wavelengths of the antibodies to be highlighted. The first wavelength was 488 nm and highlights the auto-fluorescence of the samples. The second wavelength used was 546 nm to highlight the peripherin. The displacement limit in the z-axis was 7mm. The acquisition lasted between 30 and 60 minutes for a hemi-pelvis.



FIGURE 7.5: Positioning the hemi-pelvis in the microscope box.

7.2.4 Image post-processing

MRI images: Volumic and diffusion sequences were loaded in Slicer 3D. The organ segmentation was entirely manual. The pelvic tractogram was obtained using the ROI based method described in Chapter 5.

LSFM images: these images were post-processed by P.Meignan using the Imaris software. Each nervous structure had to be manually segmented on a stack of 2D images. The mean segmentation time for one fetus was 14 days, once getting acquainted with the software. 4 To of data was generated for all the fetuses.

7.3 Results

All the fetuses that were included in this study are described in Table 7.1. Only fetuses 6 and 7 benefited from both MRI and LSFM exploration.

TABLE 7.1: Fetuses' characteristics included in the study.

Fetus	Term	Sex	MRI	LSFM
1	36	M	x	
2	25	F		x (failure)
3	28	F	x	x (failure)
4/5	16	F		x
6	22	M	x	x
7	17	F	x	x

7.3.1 Fetus 1

The first fetus was only explored by MRI due to the lack of parental agreement for autopsy. It was a male fetus, 36 WG, presenting a corpus callosum agenesis that led to the termination of the pregnancy. The MRI acquisition protocol was identical to the protocol applied to paediatric patient and allowed for testing it on a fetal specimen:

- anatomical sequence: coro T2 cube, TR 2500, TE 53, Voxel size = $0.5 \times 0.5 \times 0.6$ mm , Matrix = 512×512
- diffusion sequence: DTI 60 directions b1000 TR 4149 TE 62 2 NEX Matrix = 128×128 Voxel size: $0.9 \times 0.9 \times 3.5$ mm³ (non-isotropic acquisition)

The pelvic tractogram included L4, L5, S1 and S2 roots, but S3, S4 roots and pudendal plexus were missing (see Figure 7.6).



FIGURE 7.6: 3D modeling and tractography of a 36 WG old fetus, visualized using the software software designed by A. Delmonte as described in Chapter 4.

7.3.2 Fetus 2

The second fetus was only scheduled for immunochemistry due to the lack of parental agreement for the MRI. It was a female fetus, 25 WG, weighting 892.5 grams, the reason for the termination of pregnancy being a severe maternal paludism access. This was the first fetus that was explored using the clearing and immunochemistry protocol in collaboration with l'Institut de la vision. LSFM acquisition did not show any immunofluorescence, probably due to a lack of fixation of the sample in which the PFA did not completely penetrate. The fixation protocol was therefore modified with a fixation time of 3 weeks instead of 8 days. Moreover, during the pathological examination, we also added the intra-aorta injection of PFA to maximize the fixation process.

7.3.3 Fetus3

The third fetus was scheduled for both MRI and immunochemistry. It was a female fetus, 28 WG, an hydrocephaly from unknown origin being the reason for the termination of pregnancy.

The voxel sizes of both the volumic and diffusion sequences were modified to obtain more isotropic acquisitions: $0.8 \times 0.8 \times 0.8 \text{ mm}^3$ (coroT2), $1 \times 1 \times 2 \text{ mm}^3$ (diffusion). The corresponding tractogram showed all sacral plexus roots from L5 to S4 (see figure 7.7).

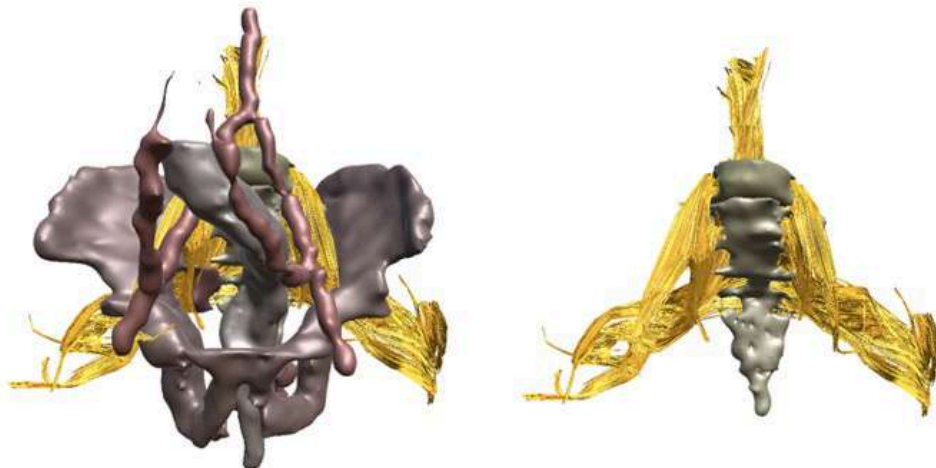


FIGURE 7.7: 3D modeling and tractography of a 25 WG old fetus, with all sacral plexus roots from L5 to S4.

The LSFM acquisition was not possible on the whole hemi-pelvis because of its size, it did not fit in the microscope box (see Figure 7.8). A verification of immunostaining in a small sample of the pubic area of the pelvis was performed and found positive. A verification of immunostaining on the whole pelvis with a microscope was also performed and found positive. This led to the conclusion of a better fixation in PFA thanks to the modified protocol of sample preparation. The decision was made to split in 4 the fetal pelvis to fit in the microscope box, but in the mean time happened a re-opacification of the sample that needed re-clearing. However, no information could be extracted from these samples, most probably because of the iterative split and the re clearing process.

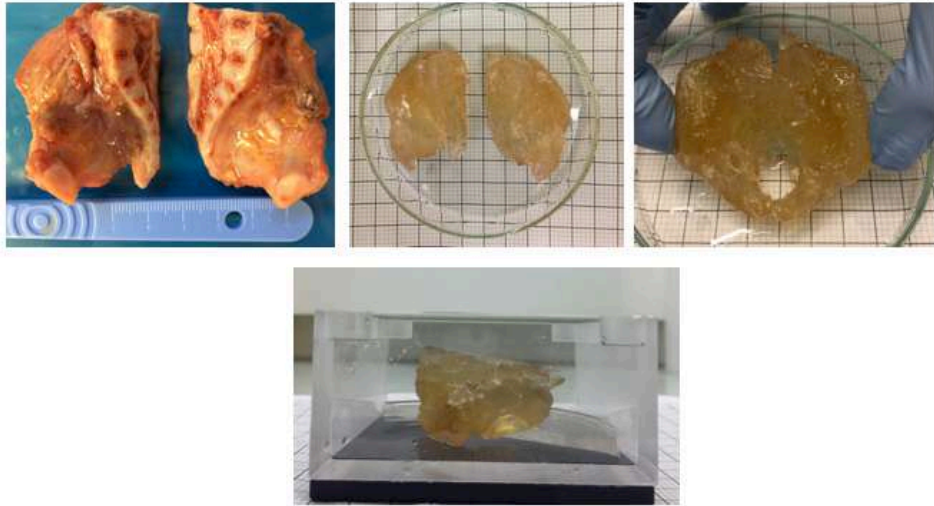


FIGURE 7.8: Pelvis of fetus 3 after dissection and clearing.

7.3.4 Fetuses 4 and 5

Two female cephalo-thoracopages siamese of 16 WG were included in the study. The two pelvis were not involved in the malformation. MRI acquisition was not scheduled for organizational reasons. LSFM was successful on the 4 hemi-pelvis, and the segmentation of the nervous structures was performed by P. Meignan, as shown in Figure 7.9.

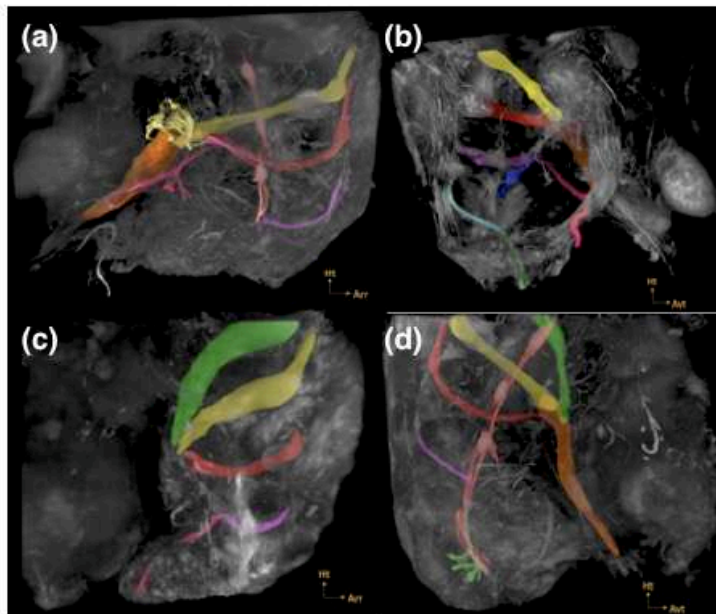


FIGURE 7.9: Right (a,c) and left (b,d) hemi-pelvis of the siamese: fetus 4 (a,b) and 5 (c,d). Nerve segmentation was performed using the Imaris software. Green = L4 root; Red: L5 root; Purple: S1 root; Dark blue: S3 root; Light blue: S4 root; Orange: sciatic nerve; Light green: coccygeal plexus; Salmon red: pre vertebral sympathetic chain; Ocre: hypogastric plexus.

7.3.5 Fetus 6

The sixth fetus was 22 WG, aborted for a severe cardiac malformation, and explored by both MRI and LSFM. The parameters of the diffusion sequence have been optimized to increase the quality of the acquired signal while maintaining an acceptable acquisition time. Thus the size of the voxel was reduced to $0.47 \times 0.47 \times 1 \text{mm}$ to increase the accuracy and detection of small fibers, and the number of NEX increased from 2 to 6 to reduce the noise. Regarding the acquisition of the coro T2 cube anatomical sequence, it was later found that the size of the acquisition box (that is, the volume acquired as a diffusion tensor) was not large enough and excluded the L5 vertebra and the cranial part of the iliac crests. While performing the tractography, it was therefore not possible to take the sacral canal as a starting point for the fibers since this region was outside the acquisition field. Only the part of the sacral canal that was acquired could be used to place the ROIs. The tractogram obtained was therefore poor with the absence of roots L4 and L5. However, we could identify fibers that could correspond to the roots S1, S2 and S3 (see Figure 7.10).



FIGURE 7.10: 3D modeling and tractography of a 22 WG old fetus (fetus 6). L4, L5 and S4 roots are missing.

The placing of the samples in the microscope box was very difficult with the impossibility of moving in the three planes of space because of the size and shape of the hemi-pelvis. LSFM acquisition showed positive immunostaining for the peripherin (see Figure 7.11).

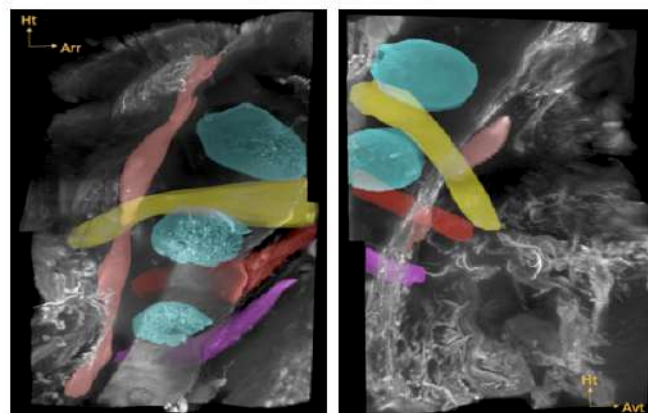


FIGURE 7.11: Left: right hemi-pelvis, Right: left hemi-pelvis. Nerve segmentation was performed using the Imaris software. Light blue: vertebral bodies; Yellow: L5 root; Red: S1 root; Purple: S2 root; Salmon red: pre-vertebral sympathetic chain.

7.3.6 Fetus7

The seventh fetus was 17 WG, aborted for a severe severe cardiac malformation and explored by both MRI and LSFM. The MRI sequence parameters remained unchanged, as for the LSFM resolution. The tractogram showed sacral plexus roots from L5 to S4 (see Figure 7.12). Placing the samples in the microscope box was easier, thanks to the smaller size of the sample. However, the top and bottom of each hemi-pelvis were acquired separately to cover the whole sample volume, which was not possible during a single acquisition because of the too small size of the microscope box. LSFM acquisition showed positive immunostaining for the peripherin (see Figure 7.13).

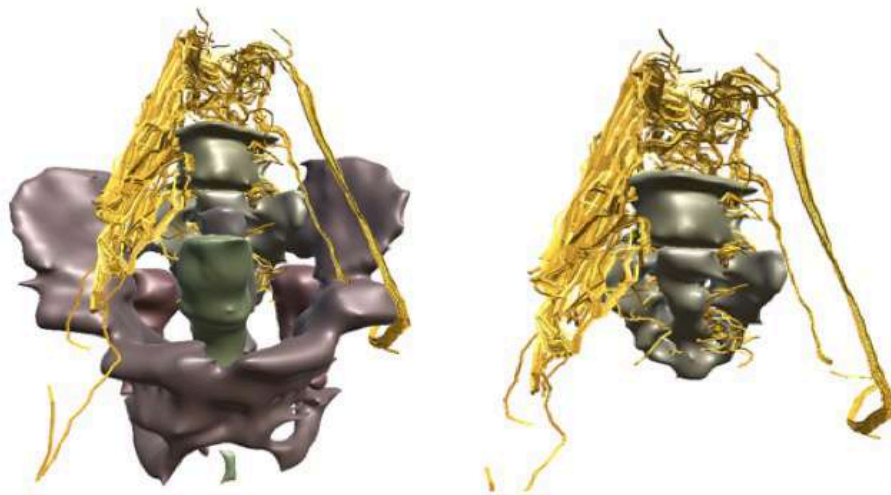


FIGURE 7.12: 3D modeling and sacral plexus tractography of a 17 WG old fetus (fetus7).

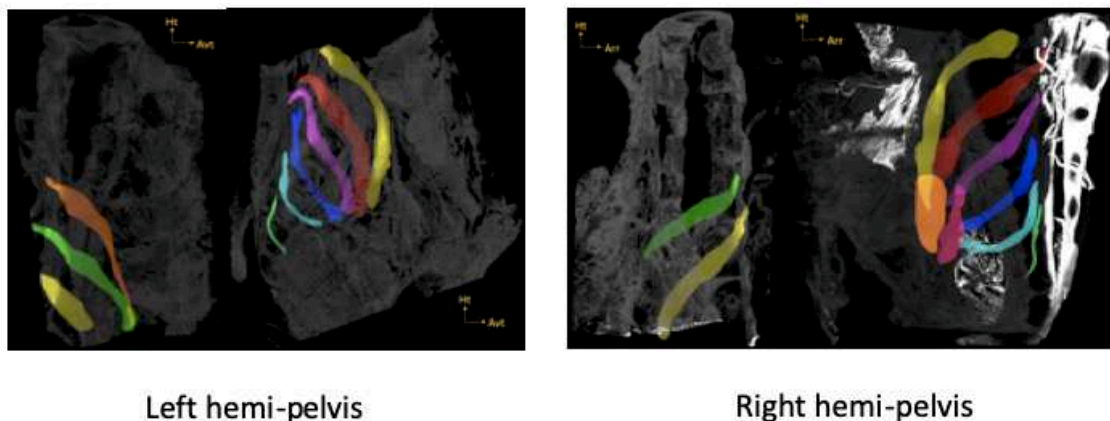


FIGURE 7.13: Sacral plexus segmentation of fetus 7 performed using the Imaris software. Orange: L3 root; Green: L4 root; Yellow: L5 root; Red: S1 root; Purple: S2 root; Dark blue: S3 root; Light blue: S4 root; Light green: S5 root.

7.3.7 Comparison between tractography and LFSM results

The comparison was performed by P. Meignan in collaboration with A. Delmonte [136] and will be briefly summarized here. The objective was to gather and register in the same space the segmented surfaces on the LFSM acquisition and the tractography from the MRI acquisition. Each surface corresponds to a volume in 3D representing an anatomical structure. The segmentation of the fetal MRI acquisitions was performed using 3D Slicer. The segmentation of LFSM acquisitions was carried out using Imaris.

The software chosen for the registration was 3D Slicer. The registration relies on common anatomical structures, identifiable and segmentable in both acquisitions. We chose the L4-L5 and L5-S1 inter-vertebral discs clearly visible on the MRI and the LFSM. These structures (landmarks) were superimposed and served as a reference for transformations applied to all nervous structures.

The registration process consisted of several steps: compression and exportation of LFSM images in 3D Slicer, rigid registration of the landmarks, and tractogram importation. The degree of correspondence between the nervous structures issued from the two techniques was only visually and qualitatively evaluated in the two fetuses that were explored by MRI and LFSM (N°6 and 7). A partial correspondence was found between L4, L5, S1 and S2 roots, as seen in Figure 7.14.

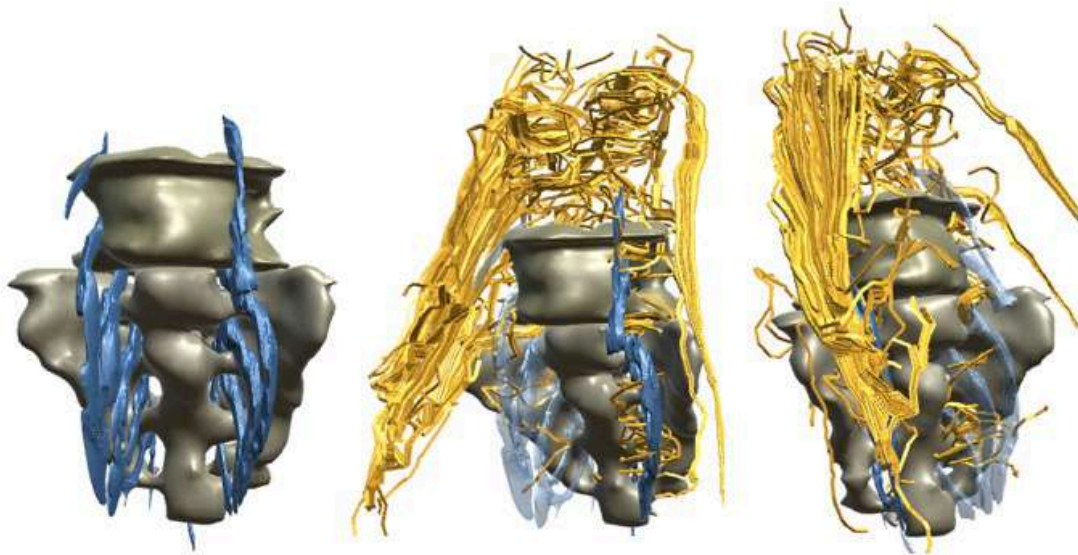


FIGURE 7.14: Final result for Fetus 7 after a rigid registration between tractography results (yellow) and LFSM data (in blue).

7.4 Conclusion and Discussion

Tractography still needs comparative anatomical studies in order to be trusted in clinical applications. To our knowledge, this study was the first attempt to validate peripheral nerve tractography by LSFM. It allowed us to develop MRI and LSFM acquisition protocols that provided reliable and analyzable images, for fetuses interrupted around 18 WG. We also proved that the registration process between the MRI and LSFM acquisitions was feasible and therefore makes it possible to evaluate the tractography method. Further fetal acquisitions are needed to more robustly and quantitatively compare the two types of acquisition.

The adaptation of fetal MRI sequences was governed by two principles: gain spatial resolution to improve the accuracy of 3D reconstruction and tractography but also maintain an acceptable acquisition time, i.e. 30 minutes for both sequences. In clinical practice, if these sequences are used for neonates with pelvic defects, acquisition times must be reasonable. The parameters of the cube anatomical sequence allowing for the 3D reconstruction were not much modified because they allowed for a qualitative 3D modeling since the first fetus. The parameters of the diffusion sequence have been modified to improve the quality of the tractography. Thus the first evolution between the acquisitions of fetuses 1 and 3 was the passage from a very anisotropic voxel (1x1x3.5mm) to a voxel closer to isotropy (1x1x2mm) in order to avoid the over-representation of cranio-caudal fibers. The tractography of the fetus 3 allowed highlighting the sacral roots down to S4 in contrast to only S2 root for the fetus 1. The size of the voxel (0.47x0.47x1mm) and thus the resolution were improved with the acquisition of the fetus 6 and 7. The number of NEX also increased from 2 to 6 to reduce the noise.

The seven fetuses interrupted at different stages of development, from 16 to 36 WG, were of very different size. The optimal stage of development for analyzable MRI and LSFM acquisitions was between 16 and 18 GS. Above 18 WG, placement of the entire sample in the microscope box was impossible. Before 16 WG the resolution of our MRI sequences seemed too limited to obtain a correct 3D reconstruction and tractogram.

Regarding the comparison between tractography and LSFM data, the assessment of the reliability of the registration was limited because it was purely visual and not quantitative. The discrepancies may also be explained by the time factor: the MRI was performed in immediate post-mortem while the LSFM acquisition took place three months later. The manipulations to achieve immunostaining and transparency which comprise several phases of hydration and dehydration, and therefore of volume variation of the sample, may have also slightly modified the anatomical relationships.

Seven fetuses were necessary to develop and then adapt the MRI and LSFM protocols and finally obtain the first results. One of the limitations of this study is the number of fetuses included. This fact is explained by several factors: the narrow limits of potentially eligible termination terms; the complexity of the organization of the MRI acquisition and fetopathological examination with the mandatory agreements of the parents, the obstetrics, radiology, fetopathology and surgery teams; the long time of the process: three months for one fetus. Before fetus N° 6, the available data did not allow attempting a registration and thus comparing the tractography obtained by MRI and LSFM data.

The use of an animal model may have resulted in faster results but would have had no impact on clinical management. Although the chosen human fetal model was more complex to implement, it allowed for fine tuning of fetal MRI acquisition parameters in the scope of fetal pelvic tractography.

Thanks to the LSFM data, it also brought for the first time the opportunity to visualize in 3D the growth of the pelvic nervous system during human development. Indeed, if the caudal development of the embryo before 5WG has been relatively well described during the last century thanks to dissections and immunohistochemical studies, the development beyond 6 WG is little known. According to some authors [7], pelvic innervation is mature enough and does not undergo fundamental changes during growth in fetal and post-fetal periods after 8 WG. The inferior hypogastric plexus has an aspect and relationships comparable to those of an adult and the fetus constitutes a pertinent experimental model

for pelvic innervation studies [5, ?]. However, these are only assumptions that shall be proved by embryological studies in older fetal ages.

Within this scope, our collaboration with A. Chedotal's team of Institut de la Vision allowed us to explore their fetal database of more than 200 specimen. It contained 32 fetus with pelvic nervous immuno-chemistry between 7 and 14 WG, that have never been analyzed so far. After a preliminary evaluation of the quality of the specimen, we selected 7 fetus with peripherin immuno-staining, that were pooled with the fetuses included in our study in order to perform a developmental observation of the growth of the pelvic nervous system between 7 and 22 WG. The post-processing of the data was carried out by P.Meignan and led to interesting results [136]:

- Sacral roots L5 to S4 globally grow with the developmental age but relatively less compared to the volume of L5 vertebra. Nervous structures volume is less and less important relatively to the global fetal volume with aging. Coccygeal roots were observed till 8.5 WG in our study. They were smaller than sacral roots, with no apparent ganglia. Their volume progressively decreased with developmental age till complete disappearance. Cellular regression or differential growth according to organs are not well documented nor understood yet;
- LSFM provided detailed anatomical information of distal nerves such as the perineal nerve till its termination into the clitoridian or penian branch. This observation confirm Arango et al's work stating that all pelvic nervous structures are present since very early ages of development [7];
- The analysis of the volume of the sacral roots led to the observation of a clear symmetry between left and right sides of the sacral plexus. Several works have been carried out about the set up of the body left-right axis [120]. Molecular mechanism involving the morphogenic genes such as Sonic hedgehog and Nodal may explain that the heart is left sided and the liver right sided for example. However, pair and symmetric organs still present discrepancies which underlying mechanisms are still not discovered. The symmetry was particularly obvious till 11 WG in our study, which is consistent with the literature that localize the initiation of left-right asymmetry at or shortly after gastrulation (12WG) in most of the species [120].



Chapter 8

Conclusion and Perspectives

8.1 Conclusion

As pediatric surgeons dealing with rare diseases such as pelvic tumors and malformations, our aim is to ensure an optimal surgical management. This includes either to entirely remove the tumor or to restore a normal anatomy, while lowering the surgical trauma. In that scope, we need to preserve at best the surrounding healthy organs, and especially the PNN, which handles the function of the pelvic organs. Maintaining the PNN integrity is the key factor for both a good functional outcome and a satisfying life quality for the children. This goal requires a good pre-operative knowledge of the PNN anatomy in every patient.

After performing the extensive state of art of the methods allowing for exploring the PNN anatomy in a in-vivo and non-invasive manner, we chose to use diffusion MRI combined with DTI tractography. We benefited from the high income of patients presenting pelvic rare diseases managed in Necker Hospital to build a representative database. Taking into account the current advantages and limitations due to soft and hardware diffusion MRI characteristics, we designed our own pre- and post-processing method. We then optimized it according to the tractography results embedded in the 3D patient specific models analyzed thanks to our anatomical knowledge of the PNN.

This method proved to be robust and efficient for PNN representation, both in adults and pediatric patients either with normal and abnormal pelvic anatomy. During this process, we benefited from daily interactions between research engineers in medical imaging and surgeons, that allowed for using the state of art tools in tractography and analyzing the results from a clinical point of view. Regarding the results in ARM patients, the most interesting finding was that after the age of five, the volume of the sacral roots seemed to reach a plateau, as if their growth really slows down after that age, in opposition to the other structures of the body. ARM patients also presented the tendency to have a prominent right side in the sacral plexus roots. If confirmed by further studies, it may lead to unveil common molecular determinants between ARM and left-right asymmetry set up. Regarding the influence of spinal dysraphism, we found a tendency in patients with SA and/or SD to present smaller and shorter sacral plexus roots, in concordance with the hypothesis that an abnormal spine development would impair the sacral plexus roots development, especially in terms of volume and length. Regarding the influence of the level of ARM, our results were also coherent with our clinical knowledge of high ARM bearing a worse continence prognosis than low ARM. Unfortunately, we were not able to explore the inferior hypogastric plexus in pediatric patients.

Finally, in order to bring confidence into tractography results, we tested its clinical relevance in a case of a pelvic tumor removal [146], and also designed a human fetal comparative model using LSFM, with very encouraging results. To our knowledge, this study was the first attempt to validate peripheral nerve tractography by LSFM. We proved that the registration process between the MRI and LSFM acquisitions was feasible and therefore makes it possible to evaluate the tractography method. The study of the bank of fetuses from Institut de la Vision laboratory also led to interesting results: sacral roots L5 to S4 globally grow with the developmental age but relatively less compared to the volume of L5 vertebra. Nervous structures volume is less and less important relatively to the global fetal volume with aging. Coccygeal roots were observed till 8.5 WG. LSFM also provided detailed anatomical information of distal nerves such as the perineal nerve till its termination into the clitoridian or penian branch, confirming that all pelvic nervous structures are present since very early ages of development. Finally, the analysis of the volume of the sacral roots led to the observation of a clear symmetry between left and right sides of the sacral plexus. The symmetry was particularly obvious till 11 WG in our study, which is consistent with our knowledge that localize the initiation of left-right asymmetry at or shortly after gastrulation (12WG) in most of the species.

8.2 Perspectives

This work rises numerous perspectives of both further translational research and direct clinical applications.

While diving into the subject of PNN anatomy exploration, we realized that the classical anatomy text books, even if very precise, lacked from pedagogy to really understand and memorize on the long term the complexity of the PNN. A 3D visualization of these complex networks, with an interactive anatomical representation, would be of great help for students learning anatomy, but also junior and senior surgeons willing to refresh their knowledge before operating on a pelvis. In that scope, developing the field of PNN tractography may lead to the constitution of numerical 3D atlases, of both normal and abnormal anatomy. They do not exist to date, but would constitute a real asset for both teaching anatomy and enhancing surgical practice.

Always exploring the atlas topic, the human fetal model project could lead if implemented with more subjects to build developmental fetal atlases of the PNN. It may highlights differences in sexual differentiation, or be the reference for studies in abnormal fetal pelvic anatomy. Indeed, several pelvic pathologies can be diagnosed prenatally and therefore raise the need for prenatal counselling, such as ano-rectal malformations, Currarino syndrome, spina bifida, or spinal dysraphism. Any supplementary knowledge about the pelvic nerves developmental status would be of great help in more fine tuning of prognosis evaluation. In the same scope, enhancing our knowledge of the development of pelvic nerves during the embryonic period could also lead to useful genotype-phenotype correlations.

In the actual context of surgery enhanced with new technological tools, this thesis highlights all the possibilities brought by visualizing patient-specific 3D models including nervous anatomy. It however requires a complex work-flow including MRI acquisition within the radiological department, pre- and post-processing methods of the images, and portability of the 3D models. This process will benefit in the incoming years from the increasing performance of MRI scanners, automatizing the process of image segmentation thanks to deep learning algorithm in image recognition, and technological upgrade of portable devices usable in a medical environment. The key point of this evolution is to achieve an efficient but complex association between: the state of the art methods in medical image processing that require a solid engineering and coding background, and their translation into user friendly tools usable by medical practitioners possessing the medical and anatomical background required for an accurate analysis of the patients 3D model. In parallel of this evolution, surgeons will be progressively able to use these models in their daily medical practice.

Before the surgery, the off-line computed 3D patient specific model including the segmentation of the organs and the nerves may be used to plan the surgery during the medical staff, analyse the eventual difficulties and anticipate potential complications such as neurological sequels, especially in difficult cases. The surgeons could also define the best surgical approach among the several possible state of the art or innovative techniques, such as the robotics for example. Also, thanks to the innovations in virtual reality, we can also imagine virtual training sessions based on the patient anatomy, in order to include a close-to-reality cognitive simulation for the surgeon before performing surgery onto the patient. This could soon become a mandatory gold standard in optimized surgical practice, in analogy with flying pilot training.

During the surgery, in the operative room, the 3D model may be displayed on an additional screen near the surgical field to help the surgeon localize critical structures such as vessels and nerves. In a near future, we can also imagine technological breakthroughs in morphing algorithms for example that would allow for real time image guided surgery with image overlay in soft, moving and deformable structures defining the abdomino-pelvic area. This may especially be possible using robotic surgery, as the robotic platform is a perfect set-up for implementing medical imaging in real time. It would also be possible in open surgery using the glasses providing an overlay between reality and computed 3D models.

After the surgery, the 3D model may be used to evaluate the consequences of surgery on pelvic innervation, correlated with the clinical evaluation of the patient, regarding urinary, digestive and genital functions. Surgical techniques, are numerous, experience and anatomical knowledge of complex areas such as the pelvis are sometimes variable among the surgeons. A surgical expertise may be reached more easily and rapidly with the help of an impartial tool such as radiology, instead of subjective and sometimes confidential clinical evaluation of our own surgical results. 3D models with nervous anatomy may also be used to evaluate and adapt adjuvant therapies such as radiotherapy, physiotherapy, or bio-feed back. Sole clinical evaluation of continence and sexual function after these treatments is a complex matter, because it involves a high adhesion of the patients in filling sometimes long and complex questionnaires, and a very strict and regular follow-up by highly specialized clinicians. All the management chain would highly benefit from a radiological and anatomical input. A lot has to be done in that field, especially in pediatric care.

Through-out the surgical management, the 3D patient's specific model may also be used within the portability work-flow to communicate with the patient and the parents: once the 3D model is computed off-line, it is displayed on a tablet using a 3D visualization application, that allows for an easier understanding of the pathology for the patient and/or the parents. Our preliminary experience with our portability workflow showed an undeniable improved communication with our patients. 3D color full images really help the patients, even without any anatomical knowledge, to understand what they are treated for, and what are the possible difficulties and complications of the surgery. This enlightened comprehension is very valuable for the adhesion to the treatment, the overall prognosis, and the patient-doctor confidence relationship. This first impression should however be proved by a rigorous evaluation of the input of patient-specific 3D visualization for both the surgeon and the patient or his/her parents using the use of satisfaction questionnaires and a retrospective analysis.

As a final conclusion, a multidisciplinary approach on a daily basis within the same laboratory is rarely achieved worldwide, especially in pediatrics, and motivated the creation of the IMAG2 laboratory. It is a difficult goal to reach, regarding the various knowledge backgrounds, the different vocabulary, and mainly the different ways of thinking science in biology, physics and mathematics. It is however the only way to build efficient and durable bridges between scientific communities and achieve qualitative interdisciplinary research.

Chapter 9

Appendix

9.1 Figures

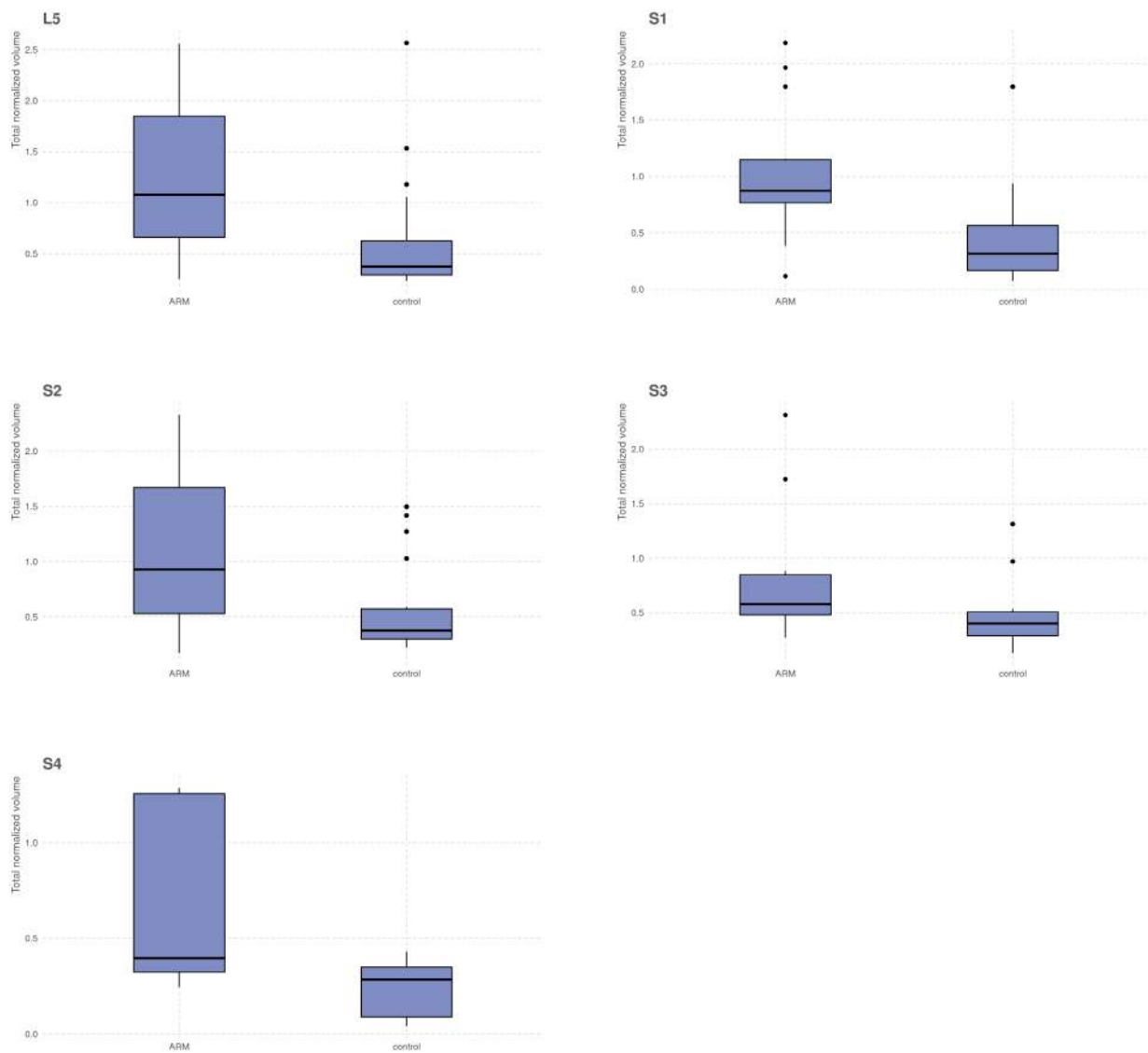


FIGURE 9.1: Scattering of total normalized volume values of sacral plexus roots in ARM patients and controls.

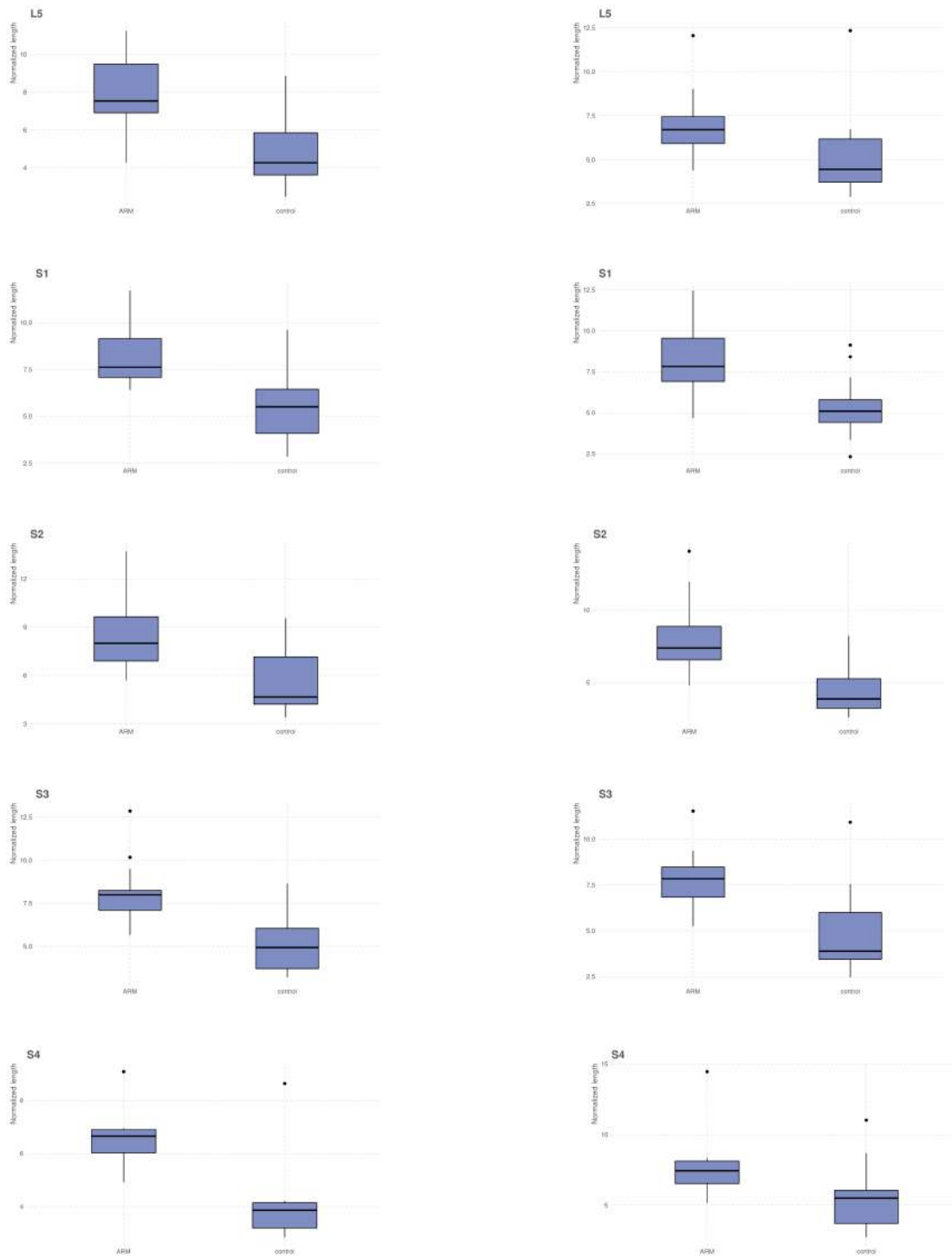


FIGURE 9.2: Scattering of normalized length values of sacral plexus roots in ARM patients and controls. On the left are represented the left roots, on the right, the right roots.

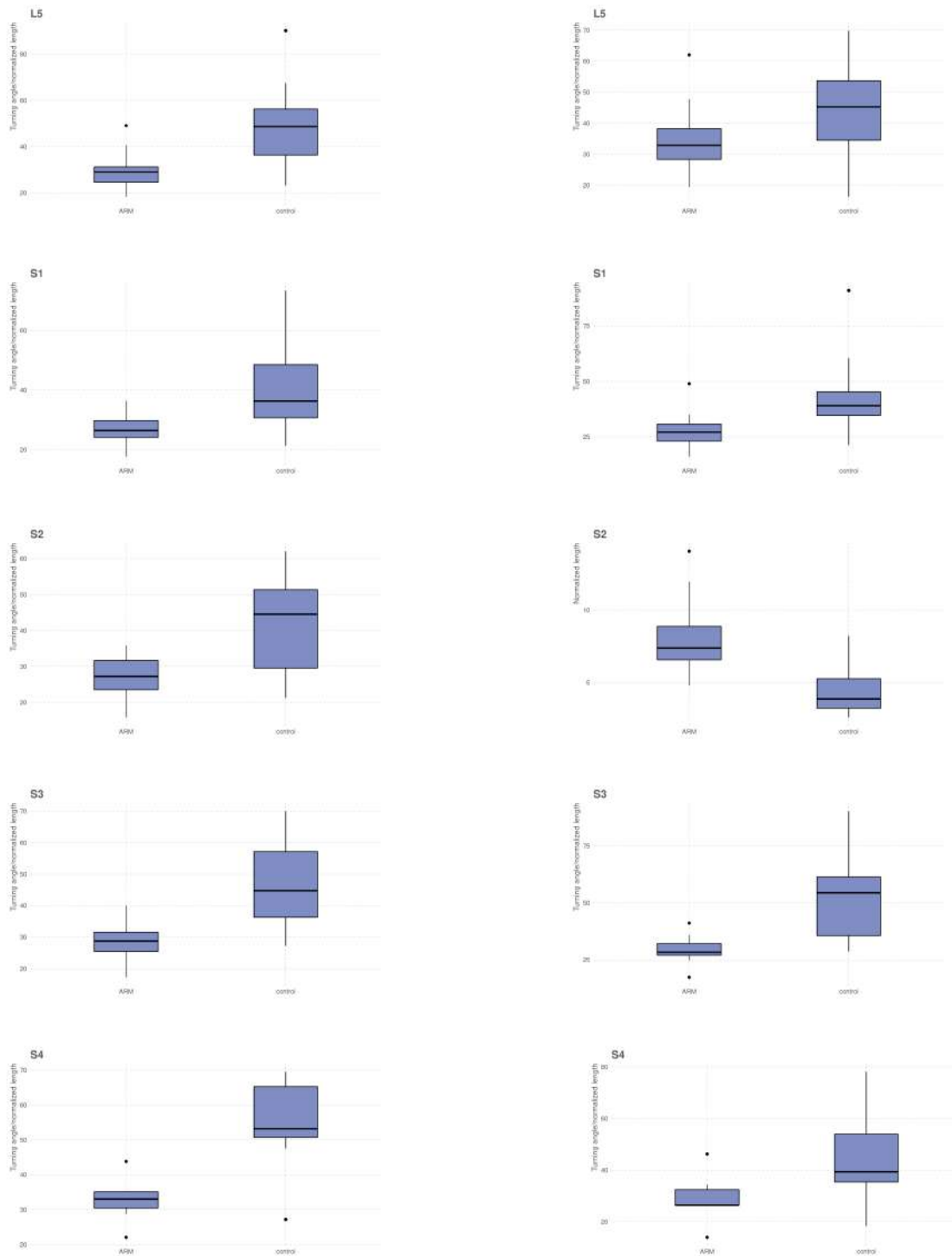


FIGURE 9.3: Scattering of angle/normalized length values of sacral plexus roots in ARM patients and controls. On the left are represented the left roots, on the right, the right roots.

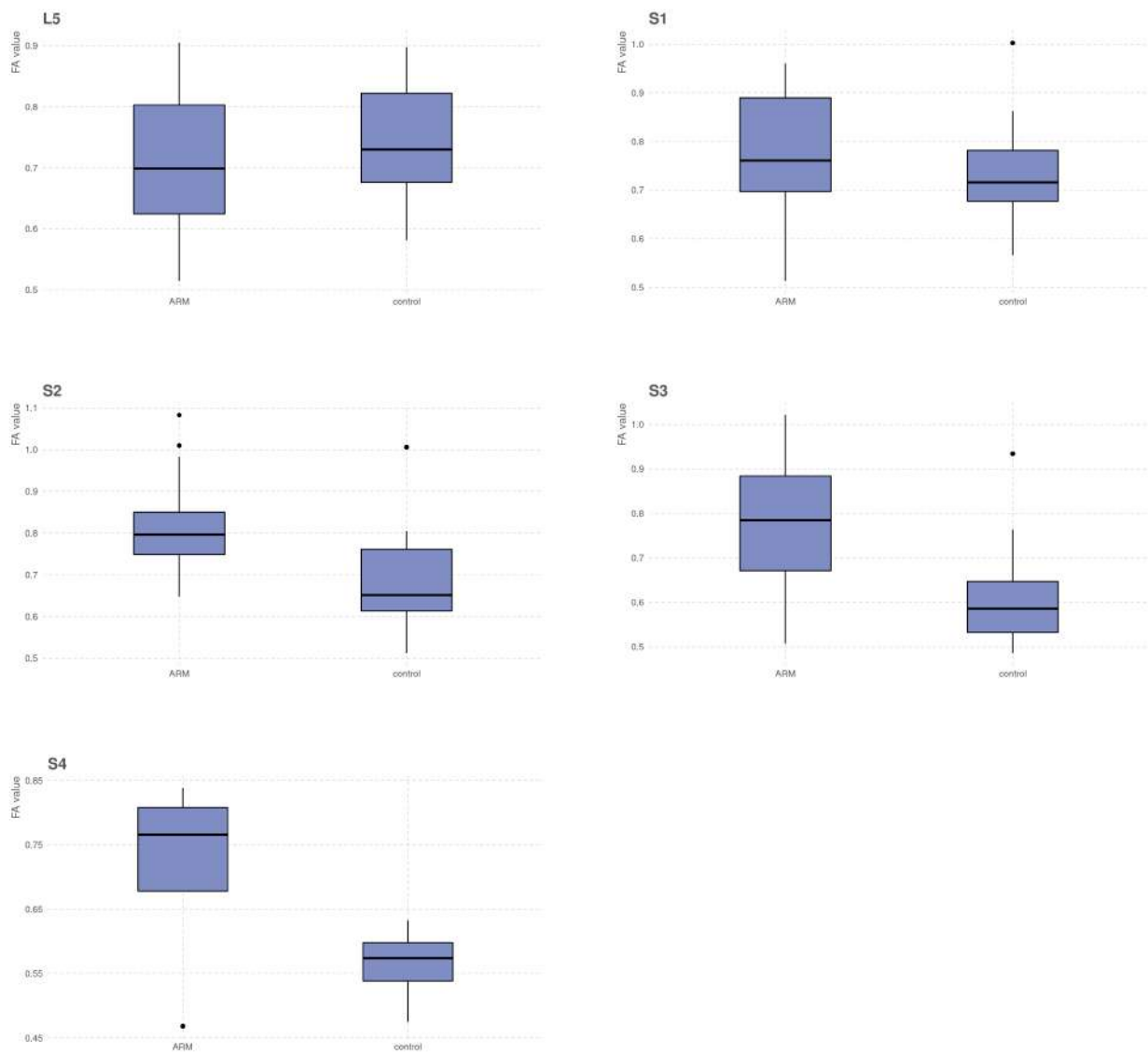


FIGURE 9.4: Scattering of mean FA values of sacral plexus roots in ARM patients and controls.

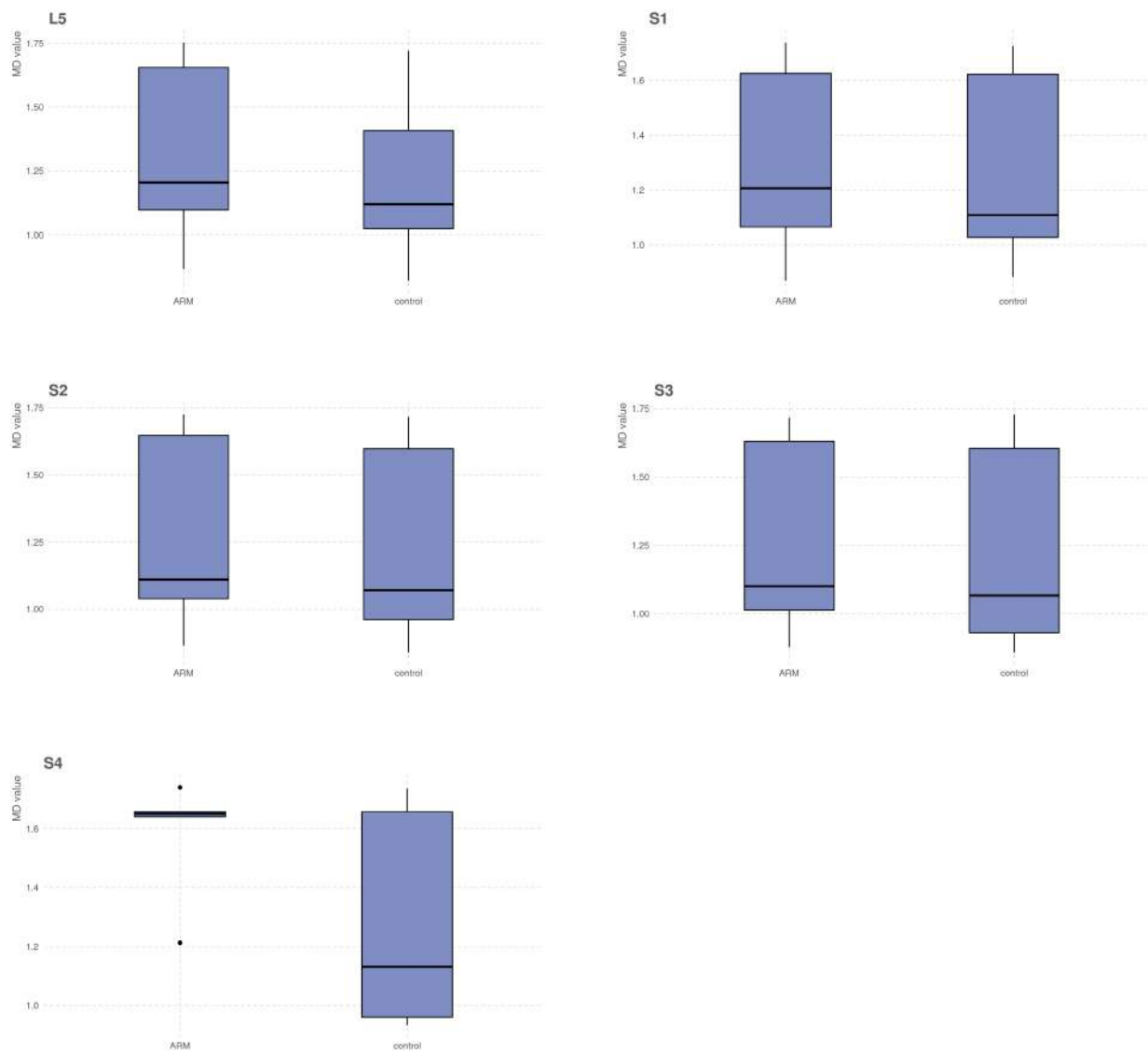


FIGURE 9.5: Scattering of mean MD values of sacral plexus roots in ARM patients and controls.

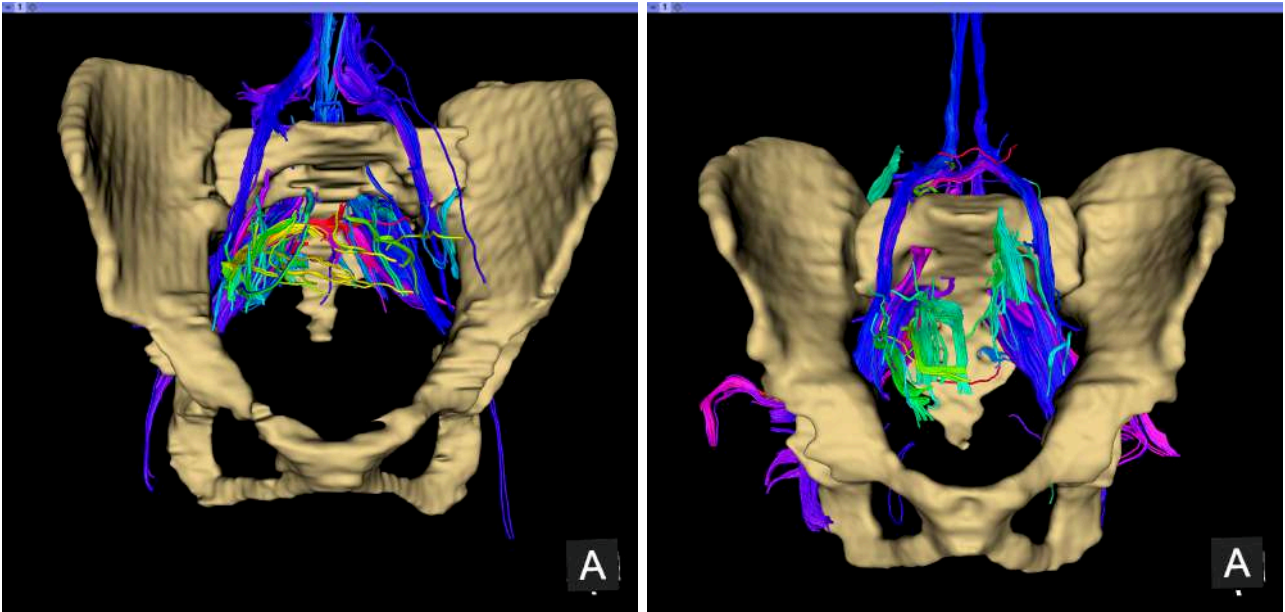


FIGURE 9.6: Examples of control patients. On the left: 3D model including PNN tractogram in a 14 years old girl with a left ovarian teratoma. On the right: 3D model including PNN tractogram in a 13 years old boy with a veino-lymphatic malformation of the bladder.

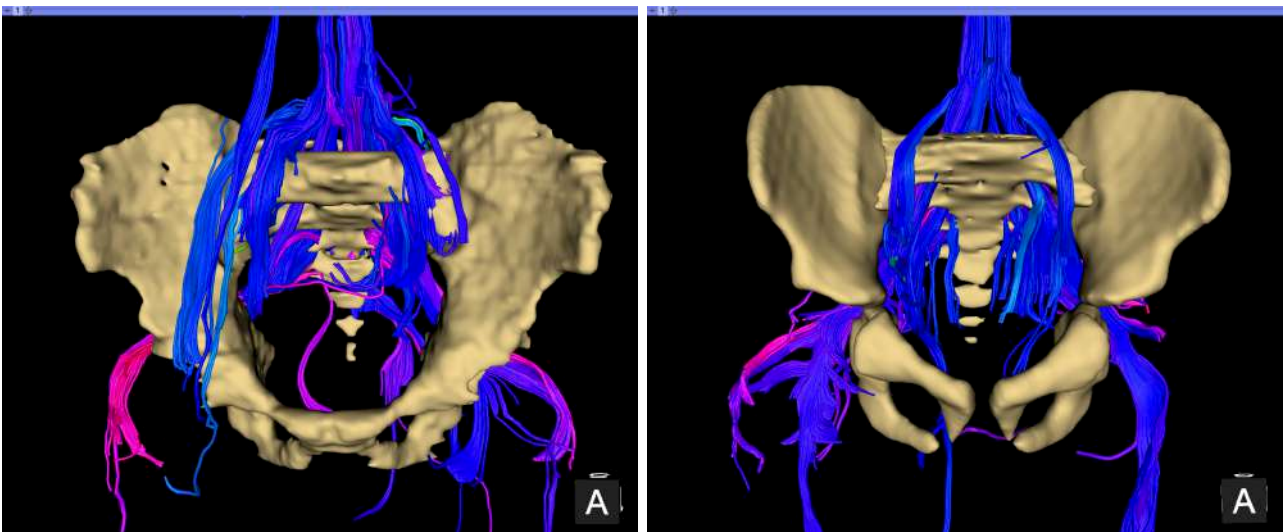


FIGURE 9.7: Examples of ARM patients without SA or SD. On the left: 3D model including PNN tractogram in a 4 years old girl with a low ARM. On the right: 3D model including PNN tractogram in a 5 years old boy with a low ARM.

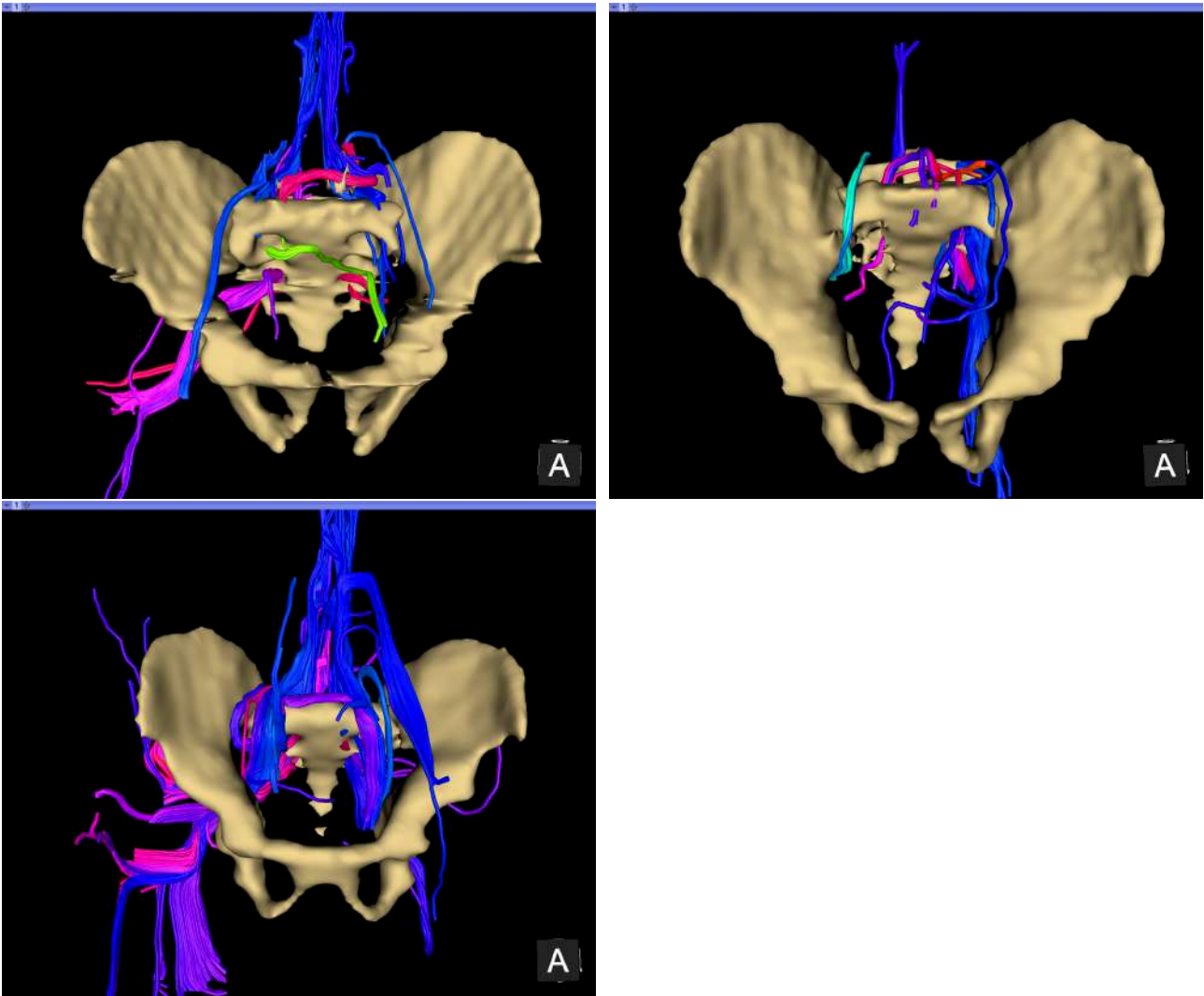


FIGURE 9.8: Examples of ARM patients without SA or SD. On the top: 3D model including PNN tractogram in 2 boys of 6 months old with high ARMs. On the bottom: 3D model including PNN tractogram in a 6 months old girl with a high ARM.

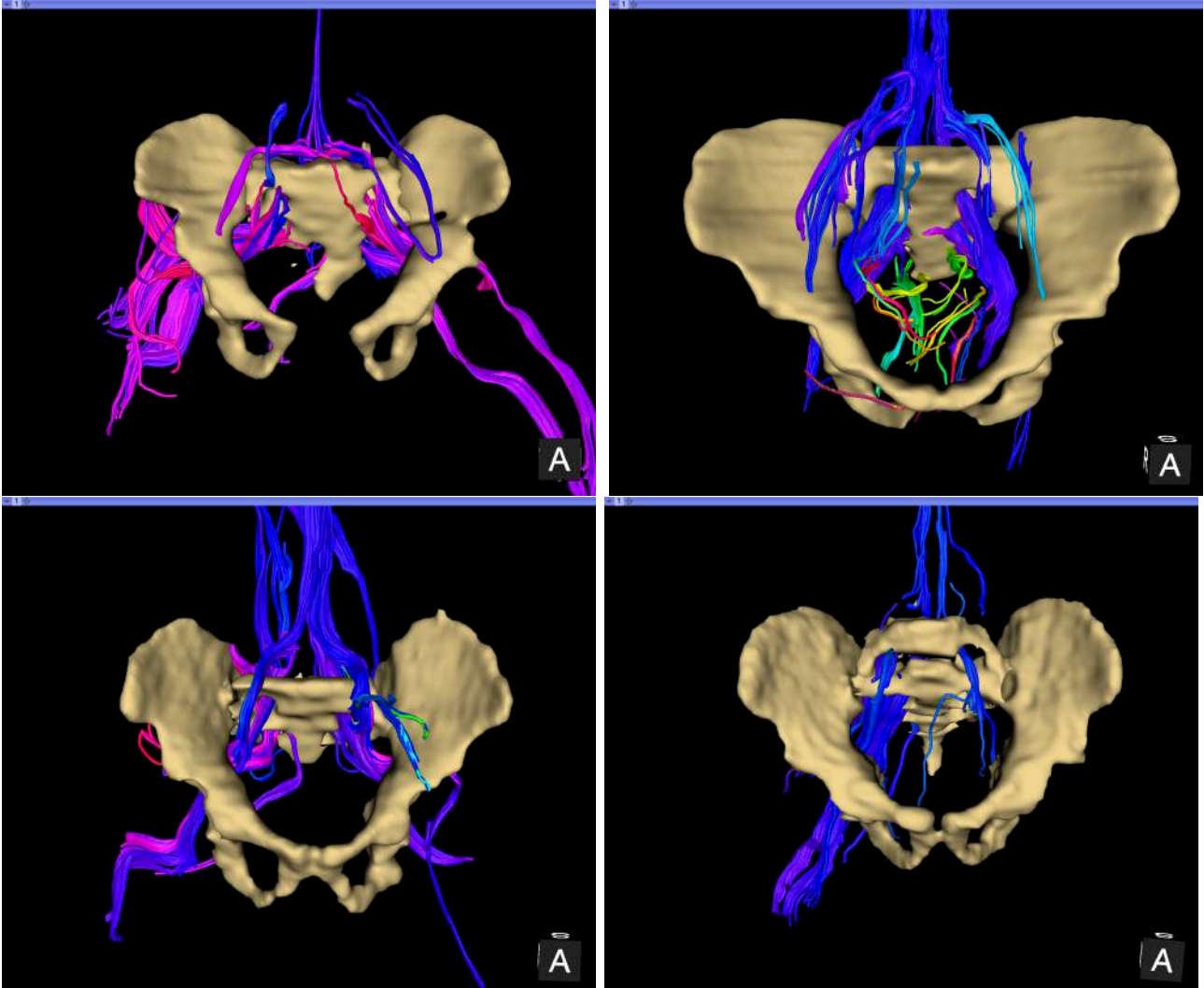


FIGURE 9.9: Examples of ARM patients with SA and/or SD. Top-left: 3D model including PNN tractogram in a 3 months old boy with a sacral agenesis below S2 associated with a tethered chord and a secondary syringomyelia, in the context of a very complex caudal pole malformation called a caudal duplication: diphalia, bladder duplication, rectal and colic duplication, thoracic vertebra malformation, and right club foot. Top-right: 3D model including PNN tractogram in a 9 years old girl with a SA below S2 in the context of a high cloacal malformation. Bottom-left: 3D model including PNN tractogram in a 6 months old boy with a SA below S2 associated with a short spinal chord (conus medullaris terminating abruptly in L1) in a context of a low ARM. Bottom-right: 3D model including PNN tractogram in a 2 years old girl with a non operated filum lipoma in the context of a Pallister Hall syndrome with a low ARM, a vaginal atresia, a Hirschsprung disease, an hypothalamic hamartoma, a choanal atresia and a laryngeal diastema.

9.2 Publications

Journal Articles:

- Virzi A ; **Muller C.O** ; Marret J-B ; Mille E ; Berteloot L ; Boddaert N ; Gori P ; Sarnacki S ; and Bloch I. Comprehensive review of 3D segmentation software tools for pediatric MRI usable for pelvic and abdominal surgery planning. *Journal of Digital Imaging*. February 2020;33(1):99-110.
- **Muller C.O** ; Mille E ; Virzi A ; Gori P ; Marret J-B ; Berteloot L ; Grevent D ; Blanc T ; Boddaert N ; Bloch I ; Sarnacki S. Integrating tractography in pelvic surgery: a proof of concept. *Journal of Pediatric Surgery Case report*. September 2019;Vol 48;101268.

Congress with proceedings:

- Virzi A ; **Muller C.O** ; Marret J-B ; Berteloot L ; Boddaert N ; Sarnacki S and Bloch I. A new method based on template registration and deformable models for pelvic bones semi-automatic segmentation in pediatric MRI. *IEEE 14th ISBI*, 2017, 323-326.
- **Muller C.O**, Virzi A ; Marret J-B ; Mille E ; Berteloot L ; Grevent D ; Blanc T ; Garcelon N ; Buffet I ; Hullier Amnard E ; Gori P ; Boddaert N ; Bloch I ; Sarnacki S. Towards building 3D individual models from MRI segmentation and tractography to enhance pediatric surgery planning of pelvic tumors and malformations. *Surgetica 2017*, Strasbourg, France, 2017, pp. 113-115.
- Virzi A ; Gori P ; **Muller C.O**; Mille E ; Peyrot Q ; Berteloot L ; Boddaert N ; Sarnacki S ; Bloch I. Segmentation of pelvic vessels in pediatric MRI using a patch-based deep learning approach. *MICCAI 2018*.
- **Muller CO** ; Delmonte A ; Meignan P ; Peyrot Q ; Virzi A ; Berteloot L ; Grevent D ; Blanc T ; Boddaert N ; Bloch I ; Sarnacki S. Nervous System Exploration Using Tractography To Enhance Pelvic Surgery. *Surgetica*, Rennes, France, 2019.

Congress without proceedings:

- **Muller C.O** ; Virzi A ; Gori P ; Marret J-B ; Mille E ; Berteloot L ; Grevent D ; Cretolle C ; Blanc T ; Boddaert N ; Bloch I ; Sarnacki S. Analysis of the sacral plexus anatomy using diffusion tensor MRI based neurotractography, according to spinal dysraphism, sacral anomaly and type of anorectal malformation. *EUPSA 2018 Paris*.
- **Muller CO** ; Delmonte A ; Meignan P ; Peyrot Q ; Virzi A ; Berteloot L ; Grévent D ; Blanc T ; Gori P ; Boddaert N ; Bloch I ; Sarnacki S. Etude exploratoire du réseau nerveux pelvien par tractographie. *SFCP Strasbourg 2019*.
- Meignan P ; **Muller CO** ; Delmonte A ; Meignan P ; Peyrot Q ; Belle M ; Berteloot L ; Grévent D ; Blanc T ; Gori P ; Boddaert N ; Chedotal A ; Bloch I ; Sarnacki S. Etude du développement du système nerveux périphérique pelvien : du fœtus à l'enfant porteur de malformations et tumeurs pelviennes. *SFCP Strasbourg 2019*.
- Peyrot Q ; **Muller CO** ; Delmonte A ; Meignan P ; Peyrot Q ; Virzi A ; Berteloot L ; Grévent D ; Blanc T ; Gori P ; Boddaert N ; Bloch I ; Sarnacki S. Reconstruction 3d en IRM du pelvis de l'enfant : segmentation des structures osseuses par intelligence artificielle. *SFCP Strasbourg 2019*.

Bibliography

- [1] S.K. Ahmed, S.I. Robinson, C.A. Arndt, I.A. Petersen, M.G. Haddock, P.S. Rose, and N.N. Issa Laack. Pelvis Ewing sarcoma: Local control and survival in the modern era. *Pediatric Blood & Cancer*, 64(9), September 2017.
- [2] Y. Aigrain, A. El Ghoneimi, and P. de Lagausie. *Reflux vésico-urétéral de l'enfant et malformations vésicales*. Sauramps Médical, Montpellier, December 2001.
- [3] L. Alamo, B.J. Meyrat, J-Y. Meuwly, R.A. Meuli, and F. Gudinchet. Anorectal Malformations: Finding the Pathway out of the Labyrinth. *Radiographics*, 33(2):491–512, March 2013.
- [4] P. Alessandrini, G. Audry, C.-L. Borrione, and M. Chabaud. *Les anomalies gynécologiques en pédiatrie*. Sauramps Médical, Montpellier, December 2005.
- [5] B. Alsaid, T. Bessede, D. Diallo, I. Karam, J-F. Uhl, V. Delmas, S. Droupy, and G. Benoît. Computer-assisted anatomic dissection (CAAD): evolution, methodology and application in intra-pelvic innervation study. *Surgical and radiologic anatomy*, 34(8):721–729, October 2012.
- [6] R. P. Altman, J. G. Randolph, and J. R. Lilly. Sacrococcygeal teratoma: American Academy of Pediatrics Surgical Section Survey-1973. *Journal of Pediatric Surgery*, 9(3):389–398, June 1974.
- [7] O. Arango-Toro and J. M. Domenech-Mateu. Development of the pelvic plexus in human embryos and fetuses and its relationship with the pelvic viscera. *European Journal of Morphology*, 31(3):193–208, September 1993.
- [8] W. Ashcraft. *Pediatric Surgery* - Keith W. Ashcraft - Google Livres, 2005.
- [9] A. Attyé, A. Karkas, I.M. Troprès, M. Roustit, A. Kastler, G. Bettega, L. Lamalle, F. Renard, C. Righini, and A. Krainik. Parotid gland tumours: MR tractography to assess contact with the facial nerve. *European Radiology*, 26(7):2233–2241, July 2016.
- [10] D. Aubert and J.-M. Guys. *La vessie neurologique de l'enfant*. Sauramps Médical, Montpellier, 1998.
- [11] D.E. Azagury, M. Dua, J. Barrese, J. Henderson, N. Buchs, F. Ris, J.M. Cloyd, J.B. Martinie, S. Razzaque, S. Nicolau, L. Soler, J. Marescaux, and B.C. Visser. Image-guided surgery. *Current Problems in Surgery*, 52(12):476–520, December 2015.
- [12] C. Baayen, F. Feuillet, P. Clermidi, C. Crétole, S. Sarnacki, G. Podevin, and J-B. Hardouin. Validation of the French versions of the Hirschsprung's disease and Anorectal malformations Quality of Life (HAQL) questionnaires for adolescents and adults. *Health and Quality of Life Outcomes*, 15:1–10, January 2017.
- [13] R. Bagatell, K. McHugh, A. Naranjo, C. Van Ryn, C. Kirby, P. Brock, K.A. Lyons, L.J. States, Y. Rojas, A. Miller, S.L. Volchenboum, T. Simon, B. Krug, S. Sarnacki, D. Valteau-Couanet, D. von Schweinitz, B. Kammer, C. Granata, L. Pio, J.R. Park, and J. Nuchtern. Assessment of Primary Site Response in Children With High-Risk Neuroblastoma: An International Multicenter Study. *Journal of Clinical Oncology*, 34:740–746, March 2016.

-
- [14] V. Balaya, F. Guimiot, Jean-François Uhl, C. Ngo, M. Delomenie, H. Bonsang-Kitzis, M. Gosset, M. Mimouni, A-S. Bats, V. Delmas, R. Douard, and F. Lécuro. Three-Dimensional Modelization of the Female Human Inferior Hypogastric Plexus: Implications for Nerve-Sparing Radical Hysterectomy. *Gynecologic and Obstetric Investigation*, 84(2):196–203, 2019.
- [15] V. Balbi, J-F. Budzik, A. Duhamel, A. Bera-Louville, V. Le Thuc, and A. Cotten. Tractography of lumbar nerve roots: initial results. *European Radiology*, 21(6):1153–1159, June 2011.
- [16] V. Baliyan, C.J. Das, R. Sharma, and A.K. Gupta. Diffusion weighted imaging: Technique and applications. *World Journal of Radiology*, 8(9):785–798, September 2016.
- [17] Y. Bar Yosef, J. Binyamini, H. Matzkin, and J. Ben-Chaim. Midline dorsal plication technique for penile curvature repair. *The Journal of Urology*, 172(4 Pt 1):1368–1369, October 2004.
- [18] C.W. Barth and S.L. Gibbs. Direct Administration of Nerve-Specific Contrast to Improve Nerve Sparing Radical Prostatectomy. *Theranostics*, 7(3):573–593, 2017.
- [19] L. S. Baskin, A. Erol, Y. W. Li, and G. R. Cunha. Anatomical studies of hypospadias. *The Journal of Urology*, 160(3 Pt 2):1108–1115; discussion 1137, September 1998.
- [20] L. S. Baskin, A. Erol, Y. W. Li, and W. H. Liu. Anatomy of the neurovascular bundle: is safe mobilization possible? *The Journal of Urology*, 164(3 Pt 2):977–980, September 2000.
- [21] L. S. Baskin, A. Erol, Y. W. Li, W. H. Liu, E. Kurzrock, and G. R. Cunha. Anatomical studies of the human clitoris. *The Journal of Urology*, 162(3 Pt 2):1015–1020, September 1999.
- [22] L.S. Baskin. Restoring normal anatomy in female patients with atypical genitalia. *Seminars in Perinatology*, 41(4):227–231, June 2017.
- [23] P. J. Basser and C. Pierpaoli. Microstructural and physiological features of tissues elucidated by quantitative-diffusion-tensor MRI. *Journal of Magnetic Resonance. Series B*, 111(3):209–219, June 1996.
- [24] P.J. Basser, S. Pajevic, C. Pierpaoli, J. Duda, and A. Aldroubi. In vivo fiber tractography using DT-MRI data. *Magnetic Resonance in Medicine*, 44(4):625–632, October 2000.
- [25] C. Beaulieu. The basis of anisotropic water diffusion in the nervous system - a technical review. *NMR in biomedicine*, 15(7-8):435–455, November 2002.
- [26] M. Belle, D. Godefroy, G. Couly, S.A. Malone, F. Collier, P. Giacobini, and A. Chedotal. Tridimensional Visualization and Analysis of Early Human Development. *Cell*, 169(1):161–173.e12, March 2017.
- [27] M. Belle, D. Godefroy, C. Dominici, C. Heitz-Marchaland, P. Zelina, F. Hellal, F. Bradke, and A. Chédotal. A Simple Method for 3d Analysis of Immunolabeled Axonal Tracts in a Transparent Nervous System. *CellReports*, 9:1191–1201, November 2014.
- [28] M. M. Bertrand, F. Macri, R. Mazars, S. Droupy, J. P. Beregi, and M. Prudhomme. MRI-based 3d pelvic autonomous innervation: a first step towards image-guided pelvic surgery. *European Radiology*, 24(8):1989–1997, August 2014.
- [29] T. Bessede, P. Sooriakumaran, A. Takenaka, and A. Tewari. Neural supply of the male urethral sphincter: comprehensive anatomical review and implications for continence recovery after radical prostatectomy. *World Journal of Urology*, 35(4):549–565, April 2017.
- [30] I. Bloch. Fuzzy relative position between objects in image processing: a morphological approach. *IEEE Transactions on Pattern Analysis and Machine Intelligence*, 21(7):657–664, July 1999.
- [31] I. Bloch. On fuzzy distances and their use in image processing under imprecision. *Pattern Recognition*, 32(11):1873–1895, November 1999.

-
- [32] I. Bloch. Fuzzy spatial relationships for image processing and interpretation: a review. *Image and Vision Computing*, 23(2):89–110, February 2005.
- [33] I. Bloch. Duality vs. adjunction for fuzzy mathematical morphology and general form of fuzzy erosions and dilations. *Fuzzy Sets and Systems*, 160(13):1858–1867, July 2009.
- [34] I. Bloch. Fuzzy sets for image processing and understanding. *Fuzzy Sets and Systems*, 281:280–291, December 2015.
- [35] I. Bloch, O. Colliot, and R.M. Cesar. On the ternary spatial relation "Between". *IEEE Transactions on Systems, Man and Cybernetics, Part B (Cybernetics)*, 36(2):312–327, April 2006.
- [36] H.J. Brisse, T. Blanc, G. Schleiermacher, V. Mosseri, P. Philippe-Chomette, I. Janoueix-Lerosey, G. Pierron, E. Lapouble, M. Peuchmaur, P. Fréneaux, L. Galmiche, N. Algret, M. Peycelon, J. Michon, O. Delattre, and S. Sarnacki. Radiogenomics of neuroblastomas: Relationships between imaging phenotypes, tumor genomic profile and survival. *PLOS ONE*, 12:e0185190–17, September 2017.
- [37] J-F. Budzik, S. Verclytte, G. Lefebvre, A. Monnet, G. Forzy, and A. Cotten. Assessment of reduced field of view in diffusion tensor imaging of the lumbar nerve roots at 3 T. *European Radiology*, 23(5):1361–1366, May 2013.
- [38] O. Camara, G. Delso, O. Colliot, A. Moreno-Ingelmo, and I. Bloch. Explicit Incorporation of Prior Anatomical Information Into a Nonrigid Registration of Thoracic and Abdominal CT and 18-FDG Whole-Body Emission PET Images. *IEEE Transactions on Medical Imaging*, 26(2):164–178, February 2007.
- [39] J. Canny. A Computational Approach to Edge Detection. *IEEE Transactions on Pattern Analysis and Machine Intelligence*, PAMI-8(6):679–698, November 1986.
- [40] M. Catani and M. Thiebautdeschotten. A diffusion tensor imaging tractography atlas for virtual in vivo dissections. *Cortex*, 44:1105–1132, September 2008.
- [41] K.A. Cauley and C.G. Filippi. Diffusion-tensor imaging of small nerve bundles: cranial nerves, peripheral nerves, distal spinal cord, and lumbar nerve roots—clinical applications. *American journal of roentgenology*, 201(2):W326–335, August 2013.
- [42] V. Celentano. Nerve-sparing surgery and sexual and urinary dysfunction after multimodality treatment for rectal cancer. *Techniques in Coloproctology*, 21:325–325, February 2017.
- [43] T.F. Chan and L.A. Vese. Active contours without edges. *IEEE Transactions on Image Processing*, 10(2):266–277, February 2001.
- [44] T. M. Chandler, L. S. Machan, P. L. Cooperberg, A. C. Harris, and S. D. Chang. Mullerian duct anomalies: from diagnosis to intervention. *The British Journal of Radiology*, 82(984):1034–1042, December 2009.
- [45] C. Chargari, C. Haie-Meder, F. Guérin, V. Minard-Colin, G. de Lambert, R. Mazon, A. Escande, F. Marsolat, I. Dumas, E. Deutsch, D. Valteau-Couanet, G. Audry, O. Oberlin, and H. Martelli. Brachytherapy Combined With Surgery for Conservative Treatment of Children With Bladder Neck and/or Prostate Rhabdomyosarcoma. *International Journal of Radiation Oncology, Biology, Physics*, 98(2):352–359, January 2017.
- [46] A. Cheikhelard, S. Irtan, D. Orbach, V. Minard-Colin, J. Rod, H. Martelli, and S. Sarnacki. Urachal rhabdomyosarcoma in childhood: a rare entity with a poor outcome. *Journal of Pediatric Surgery*, 50:1329–1333, August 2015.
- [47] D.Q. Chen, J. Quan, A. Guha, M. Tymianski, D. Mikulis, and M. Hodaie. Three-dimensional in vivo modeling of vestibular schwannomas and surrounding cranial nerves with diffusion imaging tractography. *Neurosurgery*, 68(4):1077–1083, April 2011.

-
- [48] Y-Y. Chen, X-F. Lin, F. Zhang, X. Zhang, H-J. Hu, D-J. Wang, L-J. Lu, and J. Shen. Diffusion Tensor Imaging of Symptomatic Nerve Roots in Patients with Cervical Disc Herniation. *Academic Radiology*, 21(3):338–344, March 2014.
- [49] T. L. Chenevert, J. A. Brunberg, and J. G. Pipe. Anisotropic diffusion in human white matter: demonstration with MR techniques in vivo. *Radiology*, 177(2):401–405, November 1990.
- [50] G.S. Chilla, C.H. Tan, C. Xu, and C.L. Poh. Diffusion weighted magnetic resonance imaging and its recent trend—a survey. *Quantitative Imaging in Medicine and Surgery*, 5(3):407–422, June 2015.
- [51] K.S. Choi, M.S. Kim, H-G. Kwon, S-H. Jang, and O-L. Kim. Preoperative Identification of Facial Nerve in Vestibular Schwannomas Surgery Using Diffusion Tensor Tractography. *Journal of Korean Neurosurgical Society*, 56(1):11, 2014.
- [52] L. Chuanting, W. Qingzheng, X. Wenfeng, H. Yiyi, and Z. Bin. 3.0t MRI tractography of lumbar nerve roots in disc herniation. *Acta Radiologica*, 55(8):969–975, October 2014.
- [53] A. O. Ciftci, M. Bingöl-Koloğlu, M. E. Senocak, F. C. Tanyel, M. Büyükpamukçu, and N. Büyükpamukçu. Testicular tumors in children. *Journal of Pediatric Surgery*, 36(12):1796–1801, December 2001.
- [54] P. Clermidi, G. Podevin, C. Crétole, S. Sarnacki, and J-B. Hardouin. The challenge of measuring quality of life in children with Hirschsprung’s disease or anorectal malformation. *Journal of Pediatric Surgery*, 48:2118–2127, October 2013.
- [55] O. Colliot, O. Camara, and I. Bloch. Integration of fuzzy spatial relations in deformable models—Application to brain MRI segmentation. *Pattern Recognition*, 39(8):1401–1414, August 2006.
- [56] P. Combemale, L. Valeyrie-Allanore, F. Giammarile, S. Pinson, B. Guillot, D.M. Goulart, P. Wolkenstein, J-Y. Blay, and T. Mognetti. Utility of 18f-FDG PET with a semi-quantitative index in the detection of sarcomatous transformation in patients with neurofibromatosis type 1. *PloS One*, 9(2):e85954, 2014.
- [57] V.E. Coterio, S.Y. Kimm, T.M. Siclovan, R. Zhang, E.M. Kim, K. Matsumoto, T. Gondo, P.T. Scardino, S. Yazdanfar, V.P. Laudone, and C.A. Tan Hehir. Improved Intraoperative Visualization of Nerves through a Myelin-Binding Fluorophore and Dual-Mode Laparoscopic Imaging. *PloS One*, 10(6):e0130276, 2015.
- [58] J. Courtier, A.G. Rao, and S.A. Anupindi. Advanced imaging techniques in pediatric body MRI. *Pediatric Radiology*, 47(5):522–533, May 2017.
- [59] M. Cox, S.W. Gould, D.J. Podberesky, and M. Epelman. Magnetic resonance imaging of acquired disorders of the pediatric female pelvis other than neoplasm. *Pediatric Radiology*, 46(6):806–817, May 2016.
- [60] C. Cretolle, G. Podevin, V. Rousseau, H. Lottmann, I. Alova, S. Irtan, S. Lortat-Jacob, A. Cazenave, G. Disnan, P. Slamani, C. Tonatello, H. Kahia-Aoul, Y. Aigrain, P. A. Lehur, and S. Sarnacki. Apports du plan maladies rares à la prise en charge des malformations anorectales. *Archives de pédiatrie*, 20:720–722, July 2013.
- [61] C. Cretolle, V. Rousseau, H. Lottmann, S. Irtan, S. Lortat-Jacob, I. Alova, J. L. Michel, Y. Aigrain, G. Podevin, P. A. Lehur, and S. Sarnacki. Malformations ano-rectales. *Archives de pédiatrie*, 20:S19–S27, September 2013.
- [62] C. Cretolle, S. Sarnacki, J. Amiel, D. Geneviève, F. Encha-Razavi, S. Zrelli, M. Zérah, C. Nihoul Fékété, and S. Lyonnet. Currarino syndrome shown by prenatal onset ventriculomegaly and spinal dysraphism. *American Journal of Medical Genetics Part A*, 143A:871–874, April 2007.

-
- [63] A. Crucis, W. Richer, L. Brugières, C. Bergeron, A. Marie-Cardine, J-L. Stephan, P. Girard, N. Corradini, M. Munzer, B. Lacour, V. Minard-Colin, S. Sarnacki, D. Ranchere-Vince, D. Orbach, and F. Bourdeaut. Rhabdomyosarcomas in children with neurofibromatosis type I: A national historical cohort. *Pediatric Blood and Cancer*, 62:1733–1738, April 2015.
- [64] C. Crétolle, M. Zérah, F. Jaubert, S. Sarnacki, Y. Révillon, S. Lyonnet, and C. Nihoul-Fékété. New clinical and therapeutic perspectives in Currarino syndrome (study of 29 cases). *Journal of Pediatric Surgery*, 41(1):126–131; discussion 126–131, January 2006.
- [65] G. Currarino, D. Coln, and T. Votteler. Triad of anorectal, sacral, and presacral anomalies. *AJR. American journal of roentgenology*, 137(2):395–398, August 1981.
- [66] F. De Corti, S. Sarnacki, C. Patte, V. Mosseri, M. C. Baranzelli, H. Martelli, C. Conter, D. Frappaz, and D. Orbach. Prognosis of malignant sacrococcygeal germ cell tumours according to their natural history and surgical management. *Surgical Oncology*, 21:e31–e37, June 2012.
- [67] A. Delmonte, I. Bloch, D. Hasboun, C. Mercier, J. Pallud, and P. Gori. Segmentation of White Matter Tractograms Using Fuzzy Spatial Relations. *Human Brain Mapping (OHBM)*, 2018.
- [68] M. Descoteaux, R. Deriche, T.R. Knösche, and A. Anwander. Deterministic and probabilistic tractography based on complex fibre orientation distributions. *IEEE transactions on medical imaging*, 28(2):269–286, February 2009.
- [69] A. Di Cesare, E. Leva, F. Macchini, L. Canazza, G. Carrabba, M. Fumagalli, F. Mosca, and M. Torricelli. Anorectal malformations and neurospinal dysraphism: is this association a major risk for continence? *Pediatric surgery international*, 26(11):1077–1081, November 2010.
- [70] J. Dolz, C. Desrosiers, and I. Ben Ayed. 3d fully convolutional networks for subcortical segmentation in MRI: A large-scale study. *NeuroImage*, 170:456–470, April 2018.
- [71] R.L. Drake, W. Vogl, A.W. Mitchell, and H. Gray. *Gray’s anatomy for students*. Churchill Livingstone/Elsevier, Philadelphia, PA, third edition edition, 2015.
- [72] G.P. Dunn, K. Spiliopoulos, S.R. Plotkin, F.J. Hornicek, D.C. Harmon, T.F. Delaney, and Z. Williams. Role of resection of malignant peripheral nerve sheath tumors in patients with neurofibromatosis type 1. *Journal of Neurosurgery*, 118(1):142–148, January 2013.
- [73] B. M. Dunning-Davies and A. P. J. Parker. Annual review of children with neurofibromatosis type 1. *Archives of Disease in Childhood. Education and Practice Edition*, 101(2):102–111, April 2016.
- [74] T.B. Dyrby, L.V. Søgaard, G.J. Parker, D.C. Alexander, N.M. Lind, W.F. Baaré, A. Hay-Schmidt, N. Eriksen, B. Pakkenberg, O.B. Paulson, and J. Jelsing. Validation of in vitro probabilistic tractography. *NeuroImage*, 37(4):1267–1277, October 2007.
- [75] Y. Eguchi, S. Ohtori, S. Orita, H. Kamoda, G. Arai, T. Ishikawa, M. Miyagi, G. Inoue, M. Suzuki, Y. Masuda, H. Andou, M. Takaso, Y. Aoki, T. Toyone, A. Watanabe, and K. Takahashi. Quantitative Evaluation and Visualization of Lumbar Foraminal Nerve Root Entrapment by Using Diffusion Tensor Imaging: Preliminary Results. *American Journal of Neuroradiology*, 32(10):1824–1829, November 2011.
- [76] W.I. Essayed, F. Zhang, P. Unadkat, G.R. Cosgrove, A.J. Golby, and L.J. O’Donnell. White matter tractography for neurosurgical planning: A topography-based review of the current state of the art. *NeuroImage. Clinical*, 15:659–672, 2017.
- [77] D. G. R. Evans, M. E. Baser, J. McGaughan, S. Sharif, E. Howard, and A. Moran. Malignant peripheral nerve sheath tumours in neurofibromatosis 1. *Journal of Medical Genetics*, 39(5):311–314, May 2002.
- [78] H. Fan, Z. Guo, J. Fu, X. Li, J. Li, and Z. Wang. Surgical management of pelvic Ewing’s sarcoma in children and adolescents. *Oncology Letters*, 14(4):3917–3926, October 2017.

-
- [79] J.C. Fernandez-Miranda, S. Pathak, J. Engh, K. Jarbo, T. Verstynen, F-C. Yeh, Y. Wang, A. Mintz, F. Boada, W. Schneider, and R. Friedlander. High-definition fiber tractography of the human brain: neuroanatomical validation and neurosurgical applications. *Neurosurgery*, 71(2):430–453, August 2012.
- [80] R.E. Ferner and D.H. Gutmann. International consensus statement on malignant peripheral nerve sheath tumors in neurofibromatosis. *Cancer Research*, 62(5):1573–1577, March 2002.
- [81] V. Ferrari, M. Carbone, C. Cappelli, L. Boni, F. Melfi, M. Ferrari, F. Mosca, and A. Pietrabissa. Value of multidetector computed tomography image segmentation for preoperative planning in general surgery. *Surgical Endoscopy*, 26(3):616–626, March 2012.
- [82] D. S. Finley, B. M. Ellingson, S. Natarajan, T. M. Zaw, S. S. Raman, P. Schulam, R. E. Reiter, and D. Margolis. Diffusion Tensor Magnetic Resonance Tractography of the Prostate: Feasibility for Mapping Periprostatic Fibers. *Urology*, 80:219–223, July 2012.
- [83] The R foundation. The R Project for Statistical Computing, 2019.
- [84] G. Fouquier, J. Atif, and I. Bloch. Sequential model-based segmentation and recognition of image structures driven by visual features and spatial relations. *Computer Vision and Image Understanding*, 116(1):146–165, January 2012.
- [85] A. G. Franchini Melani, M. Diana, and J. Marescaux. The quest for precision in transanal total mesorectal excision. *Techniques in Coloproctology*, 20(1):11–18, January 2016.
- [86] T. Garzon-Muvdi, A. Belzberg, M.E. Allaf, and J-P. Wolinsky. Intraoperative Nerve Monitoring in Robotic-Assisted Resection Of Presacral Ganglioneuroma: Operative Technique. *Operative Neurosurgery (Hagerstown, Md.)*, 16(1):103–110, January 2019.
- [87] R. Gasparotti, G. Lodoli, A. Meoded, F. Carletti, D. Garozzo, and S. Ferraresi. Feasibility of diffusion tensor tractography of brachial plexus injuries at 1.5 T. *Investigative Radiology*, 48(2):104–112, February 2013.
- [88] J. P. Gearhart, A. Burnett, and J. H. Owen. Measurement of pudendal evoked potentials during feminizing genitoplasty: technique and applications. *The Journal of Urology*, 153(2):486–487, February 1995.
- [89] S. Gouttard, C.B. Goodlett, M. Kubicki, and G. Gerig. Measures for validation of DTI tractography. page 83140J, San Diego, California, USA, February 2012.
- [90] D.H. Gutmann, R.E. Ferner, R.H. Listernick, B.R. Korf, P.L. Wolters, and K.J. Johnson. Neurofibromatosis type 1. *Nature Reviews. Disease Primers*, 3:17004, February 2017.
- [91] D. Haak, C. Page, and T. Deserno. A Survey of DICOM Viewer Software to Integrate Clinical Research and Medical Imaging. *Journal of Digital Imaging*, 29(2):206–215, April 2016.
- [92] W. Haakma, P. Dik, B. ten Haken, M. Froeling, R.A. Nivelstein, I. Cuppen, T.P. de Jong, and A. Leemans. Diffusion tensor magnetic resonance imaging and fiber tractography of the sacral plexus in children with spina bifida. *The Journal of Urology*, 192(3):927–933, September 2014.
- [93] W. Haakma, J. Hendrikse, L. Uhrenholt, A. Leemans, L. Warner Thorup Boel, M. Pedersen, and M. Froeling. Multicenter reproducibility study of diffusion MRI and fiber tractography of the lumbosacral nerves: DTI of the Lumbosacral Nerves. *Journal of Magnetic Resonance Imaging*, 48(4):951–963, October 2018.
- [94] E. E. Hartman, F. J. Oort, D. C. Aronson, and M. A. Sprangers. Quality of life and disease-specific functioning of patients with anorectal malformations or Hirschsprung’s disease: a review. *Archives of Disease in Childhood*, 96:398–406, March 2011.
- [95] S.H. Heo, J.W. Kim, S.S. Shin, S.I. Jeong, H.S. Lim, Y.D. Choi, K.H. Lee, W.D. Kang, Y.Y. Jeong, and H.K. Kang. Review of ovarian tumors in children and adolescents: radiologic-

-
- pathologic correlation. *Radiographics: A Review Publication of the Radiological Society of North America, Inc*, 34(7):2039–2055, November 2014.
- [96] J. Hiltunen, T. Suortti, S. Arvela, M. Seppä, R. Joensuu, and R. Hari. Diffusion tensor imaging and tractography of distal peripheral nerves at 3 T. *Clinical Neurophysiology*, 116(10):2315–2323, October 2005.
- [97] P.J. Houck, M. Haché, and L.S. Sun. *Handbook of pediatric anesthesia*. Lange, 2015.
- [98] X. Huang, L. Wang, X. Zheng, and X. Wang. Comparison of perioperative, functional, and oncologic outcomes between standard laparoscopic and robotic-assisted radical prostatectomy: a systemic review and meta-analysis. *Surgical Endoscopy*, 31(3):1045–1060, March 2017.
- [99] S. Irtan, H.J. Brisse, V. Minard-Colin, G. Schleiermacher, S. Canale, and S. Sarnacki. Minimally invasive surgery of neuroblastic tumors in children: Indications depend on anatomical location and image-defined risk factors. *Pediatric Blood & Cancer*, 6, October 2014.
- [100] S. Irtan, H.J. Brisse, V. Minard-Colin, G. Schleiermacher, L. Galmiche-Rolland, C. Le Cossec, C. Elie, S. Canale, J. Michon, D. Valteau-Couanet, and S. Sarnacki. Image-defined risk factor assessment of neurogenic tumors after neoadjuvant chemotherapy is useful for predicting intraoperative risk factors and the completeness of resection. *Pediatric Blood & Cancer*, 62:1543–1549, March 2015.
- [101] S. Irtan, D. Orbach, S. Helfre, and S. Sarnacki. Ovarian transposition in prepubescent and adolescent girls with cancer. *Lancet Oncology*, 14:e601–e608, November 2013.
- [102] B. Jeurissen, M. Descoteaux, S. Mori, and A. Leemans. Diffusion MRI fiber tractography of the brain. *NMR in Biomedicine*, page e3785, September 2017.
- [103] H. Johansen-Berg, T.E. Behrens, E. Sillery, O. Ciccarelli, A.J. Thompson, S.M. Smith, and P.M. Matthews. Functional-anatomical validation and individual variation of diffusion tractography-based segmentation of the human thalamus. *Cerebral Cortex (New York, N.Y.: 1991)*, 15(1):31–39, January 2005.
- [104] F.A. Jolesz, editor. *Intraoperative imaging and image-guided therapy*. Springer, New York, 2014.
- [105] P. Kamina. *Anatomie clinique*. Maloine, Paris, 2009.
- [106] A. Kavallaris, D. Zygouris, A. Dafopoulos, I. Kalogiannidis, and E. Terzakis. Nerve sparing radical hysterectomy in early stage cervical cancer. Latest developments and review of the literature. *European Journal of Gynaecological Oncology*, 36(1):5–9, 2015.
- [107] E. Kellner, B. Dhital, V. Kiselev, and M. Reiser. Gibbs-ringing artifact removal based on local subvoxel-shifts. *Magnetic Resonance in Medicine*, 76(5):1574–1581, November 2016.
- [108] N.K. Kim, Y.W. Kim, and M.S. Cho. Total mesorectal excision for rectal cancer with emphasis on pelvic autonomic nerve preservation: Expert technical tips for robotic surgery. *Surgical Oncology*, pages 1–8, June 2015.
- [109] K. Kitajima, S. Takahashi, Y. Ueno, H. Miyake, M. Fujisawa, and K. Sugimura. Visualization of periprostatic nerve fibers before and after radical prostatectomy using diffusion tensor magnetic resonance imaging with tractography. *Clinical Imaging*, 38(3):302–306, May 2014.
- [110] A. Klein, J. Andersson, B.A. Ardekani, J. Ashburner, Brian Avants, M-C. Chiang, G.E. Christensen, D.E. Collins, J. Gee, P. Hellier, J.H. Song, M. Jenkinson, C. Lepage, D. Rueckert, P. Thompson, T. Vercauteren, R.P. Woods, J.J. Mann, and R.V. Parsey. Evaluation of 14 non-linear deformation algorithms applied to human brain MRI registration. *NeuroImage*, 46(3):786–802, July 2009.
- [111] H. M. Knight, N. J. Phillips, and P. D. Mouriquand. Female hypospadias: a case report. *Journal of Pediatric Surgery*, 30(12):1738–1740, December 1995.

-
- [112] T.R. Knösche, A. Anwander, M. Liptrot, and T.B. Dyrby. Validation of tractography: Comparison with manganese tracing. *Human Brain Mapping*, 36(10):4116–4134, October 2015.
- [113] S. Kornetsky. Research Blood Drawing Guidelines. The Clinical Investigation Policy and Procedure Manual, Boston Children’s Hospital, 2012.
- [114] S.J. Kraus, M.A. Levitt, and A. Peña. Augmented-pressure distal colostogram: the most important diagnostic tool for planning definitive surgical repair of anorectal malformations in boys. *Pediatric Radiology*, August 2017.
- [115] N.C. Lawes, T.R. Barrick, V. Murugam, N. Spierings, D.R. Evans, M. Song, and C.A. Clark. Atlas-based segmentation of white matter tracts of the human brain using diffusion tensor tractography and comparison with classical dissection. *NeuroImage*, 39:62–79, January 2008.
- [116] D. Le Bihan, E. Breton, D. Lallemand, P. Grenier, E. Cabanis, and M. Laval-Jeantet. MR imaging of intravoxel incoherent motions: application to diffusion and perfusion in neurologic disorders. *Radiology*, 161(2):401–407, November 1986.
- [117] D. Le Bihan, J. F. Mangin, C. Poupon, C. A. Clark, S. Pappata, N. Molko, and H. Chabriat. Diffusion tensor imaging: concepts and applications. *Journal of magnetic resonance imaging: JMRI*, 13(4):534–546, April 2001.
- [118] P.A. Lee, A. Nordenström, C.P. Houk, S.F. Ahmed, R. Auchus, A. Baratz, K. Baratz Dalke, L-M. Liao, K. Lin-Su, L.H. Looijenga, T. Mazur, H.F. Meyer-Bahlburg, P. Mouriquand, C.A. Quigley, D.E. Sandberg, E. Vilain, S. Witchel, and Global DSD Update Consortium. Global Disorders of Sex Development Update since 2006: Perceptions, Approach and Care. *Hormone Research in Paediatrics*, 85(3):158–180, 2016.
- [119] N. Lemos and S. Caroline. Laparoscopic anatomy of the autonomic nerves of the pelvis and the concept of nerve-sparing surgery by direct visualization of autonomic nerve bundles. *Fertility and Sterility*, pages 1–2, August 2015.
- [120] M. Levin. Left-right asymmetry in embryonic development: a comprehensive review. *Mechanisms of Development*, 122(1):3–25, January 2005.
- [121] M.A. Levitt, M. Patel, G. Rodriguez, D.S. Gaylin, and A. Pena. The tethered spinal cord in patients with anorectal malformations. *Journal of Pediatric Surgery*, 32(3):462–468, March 1997.
- [122] M.A. Levitt and A. Peña. Anorectal malformations. *Orphanet Journal of Rare Diseases*, 2:33, July 2007.
- [123] H. Li, L. Wang, S. Hao, D. Li, Z. Wu, L. Zhang, and J. Zhang. Identification of the Facial Nerve in Relation to Vestibular Schwannoma Using Preoperative Diffusion Tensor Tractography and Intraoperative Tractography-Integrated Neuronavigation System. *World Neurosurgery*, 107:669–677, November 2017.
- [124] P. Li, P. Liu, C. Chen, H. Duan, W. Qiao, and O.H. Ognami. The 3d reconstructions of female pelvic autonomic nerves and their related organs based on MRI: a first step towards neuronavigation during nerve-sparing radical hysterectomy. *European Radiology*, 28(11):4561–4569, November 2018.
- [125] W. Liao, T.M. Deserno, and K. Spitzer. Evaluation of Free Non-Diagnostic DICOM Software Tools. volume 6919, pages 691903–691903, 2008.
- [126] K.K. Lim, G. Noe, E. Hornsey, and R.P. Lim. Clinical applications of 3d T2-weighted MRI in pelvic imaging. *Abdominal Imaging*, 39:1052–1062, April 2014.
- [127] G. Lo Presti, M. Carbone, D. Ciriaci, D. Aramini, M. Ferrari, and V. Ferrari. Assessment of DICOM Viewers Capable of Loading Patient-specific 3d Models Obtained by Different Segmentation Platforms in the Operating Room. *Journal of Digital Imaging*, 28(5):518–527, October 2015.

-
- [128] L. Manganaro, M.G. Porpora, V. Vinci, S. Bernardo, P. Lodise, P. Sollazzo, M.E. Sergi, M. Saldari, G. Pace, G. Vittori, C. Catalano, and P. Pantano. Diffusion tensor imaging and tractography to evaluate sacral nerve root abnormalities in endometriosis-related pain: a pilot study. *European radiology*, 24(1):95–101, January 2014.
- [129] S. Mantoo, G. Meurette, V. Wyart, J. Hardouin, C. Cretolle, C. Capito, S. Sarnacki, G. Podevin, and P. A. Lehur. The impact of anorectal malformations on anorectal function and social integration in adulthood: report from a national database. *Colorectal Disease*, 15:e330–e335, June 2013.
- [130] J. Marescaux and M. Diana. Inventing the future of surgery. *World Journal of Surgery*, 39(3):615–622, March 2015.
- [131] J. Marescaux and M. Diana. Next step in minimally invasive surgery: hybrid image-guided surgery. *Journal of Pediatric Surgery*, 50(1):30–36, January 2015.
- [132] J.M. Maris. Recent advances in neuroblastoma. *The New England journal of medicine*, 362(23):2202–2211, June 2010.
- [133] H. Martelli. Tumeurs mésoenchymateuses malignes (TMM), 2008. DESC Chirurgie Pédiatrique.
- [134] D. Mattes, D.R. Haynor, H. Vesselle, T.K. Lewellyn, and W. Eubank. Nonrigid multimodality image registration. pages 1609–1620, San Diego, CA, July 2001.
- [135] G. Megali, V. Ferrari, C. Freschi, B. Morabito, F. Cavallo, G. Turini, E. Troia, C. Cappelli, A. Pietrabissa, O. Tonet, A. Cuschieri, P. Dario, and F. Mosca. EndoCAS navigator platform: a common platform for computer and robotic assistance in minimally invasive surgery. *The international journal of medical robotics + computer assisted surgery: MRCAS*, 4(3):242–251, September 2008.
- [136] P. Meignan. Étude du développement normal et pathologique du système nerveux périphérique pelvien : du fœtus à l’enfant porteur de malformations et tumeurs pelviennes. Master 2 report, IMAG2 laboratory, September 2019.
- [137] F. Mertens and R. Lothe. Nervous system: Peripheral nerve sheath tumors. *Atlas of Genetics and Cytogenetics in Oncology and Haematology*, (3), February 2011.
- [138] V. Minard-Colin, D. Walterhouse, G. Bisogno, H. Martelli, J. Anderson, D.A. Rodeberg, A. Ferrari, M. Jenney, S. Wolden, G. De Salvo, C. Arndt, J.H. Merks, S. Gallego, D. Schwob, C. Haie-Meder, C. Bergeron, M.C. Stevens, O. Oberlin, D. Hawkins, and International Society of Pediatric Oncology Sarcoma Committee, the Children’s Oncology Group, the Italian Cooperative Soft Tissue Sarcoma Group, and the European pediatric Soft tissue sarcoma Study Group. Localized vaginal/uterine rhabdomyosarcoma-results of a pooled analysis from four international cooperative groups. *Pediatric Blood & Cancer*, page e27096, May 2018. mori.
- [139] C. Mitter, A. Jakab, P.C. Brugger, G. Ricken, Gerlinde M. Gruber, D. Bettelheim, A. Scharrer, G. Langs, J.A. Hainfellner, D. Prayer, and G. Kasprian. Validation of In utero Tractography of Human Fetal Commissural and Internal Capsule Fibers with Histological Structure Tensor Analysis. *Frontiers in Neuroanatomy*, 9, December 2015.
- [140] S. Mori and P. B. Barker. Diffusion magnetic resonance imaging: its principle and applications. *The Anatomical Record*, 257(3):102–109, 1999.
- [141] S. Mori and P.C. van Zijl. Fiber tracking: principles and strategies - a technical review. *NMR in biomedicine*, 15(7-8):468–480, November 2002.
- [142] D. Moszkowicz. *Etude anatomique et fonctionnelle de l’innervation pelviperineale de la femme : cartographie tridimensionnelle de l’expression de la forme neurale de l’enzyme de synthese de l’oxyde nitrique (nNOS)*. PhD thesis, October 2015.

-
- [143] D. Moszkowicz, B. Alsaid, T. Bessedé, M. Zaitouna, C. Penna, G. Benoît, and F. Peschaud. Neural Supply to the Clitoris: Immunohistochemical Study with Three-Dimensional Reconstruction of Cavernous Nerve, Spongious Nerve, and Dorsal Clitoris Nerve in Human Fetus. *The Journal of Sexual Medicine*, 8:1112–1122, April 2011.
- [144] N. Mottet, Y. Chaussy, F. Auber, F. Guimiot, F. Arbez-Gindre, D. Riethmuller, C. Cretolle, and A. Benachi. How to Explore Fetal Sacral Agenesis Without Open Dysraphism: Key Prenatal Imaging and Clinical Implications. *Journal of Ultrasound in Medicine: Official Journal of the American Institute of Ultrasound in Medicine*, 37(7):1807–1820, July 2018.
- [145] C.O. Muller, C. Crétolle, T. Blanc, I. Alova, J-P. Jais, S. Lortat-Jacob, Y. Aigrain, M. Zérah, and S. Sarnacki. Impact of spinal dysraphism on urinary and faecal prognosis in 25 cases of cloacal malformation. *Journal of Pediatric Urology*, 10:1199–1205, December 2014.
- [146] C.O. Muller, E. Mille, A. Virzi, J-B. Marret, Q. Peyrot, A. Delmonte, L. Berteloot, P. Gori, T. Blanc, D. Grevent, N. Boddaert, I. Bloch, and S. Sarnacki. Integrating tractography in pelvic surgery: a proof of concept. *Journal of Pediatric Surgery Case Reports*, 48:101268, September 2019.
- [147] F.J. Muniz Neto, E.N. Kihara Filho, F.C. Miranda, L.A. Rosemberg, D.C. Santos, and A.K. Taneja. Demystifying MR Neurography of the Lumbosacral Plexus: From Protocols to Pathologies. *BioMed Research International*, 2018:9608947, 2018.
- [148] A. Naraghi, H. Awdeh, V. Wadhwa, G. Andreisek, and A. Chhabra. Diffusion Tensor Imaging of Peripheral Nerves. *Seminars in Musculoskeletal Radiology*, 19(02):191–200, March 2015.
- [149] O. Nempont, J. Atif, and I. Bloch. A constraint propagation approach to structural model based image segmentation and recognition. *Information Sciences*, 246:1–27, October 2013.
- [150] F.H. Netter. *Atlas of Human Anatomy*. Elsevier Health Sciences, May 2010.
- [151] L.N. Nguyen, L. Head, K. Witiuk, N. Punjani, R. Mallick, S. Cnossen, D.A. Fergusson, I. Cagianos, L.T. Lavallée, C. Morash, and R.H. Breau. The Risks and Benefits of Cavernous Neurovascular Bundle Sparing during Radical Prostatectomy: A Systematic Review and Meta-Analysis. *The Journal of Urology*, 198(4):760–769, October 2017.
- [152] K. Nyangoh Timoh, T. Bessedé, C. Lebacle, M. Zaitouna, J. Martinovic, Djibril Diallo, Maud Creze, Jean-Marc Chevallier, Emile Darai, Gérard Benoît, and David Moszkowicz. Levator ani muscle innervation: Anatomical study in human fetus. *Neurourology and Urodynamics*, pages 1464–1471, August 2017.
- [153] L.J. O’Donnell and C.F. Westin. Automatic Tractography Segmentation Using a High-Dimensional White Matter Atlas. *IEEE*, 26:1562–1575, October 2007.
- [154] B.R. O’Neill, D. Gallegos, A. Herron, C. Palmer, N.V. Stence, T.C. Hankinson, C. Corbett Wilkinson, and M.H. Handler. Use of magnetic resonance imaging to detect occult spinal dysraphism in infants. *Journal of Neurosurgery. Pediatrics*, 19(2):217–226, February 2017.
- [155] D. Orbach, S. Sarnacki, H.J. Brisse, M. Gauthier-Villars, P-H. Jarreau, V. Tsatsaris, A. Baruchel, M. Zerah, E. Seigneur, M. Peuchmaur, and F. Doz. Review Neonatal cancer. *Lancet Oncology*, 14:e609–e620, November 2013.
- [156] N. Otsu. A Threshold Selection Method from Gray-Level Histograms. *IEEE Transactions on Systems, Man, and Cybernetics*, 9(1):62–66, January 1979.
- [157] L.J. O’Donnell and C-F. Westin. An Introduction to Diffusion Tensor Image Analysis. *Neurosurgery Clinics of North America*, 22(2):185–196, April 2011.
- [158] A. Patel and K. Mehta. 3d Modeling and Rendering of 2d Medical Image. pages 149–152. *IEEE*, May 2012.

-
- [159] C.P. Pavlovich, B. Rocco, S.C. Druskin, and J.W. Davis. Urinary continence recovery after radical prostatectomy - anatomical/reconstructive and nerve-sparing techniques to improve outcomes. *BJU international*, 120(2):185–196, August 2017.
- [160] E.J. Perlman and C. Kretschmar. Pediatric germ cell tumors. *Cancer Treatment and Research*, 92:163–200, 1997.
- [161] A. Peña. Anorectal malformations. *Seminars in Pediatric Surgery*, 4(1):35–47, February 1995.
- [162] C. Pierpaoli, P. Jezzard, P. J. Basser, A. Barnett, and G. Di Chiro. Diffusion tensor MR imaging of the human brain. *Radiology*, 201(3):637–648, December 1996.
- [163] C. Piolat, F. Lavrand, and S. Sarnacki. Séquelles des chirurgies thoraco-abdomino-pelviennes réalisées pour tumeurs chez l’enfant. *Bulletin du Cancer*, 102:586–592, June 2015.
- [164] F.P. Prete, A.F. Pezzolla, F. Prete, M. Testini, R. Marzaioli, A. Patriti, R.M. Jimenez-Rodriguez, A. Gurrado, and G.F. Strippoli. Robotic Versus Laparoscopic Minimally Invasive Surgery for Rectal Cancer: A Systematic Review and Meta-analysis of Randomized Controlled Trials. *Annals of Surgery*, 267(6):1034–1046, June 2018.
- [165] N. Proscia, T.A. Jaffe, A.M. Neville, C.L. Wang, B.M. Dale, and E.M. Merkle. MRI of the Pelvis in Women: 3d Versus 2d T2-Weighted Technique. *American Journal of Roentgenology*, 195:254–259, 2010.
- [166] P. Puri and M. Höllwarth. *Pediatric Surgery*. Springer Berlin Heidelberg, Berlin, Heidelberg, 2006.
- [167] J.M. Ream. Advances in T1-Weighted and T2-Weighted Imaging in the Abdomen and Pelvis. *Radiologic Clinics of NA*, 53:583–598, May 2015.
- [168] D.E. Reichman and M.R. Laufer. Mayer-Rokitansky-Küster-Hauser syndrome: fertility counseling and treatment. *Fertility and Sterility*, 94(5):1941–1943, October 2010.
- [169] N. Renier, Z. Wu, D.J. Simon, J. Yang, P. Ariel, and M. Tessier-Lavigne. iDISCO: a simple, rapid method to immunolabel large tissue samples for volume imaging. *Cell*, 159(4):896–910, November 2014.
- [170] M. Riccabona. Imaging of the neonatal genito-urinary tract. *European Journal of Radiology*, 60(2):187–198, November 2006.
- [171] R. Rintala, L. Mildh, and H. Lindahl. Fecal continence and quality of life in adult patients with an operated low anorectal malformation. *Journal of Pediatric Surgery*, 27:902–905, July 1992.
- [172] R. Rintala, L. Mildh, and H. Lindahl. Fecal continence and quality of life for adult patients with an operated high or intermediate anorectal malformation. *Journal of Pediatric Surgery*, 29:777–780, June 1994.
- [173] J. Rod, C. Cretolle, L. Faivre, C. Jacquot, O. Yacoub, P. Ravasse, N. Cheynel, and S. Sarnacki. Malignant transformation of presacral mass in Currarino syndrome. *Pediatric Blood & Cancer*, 66(6):e27659, June 2019.
- [174] A. J. Ross, V. Ruiz-Perez, Y. Wang, D. M. Hagan, S. Scherer, S. A. Lynch, S. Lindsay, E. Custard, E. Belloni, D. I. Wilson, R. Wadey, F. Goodman, K. H. Orstavik, T. Monclair, S. Robson, W. Reardon, J. Burn, P. Scambler, and T. Strachan. A homeobox gene, HLXB9, is the major locus for dominantly inherited sacral agenesis. *Nature Genetics*, 20(4):358–361, December 1998.
- [175] X. Santarelli, G. Garbin, M. Ukmar, and R. Longo. Dependence of the fractional anisotropy in cervical spine from the number of diffusion gradients, repeated acquisition and voxel size. *Magnetic Resonance Imaging*, 28(1):70–76, January 2010.
- [176] S. Sarnacki. Ovarian tissue cryopreservation in children with cancer. *Lancet Oncology*, 15:1049–1050, August 2014.

-
- [177] S. Sarnacki and H.J. Brisse. Surgery of Ovarian Tumors in Children. *Hormone Research in Paediatrics*, 75:220–224, 2011.
- [178] M. Schmidt, G. Kasprian, G. Amann, D. Duscher, and O.C. Aszmann. Diffusion tensor tractography for the surgical management of peripheral nerve sheath tumors. *Neurosurgical Focus*, 39:E17–6, September 2015.
- [179] E. Schmiedeke, I. Blaauw, M. Lacher, S. Grasshoff-Derr, A.G. Vazquez, S. Giuliani, P. Midrio, P. Gamba, B. D. Iacobelli, P. Bagolan, G. Brisighelli, E. Leva, C. Cretolle, S. Sarnacki, P. Broens, C. Sloots, I. Rooij, N. Schwarzer, D. Aminoff, M. Haanen, and E. Jenetzky. Towards the perfect ARM center: the European Union’s criteria for centers of expertise and their implementation in the member states. A report from the ARM-Net. *Pediatric Surgery International*, 31:741–745, July 2015.
- [180] J. Schober, T. Cooney, D. Pfaff, L. Mayoglou, and N. Martin-Alguacil. Innervation of the labia minora of prepubertal girls. *Journal of Pediatric and Adolescent Gynecology*, 23(6):352–357, December 2010.
- [181] A. K. Seehaus, A. Roebroek, O. Chiry, D.-S. Kim, I. Ronen, H. Bratzke, R. Goebel, and R. A. W. Galuske. Histological Validation of DW-MRI Tractography in Human Postmortem Tissue. *Cerebral Cortex*, 23(2):442–450, February 2013.
- [182] Y. R. Shin, S. E. Rha, B. G. Choi, S. N. Oh, M. Y. Park, and J. Y. Byun. Uterine cervical carcinoma: a comparison of two- and three-dimensional T2-weighted turbo spin-echo MR imaging at 3.0 T for image quality and local-regional staging. *European Radiology*, 23:1150–1157, July 2012.
- [183] J.M. Soares, P. Marques, V. Alves, and N. Sousa. A hitchhiker’s guide to diffusion tensor imaging. *Frontiers in Neuroscience*, 7, 2013.
- [184] L. Soler, S. Nicolau, J. B. Fasquel, V. Agnus, A. Charnoz, A. Hostettler, J. Moreau, C. Forest, D. Mutter, and J. Marescaux. Virtual reality and augmented reality applied to laparoscopic and notes procedures. In *2008 5th IEEE International Symposium on Biomedical Imaging: From Nano to Macro*, pages 1399–1402, May 2008.
- [185] W.M. Spees, N. Buhl, P. Sun, J.J. Ackerman, J.J. Neil, and J.R. Garbow. Quantification and compensation of eddy-current-induced magnetic-field gradients. *Journal of Magnetic Resonance*, 212(1):116–123, September 2011.
- [186] V. Staedtke, R-Y. Bai, and J.O Blakeley. Cancer of the Peripheral Nerve in Neurofibromatosis Type 1. *Neurotherapeutics: The Journal of the American Society for Experimental NeuroTherapeutics*, 14(2):298–306, April 2017.
- [187] A. A. Stec, A. Tekes, G. Ertan, T. M. Phillips, T. E. Novak, M. Solaiyappan, T. A. G. M. Huisman, P. D. Sponseller, and J. P. Gearhart. Evaluation of Pelvic Floor Muscular Redistribution After Primary Closure of Classic Bladder Exstrophy by 3-Dimensional Magnetic Resonance Imaging. *Journal of Urology*, 188:1535–1542, October 2012.
- [188] V.J. Sydnor, A.M. Rivas-Grajales, A.E. Lyall, F. Zhang, S. Bouix, S. Karmacharya, M.E. Shenton, C-F. Westin, N. Makris, D. Wassermann, L.J. O’Donnell, and M. Kubicki. A comparison of three fiber tract delineation methods and their impact on white matter analysis. *NeuroImage*, 178:318–331, September 2018.
- [189] A. Tagliafico, M. Calabrese, M. Puntoni, D. Pace, G. Baio, C.E. Neumaier, and C. Martinoli. Brachial plexus MR imaging: accuracy and reproducibility of DTI-derived measurements and fibre tractography at 3.0-T. *European Radiology*, 21(8):1764–1771, August 2011.
- [190] S.T. Tang, G.Q. Cao, Y.Z. Mao, Y. Wang, S.W. Li, Y. Yang, and Q.S. Tong. Clinical value of pelvic 3-dimensional magnetic resonance image reconstruction in anorectal malformations. *Journal of Pediatric Surgery*, 44:2369–2374, December 2009.

-
- [191] T. Taoka, H. Hirabayashi, H. Nakagawa, M. Sakamoto, K. Myochin, Shinji Hirohashi, Satoru Iwasaki, Toshisuke Sakaki, and Kimihiko Kichikawa. Displacement of the facial nerve course by vestibular schwannoma: Preoperative visualization using diffusion tensor tractography. *Journal of Magnetic Resonance Imaging*, 24:1005–1010, 2006.
- [192] A. Tekes, G. Ertan, M. Solaiyappan, A. A. Stec, P. D. Sponseller, T. A. Huisman, and J. P. Gearhart. 2d and 3d MRI features of classic bladder exstrophy. *Clinical Radiology*, 69:e223–e229, May 2014.
- [193] F. Tensaouti, I. Lahlou, P. Clarisse, J.A. Lotterie, and I. Berry. Quantitative and reproducibility study of four tractography algorithms used in clinical routine. *Journal of Magnetic Resonance Imaging*, 34:165–172, May 2011.
- [194] P. Tortori-Donati, A. Rossi, and A. Cama. Spinal dysraphism: a review of neuroradiological features with embryological correlations and proposal for a new classification. *Neuroradiology*, 42(7):471–491, September 2000.
- [195] G. Totonelli, R. Messina, F. Morini, G. Mosiello, Paolo Palma, M. Scuglia, B.D. Iacobelli, and P. Bagolan. Embryological and clinical implications of the association between anorectal malformations and spinal dysraphisms. *Pediatric Surgery International*, 33(8):843–847, August 2017.
- [196] J-D. Tournier, S. Mori, and A. Leemans. Diffusion tensor imaging and beyond. *Magnetic Resonance in Medicine*, 65(6):1532–1556, June 2011.
- [197] R. Trivedi, N. Husain, R.K. Rathore, S. Saksena, S. Srivastava, G.K. Malik, V. Das, M. Pradhan, C.M. Pandey, and R.K. Gupta. Correlation of Diffusion Tensor Imaging with Histology in the Developing Human Frontal Cerebrum. *Developmental Neuroscience*, 31(6):487–496, 2009.
- [198] G. Valeri, F.A. Mazza, S. Maggi, D. Aramini, L. La Riccia, G. Mazzoni, and A. Giovagnoni. Open source software in a practical approach for post processing of radiologic images. *La radiologia medica*, 120(3):309–323, March 2015.
- [199] P. van der Jagt, P. Dik, M. Froeling, T.C. Kwee, R. Nievelstein, B. ten Haken, and A. Leemans. Architectural configuration and microstructural properties of the sacral plexus: a diffusion tensor MRI and fiber tractography study. *NeuroImage*, 62(3):1792–1799, September 2012.
- [200] M.I. Vargas, M. Viallon, D. Nguyen, J. Delavelle, and M. Becker. Diffusion tensor imaging (DTI) and tractography of the brachial plexus: feasibility and initial experience in neoplastic conditions. *Neuroradiology*, 52(3):237–245, March 2010.
- [201] J. Veraart, E. Fieremans, and D.S. Novikov. Diffusion MRI noise mapping using random matrix theory: Diffusion MRI Noise Mapping. *Magnetic Resonance in Medicine*, 76(5):1582–1593, November 2016.
- [202] J. Veraart, D.S. Novikov, D. Christiaens, B. Ades-aron, J. Sijbers, and E. Fieremans. Denoising of diffusion MRI using random matrix theory. *NeuroImage*, 142:394–406, November 2016.
- [203] A. Verma and U. Bashir. Diffusion weighted imaging. <https://radiopaedia.org/articles/diffusion-weighted-imaging-1>.
- [204] H.P. Versteegh, I. van Rooij, M. Levitt, C. Sloots, R. Wijnen, and I. de Blaauw. Long-term follow-up of functional outcome in patients with a cloacal malformation: A systematic review. *Journal of Pediatric Surgery*, 48:2343–2350, November 2013.
- [205] A. Virzì, P. Gori, C. O. Muller, E. Mille, Q. Peyrot, L. Berteloot, N. Boddaert, S. Sarnacki, and I. Bloch. Segmentation of Pelvic Vessels in Pediatric MRI Using a Patch-Based Deep Learning Approach. In *Data Driven Treatment Response Assessment and Preterm, Perinatal, and Paediatric Image Analysis*, volume 11076, pages 97–106. Springer International Publishing, Cham, 2018.

-
- [206] A. Virzì, J. B. Marret, C. O. Muller, L. Berteloot, N. Boddaert, S. Sarnacki, and I. Bloch. A new method based on template registration and deformable models for pelvic bones semi-automatic segmentation in pediatric MRI. pages 323–326, 2017.
- [207] A. Virzì, C.O. Muller, J-B. Marret, E. Mille, L. Berteloot, D. Grévent, N. Boddaert, P. Gori, S. Sarnacki, and I. Bloch. Comprehensive Review of 3d Segmentation Software Tools for MRI Usable for Pelvic Surgery Planning. *Journal of Digital Imaging*, June 2019.
- [208] S. Wakana, A. Caprihan, M.M. Panzenboeck, J.H. Fallon, M. Perry, R.L. Gollub, K. Hua, J. Zhang, H. Jiang, P. Dubey, A. Blitz, P. van Zijl, and S. Mori. Reproducibility of quantitative tractography methods applied to cerebral white matter. *NeuroImage*, 36:630–644, July 2007.
- [209] S. Wakana, H. Jiang, L.M. Nagae-Poetscher, P.C. van Zijl, and S. Mori. Fiber tract-based atlas of human white matter anatomy. *Radiology*, 230(1):77–87, January 2004.
- [210] J.Y. Wang, H. Abdi, K. Bakhadirov, R. Diaz-Arrastia, and M.D. Devous. A comprehensive reliability assessment of quantitative diffusion tensor tractography. *NeuroImage*, 60(2):1127–1138, April 2012.
- [211] S. A. Warne, D. T. Wilcox, S. Creighton, and P. G. Ransley. Long-Term Gynecological Outcome of Patients with Persistent Cloaca. *The Journal of Urology*, 170:1493–1496, October 2003.
- [212] D. Wassermann, N. Makris, Y. Rathi, M. Shenton, R. Kikinis, M. Kubicki, and C-F. Westin. The white matter query language: a novel approach for describing human white matter anatomy. *Brain Structure & Function*, 221(9):4705–4721, December 2016.
- [213] D. Wassermann, N. Makris, Y. Rathi, M. Shenton, R. Kikinis, M. Kubicki, and C_F. Westin. On describing human white matter anatomy: the white matter query language. *MICCAI*, 16(Pt 1):647–654, 2013.
- [214] M. Weber, M. Mickoleit, and J. Huisken. Light sheet microscopy. *Methods in Cell Biology*, 123:193–215, 2014.
- [215] V.J. Wedeen, D.L. Rosene, R. Wang, G. Dai, F. Mortazavi, P. Hagmann, J.H. Kaas, and W-Y. Tseng. The geometric structure of the brain fiber pathways. *Science*, 335(6076):1628–1634, March 2012.
- [216] C.H. Wijers, I. de Blaauw, C.L. Marcelis, R.M. Wijnen, H. Brunner, P. Midrio, P. Gamba, M. Clementi, E.D. Bigler, N. Zwink, H. Reutter, E. Bartels, S. Grasshoff-Derr, S. Holland-Cunz, S. Hosie, S. Märzheuser, E. Schmiedeke, C. Crétolle, S. Sarnacki, M.A. Levitt, N.V. Knoers, N. Roeleveld, and I.A. van Rooij. Research perspectives in the etiology of congenital anorectal malformations using data of the International Consortium on Anorectal Malformations: evidence for risk factors across different populations. *Pediatric Surgery International*, 26:1093–1099, August 2010.
- [217] A. R. Wijsmuller, C. Giraudeau, J. Leroy, G. J. Kleinrensink, E. Rociu, L. G. Romagnolo, A. G. F. Melani, V. Agnus, M. Diana, L. Soler, B. Dallemagne, J. Marescaux, and D. Mutter. A step towards stereotactic navigation during pelvic surgery: 3d nerve topography. *Surgical Endoscopy*, 32(8):3582–3591, August 2018.
- [218] Wikipedia. Diffusion MRI.
- [219] Wikipedia. Test de Student.
- [220] M.J. Witvliet, A. Slaar, H.A. Heij, and A.F. van der Steeg. Qualitative analysis of studies concerning quality of life in children and adults with anorectal malformations. *Journal of Pediatric Surgery*, 48:372–379, February 2013.

-
- [221] Z. Xue, X. Zhu, and Y. Teng. Comparison of Nerve-Sparing Radical Hysterectomy and Radical Hysterectomy: a Systematic Review and Meta-Analysis. *International Journal of Experimental Cellular Physiology, Biochemistry, and Pharmacology*, 38(5):1841–1850, 2016.
- [222] A. Yendiki. Automated probabilistic reconstruction of white-matter pathways in health and disease using an atlas of the underlying anatomy. *Neuroinformatics*, pages 1–12, October 2011.
- [223] M. Zerah and A.V. Kulkarni. Spinal cord malformations. *Handbook of clinical neurology*, 112:975–991, 2013.
- [224] Y. Zhang, J. Zhang, K. Oishi, A.V. Faria, H. Jiang, X. Li, K. Akhter, P. Rosa-Neto, B. Pike, A. Evans, A.W. Toga, R. Woods, J.C. Mazziotta, M.I. Miller, P.C. van Zijl, and S. Mori. Atlas-guided tract reconstruction for automated and comprehensive examination of the white matter anatomy. *NeuroImage*, 52(4):1289–1301, October 2010.